Sapienza - University of Rome

DEPARTMENT OF MECHANICAL AND AEROSPACE ENGINEERING
Ph.D. degree in Aeronautical and Space Engineering

Numerical study of transonic buffet on supercritical airfoil with different boundary layer states

Candidate:
Antonio Memmolo

Thesis advisor:
Prof. Sergio Pirozzoli

Submitted in partial fulfillment of the requirements for the degree of Doctor of Philosophy in Aeronautical and Space Engineering

Abstract

Accurate numerical simulations of flow over airfoils play an increasingly important role in the design of aircraft major components such as wings and turbomachinery blades. These lifting devices often operate in demanding aerodynamic conditions for optimum performances, and may experience the presence of shock waves in operating conditions. Shocks may become unsteady under specific conditions, undergoing a large-scale, low-frequency periodic motion, which affects the entire flow-field. This unsteady phenomenon, named *transonic buffet*, is the subject of the present numerical investigation, with an oscillating shock over the suction side of the airfoil.

In this study, a range of transonic Mach numbers and angles of incidence are considered, but the bulk of the analysis is carried out for flow conditions at free-stream Mach number $M_\infty = 0.7$ and angle of incidence $\alpha = 7°$, which show well established buffet. Large-eddy simulations (LES) with natural and forced transition carried out at chord Reynolds number $Re_c = 3 \times 10^6$ clearly highlight the effects of the incoming boundary-layer state on the shock oscillations. While a laminar upstream boundary layer yields weak oscillations of the shock, a turbulent incoming boundary layer yields significant buffet. The LES database has been used to establish veracity (or not) of suggested buffet pathways, mainly based on the alleged existence of an acoustic feedback loop. This mechanism is actually found to consist of two separate patterns: coherent pressure disturbances convected from the shock to the trailing edge, and acoustic waves scattered at the trailing edge, feeding the shock motion. Additional exploration of the pressure side role in the unsteadiness reveals that is has but marginal effect on the phenomenon.

Direct numerical simulations (DNS) at lower Reynolds number ($Re_c = 3 \times 10^5$) suggest a reversal in the previously observed trend. In this case, a laminar incoming boundary layer yields stronger buffet as compared to its turbulent counterpart, highlighting strong dependence of the buffet phenomenon on the Reynolds number when natural transition is considered. In order to passively control buffet, we consider devices whose design is similar to large-eddy break-up devices (LEBU), consisting of a thin circular-arc airfoil placed between shock and trailing edge, with the main goal of: i) breaking the eddies originating at the shock, responsible for the acoustic scattering at the trailing edge; ii) manipulating the acoustic field in the aft part of the airfoil. RANS simulations show potential for this kind of device for complete stabilization of buffet. On the other hand, DNS shows that the device is able to curtail the buffet, but not to eliminate it. Additional tests are needed in order to assess the effectiveness of the control device, whose practical impact might be very large.

Acknowledgements

My first thought goes necessarily to my advisor Prof. Sergio Pirozzoli for his daily support and advice. Without him, this work wouldn't be possible. I would like to thank Prof. Matteo Bernardini for his trust and his financial support, Prof. Paolo Orlandi for our stimulating discussions, and Dr. Davide Modesti, together we also shared hard times. My gratitude goes also to prof. Renato Paciorri for his helpful suggestions on the first review of this manuscript. I further acknowledge that most of the results shown in this manuscript have been achieved using the PRACE Research Infrastructure resource MARCONI based at CINECA, Casalecchio di Reno, Italy.

I must also thank my friends Davide and Lorenzo, for teaching me how to turn bitterness in joy and how funny it can be writing a script. Last but not least, I have to thank my parents. Without them, I wouldn't have come so far

Contents

List of Figures

List of Tables

Nomenclature

C_d	Drag coefficient
C_l	Lift coefficient
C_p	Pressure coefficient
E	Total internal energy per unit mass
$G(\mathbf{r}, \mathbf{x})$	Filter function for LES
H	Total enthalpy per unit mass
K	Thermal conductivity coefficient
K_T	Turbulent thermal conductivity coefficient
L_s	Distance of trailing edge from mean shock
L_v	Size of coherent pressure disturbances
L_z	Domain spanwise length
$L_{T.E.}$	Length of the trailing edge splitter plate
M	Mach number
M_L	Lower bound on Mach number for buffet of first kind
M_U	Upper bound on Mach number for buffet of first kind
M_s	Relative Mach number ahead of the shock
M_∞	Free-stream Mach number
N_x	Number of cells in the airfoil tangential direction
N_y	Number of cells in the wall-normal direction
N_z	Number of cells in the spanwise direction
Pr	Prandtl number ($Pr = 0.72$)
Pr_T	Turbulent Prandtl number ($Pr_T = 0.6$, 0.9)
R	Gas constant per unit mass ($p = \rho RT$)
S_{ij}	Strain tensor $S_{ij} = \frac{1}{2}\left(\frac{\partial u_i}{\partial x_j} + \frac{\partial u_j}{\partial x_i}\right)$
St_c	Chord based Strouhal number
$St_{c,\,Lee}$	Chord based Strouhal number obtained from Lee's model
T	Temperature
Δ	Filter width for LES, grid size for DES, DDES
Re_c	Chord based Reynolds number
$\hat{E}$	Total internal energy of averaged quantities
$\hat{H}$	Total enthalpy of averaged quantities
$\mathbf{F}'$	$\mathbf{F}' = \mathbf{F}_j \hat{n}_j$
$\mathbf{F}_j$	Generalized flux vectors
$\mathbf{G}'$	$\mathbf{G}' = \mathbf{G}_j \hat{n}_j$
$\mathbf{G}_j$	Viscous flux vectors
$\mathbf{P}_j$	Vectors accounting for pressure contribution to stresses
$\mathbf{U}$	Vector of conservative variables
$\mathbf{n_f}$	Normal to the wavefront
$\mathbf{n_w}$	Normal to the wall

$\mathbf{n}$	Integration surface normal
$\mathbf{q}$	Convective heat flux
$\mathbf{s}$	Wave-slowness vector
$\mathbf{v}$	Ambient medium velocity
$\mathbf{x_0}$	Starting point for the computation of $\mathbf{x}$
$\mathbf{x}$	Trajectory of acoustic disturbance
$\mathbf{x}^c_{i,j}$	Centroid of cell (i, j)
$\mathbf{x}^v_{i+1/2,j+1/2}$	Coordinate of vertex at the intersection of faces $i + 1/2$ and $j + 1/2$
$\mathcal{K}$	Transonic similarity parameter
$\mathcal{V}_{i,j,k} = \mathcal{V}_{i,j}$	Volume of cell (i, j, k)
$\overline{\mathbf{q}}^R$	Turbulent heat flux
$\overline{\mathbf{q}}^T$	Total heat flux
$\overline{u_i'^2}$	Mean square of velocity fluctuations in i direction ($i = 1$ wall parallel, $i = 2$ wall normal)
a	Sound speed
a_∞	Free-stream sound speed
c	Chord
c_p	Specific heat at constant pressure
c_v	Specific heat at constant volume
d	Distance from nearest wall
d_t	Distance from the trip (Spalart-Allmaras model)
e	Internal energy per unit mass
f	Frequency
f_{Lee}	Frequency obtained from Lee's model
h	Enthalpy per unit mass
h_{max}	Maximum airfoil thickness
k	Turbulent kinetic energy
k_r	Reduced frequency ($k_r = \frac{\Omega(c/2)}{u_\infty}$)
p	Pressure
p_{RMS}	Root Mean Square of pressure fluctuations
p_{x_0}	Pressure-time signal in x_0 (reference for cross-correlation)
s	Distance (curvilinear coordinate) between signals to be cross-correlated
t	Time
t_c	Travel time of the instability waves originating at the shock foot
t_s	Travel time of acoustic waves from trailing edge to shock (pressure side)
t_u	Travel time of acoustic waves from trailing edge to shock (suction side)
u_a	Estimate of the upstream propagating acoustic disturbances
u_d	Tangential convection velocity of coherent pressure disturbances
u_i	Velocity components
u_∞	Free-stream velocity
x, y	Cartesian coordinates
x_0	Reference point for cross-correlation
x_i	$i = 1, 2, 3$, Alternative expression for Cartesian coordinates
Ω	Angular frequency
α	Angle of incidence
δ_{ij}	Kronecker delta
γ	Specific heat ratio
$\hat{\nu}$	Spalart-Allmaras turbulence model variable
κ	Kármán constant
λ	Second coefficient of viscosity
μ	Dynamic viscosity
μ_T	Turbulent viscosity

ν	Kinematic viscosity
ν_T	Kinematic eddy viscosity
ω	Vorticity
$\overline{\sigma}_{ij}^{R}$	Reynolds stresses
$\overline{\sigma}_{ij}^{T}$	Total viscous stresses
$\overline{\varphi}$	Averaged (filtered) quantity
$\overline{\varphi}_{i+1/2}$	Arithmetic average on face $i+1/2$
ρ	Density
σ_{ij}	Viscous stresses
τ	Cross-correlation independent variable (time delay)
$\tilde{\varphi}$	Favre averaged (filtered) quantity
ε	Rate of dissipation of turbulent kinetic energy
φ'	Quantity fluctuations, such that $\varphi = \overline{\varphi} + \varphi'$
φ''	Quantity fluctuations, such that $\varphi = \tilde{\varphi} + \varphi''$
$\Delta\hat{u}$	Difference between velocity at the field point and at the trip (Spalart-Allmaras model)
$\Delta\omega_t$	Wall vorticity at the trip (Spalart-Allmaras model)
Δt	Time-step
Δx_t	Grid spacing along the wall at the trip (Spalart-Allmaras model)
Δy	Wall-normal spacing at the wall
Δy^+	Wall normal spacing at the wall, in wall units

Chapter 1

Introduction

1.1 Introduction

Literally, "buffeting" is the dynamical answer of a structure subjected to unsteady loads; even for a fixed structure, the aerodynamic force may become unsteady in subsonic, transonic and supersonic regimes. One of the most critical scenarios is the transonic one, where the shock usually present at this Mach number may start a periodic motion, with a consequent low-frequency unsteadiness which involves the entire flow-field. The essential ingredients of this large-scale unsteadiness seem to be the interaction of a shock-wave with a boundary layer and the presence of a subsonic flow-field downstream of this interaction, which allows the upstream propagation of perturbations. When downstream of the interaction the flow is still supersonic, the flow-field appears to be free of these large-scale instabilities.

Generally, by saying "transonic buffet" one refers directly to the shock motion; the phenomenon is also named as "shock buffet" or "shock-induced oscillations". The shock motion occurs at certain combinations of Mach number and angle of incidence, leading to flow alterations which cause strong variation of the aerodynamic coefficients, dangerous both for the control and for the integrity of the structure, thus limiting the flight envelope. The instability is inherent to the flow, showing itself in computations where the structure is kept exactly fixed. When the phenomenon is observed experimentally, the periodic variation of the aerodynamic loads leads to structure vibrations, making possible the presence of resonance phenomena which may amplify the structure oscillations. We will focus our attention on flows over airfoils, but those large-scale unsteadinesses involving shock motion are found also in other circumstances, such as for inlet buzz, engine unstart or on turbo-machinery blades. The aerodynamic performance in these applications strongly depends on the unsteady interaction between shock and boundary layer.

In the following we will try to give a description of the main aspects of transonic buffet over an airfoil, a classification of the phenomenon, the mechanisms suggested in literature to explain it, and some possible strategies to enhance the stability boundaries of the phenomenon.

1.2 Main features

1.2.1 Viscous phenomenon

Transonic buffet is a viscous phenomenon. Mabey (1980) in his work on biconvex airfoils of different thicknesses at zero angle of incidence justifies this assertion using the following arguments:

- If the phenomenon is only tied to the external inviscid flow, the transonic similarity parameter in correspondence of the start and stop of the instability should be the same for the different thicknesses he tries, since they belong to the same airfoil family (affinely similar airfoils). Fig. 1.1 clearly shows that this is not the case
- The instability disappears in simulations where the viscosity is set to zero

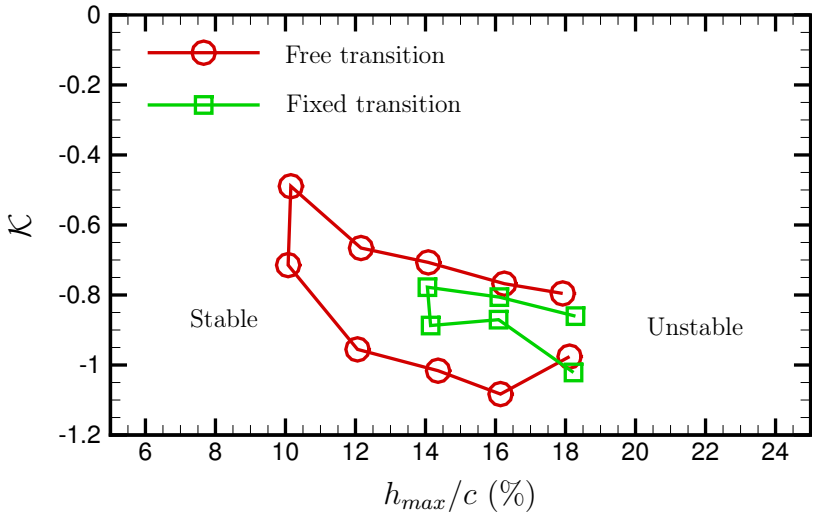

Figure 1.1: *Stability boundary as a function of $\mathcal{K}$ (transonic similarity parameter) and h_{max}/c (relative thickness) on biconvex circular arc airfoil at zero angle of incidence. If transonic buffet is only tied to the external inviscid flow, the curves should have been horizontal lines. Data from Fig. 10 of (Mabey, 1980).*

The viscous nature of the unsteady phenomenon is also suggested from the strong correlation there is between shock motion and near wake. More support to this hypothesis is offered by Edwards' results (Edwards, 1996), who uses a coupling method between the external inviscid solution and the inner viscous solution to accurately reproduce the buffet stability boundaries.

One of the key phenomenon for the triggering of the instability appears to be the Shock/Boundary Layer Interaction (SBLI), since it is not present in non viscous flows. Both numerically and experimentally disturbances originating at the shock foot have been detected, which are a direct consequence of SBLI and which are

thought to be the basis for the self-sustaining of the periodic shock motion (Lee, 2001).

Crouch et al. (2007) were the first to apply global instability theory on a mean field obtained with a turbulence model to recover transonic buffet stability boundaries over a NACA-0012 airfoil at different angles of incidence. Their analysis is able to detect buffet onset when also perturbations on $\hat{\nu}$ (Spalart-Allmaras turbulence model variable) are allowed, while the same conditions are stable when the $\hat{\nu}$ perturbations are disregarded, thus providing further support to the hypothesis of buffet being a viscous phenomenon, since the turbulence model variable only acts as an increase of the physical viscosity. In their flow picture, the unsteadiness is characterized by a coupled modulation of the shock and the separated shear layer.

1.2.2 SBLI description and classification

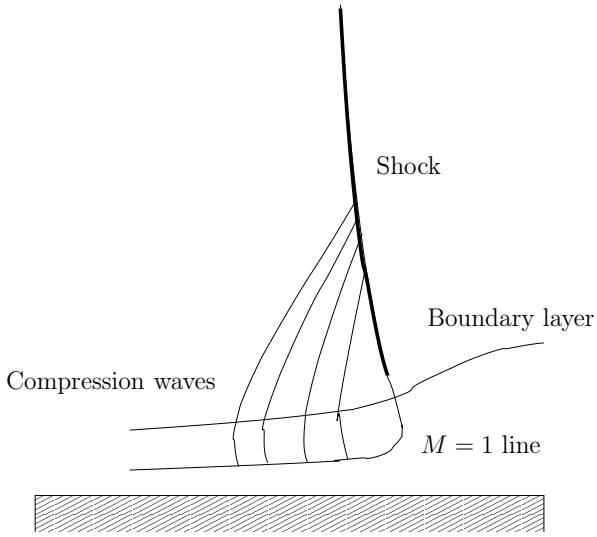

Figure 1.2: *Sketch of a weak transonic SBLI.*

Since SBLIs play an important role in the phenomenon under investigation, it is appropriate to characterize them. They are a complex phenomenon, involving a mutual interaction between the shock and the boundary layer. If we first consider the effect of the impinging shock, it imposes a strong adverse pressure gradient on the boundary layer, which may cause thickening or separation of the boundary layer, also upstream of the shock region since the inner part of the boundary layer is always subsonic and the upstream propagation of disturbances is not inhibited. Since the subsonic part of the boundary layer cannot hold a shock wave, the pressure adjusts more gradually, and the pressure rise is spread this way also ahead of the main shock. On the other hand, the thickening of the boundary layer causes a deflection of the supersonic streamlines, bringing an isentropic compression of the flow ahead of the shock region. The compression waves can then coalesce to bring another shock, which interacts with the main shock, and since part of the pressure rise occurred ahead of it, it weakens in the interaction process in the part closer to the boundary

layer, until it vanishes when it reaches the boundary layer sonic line. This mutual interaction can greatly affect the flow past a transonic airfoil or inside an air-intake. If the shock is not strong enough to cause separation, the flow structure is relatively simple, predominantly inviscid (a simple sketch is drawn in Fig. 1.2); on the other hand, if the shock is strong enough to cause separation, the entire flow-field may be affected, with the formation of intense vortices or complex shock patterns (Babinsky and Harvey, 2011), as in the case of transonic buffet.

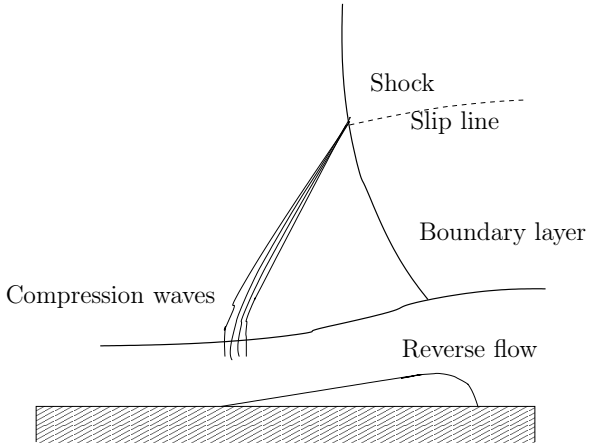

Figure 1.3: *Sketch of a strong transonic SBLI.*

For what concerns possible scenarios on transonic flows over airfoils, the first to investigate the phenomenon were Liepmann (1946) and Ackeret et al. (1947), who found multiple shocks for the laminar boundary layer for Mach numbers close to one, with their number decreasing as the Mach number is increased. Eventually, only a λ shock is present, with the oblique shock coming from the merging of compression waves generated ahead of the main shock, and the latter being normal (a simple sketch is drawn in Fig. 1.3). The figure also shows the slip line, which accounts for the different levels of mechanical energy dissipation encountered by fluid passing through the single shock and the shock pair. No pressure jumps are found at wall, since the laminar boundary layer cannot withstand them, and the adverse pressure gradient effect is spread on much longer distances, in particular in locations upstream the shock. In the turbulent case, only a normal shock is found on the airfoils, and the pressure rise is sharper than in the laminar counterpart. Also, unlike the incompressible case, in the vicinity of the shock the pressure gradient has wall normal and wall parallel components of comparable magnitude. Soon after the pressure rise in correspondence of the shock, there is an expansion, due to a readjustment of the two-dimensional, inviscid flow field, which is typical of the transonic interaction and which increases with the shock strength. Both in the laminar and turbulent cases, the boundary layer thickness increases considerably. Chapman et al. (1958) investigated the flow separation associated with steps, bases, compression corners, curved surfaces, shock-wave boundary-layer reflections, and configurations producing leading-edge separation. They found that the transition location relative to the reattachment and separation positions is the principal

variable controlling pressure distribution in the separated flow. By this means of classification they state rather general results regarding the steadiness of flow and the influence of Reynolds number within each regime.

Their conclusions apply to boundary layers of constant pressure preceding two-dimensional separated region. "Pure laminar" separations (transition downstream of reattachment zone) are steady and only show little dependence on the Reynolds number. "Transitional" separations (transition between separation and reattachment) generally are unsteady and often depend markedly on Reynolds number. In transitional separation an abrupt pressure rise often occurs at the location of transition, especially when transition is only a short distance upstream of reattachment. "Turbulent" separations (transition upstream of separation) depends only to a minor extent on Reynolds number. Another merit of their work is having introduced a simplified analysis describing the interaction in a region where boundary layer and external flow interact freely, the so called free-interaction theory, which works well for supersonic interactions.

The essential features of an interacting boundary-layer were established by Lighthill (1950, 1953), who first explored the mechanism for the upstream propagation of the disturbances in a boundary layer. Lighthill recognized that the interaction takes place over a short distance, when compared to a length scale representative of the boundary-layer development, such as its thickness. As a consequence, Lighthill showed that the boundary-layer flow develops a two-layer structure comprising i) a thick outer rotational region, which may be considered inviscid, since the rapid variation in the stream-wise direction in the little interaction domain overcome the viscous effects, ii) a thin viscous sublayer attached to the wall, which is necessary to let the flow at the wall withstand an adverse pressure gradient. The outer region of the boundary layer plays a passive role, displacing the streamlines outwardly in the boundary-layer and simultaneously transmitting the pressure perturbations unchanged to the viscous sublayer (Délery et al., 1986). The theory predicts the initial pressure rise close to the separation point, and the agreement between the calculated and the experimental pressure distribution close to the separation point is excellent for supersonic interactions.

For the transonic interaction, which is the one involved in transonic buffet, the free-interaction theory fails, since the supersonic linear relation between flow deviation and pressure used just outside the boundary layer is no more valid for Mach numbers close to unity. Scaling laws for the different layers can be corrected taking into account the transonic small-disturbance theory, which indicates that the pressure changes are of the same order of the two-thirds power of the flow deflection angle, as done by Feo et al. (1971).

Also global stability analysis was employed to study the interaction region both in the laminar (Robinet, 2007) and turbulent (Touber and Sandham, 2009; Pirozzoli et al., 2010a) cases for the supersonic interaction. In the laminar case, three-dimensional structures are found in the separated bubble, which induce a low-frequency bubble breathing; Robinet (2007) emphasizes that the bubble breathing is connected to three-dimensional movement with important span-wise component.

Transitional effects have been disregarded throughout the analysis, i.e. the described mechanism is a purely laminar one. The low-frequency content is found in all part of the flow, except for the upstream zone of the incident shock. In contrast, in the turbulent case (Touber and Sandham, 2009) the most unstable mode is two-dimensional, and it is connected with the low-frequency motion of the reflected shock. This global mode was seen to affect the separation bubble by displacing the separation and reattachment points (in phase) and potentially breaking it up or enhancing the bubble in its upstream section. Pirozzoli et al. (2010a) confirm Touber and Sandham (2009) results, and also describe the emergence of several oscillatory, weakly damped modes, with frequencies comparable with the one they found in their computations. They low-pass filter the data, finding resemblance between mode shapes and breathing motions of the separation bubble.

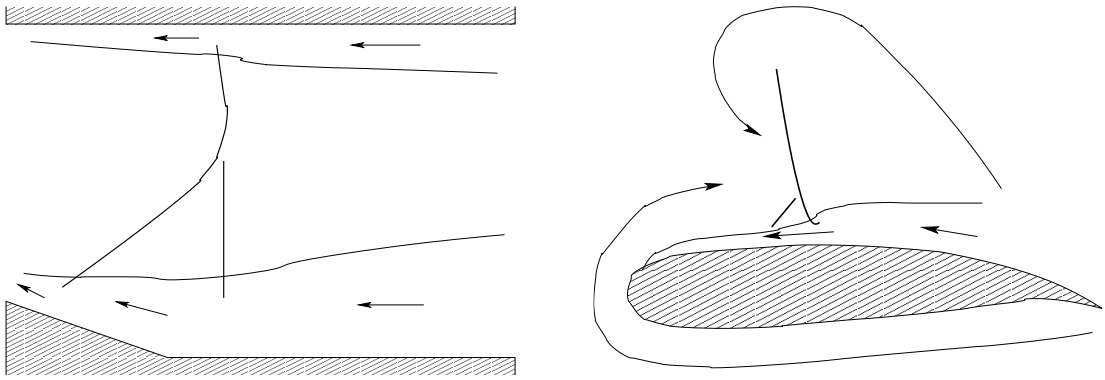

Figure 1.4: *Upstream propagation of disturbances in the supersonic stream for channel (left) and airfoil (right).*

Sartor et al. (2015) proved the global stability analysis to fail in the case of transonic turbulent interaction in a channel. The analysis performed on the linearized RANS equations shows the flow to be (statistically) steady, against the evidence of the low-frequency shock motion. They were able to show that the unsteadiness is a consequence of transient growth mechanisms. Regarding the origin of the unsteadiness, they show that both perturbations in the incoming flow and in the recirculation bubble may trigger shock unsteadiness. Their result apparently contrasts with Crouch et al. (2009) results, where transonic buffet on an airfoil is shown to be related to global instability. The differences may be related to having considered closed and open environments, respectively. For the closed environment (channel), the upstream propagation of disturbances in the supersonic stream can only occur through the boundary layers, while in the open one (airfoil) disturbances may reach the supersonic stream by traveling around the shock or around the airfoil, on pressure side (Fig. 1.4).

Since transonic SBLI are the ones involved in transonic buffet, we give a more detailed description of them. Following Babinsky and Harvey (2011), we can subdivide the interaction region in two different region:

Region I: is the supersonic region ahead of the main shock. In this region, except very near the surface, the flow is supersonic and mainly depends on upstream

conditions. Free-interaction theory may successfully be applied to describe this region. The compression is achieved by waves which make the pressure changes rapid. The skin friction, as a result of the deceleration of the flow, decreases rapidly and the boundary-layer shape factor increases. The growth of the boundary-layer displacement is linked to inviscid mechanisms. Typically, region I starts a few boundary-layer thicknesses upstream of the main shock and ends where the boundary-layer-edge velocity and surface pressure indicate $M = 1$. The length of this region is strongly influenced by the incompressible shape parameter of the incoming flow, while it is almost independent of the Mach number.

Region II: is the subsonic region downstream of the main shock - except for supersonic tongues, which often arises in transonic interactions since the boundary-layer-edge Mach number is close to unity. In this region, the flow changes much more slowly. As a result, the pressure shows two distinct behaviour at left and right of the point where the critical value is found (the one corresponding to the isentropic pressure at $M = 1$). Boundary layer parameters also change much more slowly, and the flow development is strongly influenced by downstream events. Region II is typically larger than region I, it can take many tens of boundary-layer thicknesses.

Separation for laminar flows occurs almost any time there is a shock wave. In case of turbulent flows, separation generally occurs for a Mach number ahead of the shock in the range $M_s = 1.3 - 1.35$. The incompressible shape parameter has not a great influence on separation onset. Typically, a sharp pressure increase is observed ahead of separation, followed by a near constant pressure in the separation region, and by a subsequent pressure rise, slower than the first. Strong anisotropy develops in the first part of the interaction, where $\overline{u_1'^2}$ grows more rapidly than $\overline{u_2'^2}$. Anisotropy tends to promote turbulent kinetic energy production.

Once separation occurs, at the separation point the boundary layer is displaced from the wall, bunching up the compression waves which merge into a leg of the consequent λ shock. The separated shear layer cannot sustain a strong adverse-pressure-gradient, and if the rear shock leg impinges on it, an expansion fan is reflected. As a result, there is typically a supersonic tongue behind the λ region. Separation is also influenced by curvature effects: on an airfoil, the shock strength required for separation is greater. However, the most significant effect is found downstream of the interaction region, since the convex surface accelerates the flow, making more likely the presence of secondary supersonic regions (and shocks) or increasing their size. This is particularly true in laminar interactions, where even a weak shock causes separation; then the flow curvature at reattachment combines with the surface curvature to reaccelerate the flow to supersonic velocities. This can happen more than once.

Lee (1990) classified shock/boundary layer interaction to be of four types on a supercritical airfoil, where for the first three types he refers to the work of Mundell and Mabey (1986) (for steady shock on conventional airfoil):

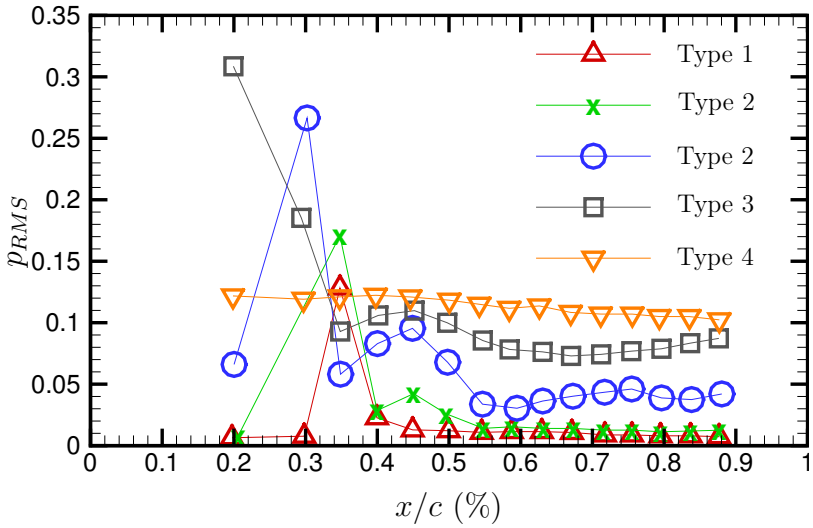

Figure 1.5: *Pressure fluctuations on upper surface of BGK No. 1 airfoil at various α. Data from Fig. 7 of (Lee, 1990).*

Type 1: the steady shock has just the effect of thickening the boundary layer. Pressure RMS (Root Mean Square) shows a peak soon after the shock foot

Type 2: the steady shock is strong enough to cause separation, but the flow is able to reattach downstream, and a recirculating bubble is created with its origin at the shock foot. Pressure RMS shows again a peak at the shock foot, and a new peak induced by the separation bubble

Type 3: the steady shock is so strong to prevent the reattachment of the flow downstream, and the separation extends to the trailing edge (shock stall). Pressure RMS shows the same behaviour of type 2 case, but after the second peak it does not recover to the tunnel noise level

Type 4: there is an unsteady shock. Pressure RMS gradually decreases downstream of the shock, with a value which remains greater than the tunnel noise level

The RMS behaviour is better seen in Fig. 1.5. The different behaviour for type 4 is easily understood if one considers that as a consequence of the shock motion, its effects are spread on a larger area - the same effect is usually observed also on the time-averaged pressure coefficient, where the instantaneous pressure jump is replaced by a more gradual pressure increase. Extrapolating from Chapman et al. (1958) results (sec. 1.2.2 on page 5), a classification of the interaction type from the pressure RMS is possible until the interaction is not purely laminar, which is the only one where it is steady, and pressure RMS is expected to carry less recognizable informations.

Even if the shock is not strong enough to cause separation in the interaction region, it indirectly may cause separation near the trailing edge, since a thicker boundary layer is more sensitive to adverse pressure gradients.

1.2.3 Two-dimensional phenomenon

Transonic buffet dynamics is essentially two-dimensional. A first clue is brought by two-dimensional simulations, in which the shock may undergo a periodic motion. This is true both for two-dimensional simulations with a turbulence model, which can model the effects of three-dimensional features of the separated boundary layer in average and are less or more physical, and also for two-dimensional simulations without a turbulence model, in which case only laminar boundary layers can be considered and where the unavoidable boundary layer separation cannot show a physical behaviour (no vortex-stretching term, hence no energy transfer to smaller scales). Other clues necessarily come from wall tunnel experiments, where on shock

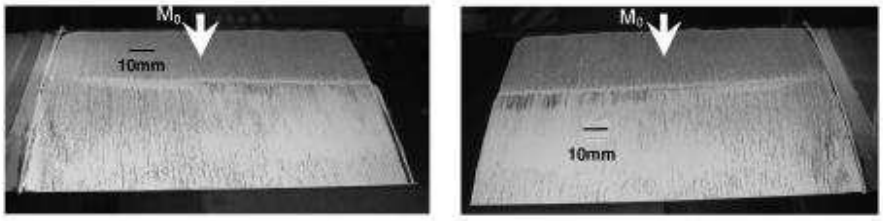

Figure 1.6: *Shock trace on airfoil suction side, $M_\infty = 0.73$, $\alpha = 2.5\,deg$, supercritical profile OAT15A; one can see that the mean shock is parallel to the leading edge away from side walls; figure from (Jacquin et al., 2009)*

surface one does not observe three-dimensional deformations, with the exception of the wing edges (Fig. 1.6). Moreover, the pressure spectral analysis shows a substantially two-dimensional dynamics (Fig. 1.7), highlighting the periodicity of the phenomenon (Jacquin et al., 2009).

Nevertheless, the limits of a two-dimensional theory must be outlined.

Limits of a two-dimensional theory

In three-dimensional simulations, pressure fluctuations at the trailing edge are significantly reduced, since the coherent structures developing as a consequence of separation may become three-dimensional, without concentrating their effects only in two dimensions (Garnier and Deck, 2010). Since the acoustic waves are an important ingredient of transonic buffet - according to Lee (2001), the shock motion is self-sustained trough an acoustic feed-back loop mechanism - one may then expect the oscillations amplitude to be smaller in the three-dimensional case. Also, if the shock oscillations become too large, then at the wall, in the separated region, a three-dimensional motion is observed (Fig. 1.8). This kind of motion survives the detachment/reattachment of the boundary layer dynamics for transonic buffet, and it may also be a universal feature for highly separated flows (Jacquin et al., 2009). Since this motion happens at the wall, the associated velocity is small compared to the one of the two-dimensional dynamics. Another factor which may contribute to this three-dimensionality is the presence of the side walls of

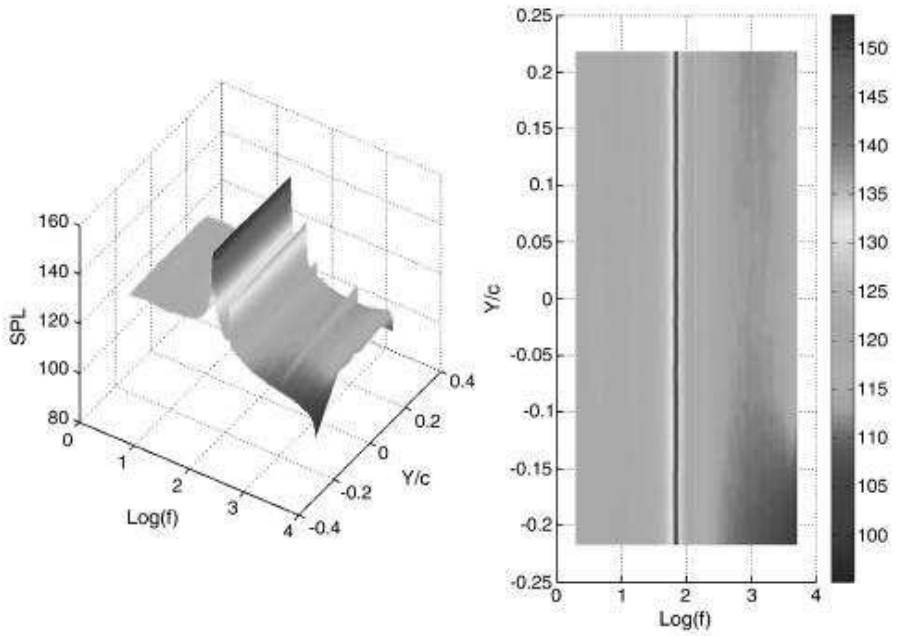

Figure 1.7: *pressure spectra along the span. Left figure: 3D visualization. Right figure: 2D visualization. The spectra also shows a two-dimensional behaviour of the flow. Figure from (Jacquin et al., 2009).*

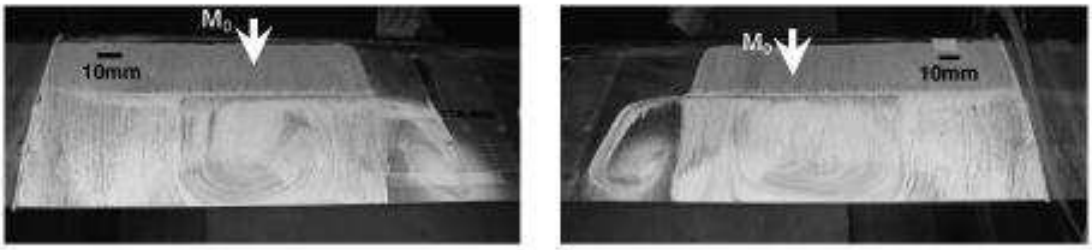

Figure 1.8: *3D motion at the wall, $M_\infty = 0.73$, $\alpha = 3.5\,deg$, supercritical profile OAT15A. Velocity associated with the 3D motion are much lower that the one associated with the 2D one. Figure from (Jacquin et al., 2009).*

wind tunnel. Implementing the lateral walls in a numerical simulations appears to promote this kind of motion (Thiery and Coustols, 2005).

Regarding a three-dimensional description of the flow: since the acoustic waves originating at the trailing edge play an important role, and considering the effectiveness of chevron nozzles in the suppression of the acoustic noise in turbojets, an interesting attempt could be the adoption of a particular geometry of the trailing edge suggested by such nozzles. A sawtooth trailing edge could be able to reduce the acoustic production, with the possible consequence of enlarging transonic buffet stability limits. The code manipulation for considering such a geometry is not very easy, and there was no time to try it during the Ph.D. Another, perhaps more promising, attempt that could be tried is the addition of an "optimum" porous medium to the trailing edge, which, as found by Schulze and Sesterhenn (2013), is able to greatly reduce trailing edge noise. With this solution no geometry change is required, since the addition of the porous media is effectuated at the equations level.

1.2.4 Hysteresis

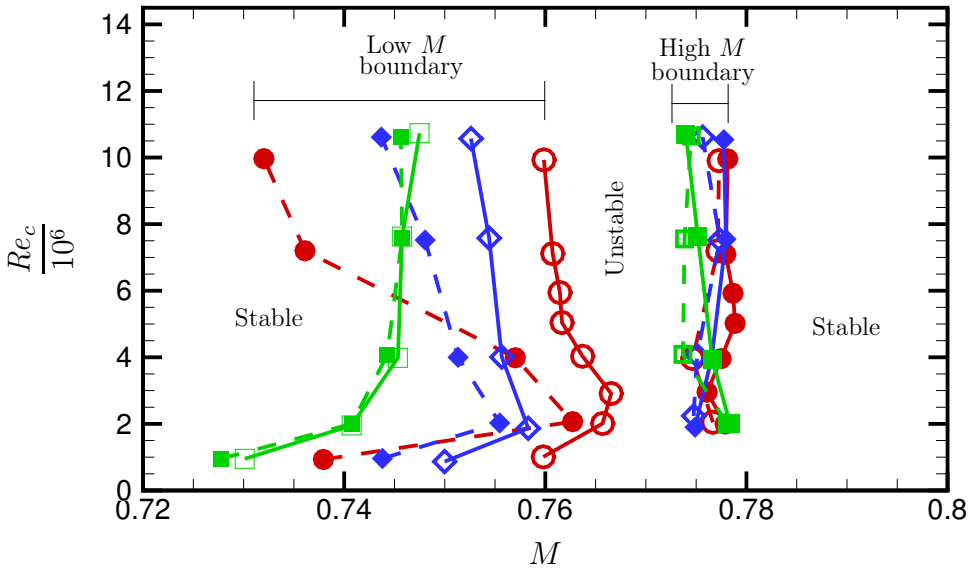

Figure 1.9: *Influence of the sign of the Mach number variation on buffet limits (hysteresis). Red: $\alpha = 0°$; blue: $\alpha = 2°$; green: $\alpha = 4°$. Solid lines: increasing Mach numbers; dashed lines: decreasing Mach numbers. Empty symbols: entering the unstable region; solid symbols: exiting the unstable region. Data from (McDevitt, 1979) for a 18% thick circular-arc airfoil.*

Another features of buffet which is typical of large separation phenomena is hysteresis: the flow reacts in different ways if reaching a certain Mach number from higher or lower Mach numbers. In other words, we find different stability limits if we define them by entering in the unstable regime or by exiting from it through Mach number variations. This is particularly true for the lower Mach number limit

(McDevitt et al., 1976). McDevitt (1979) extended McDevitt et al. (1976) work, but always considering a circular arc airfoil. In particular, he considered also angles of incidence different from zero, and he found that the hysteresis phenomenon is greatly reduced when the angle of incidence is increased (shocks are still present both on suction and pressure sides).

Fig. 1.9 shows the experimental stability boundaries at different Reynolds number and different angles of incidence for a circular-arc airfoil with maximum relative thickness of 18% obtained by McDevitt (1979). Solid lines indicate boundaries obtained for increasing Mach number, dashed lines identify boundaries for decreasing Mach numbers; red, blue and green lines denote angles of incidence of, respectively, 0°, 2°, 4°. Symbols are just an attempt to make the figure easier to understand: solid symbols indicate that the line they refer to is obtained for a Mach number variation such that we are exiting from the unstable region, while empty symbols indicate we are entering from there in the unstable region. We can see that at zero angle of incidence the stability limit for the lower Mach number changes appreciably, while at 4° of incidence the hysteresis seems to disappear. The boundaries for higher Mach number are almost always the same. There are Reynolds number effects, but it seems like the flow tends to reach an asymptotic state for sufficiently high Reynolds number, as can be seen from the slopes; apparently, no attempts have been made in the experiments to fix transition.

McDevitt and Okuno (1985) - working on a NACA-0012 airfoil - did not discern any hysteresis effect, but they detect buffet onset through "α sweeps" rather than "M sweeps". Nitzsche (2009) used Unsteady RANS approach with the 2-equations LEA (Linearised Explicit Algebraic) $k-\omega$ model on the supercritical BAC 3-11/RES/30/21 at free-stream Mach number $M_\infty = 0.75$ and Reynolds number $Re_c = 4.5 \times 10^6$. To detect buffet onset he gradually changes the angle of incidence from 0° to 6°, and then from 6° to 0°. He observes hysteresis, since when he performs the sweep up, the critical angle is 5.5°, while during the sweep down buffet persists beyond the critical angle, namely 4.5°, thus for $4.5° < \alpha < 5.5°$ both steady and unsteady solutions are possible.

1.2.5 Classification of transonic buffet

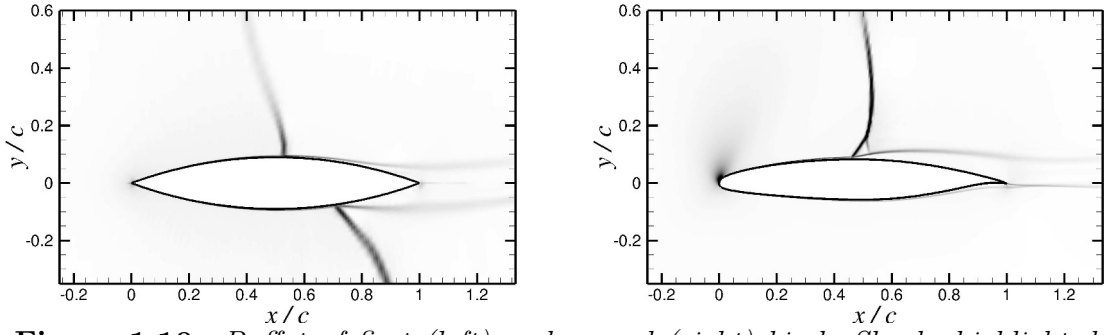

Figure 1.10: *Buffet of first (left) and second (right) kind. Shocks highlighted through numerical schlieren contours.*

Based on the physics of the phenomenon in the case of profiles, we can recognise two kinds of buffet:

Buffet of the first kind: shows shock oscillations on both suction and pressure sides, and typically is observed at zero angle of incidence for symmetrical airfoils (left panel of Fig. 1.10)

Buffet of the second kind: is associated with shock oscillations on suction side and is typically observed on lifting airfoils (right panel of Fig. 1.10).

Buffet of the first kind has been studied predominantly on biconvex circular arc airfoils, particularly at zero angle of incidence. With respect the second kind, buffet of the first kind appears in a narrower Mach number range, the Reynolds number has a stronger influence on its stability limits, and doesn't show itself for a sufficiently thin airfoil (Lee, 2001). As will be pointed out in sec. 1.3, these two kinds of buffet appear to be two distinct objects.

The reduced frequency of the shock motion, defined as $k_r = \Omega(c/2)/u_\infty$ (where Ω is the angular frequency), appears to be able to discriminate the two different kinds of buffet, with a value of order $k_r = O(1)$ for buffet of the first kind, and $k_r = O(0.5)$ for buffet of the second kind. Referring to Lee's review (Lee, 2001), these values are quite typical for different airfoil shapes, but k_r still shows some dependence on the Reynolds and on the Mach numbers, although the dependence on the Reynolds number is lower for high values of it; a stronger Reynolds dependence is present in the definition of the stability limits for laminar and transitional flows, as is also described in sec. 1.2.4. Reduced frequency increases when Mach number increases.

A further subdivision of the buffet typology may be based on the most descriptive characteristic of the phenomenon: the shock motion. Based on that, following Tijdeman (1977) - who effectuates his classification based on the shock motion in presence of a moving flap - we can identify three distinct typologies:

type A: The shock describes a sinusoidal motion. The shock is present throughout the period

type B: The shock still describes a periodic motion both in the downstream and upstream directions, but during part of the cycle the shock degenerates in weak compression waves. The amplitude of the oscillations is greater than type A

type C: The motion is still periodic, but the shock moves only in the upstream direction. When the shock leaves the leading edge, other compression waves are produced which coalesce in a shock wave, and the process repeat itself. Among the three buffet types, this is the one with the larger oscillations

1.2.6 Dependence on numerical schemes and turbulence models

Numerical predictions on frequency of the periodic shock motion, on stability limits and on pressure fluctuations, are fair, even when turbulence models are used

(given that suitable models are used), which are the dominant error source in the numerical simulations.

A big flaw of numerical simulations is indeed the need for turbulence model, since solving all the flow scales would lead to a not sustainable computational cost, which increases as the Reynolds number increases. Such turbulence models do have influence on the numerical solution, altering the shock position and in some cases also suppressing transonic buffet. Barakos and Drikakis (2000) try different turbulence models, namely the algebraic Baldwin and Lomax (1978) model, the one-equation model of Spalart et al. (1994), the Launder and Sharma (1974) and Nagano and Kim (1988) linear $k-\varepsilon$ models, as well as the $k-\omega$ version of the non-linear eddy-viscosity model of Craft et al. (1996), and assess their effects. What they find is that non-linear two-equation models in conjunction with a non constant c_μ (a coefficient of the model) for the calculation of the eddy-viscosity provide satisfactory results for transonic buffet flows; more interestingly, they find that the Spalart-Allmaras one-equation model provides comparable results at a cheaper cost. The other models they try furnishes worse results, with the linear $k-\varepsilon$ models unable to even detect the unsteadiness. Thiery and Coustols (2005) also come to the conclusions that the Spalart-Allmaras model is suitable for the computation of the unsteadiness. Nitzsche (2009) uses the 2-equations LEA (Linearised Explicit Algebraic) $k-\omega$ model, reporting that it is also a suitable turbulence model.

The error introduced by the numerical scheme itself is much less important with respect the one introduced by the turbulence model. An important feature that turbulence models must have is being able to describe the correct SBLI type (sec. 1.2.2).

A numerical domain typically will not spread infinitely, and the boundary is another error source. Jones et al. (2006) performed two-dimensional simulations on a NACA-0012 at zero angle of incidence, trying different Mach numbers. What they found is the domain size and the boundary conditions affect the solution for small Mach numbers, while for transonic Mach numbers there is a very small sensitivity to them. In particular, they found that the most problematic boundary is the outflow, and the strength of the boundary reflections reaching the airfoil is higher for lower Mach numbers, since pressure waves will travel a longer distance before dissipating. For transonic Mach numbers, the problem is nearly absent.

Garnier and Deck (2010) use two computational strategies to investigate transonic buffet. The first one is based on RANS/LES coupling where LES is used on suction side and RANS on pressure side, while the other one uses the Zonal DES approach. The computations are able to capture the unsteadiness in terms of frequency, but the pressure fluctuations are overestimated. Since their computations are three-dimensional, they also investigate the effect of the domain size in the span direction. They use a first domain size of $L_z/c = 0.0365$, then they double it keeping the same resolution. The strongest effect of the span size is found near the trailing edge, where they observe reduced fluctuations, since the structures may develop in three dimensions without concentrating their effects only in two dimensions. By contrast, Touber and Sandham (2009) find that the choice of domain width strongly

influence the interaction length.

Crouch et al. (2009) emphasize that the prediction of stability boundaries does not depend strongly on the grid. However, the critical frequency does show some grid dependence.

To summarize, the main source of error in the numerical simulations is the turbulence model. The turbulence model which appears to bring the best results at the lowest cost is the Spalart-Allmaras turbulence model, which is the one generally used.

1.3 Proposed mechanisms

1.3.1 Buffet of first kind (two oscillating shocks)

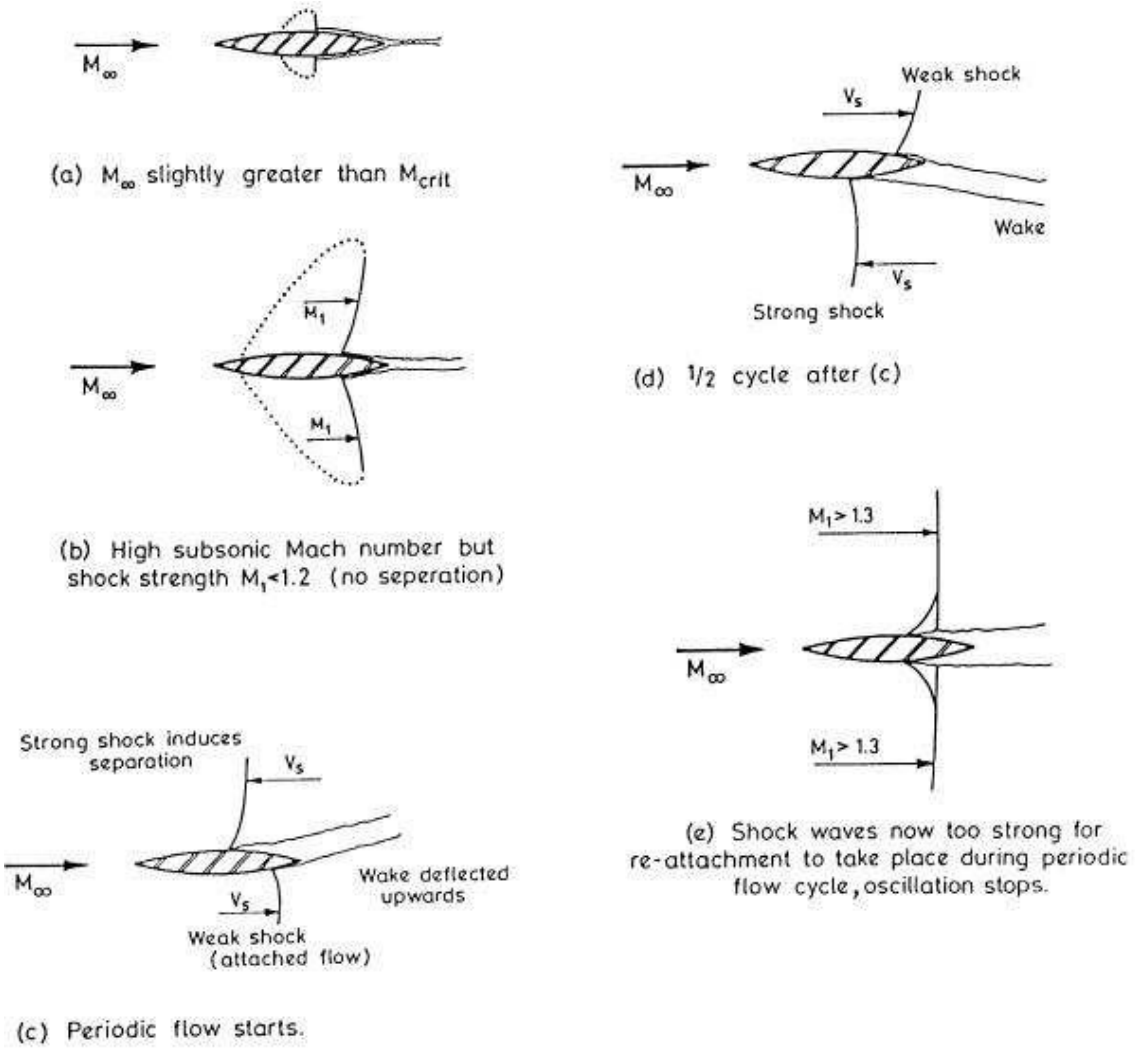

Figure 1.11: *Mechanism proposed by Mabey (1980) and Gibb (1988) for buffet of the first kind; figures from (Gibb, 1988).*

As previously stated, there are two oscillating shocks, one on suction side, the other on pressure side. Mabey (1980) and Gibb (1988) propose a working mechanism for this kind of buffet. Following Mabey, we have buffet only when the relative Mach number ahead of the shock (M_s) is in a certain range: the lower edge of this range is the minimum Mach number which may induce separation (M_L). Assuming this Mach number range is known (we have buffet if $M_L < M_s < M_U$, with M_L lower bound and M_U upper bound for buffet of first kind), Gibb proposes the following mechanism, shown in Fig. 1.11: on the airfoil we initially have a symmetric situation, with a relative Mach number ahead of the shock which is slightly lower than M_L. A pressure disturbance which reaches the shock on suction side may lead an upstream shock motion which, due to the relative motion, lead to an increase of M_s, bringing it to a value higher than M_L. This way, separation occurs on suction side which moves upwards the wake, which will act as a flap deflected upwards. On pressure side, this way, the flow tends to accelerate, moving the shock towards the trailing edge, giving a negative contribution to M_s on pressure side. The flow keeps to be attached at the shock foot as long as M_s is lower than M_L. On suction side, since the shock is moving in a slower supersonic region, its strength diminishes, and when M_s becomes lower than M_L the flow reattaches. On the other hand, on pressure side, it moves in a faster supersonic region, and it may become strong enough to induce separation and trigger the cyclic motion. The flow becomes again steady when the Mach number is high enough ($M_s > M_U$) to always bring $M_s > M_L$, and reattachment is no more possible.

Since this mechanism relies on strong flow modifications during the buffet cycle, for this kind of buffet linear theory is expected to fail, and this may explain Crouch et al. (2009) inconsistent results for the low α behaviour in the buffet onset boundary (i.e., with his theory he is able to catch buffet of the second kind, but not of the first kind).

Adding a splitter plate to the trailing edge it is possible to stabilize the shock oscillations (McDevitt, 1979), since what happens on a side of the airfoil has much more limited effects on what happens on the other side, i.e. the communication between suction and pressure side is made harder. This is particularly true when the splitter plate is made to cover the mean closure point of the wake.

The control by means of the splitter plate makes also more intuitive why buffet of the first kind is not encountered on thin enough airfoils: an airfoil thick enough to show this kind of buffet, on which a splitter plate is added, is seen by the flow as an airfoil with lower relative thickness; overturning the perspective, a thin airfoil can be seen as a thick airfoil, on which a splitter plate is added, with all the beneficial effects described above.

Another aspect which may be of some interest is the effect of the splitter plate on buffet frequency, or in other words, the effect of the distance between shock and trailing edge. As can be seen in Fig. 1.12, buffet frequency decreases as the distance between mean shock and trailing edge increases.

Jones et al. (2006) performed two-dimensional simulations (hence only laminar boundary layer) of a NACA-0012 airfoil at zero degrees incidence at low Reynolds

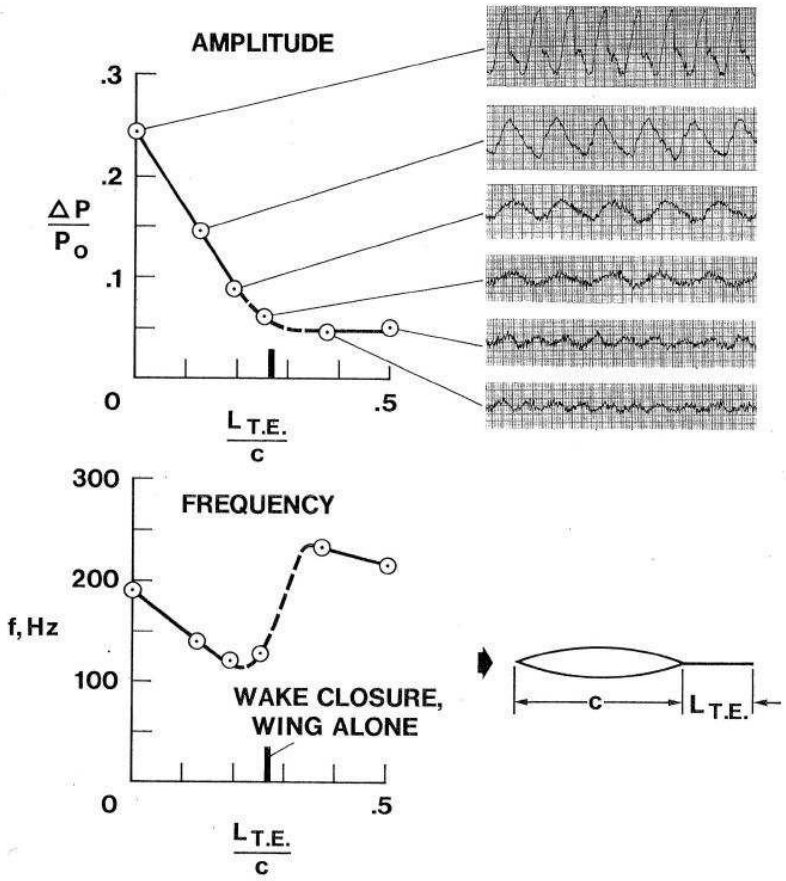

Figure 1.12: *Effect of a splitter plate at the trailing edge upon amplitude and frequency of pressure fluctuations in $x/c = 0.78$; circular-arc airfoil, $M = 0.772$, $Re_c = 8 \times 10^6$, $\alpha = 0°$; figure from (McDevitt, 1979).*

number. For a range of Mach numbers, they found a low-frequency large-scale mode of oscillation, which is the transonic buffet of the first kind when a shock is present in the flow. However they report the same dynamics also for Mach numbers such that no supersonic region (no shock) is present in the flow. Their result suggests that the low-frequency dynamics is related to the separation and reattachment dynamics of the boundary layer, whatever its causes may be. When the shock is strong enough to not allow the reattachment, the low-frequency dynamics stops. Their result however poses questions about the start of this dynamics, which appears to not be necessarily related to the shock induced separation, at least in the laminar case, where the boundary layer is more prone to separation. It is expected, however, that for a turbulent boundary layer the exposed mechanism holds, since for a zero degree incidence, separation is expected to occur only in presence of the shock.

Crouch et al. (2009) uses global instability analysis to predict buffet onset on a NACA-0012 airfoil at different angles of incidence. The theory works very well for $\alpha \neq 0$, where buffet of the second kind is expected, while the results does not match experiments for α close to zero. This, together with Jones et al. (2006) results (same flow unsteadiness even at Mach numbers such that no shock exists), may suggest that buffet of the first kind is not properly a transonic buffet, and may also explain the need of two different mechanisms for the two different phenomena: buffet of the first kind appears to be more related to the detachment and reattachment dynamics of the boundary layer, which appear to be possible even without the shock.

1.3.2 Buffet of second kind (one oscillating shock)

For the other typology various mechanisms have been proposed.

Pearcey (1958) and Pearcey and Holder (1962), who only consider airfoils with separation bubbles, propose that transonic buffet arises when the separation bubble reaches the trailing edge and bursts. The bubble bursting triggers the shock motion, driven by the periodic thickening and thinning of the separated boundary layer, highly correlated with the shock motion. Anyway, investigating the field near buffet onset, it has been understood that the triggering of the instability is independent of the bubble burst, since it may arise when the separation bubble has not yet reached the trailing edge (Crouch et al., 2009). Shock induced separation appears to be a necessary (although not sufficient) condition for buffet onset, as pointed out by Nitzsche (2009).

Raghunathan et al. (1998) hypothesize this kind of buffet being the result of the flow oscillating between two unstable states, one with an expanded separation bubble, the other with a collapsed one. The periodic expansion and collapse of the separation bubble determines the shock location. Pressure side is thought to act an important role, with the flow field in this region reacting to the wake motion in a manner similar as if there is a moving flap, so that the flow on suction side may accelerate or decelerate in a manner similar to the buffet of the first kind mechanism.

Iovnovich and Raven (2012) propose another interpretation in which the shock motion is strictly related to the separation bubble. They propose a more local

approach, in which the lead mechanism is the shock induced separation in the upstream part of the buffet cycle: during the upstream shock motion, the shock initially strengthens, so that there is always a separation bubble; during the final phase of this upstream motion, the shock weakens due to curvature effects near the leading edge, and the flow reattaches; the global flow modifications due to the attached boundary layer causes the shock to move downstream. In a manner similar to buffet of the first kind, such a mechanism involves strong flow modifications during the cycle, thus not amenable of a linear description either at onset conditions.

Another mechanism for buffet of second kind is proposed by Lee (2001). In Lee's model, the shock motion generates pressure waves, which propagate in the separated boundary layer towards the trailing edge. Here those waves generate acoustic waves which propagate towards the shock in the external flow, only on suction side, and which are able to sustain the shock motion (Fig. 1.13). The shock oscillations are

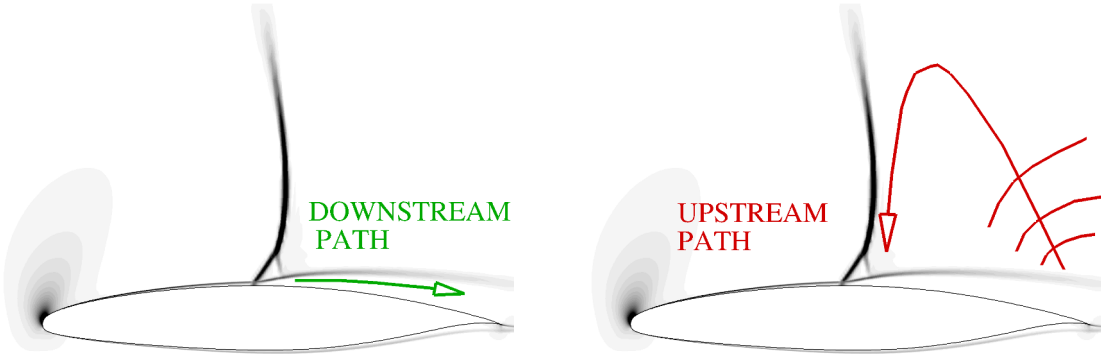

Figure 1.13: *Schematic of Lee's mechanism. Left: downstream propagation of instability waves generated at the shock foot. Right: upstream propagation of acoustic waves towards the aft part of the shock.*

self-sustained through an acoustic feed-back loop. Lee supposes then that the period of the motion may be computed as the sum of the travel time of the pressure waves in their motion from the shock to the trailing edge (t_c, instability waves), plus the travel time of the acoustic waves from the trailing edge to the shock (t_u, acoustic waves), considering for the shock its mean location

$$f = \frac{1}{t_c + t_u} \tag{1.1}$$

For the upstream propagating disturbances, one can assume a propagation velocity about equal the sound speed in the free-stream.

$$t_u = L_s/u_a \tag{1.2}$$

where L_s is the distance between mean shock and trailing edge, and

$$u_a = a_\infty - u_\infty = u_\infty(1 - M_\infty)/M_\infty \tag{1.3}$$

is the upstream acoustic propagation velocity in free-stream conditions. Colonius and Lele (2004) gave a comprehensive review of computational method for the

prediction of sound generation in turbulent flows, also dealing with the trailing edge scattering due to turbulent structures passing over it. The scattering mechanism is investigated in more detail in (Ewert and Schröder, 2004). There is no easy model for the prediction of the convection velocity of the downstream propagating pressure waves originating at the shock foot. Roos (1980) in his experimental work computes the convection velocity of disturbances using a two-point pressure cross-correlation, finding that such a convection velocity is frequency dependent, with velocity increasing as frequency increases. The convection velocities that must be considered are related to large scale disturbances traveling near the airfoil wall, hence are the one associated with the low-frequency range. If one uses for such velocities values characteristic of the Kelvin-Helmholtz instability of the shear layer, the buffet frequency obtained by Lee's model would overestimate the real value. The convection velocity can be computed from the correlation of the pressure signal on suction side, and to obtain it one must perform an experiment or a numerical simulation. Anyway, frequency obtained this way not always agree with the experimental ones or the one from numerical computations.

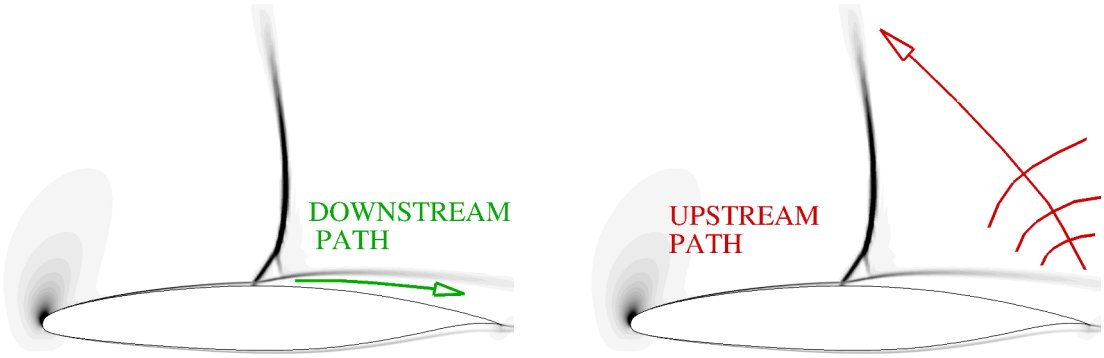

Figure 1.14: *Modification to Lee's model proposed by Hartmann et al. (2013). Upstream propagating disturbances are assumed to interact with the shock at the shock tip, where the shock is weaker.*

Hartmann et al. (2013), arguing that the shock has its highest strength near the boundary layer edge and weakens as the distance from the wall increases, propose a modification to Lee's model. It is still assumed the mechanism to be an acoustic feedback loop, but the upstream acoustic disturbances are assumed to feed the shock through its tip rather then its foot (fig: 1.14). Small deviations of the shock at its tip will cause the whole shock to react, so that a displacement of the tip results in a displacement of the whole shock. With their assumption Hartmann et al. (2013) are able to decrease the overestimation they found using Lee's model. The authors also gave a detailed description of the flow, emphasizing that the sound pressure level due to trailing edge scattering is higher when the vortices released at the shock foot are stronger, and those vortices are stronger the stronger the shock is, i.e. during the upstream shock motion. These strong vortices, generated in the separated boundary layer, reach the shock when the boundary layer has already reattached and the shear has its maximum strength. The combined effect of shear and vortices make the

trailing edge scattering the strongest during the most downstream shock location, resulting in a sound pressure level which will move the shock upstream. Conversely, the minimum level is found in the most upstream shock location, which will drive the shock in the downstream motion.

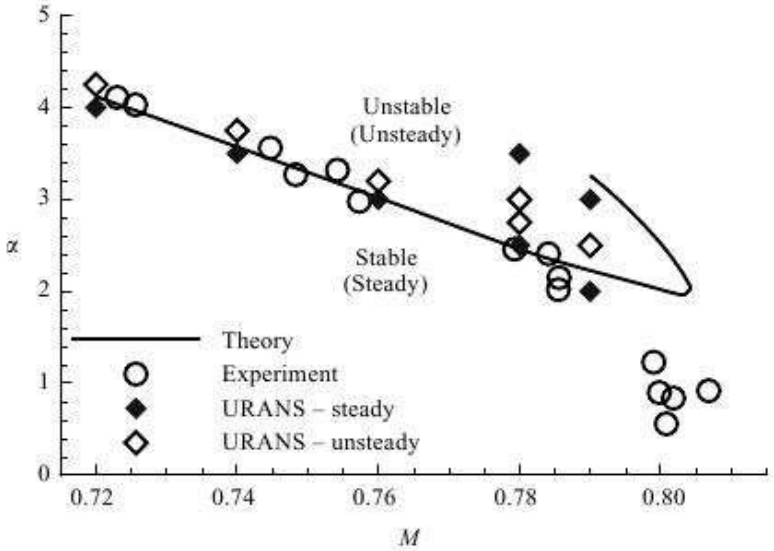

Figure 1.15: *Stability map for a NACA-0012 airfoil at $Re_c = 10^7$. Solid line refers to global instability theory. Experimental results from (McDevitt and Okuno, 1985). Figure from (Crouch et al., 2009).*

Recent studies (Crouch et al., 2009) demonstrates that this kind of shock buffeting is tied to a global instability, showing that, at least at the onset, it is a modal phenomenon. The modal nature of the phenomenon remains essentially modal also far from the onset conditions (Jacquin et al., 2009). The acoustic feedback loop would thus be the physical mechanism which feeds this global instability. The stability analysis has been effectuated through a flow division in a steady part and a fluctuating perturbation. The steady part is derived by solving the governing equations, which are the ones of RANS (Reynolds-Averaged Navier-Stokes Simulation), where the temporal derivative is not present. The fluctuating part is derived by linearization of the governing equations, which are now the ones of the Unsteady RANS, where the temporal derivative is kept since the temporal scales associated with turbulence are much more faster than the ones associated with transonic buffet - thus only low-frequency content is described in Unsteady RANS. The analysis is then effectuated solving an eigenvalue problem. The approach is able to accurately predict buffet stability limits for the lower Mach numbers, but not as effective for the higher ones (Fig. 1.15). It is not clear why the theory does not work at these Mach numbers. One reason may be the presence of numerical viscosity, which may eliminate the instabilities if they are weak enough, another one the turbulence model - needed in RANS - or also for reasons tied to the experiments, since they are effectuated in a wind tunnel. Also, more than at the higher Mach numbers, it seems the theory doesn't work for the lower angles of incidence, which

may be associated with buffet of the first kind. If this is true, then we can conclude that the theory is effective in the prediction of buffet of the second kind, but not in the prediction of buffet of the first kind. If this is the case, thus this is a proof that the two kinds of buffet rely on different mechanisms, a modal mechanism for buffet of the second kind (thus amenable of a linear description, at least at the onset), and a non-linear mechanism for buffet of the first kind (the global flow dynamics cannot be described through little perturbations theory, thus further supporting Gibb's mechanism, which involves strong modification of the flow during the cycle also at onset).

Other support to buffet of the second kind being a result of a global instability comes from the work of Nitzsche (2009), who perturbs sub-critical (stable) conditions and look at the subsequent temporal evolution of the flow. Near buffet onset, he finds resonance phenomena for frequency associated with buffet, thus confirming that, at least at the onset, buffet is a modal phenomenon; as such, a linear stability theory is able to find at least buffet stability boundaries.

Coming back to the description of the mechanism made available by the stability analysis (Crouch et al., 2009): looking at the pressure global mode, we can observe that the pressure perturbations which are produced at the shock foot propagate both downstream of the shock and along it. The disturbances which propagate towards the trailing edge turn around it and reach the shock from its front, traveling on pressure side - i.e. the upstream communication channel is the pressure side. This flow picture implies that the broadband noise production at the trailing edge does not include frequencies of the same order of the buffet frequency. Hartmann et al. (2013) estimate the frequency of scattered sound at the trailing using the relation

$$f = \frac{u_d}{L_v} \tag{1.4}$$

where u_d is the downstream convection velocity of the disturbances participating to the buffet dinamics, and L_v is their size; they find a scattered frequency for sound waves an order of magnitude higher than the buffet frequency. The result that Unsteady RANS are able to describe transonic buffet may lead to the conclusion that mechanisms involving acoustic feed-back loops are wrong, since theoretically Unsteady RANS involves a temporal averaging to filter the high frequency. Nevertheless, in the Unsteady RANS equations there is no explicit filtering, thus high frequencies are supported by the model equations. In a sense, Unsteady RANS may be seen just as a "turbulence filter". Crouch et al. (2009) flow picture in principle does not exclude the scattering of acoustic waves at frequencies higher than buffet at the trailing edge.

A correction to Lee's model, suggested by the global stability analysis and by experiments, and which appears to improve the buffet period estimate (Jacquin et al., 2009), is to assume that the disturbances propagate upstream *also* on pressure side (Fig. 1.16).

As pointed out by Nitzsche (2009), since a linear (small perturbation) theory is able to identify buffet onset, the self-sustain mechanism should not rely on strong flow-field modifications, such as the detachment/reattachment dynamics of

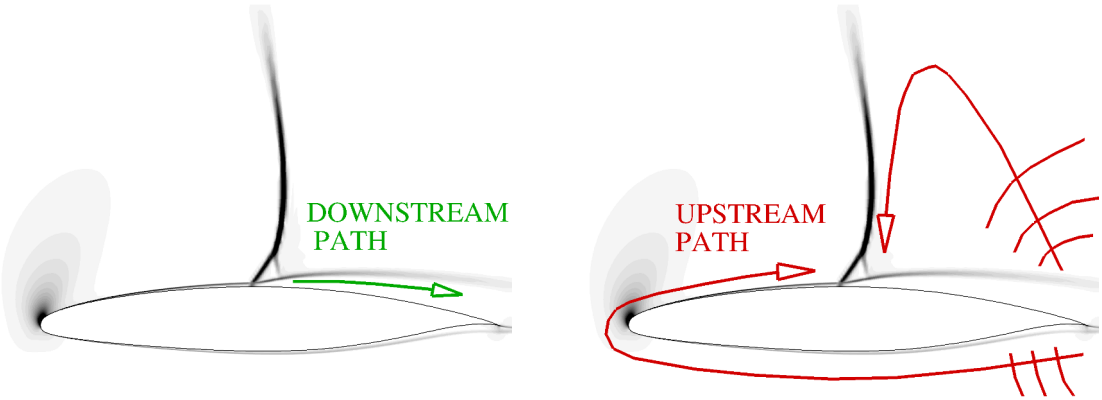

Figure 1.16: *Modification to Lee's model proposed by Jacquin et al. (2009). Upstream propagating disturbances on pressure side are assumed to also participate the buffet dynamics.*

the whole boundary layer; once identified, such a mechanism must be applicable to this complicated dynamics, too.

1.4 Control strategies

We first refer to Lee's review (Lee, 2001) for this section, where to control the oscillations, modifications to the flow in the shock-boundary layer interaction region or in the near wake by trailing edge manipulations are only taken into account.

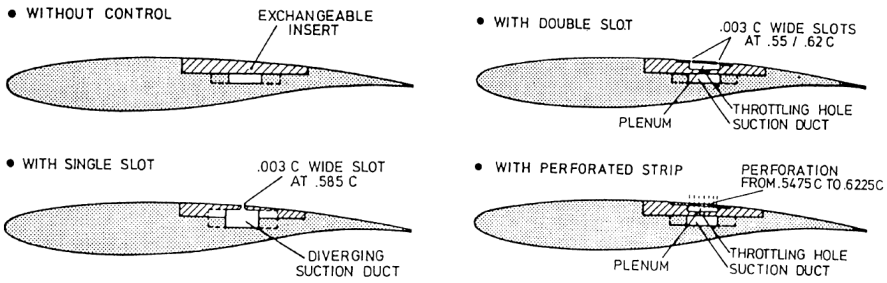

Figure 1.17: *Configurations for passive control of shock oscillations tested by Thiede et al. (1984). Figure from Lee (2001).*

To the first category of controls described by Lee belongs the ones tested by Thiede et al. (1984), shown in Fig. 1.17. The effect of applying local boundary layer suction is to delay the shock-induced separation, improving performances and delaying transonic buffet. Thiede et al. (1984) also found that similar results may be achieved with a passive control, by allowing communication between front and aft parts of the shock, through perforated surfaces. The pressure rise after the shock presses the fluid into the cavity region, which aft of the shock acts as a passive suction device, reducing separation. The fluid then escapes from the cavity in front of the shock, which acts as a passive blowing device, diminishing losses across the main

shock by starting the compression through weaker shocks caused by the boundary layer thickening. Such configuration may be achieved through different techniques. In particular, the double slot and the porous strip appear to give similar results, but the porous strip works better in transonic buffet control for higher Mach numbers, while double slot is more effective for lower ones.

A similar passive technique, with the "high-pressure hole" located on pressure side rather than on suction side, and with the "low-pressure hole" still located on suction side in front of the shock, is also able to significantly enhance flow stability.

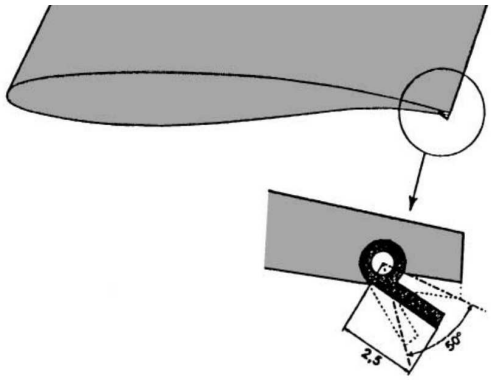

Figure 1.18: *TED device developed by ONERA. Figure from (Lee, 2001).*

The second alternative which has been tried is to control the flow at the trailing edge. In particular the TED (Trailing Edge Deflector) device developed at ONERA (Fig. 1.18), which acts similarly to a trailing edge flap. The device can act both statically, delaying buffet, or as a closed loop active control, controlled by the pressure measurements on suction side, which has a strong impact on the unsteady phenomenon, being also able to alleviate the shock motion amplitude. The 0° position coincides with the original thickness of the airfoil at the trailing edge. This is not the only control device tested at ONERA over the last decade of their research activities on transonic buffet. Dandois et al. (2013) reports an overview of their work, in particular describing the effect of mechanical vortex-generators (VG), of fluidic VG with continuous or pulsed flow rate, and of fluidic TED.

The effect of mechanical VG located at 20% of the chord is to postpone buffet onset, by strengthening the boundary layer, which is less prone to separation. Their disadvantage is that they cannot be deactivated. Fluidic VG are an attempt to reproduce the same effects of their mechanical counterpart, with the possibility to activate them only when they are needed. Fluidic VG consists of small nozzles with conical shape and supersonic exit flow, both with continuous or pulsed flow rate. The angles used in the experimental tests are also provided, assessed through previous numerical simulations. The effect of both fluidic and mechanical VG is to reduce flow separation, allowing a shift in the downstream position of the shock. The shock appears to be located more downstream with fluidic devices. The fluidic TED consists in a slot located on the pressure side, at the trailing edge. The effect of the device is not to postpone buffet to a higher angle of incidence, but to a higher lift coefficient. Also closed-loop controls have been tried, which are capable of strongly

influence the flow behavior. More success has been attained by Gao et al. (2016), who consider a linear control-law based on the lift coefficient, applied to the flap rotation. The delay time between phase of the lift and of the flap rotation plays a major role, and an estimate for the optimal one has been furnished (of about 50°). They were able to completely suppress buffet in their numerical analysis.

Chapter 2

Numerical method

In this chapter we explain the mathematical model used to describe the problem, and the numerical scheme used to solve the resulting equations. We write the continuous system of the Navier-Stokes equations and we enunciate the initial and boundary conditions which must be enforced to solve the problem. Hence, we describe the turbulence models that we will use in order to achieve some simplified solutions, and finally we describe the scheme used to obtain the numerical solution.

2.1 Basic mathematical model

Conservation principles of mass, momentum and energy can be expressed in a convenient way through an integral formulation valid for a material volume, i.e. a volume composed of always the same fluid particles (Lagrangian formulation). From this form, it is possible, through the Reynolds' transport theorem, to write the equations valid for a fixed control volume (Eulerian formulation). Using Einstein's convention of summation on repeated indices, we have (Sabetta, 2009):

$$\frac{\mathrm{d}}{\mathrm{d}t}\int_{\mathcal{V}} \mathbf{U}\,\mathrm{d}\mathcal{V} + \oint_S \mathbf{F}_j n_j\,\mathrm{d}S = \oint_S \mathbf{G}_j n_j\,\mathrm{d}S \tag{2.1}$$

having disregarded the contribution of gravity force and where the various terms are:

- Conserved variables vector

$$\mathbf{U} = \begin{Bmatrix} \rho \\ \rho u_i \\ \rho E \end{Bmatrix} \tag{2.2}$$

- Generalized flux vectors

$$\mathbf{F}_j = \mathbf{U}u_j + \mathbf{P}_j \tag{2.3}$$

- Viscous flux vectors

$$\mathbf{G}_j = \begin{Bmatrix} 0 \\ \sigma_{ij} \\ \sigma_{ij} u_i - q_j \end{Bmatrix} \tag{2.4}$$

  in which only convective heat flux is considered, i.e. we consider the Fourier's law $\mathbf{q} = -K\nabla T$. The code accounts for μ being a function of temperature, while the Prandtl number and the specific heat at constant pressure are assumed to be constant (no molecular changes), so that K is considered proportional to μ

- Vectors accounting for pressure contribution to stresses

$$\mathbf{P}_j = \begin{Bmatrix} 0 \\ p\delta_{ij} \\ pu_j \end{Bmatrix} \tag{2.5}$$

The quantities which appear in these vectors are:

- The viscous stress tensor

$$\sigma_{ij} = \mu \left(\frac{\partial u_i}{\partial x_j} + \frac{\partial u_j}{\partial x_i} \right) + \lambda \frac{\partial u_k}{\partial x_k} \delta_{ij} \tag{2.6}$$

  in which only Newtonian fluids are considered, such that there is a linear relation between stress tensor and deformation rates, as it is found for air (Batchelor, 2000). We will also make use of the Stokes' hypothesis:

$$\lambda = -\frac{2}{3}\mu \tag{2.7}$$

  which implies that pressure is retrieved as the arithmetic mean of normal stresses, and that isothermal compressions and expansion are reversible (Gad-el Hak and Bandyopadhyay, 1995).

- Total energy per unit mass

$$E = e + \frac{1}{2} u_j u_j \tag{2.8}$$

and ρ, u_i, p, T, e, μ, K, δ_{ij} are, respectively, density, velocity components, static pressure, temperature, internal energy per unit mass (for ideal gases $e = c_v T$), dynamical viscosity, thermal conductivity coefficient, and Kronecker delta.

In the frame of the integral formulation, continuity of the solution is not required, we require only its integrability.

To close the equations, two more must be added to the set, the perfect gas state equation, and an approximation of Sutherland's law, which describe viscosity variation on temperature:

- State equation

$$p = \rho R T \tag{2.9}$$

  R is the gas constant per unit mass. We are thus assuming gas thermally and (since c_p is constant) calorically perfect

- Approximation of Sutherland's law

$$\frac{\mu}{\mu_\infty} = \left(\frac{T}{T_\infty}\right)^{0.76} \tag{2.10}$$

  valid for a temperature range between $150K$ and $500K$ (Smits and Dussauge, 2006).

To close the problem, boundary and initial conditions are needed. The conditions to be assigned on the body are the impermeability one, which doesn't allow mass flux through the walls, and the no-slip condition, due to the viscous nature of the flow and which does not allow a relative tangential motion between the flow and the body. These conditions together completely determine the velocity vector at the wall, which are then Dirichlet conditions. Another boundary condition has to be imposed on temperature; in this work, we shall only consider adiabatic wall, hence we impose a condition on temperature derivative, i.e. a Neumann condition. Free-stream conditions are to be supplied at infinity.

In this work, unless otherwise stated, it is always used an initial condition which is equivalent to an impulsive start.

2.2 Turbulence models

When the considered Reynolds number is greater than a critical value, the flow undergoes a transition from an ordered state (laminar) to a rather chaotic state (turbulent), characterised by much more finer length scale and faster time scales. The higher the Reynolds number, the lower the length scale associated with turbulence. A Direct Numerical Simulation (DNS) of a turbulent flow at an engineering Reynolds number is still a challenge, since solving for all the flow scales implies a computational cost unsustainable even for today's technology. Such an approach is only possible for simple flows, as a channel or an airfoil, and only at moderate Reynolds numbers - the computational cost of a DNS increases as the cube of the Reynolds number (Pope, 2001).

Since DNS are unfeasible for engineering problems, alternative solutions have been proposed, which are less expensive in terms of computational cost.

2.2.1 RANS and Unsteady RANS

The most used approach is the Reynolds-Averaged Navier-Stokes Simulation (RANS), in which the equations are obtained by time-averaging the Navier-Stokes equations, thus only allowing a description of the averaged flow behaviour.

Even if the equations are time-averaged, they can be used to describe an unsteady phenomenon such as transonic buffet, since turbulence dynamics is much faster than buffet dynamics. Such an approach is named Unsteady RANS (URANS).

The resulting equations can be cast in a form similar to the Navier-Stokes one, but the described variables are averaged quantities and the equations show new terms, absent from the original set and arising from the averaging procedure on the non-linear terms. These additional terms act as turbulent stresses, and are named as Reynolds stresses. They are a new unknown of the problem, without additional equations to solve for them. Thus a closure problem arises, which turbulence models try to solve either empirically or theoretically, with a physical basis, with the introduction of closure equations. Many turbulence models have been developed in the years, and which one has to be chosen depends on the particular problem under investigation.

2.2.2 Time averaged equations

Following Hirsch (1990), for any quantity φ we define

$$\varphi = \overline{\varphi} + \varphi' , \qquad \varphi = \tilde{\varphi} + \varphi'' , \qquad \tilde{\varphi} = \frac{\overline{\rho\varphi}}{\overline{\rho}} \tag{2.11}$$

where $\overline{\varphi}$ is the time-averaged quantity and φ' the relative fluctuations, while $\tilde{\varphi}$ is the density-weighted (Favre) average and φ'' the relative fluctuations. From the definitions above, the relations $\overline{\varphi'} = \overline{\rho\varphi''} = 0$ hold. Time-averaging equations (2.1) yields

$$\frac{\partial\overline{\rho}}{\partial t} + \frac{\partial(\overline{\rho}\tilde{u}_j)}{\partial x_j} = 0 \tag{2.12a}$$

$$\frac{\partial(\overline{\rho}\tilde{u}_i)}{\partial t} + \frac{\partial(\overline{\rho}\tilde{u}_i\tilde{u}_j)}{\partial x_j} = -\frac{\partial\overline{p}}{\partial x_i} + \frac{\partial\overline{\sigma}^T_{ij}}{\partial x_j} \tag{2.12b}$$

$$\frac{\partial(\overline{\rho}\hat{E})}{\partial t} + \frac{\partial\overline{\rho}\hat{H}\tilde{u}_j}{\partial x_j} = \frac{\partial(\overline{\sigma}^T_{ij}\tilde{u}_i)}{\partial x_j} - \frac{\partial\overline{q}^T_j}{\partial x_j} \tag{2.12c}$$

where

$$\overline{\sigma}^T_{ij} = \overline{\sigma}_{i,j} + \overline{\sigma}^R_{ij} , \qquad \overline{\sigma}_{ij} \simeq 2\tilde{\mu}\left(\tilde{S}_{ij} - \frac{1}{3}\frac{\partial\tilde{u}_k}{\partial x_k}\delta_{ij}\right) , \qquad \overline{\sigma}^R_{ij} = -\overline{\rho u''_i u''_j} \tag{2.13}$$

$$\overline{q}^T_j = \overline{q}_j + \overline{q}^R_j , \qquad \overline{q}_j \simeq -\tilde{K}\frac{\partial\tilde{T}}{\partial x_j} , \qquad \overline{q}^R_j = \overline{\rho h'' u''_j} \tag{2.14}$$

$$\tilde{E} = \hat{E} + k , \qquad \hat{E} = \tilde{e} + \frac{1}{2}\tilde{u}_k\tilde{u}_k , \qquad \overline{\rho}k = \frac{1}{2}\overline{\rho u''_k u''_k} \tag{2.15}$$

$$\tilde{H} = \hat{H} + k , \qquad \hat{H} = \tilde{h} + \frac{1}{2}\tilde{u}_k\tilde{u}_k , \qquad h = c_p T \tag{2.16}$$

$\overline{\sigma}^R_{ij}$ is the Reynolds stress tensor, which arises from the time-averaging procedure on the non-linear, convective terms in the momentum equations, and which contains all

the effects of the turbulence on the averaged momentum conservation. Also for the energy equation it is possible to define a total heat flux $\overline{q}_j^T$. $\hat{E}$ (and $\hat{H}$) is introduced in order to use the same state relations of the instantaneous quantities also for the averaged ones. k is the turbulent kinetic energy. H and h are, respectively, total enthalpy and enthalpy.

With these choices, the same relations used for the instantaneous variables keep holding also for the averaged quantities, so that $\overline{p} = \overline{\rho} R \tilde{T}$ and $\tilde{e} = c_v \tilde{T}$. It is also assumed the Sutherland's law (2.10) as link between $\tilde{\mu}$ and $\tilde{T}$.

As can be seen by equations (2.12), turbulence is accounted for by the terms $\overline{\sigma}_{ij}^R$, $\overline{q}_j^R$. Unfortunately, no additional equations exist to relate these terms to the mean quantities, and some modellization is required, based on theoretical considerations coupled to unavoidable empirical information. As pointed out in sec. 1.2.6, the model which is usually adopted for the investigation of transonic buffet is the one of Spalart et al. (1994), which we shall now describe.

2.2.3 Spalart-Allmaras turbulence model

This is a first-order closure model. As such, following Boussinesq's hypothesis:

$$\overline{\sigma}_{ij}^R = 2\tilde{\mu}_T \left(\tilde{S}_{ij} - \frac{1}{3} \frac{\partial \tilde{u}_k}{\partial x_k} \delta_{ij} \right) - \frac{2}{3} \overline{\rho} k \delta_{ij} \tag{2.17}$$

$$\overline{q}_j^R = -\tilde{K}_T \frac{\partial \tilde{T}}{\partial x_j} \tag{2.18}$$

$$\tilde{K}_T = \frac{\tilde{\mu}_T c_p}{Pr_T} \tag{2.19}$$

Boussinesq's approximation results in the use of an eddy viscosity concept. Here, $\overline{\mu}_T$ is the *eddy viscosity* which must be obtained by the turbulence model, $\tilde{S}_{ij} = \frac{1}{2}\left(\frac{\partial \tilde{u}_i}{\partial x_j} + \frac{\partial \tilde{u}_j}{\partial x_i} \right)$ is the strain tensor, while the last term of (2.17) containing the turbulent kinetic energy is ignored in this work, since we deal with maximum velocities which are close to the sound speed. We deal with the unknown heat flux in a similar fashion, by introducing a turbulent thermal conductivity coefficient K_T, which is related to the eddy viscosity by the turbulent Prandtl number Pr_T. In this work, we use a turbulent Prandtl number $Pr_T = 0.6$.

For the Spalart et al. (1994) turbulence model, we follow the Langley Research Center online page for the model variants termed *SA-noft2* (fully turbulent boundary

layer) and *SA-Ia* (transitional boundary layer, with a trip term). We have

$$\begin{aligned}\frac{\partial\hat{\nu}}{\partial t}+\tilde{u}_j\frac{\partial\hat{\nu}}{\partial x_j} &= c_{b1}(1-f_{t2})\hat{S}\hat{\nu}+\\ &-\left[c_{w1}f_w-\frac{c_{b1}}{\kappa^2}f_{t2}\right]\left(\frac{\hat{\nu}}{d}\right)^2+\\ &+\frac{1}{\sigma}\left[\frac{\partial}{\partial x_j}\left((\tilde{\nu}+\hat{\nu})\frac{\partial\hat{\nu}}{\partial x_j}\right)+c_{b2}\frac{\partial\hat{\nu}}{\partial x_j}\frac{\partial\hat{\nu}}{\partial x_j}\right]+\\ &+f_{t1}\Delta\hat{u}^2\end{aligned} \tag{2.20}$$

where $\hat{\nu}$ is the model working variable, which is related to the eddy viscosity by

$$\tilde{\mu}_T=\overline{\rho}\hat{\nu}f_{v1} \tag{2.21}$$

Here we use the hat to denote the model working variable $\hat{\nu}$, reserving the tilde for the averaged kinematic viscosity $\tilde{\nu}=\tilde{\mu}/\overline{\rho}$. Additional definitions are given by the following equations:

$$f_{v1}=\frac{\chi^3}{\chi^3+c_{v1}^3} \tag{2.22}$$

$$\chi=\frac{\hat{\nu}}{\tilde{\nu}} \tag{2.23}$$

$$\hat{S}=\hat{\omega}+\frac{\hat{\nu}}{\kappa^2d^2}f_{v2} \tag{2.24}$$

where $\hat{\omega}$ is the magnitude of the (Favre averaged) vorticity, d is the distance from the nearest wall of the point in which the equation is considered (field point), and

$$f_{v2}=1-\frac{\chi}{1+\chi f_{v1}} \qquad f_w=g\left[\frac{1+c_{w3}^6}{g^6+c_{w3}^6}\right]^{1/6} \tag{2.25}$$

$$g=r+c_{w2}(r^6-r) \tag{2.26}$$

$$r=\min\left[\frac{\hat{\nu}}{\hat{S}\kappa^2d^2},\,10\right] \tag{2.27}$$

$$f_{t2}=c_{t3}\exp\left(-c_{t4}\chi^2\right) \tag{2.28}$$

Also we have

$$\begin{aligned} f_{t1} &= \begin{cases} c_{t1}g_t\exp\left[-c_{t2}\dfrac{\omega_t^2}{\Delta\hat{u}^2}(d^2+g_t^2d_t^2)\right] & \text{transitional}\\ 0 & \text{fully turbulent}\end{cases}\\ g_t &= \min\left[0.1,\,\frac{\Delta\hat{u}}{\omega_t\Delta x_t}\right]\end{aligned} \tag{2.29}$$

Where $\Delta\hat{u}$ is the difference between the velocity at the field point and the velocity at the trip (artificially generated by the turbulence model in the transitional case, at

the wall), Δx_t is the grid spacing along the wall at the trip, ω_t is the wall vorticity at the trip, d_t is the distance from the field point to the trip. The constants are:

$$\begin{aligned}
c_{b1} &= 0.1355\,, & \sigma &= 2/3\,,\\
c_{b2} &= 0.622\,, & \kappa &= 0.41\,,\\
c_{w2} &= 0.3\,, & c_{w3} &= 2\,,\\
c_{v1} &= 7.1\,,\\
c_{t1} &= 1\,, & c_{t2} &= 2\,, \qquad (2.30)\\
c_{t3} &= \begin{cases} 1.2 & \text{transitional} \\ 0 & \text{fully turbulent} \end{cases}, & c_{t4} &= 0.5\,,\\
c_{w1} &= \frac{c_{b1}}{\kappa^2} + \frac{1+c_{b2}}{\sigma}
\end{aligned}$$

Following Spalart communication (also listed in Langley Research Center website), we enforce

$$\hat{S} = \max(\hat{S},\, 0.3\hat{\omega}) \tag{2.31}$$

so that the allowed minimum value for $\hat{S}$ is $0.3\hat{\omega}$.

Since we are dealing with the integral form of the conservation equations, some manipulation of the (2.20) is required. Equation (2.20) multiplied by $\overline{\rho}$

$$\overline{\rho}\frac{\partial \hat{\nu}}{\partial t} + \overline{\rho}\tilde{u}_j\frac{\partial \hat{\nu}}{\partial x_j} = \overline{\rho}\, RHS \tag{2.32}$$

can be cast in a different form (divergence-like form) recalling the continuity equation

$$\frac{\partial \overline{\rho}}{\partial t} + \frac{\partial \overline{\rho}\tilde{u}_j}{\partial x_j} = 0 \tag{2.33}$$

By summing (2.32) with (2.33) multiplied by $\hat{\nu}$, we have

$$\begin{aligned}
\overline{\rho}\frac{\partial \hat{\nu}}{\partial t} + \overline{\rho}\tilde{u}_j\frac{\partial \hat{\nu}}{\partial x_j} &= \overline{\rho}\frac{\partial \hat{\nu}}{\partial t} + \hat{\nu}\frac{\partial \overline{\rho}}{\partial t} + \overline{\rho}\tilde{u}_j\frac{\partial \hat{\nu}}{\partial x_j} + \hat{\nu}\frac{\partial \overline{\rho}\tilde{u}_j}{\partial x_j} =\\
&= \frac{\partial \overline{\rho}\hat{\nu}}{\partial t} + \frac{\partial \overline{\rho}\hat{\nu}\tilde{u}_j}{\partial x_j} = \overline{\rho}\, RHS
\end{aligned} \tag{2.34}$$

thus if we multiply equation (2.20) by $\overline{\rho}$, we can write

$$\begin{aligned}
\frac{\partial \overline{\rho}\hat{\nu}}{\partial t} + \frac{\partial(\overline{\rho}\tilde{u}_j\hat{\nu})}{\partial x_j} &= c_{b1}(1-f_{t2})\hat{S}(\overline{\rho}\hat{\nu}) +\\
&- \frac{1}{\overline{\rho}}\left[c_{w1}f_w - \frac{c_{b1}}{\kappa^2}f_{t2}\right]\left(\frac{\overline{\rho}\hat{\nu}}{d}\right)^2 +\\
&+ \frac{\overline{\rho}}{\sigma}\left[\frac{\partial}{\partial x_j}\left((\tilde{\nu}+\hat{\nu})\frac{\partial \hat{\nu}}{\partial x_j}\right) + c_{b2}\frac{\partial \hat{\nu}}{\partial x_j}\frac{\partial \hat{\nu}}{\partial x_j}\right] +\\
&+ \overline{\rho}f_{t1}\Delta\hat{u}^2
\end{aligned} \tag{2.35}$$

so that at least the convective part can be cast in divergence form. We notice that the dissipative part (last term in square brackets) is left as it is, without any attempt to cast it in a conservative formulation. We shall explain how to deal with it when we will discuss the discretization procedure.

Boundary conditions on $\hat{\nu}$. At the wall $\hat{\nu}_{wall} = 0$ is enforced. At the free-stream, the condition to enforce depends on whether we consider a transitional boundary layer or a fully turbulent one. If we run a transitional case ($c_{t3} \neq 0$, $f_{t1} \neq 0$), the free-stream condition we use is $\hat{\nu}_\infty = \frac{1}{1000}\tilde{\nu}_\infty$, else if we run a fully turbulent simulation ($c_{t3} = f_{t1} = 0$) then the condition $\hat{\nu}_\infty = 5\tilde{\nu}_\infty$ is enforced. This way the effective Reynolds number changes, since $\hat{\nu}_\infty = 5\hat{\nu}_\infty$ corresponds to $\tilde{\nu}_T \simeq 1.3\tilde{\nu}_\infty$, so that the effective free-stream viscosity doubles, and the effective Reynolds number halves. We also implemented the possibility of initializing the field with the value $\hat{\nu} = 5\tilde{\nu}_\infty$, in order to activate the turbulence model, and then assigning a free-stream value $\hat{\nu}_\infty = \frac{1}{100}\tilde{\nu}_\infty$. However, the results apparently are not affected by the way we enforce the boundary conditions.

2.2.4 LES, ILES, DES and DDES

Other approaches to deal with turbulence without solving all flow scales do exist, which are however more expensive than RANS approach.

LES and ILES

The first, initially proposed by Smagorinsky (1963), is the Large Eddy Simulation (LES), in which the computational cost is reduced by filtering the Navier-Stokes equations to exclude the smallest scale, which resolution is the primary cause of the computational cost of a DNS. The small scale do have an effect on the flow, so in the filtering procedure additional terms arises - from the non-linear terms of the equations - which take into account their effects, and which must be modeled. As DNS doesn't model any flow scale at all, and RANS models every turbulence scale, LES relies on modelling only the finest scales, while the computations solve the big energy containing eddies. As such, LES computational cost is between the ones of DNS and RANS. Following Pope (2001), there are four conceptual steps in LES:

1. A filtering operation to decompose a quantity φ into the sum of a filtered (or resolved) component $\overline{\varphi}$ and a residual (or subgrid-scale, SGS) component $\overline{\varphi'}$.

$$\overline{\varphi}(\mathbf{x}, t) = \int_{\mathcal{V}} G(\mathbf{r}, \mathbf{x})\varphi(\mathbf{x} - \mathbf{r}, t)\ \mathrm{d}\mathcal{V} \tag{2.36}$$

with

$$\int_{\mathcal{V}} G(\mathbf{r}, \mathbf{x})\ \mathrm{d}\mathcal{V} = 1 \tag{2.37}$$

Similarly to what has been done for the derivation of RANS equations, here it is also convenient to introduce a density-weighted filtering $\tilde{\varphi} = \frac{\overline{\rho\varphi}}{\overline{\rho}}$ (Favre).

2. Derive the equations of the filtered variables from the Navier-Stokes equations, with the appearance of new terms which account for the SGS effects, in particular of the residual-stress tensor (or SGS stress tensor).

3. Closure is obtained by modelling the residual-stress tensor

4. Numerical solution of the model filtered equations.

A remarkable difference between RANS and LES is that while for the former we have $\overline{\varphi'} = 0$ (mean of the fluctuations is zero), in the latter we have $\overline{\varphi'} \neq 0$ (filtered residual is not zero), and that the filtering operation and the spatial derivatives does not commute, unless G doesn't depend on $\mathbf{x}$.

In a very similar fashion as what has been done in the RANS approach, we did not explicitly filter when we solve for the LES equations, we just apply the filter in deriving the equations. As happened for RANS, the LES equations show additional terms which account for turbulence and which are to be modelled. Jimenez and Moser (2000) consider the dynamic-Smagorinsky subgrid models and concluded that "the physical basis for the good *a posteriori* performance of the dynamic-Smagorinsky subgrid models in LES [...] appears to be only weakly related to their ability to correctly represent the subgrid physics." This conclusion lead them to also consider the possibility to run a LES without any subgrid model at all, considering an appropriate numerical method to provide the required dissipation (Implicit LES (ILES) approach). Such approach was already proposed by other researchers. For example, Pope (2001) refers to (Boris et al., 1992), (TAMURA and KUWAHARA, 1989), (Knight et al., 1998), (Okong'o and Knight, 1998).

Indeed, the filtering procedure and the numerical solution are not separate issues. After the filtering procedure, we have to solve for a field which does not have high frequencies anymore. As such, if we solve numerically for frequencies higher than the filter cutoff length, no additional information is provided. This consideration provides a guideline for the needed grid, which has to be of the same order of the filter width Δ (in the same view of the Nyquist's sampling theorem). In turn, the filter width Δ has to be located at the beginning of the inertial range to be able to solve for 80% of the energy (Pope, 2001). The additional terms which accounts for turbulence in the model equations are in the order of $O(\Delta)$ (filter width), which in turn, as discussed above, is in the order of the grid spacing. As such, the numerical truncation error interacts with the modelled terms. Implicit LES (ILES) is an approach in which the truncation error alone is taken as closure model. In this work, the numerical scheme we choose for ILES is the WENO scheme. Our choice is dictated by convenience, since, as will be explained when dealing with the numerical method, WENO is already implemented to deal with shock waves. Garnier et al. (1999) find that WENO can be regarded as a very dissipative subgrid scale model. Grinstein et al. (2007), on the other hand, identify the problem with WENO to be related to its formal high-order accuracy. The problem is expected to be mitigated when the high-order interpolation inherent to the scheme is applied to the reconstruction of variables rather than to the reconstruction of fluxes, as has been done in our implementation.

Here we didn't write explicitly the LES equations, since as will be shown in subsection 2.2.4 they can be considered formally equal to the RANS equation already derived. Different LES formulations may be found in (Garnier et al., 2009).

DES

Following Spalart et al. (1997), there is an easy modification of the Spalart-Allmaras turbulence model (2.20) which yields an hybrid behaviour of the model equations between RANS/LES, i.e. the RANS equations switch to subgrid scale formulation when the grid is fine enough for LES calculation, while performing RANS otherwise. (2.20) contains a destruction term proportional to $(\hat{\nu}/d)^2$, where d is the distance to the closest wall. When balanced with the production term, this term leads to an eddy viscosity $\hat{\nu} \propto Sd^2$, with S being the local deformation rate. Considering Smagorinsky's LES model, its Sub-Grid-Scale eddy viscosity is $\nu_{SGS} \propto S\Delta^2$, where Δ is the grid size. With these arguments, Spalart et al. (1997) suggested to replace d in the destruction term with $\tilde{d}$, defined by

$$\tilde{d} = \min(d,\, C_{DES}\Delta) \tag{2.38}$$

Hence in our implementation we substitute every occurrence of d with $\tilde{d}$, with the exception of the first equation of (2.29), i.e. we use d in the definition of f_{t1}, which does not appear in the destruction term. Δ in equation (2.38), as suggested by the authors, is taken as

$$\Delta = \max(\Delta x, \Delta y, \Delta z) \tag{2.39}$$

The additional constant C_{DES} is left unknown for now, we will define it in the definition of the Delayed DES (DDES) approach, which is in turn a simple modification to DES (Spalart et al., 2006). From Spalart et al. (1997) work, we can also conclude that RANS system (2.20) can be formally seen as an LES system, without the need of explicitly deriving equations also for it.

DDES

Spalart et al. (2006) proposes a modification to DES, which maintains the RANS behaviour in boundary layers independently of the wall parallel spacing relative to boundary layer thickness, without preventing LES behaviour after massive separation. The modification involves the definition of two additional variables

$$r_d = \frac{\nu_T + \nu}{\sqrt{\frac{\partial u_i}{\partial x_j}\frac{\partial u_i}{\partial x_j}}\kappa^2 d^2} \qquad\qquad f_d = 1 - \tanh\left([8r_d]^3\right) \tag{2.40}$$

where ν_T is the kinematic eddy viscosity and ν is the kinematic viscosity. In the Spalart-Allmaras model, $(\nu_T + \nu)$ can be substituted with $\hat{\nu}$ (the working variable of the Spalart-Allmaras model). Now the distance d must be redefined to be the DDES distance

$$\tilde{d} = d - f_d \max(0,\, d - C_{DES}\Delta) \tag{2.41}$$

Further improvement may be achieved by defining Δ in different ways depending on if we are inside or outside the boundary layer. In particular, we adopt the definition of equation (16) in (Deck, 2012) which reads

$$\Delta = \begin{cases} \Delta_{max} & \text{if } f_d < f_{d0} \\ \Delta_{vol} & \text{if } f_d > f_{d0} \end{cases} \tag{2.42}$$

where $\Delta_{max} = \max(\Delta x, \Delta y, \Delta z)$, $\Delta_{vol} = (\Delta x\ \Delta y\ \Delta z)^{1/3}$ and f_{d0} is taken to be $f_{d0} = 0.8$. We also adopt the same value for C_{DES}, namely

$$C_{DES} = 0.65 \tag{2.43}$$

DES with all these modifications is the DDES effectively used in this work.

2.3 Nondimensional equations

The use of nondimensional variables allows to reduce results from different experiments and/or simulations to the same solution of the nondimensional system of equations, if the nondimensional coefficients which appear in the equations have the same values between the different data sets. Another advantage of the nondimensional system is the increased numerical accuracy, since all the variables after they are made nondimensional share the same order of magnitude (assuming appropriate reference values).

From this point on, in this work we shall refer to dimensional variables denoting them with the apex $*$, reserving the unsigned symbols for the nondimensional ones.

2.3.1 Reference quantities

In principle, the choice of the reference variables is arbitrary. In this work we choose as reference variables for the thermodynamical variables, for the viscosity, and for the thermal conductivity, their free-stream values

$$\rho = \frac{\rho^*}{\rho^*_\infty}\,, \qquad p = \frac{p^*}{p^*_\infty}\,, \qquad T = \frac{T^*}{T^*_\infty}\,, \qquad \mu = \frac{\mu^*}{\mu^*_\infty}\,, \qquad K = \frac{K^*}{K^*_\infty} \tag{2.44}$$

For the velocity and for the total energy per unit mass we also use a combination of the thermodynamical variables, respectively: $\sqrt{p^*_\infty/\rho^*_\infty}$ (it is the sound speed at free-stream, less the factor $\sqrt{\gamma}$) and p^*_∞/ρ^*_∞

$$u_i = \frac{u^*_i}{\sqrt{p^*_\infty/\rho^*_\infty}}\,, \qquad\qquad E = \frac{E^*}{p^*_\infty/\rho^*_\infty} \tag{2.45}$$

As length scale we choose the airfoil chord c^*, while the nondimensional time is build from reference length and velocity

$$x_i = \frac{x^*_i}{c^*}\,, \qquad\qquad t = \frac{t^*}{c^*}\sqrt{\frac{p^*_\infty}{\rho^*_\infty}} \tag{2.46}$$

Also, we define nondimensional specific heats

$$c_v = \frac{c_v^*}{R^*} = \frac{1}{\gamma - 1}\,, \qquad\qquad c_p = \frac{c_p^*}{R^*} = \frac{\gamma}{\gamma - 1} \tag{2.47}$$

where $R^* = \dfrac{p_\infty^*}{\rho_\infty^* T_\infty^*}$.

2.3.2 Some considerations on nondimensional variables

Dealing with nondimensional variables may be confusing when the obtained data have to be manipulated, such as to obtain the aerodynamic coefficients. Any data manipulation must be done in dimensional terms, then one has to link the dimensional quantities to the nondimensional variables. There is an easy way to deal with this problem.

First, consider the Π theorem (Sedov, 1993), which states that a problem described by N_T dimensional parameters, with N_F fundamental dimensions, can be characterised by $N_T - N_F$ independent nondimensional groups. Referring to equations (2.1)-(2.10), we have a total number of parameters $N_T = 15$ given by: t^*, x^*, ρ^*, u^*, p^*, μ^*, E^*, K^*, T^*, R^*, c_v^*, c_p^*, e^*, Pr, γ. We have a number of fundamental dimensions $N_F = 4$ given by: time $[s]$, length $[m]$, mass $[Kg]$, temperature $[K]$. If we didn't know anything else about the system under investigation, the total number of independent nondimensional groups would be of $15 - 4 = 11$. Since some relations between the parameters are explicitly known, they can be used to reduce the number of the parameters needed to describe the problem. The relations to consider are the $N_K = 7$:

$$p^* = \rho^* R^* T^* \qquad \frac{\mu^*}{\mu_\infty^*} = \left(\frac{T^*}{T_\infty^*}\right)^{0.76} \qquad e^* = c_v^* T^* \qquad c_v^* = \frac{R^*}{\gamma - 1}$$

$$E^* = e^* + \frac{1}{2}u^{*2} \qquad K^* = \frac{\mu^* c_p^*}{Pr} \qquad c_p^* = \frac{R^* \gamma}{\gamma - 1}$$

so that the actual number of needed parameters to describe the problem is $N_T - N_K = 8$, and for the Π theorem we need just $N_T - N_K - N_F = 4$ nondimensional groups to fully characterise the problem. The choice is not unique, and in this work we choose to consider as independent nondimensional parameters:

- Specific heat ratio

$$\gamma = \frac{c_p^*}{c_v^*} \tag{2.48}$$

- Free-stream Mach number

$$M_\infty = \frac{u_\infty^*}{\sqrt{\gamma p_\infty^* / \rho_\infty^*}} \tag{2.49}$$

- Chord Reynolds number

$$Re_c = \frac{\rho^*_\infty u^*_\infty c^*}{\mu^*_\infty} \tag{2.50}$$

- Prandtl number

$$Pr = \frac{\mu^* c^*_p}{K^*} \tag{2.51}$$

  which we assume constant, $Pr = 0.72$.

When we have chosen the nondimensional variables, we used as fundamental reference quantities p^*_∞, ρ^*_∞, T^*_∞, $R^* = \frac{p^*_\infty}{\rho^*_\infty T^*_\infty}$, μ^*_∞, K^*_∞, and c^*. Until the nondimensional groups γ, M_∞, Re_c and Pr are assigned, the reference variables may assume in principle any value. A convenient choice is to assume $p^*_\infty = 1$, $\rho^*_\infty = 1$, $T^*_\infty = 1$ ($R^* = \frac{p^*_\infty}{\rho^*_\infty T^*_\infty} = 1$) and $c^* = 1$, and retrieve all the other free-stream variables using these dimensional values together with the nondimensional groups:

- γ is given, and no free-stream quantity appears in its definition
- The Mach number is used to obtain u^*_∞

$$M_\infty = \frac{u^*_\infty}{\sqrt{\gamma p^*_\infty / \rho^*_\infty}} \qquad \Rightarrow u^*_\infty = \sqrt{\gamma} M_\infty \tag{2.52}$$

- The Reynolds number is used to obtain μ_{∞^*}

$$Re_c = \frac{\rho^*_\infty u^*_\infty c^*}{\mu^*_\infty} \qquad \Rightarrow \mu^*_\infty = \sqrt{\gamma}\frac{M_\infty}{Re_c} \tag{2.53}$$

- The Prandtl number is used to obtain K^*_∞

$$\begin{aligned} Pr = \frac{\mu^*_\infty c^*_p}{K^*_\infty} = \sqrt{\gamma}\frac{M_\infty}{Re_c}\, c_p R^*\, \frac{1}{K^*_\infty} = \sqrt{\gamma}\frac{M_\infty}{Re_c}\frac{\gamma}{\gamma-1}\frac{1}{K^*_\infty} \quad \Rightarrow \\ \Rightarrow \quad K^*_\infty = \sqrt{\gamma}\frac{M_\infty}{Re_c}\frac{\gamma}{\gamma-1}\frac{1}{Pr} \end{aligned} \tag{2.54}$$

Hence we are allowed to use $p^*_\infty = 1$, $\rho^*_\infty = 1$, $T^*_\infty = 1$ ($R^* = 1$), $c^* = 1$, but all the other free-stream quantities are assigned. With this trick, the dimensional counterparts of the nondimensional variables are:

$$\rho^* = \rho\,, \qquad p^* = p\,, \qquad T^* = T\,, \qquad R^* = 1\,, \tag{2.55a}$$

$$u^*_i = u_i\,, \qquad E^* = E\,, \qquad x^*_i = x_i\,, \qquad t^* = t\,, \tag{2.55b}$$

$$\mu^* = \sqrt{\gamma}\frac{M_\infty}{Re_c}\mu\,, \qquad K^* = \sqrt{\gamma}\frac{M_\infty}{Re_c}\frac{\gamma}{\gamma-1}\frac{1}{Pr}K\,, \tag{2.55c}$$

$$c^*_v = \frac{1}{\gamma-1}\,, \qquad c^*_p = \frac{\gamma}{\gamma-1} \tag{2.55d}$$

So considering equation (2.52) it is clear that in order to enforce the correct free-stream boundary condition on velocity, the Mach number must be set independently from the ratio M_∞/Re_c, even if, as it is shown in subsection 2.3.3, only this ratio appears in the nondimensional equations. In fact, in order to solve the problem we have to apply boundary conditions on the conserved variables, in particular on $\rho^*_\infty u^*_\infty = \sqrt{\gamma} M_\infty$, and M_∞ must then be set independently from the Reynolds number.

To show the usefulness of relations (2.55), consider as an example the expression for the drag coefficient

$$C_d = \frac{D^*}{\frac{1}{2}\rho^*_\infty {u^*_\infty}^2 c^*} = \frac{-\oint p^* \hat{n_w}_i \hat{u}_i \, \mathrm{d}S^* + \oint \mu^* \frac{\mathrm{d}(u^*_i \hat{u}_i)}{\mathrm{d}n_w} \, \mathrm{d}S^*}{\frac{1}{2}\rho^*_\infty {u^*_\infty}^2 c^*} \tag{2.56}$$

where $\hat{\mathbf{u}}$ is the direction of the free-stream velocity and $\hat{\mathbf{n_w}}$ is the wall-normal direction. Since the relations (2.55) hold, we can easily express it in terms of the nondimensional variables as

$$C_d = \frac{-\oint p \hat{n_w}_i \hat{u}_i \, \mathrm{d}S + \sqrt{\gamma} \frac{M_\infty}{Re_c} \oint \mu \frac{\mathrm{d}(u_i \hat{u}_i)}{\mathrm{d}n_w} \, \mathrm{d}S}{\frac{1}{2}\gamma M^2_\infty} \tag{2.57}$$

We can use the same approach to derive in an easy way the nondimensional equations.

2.3.3 Nondimensional equations

Relations (2.55) can be used to write the nondimensional equations. We have simply to write the dimensional equations and then substitute (2.55) to write the nondimensional ones. The nondimensional form of the conservation equations is then (in divergence form)

$$\frac{\partial \rho}{\partial t} + \frac{\partial (\rho u_j)}{\partial x_j} = 0 \tag{2.58a}$$

$$\frac{\partial (\rho u_i)}{\partial t} + \frac{\partial (\rho u_i u_j)}{\partial x_j} = -\frac{\partial p}{\partial x_i} + \sqrt{\gamma} \, \frac{M_\infty}{Re_c} \, \frac{\partial \sigma_{ij}}{\partial x_j} \tag{2.58b}$$

$$\frac{\partial (\rho E)}{\partial t} + \frac{\partial [(\rho E + p) u_j]}{\partial x_j} = \sqrt{\gamma} \, \frac{M_\infty}{Re_c} \, \left[\frac{\partial (\sigma_{ij} u_i)}{\partial x_j} + \frac{1}{Pr} \frac{\gamma}{\gamma - 1} \, \frac{\partial}{\partial x_j} \left(K \frac{\partial T}{\partial x_j} \right) \right] \tag{2.58c}$$

or, in vector integral form

$$\frac{\mathrm{d}}{\mathrm{d}t} \int_{\mathcal{V}} \mathbf{U} \, \mathrm{d}\mathcal{V} + \oint_S \mathbf{F}_j n_j \, \mathrm{d}S = \oint_S \mathbf{G}_j n_j \, \mathrm{d}S \tag{2.59}$$

with

$$\mathbf{U} = \begin{Bmatrix} \rho \\ \rho u_i \\ \rho E \end{Bmatrix}, \qquad \mathbf{F}_j = \mathbf{U}u_j + \mathbf{P}_j, \tag{2.60a}$$

$$\mathbf{P}_j = \begin{Bmatrix} 0 \\ p\delta_{ij} \\ pu_j \end{Bmatrix}, \qquad \mathbf{G}_j = \begin{Bmatrix} 0 \\ \sqrt{\gamma}\frac{M_\infty}{Re_c}\sigma_{ij} \\ \sqrt{\gamma}\frac{M_\infty}{Re_c}\left[\sigma_{ij}u_i + \frac{1}{Pr}\frac{\gamma}{\gamma-1}K\frac{\partial T}{\partial x_j}\right] \end{Bmatrix} \tag{2.60b}$$

and with the additional equations

$$p = \rho T, \qquad \mu = T^{0.76}, \qquad e = c_v T, \qquad E = e + \frac{1}{2}u_j u_j, \qquad K = \mu \tag{2.61a}$$

Even if in the equations the Mach and Reynolds numbers always show up as the ratio M_∞/Re_c, they must be enforced separately to satisfy the boundary conditions on velocity, as shown in subsection 2.3.2.

2.4 Finite Volume solver

In this work we use a Finite Volume (FV) solver, which is perhaps the most natural choice if one deals with the integral form of the equations, which in turn is one of the most natural form to work with when discontinuities (e.g. shocks) are present in the flow. Of course, it is not the unique technique one can use, as many different approaches have been successfully used (Finite Difference and Finite Elements among others).

As we already pointed out, the integral form of the equations is able to hold discontinuous solutions, and our direct discretization of them falls in the shock capturing scheme methodology. For the sake of clarity, we should emphasize that the real flow doesn't show any discontinuity, since viscosity would act to smooth any of them. However, in correspondence of a shock the continuous variation takes place in such a short distance that a full resolution in that zone is almost impossible. As such, from the discretization perspective, it must be regarded as a proper discontinuity, and other approaches must be used. As already pointed out, the FV approach allows discontinuous solutions. As such, they are a natural choice for dealing with compressible flows. As pointed out by Pirozzoli (2011b), "a major flaw of shock-capturing schemes ... is the reduction of accuracy near shocks". It is not the only possible approach, though. Finite Differences may also be used, but in the discretization process the fulfillment of the jump relations is not automatic, and one has to take care to use a proper discretization formula. Another attractive approach to deal with discontinuities is the use of shock-fitting techniques. In this case, one considers each discontinuity as a virtual boundary, explicitly imposing the jump conditions across it, so that the inner field is considered continuous on each side of the discontinuity. As a drawback, one has to know the discontinuity

location, and additional difficulties arise when the shock topology changes during the computation (Bonfiglioli et al., 2016), e.g. the case of two merging shocks. We shall only consider shock-capturing FV schemes for structured grids.

In this work we also make use of the MPI paradigm to parallelize the code, in order to speed up the computations, by exploiting the high number of computational cores we dispose today.

2.4.1 Discretization procedure

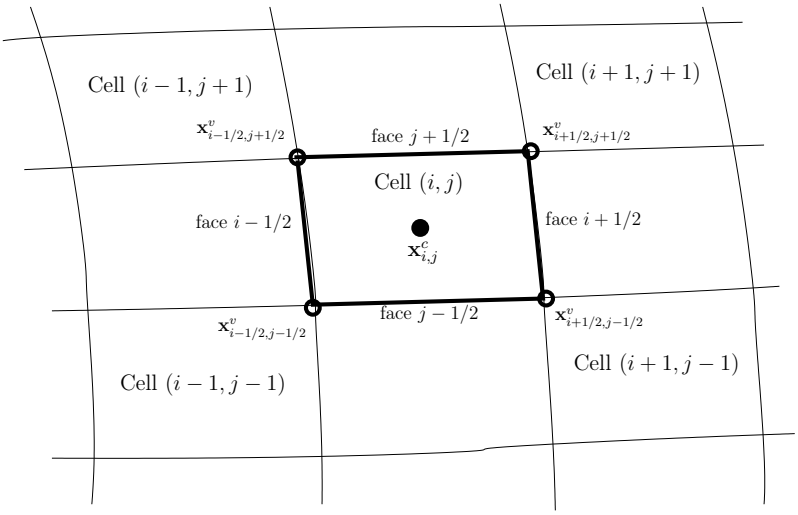

Figure 2.1: *Some of the used notation related to the grid. The sketch is related to the (x, y) plane. Grid is uniformly extruded in the third dimension.*

The discretization precedure follows the method of lines in decoupling the approximation of the spatial and temporal terms. The spatial domain is split into grid cells, and equation (2.59) is rewritten for the generic discrete volume $\mathcal{V}_{i,j,k}$ composing the grid as

$$\frac{\mathrm{d}\mathbf{U}_{i,j,k}}{\mathrm{d}t} + \frac{1}{\mathcal{V}_{i,j,k}} \sum_{\text{faces}} \left[\mathbf{F}'_f \, S_f\right] = \frac{1}{\mathcal{V}_{i,j,k}} \sum_{\text{faces}} \left[\mathbf{G}'_f \, S_f\right] \tag{2.62}$$

where the summation has to be performed on all the faces delimiting the discrete volume, which are identified by the subscript f. Since the grid is structured, (i, j, k) is used to locate the discrete volume. $\mathbf{U}_{i,j,k}$ identifies the integral mean of $\mathbf{U}$, while $\mathbf{F}'_f$ and $\mathbf{G}'_f$ are approximations of the fluxes on face f. Fig. 2.1 helps recognize the used terminology, where face f for cell (i, j) cycles through faces $i + 1/2$, $j + 1/2$, $i - 1/2$, $j - 1/2$; additional definitions are given in the following. The integral mean is defined as

$$\mathbf{U}_{i,j,k} = \frac{1}{\mathcal{V}_{i,j,k}} \int_{\mathcal{V}_{i,j,k}} \mathbf{U} \, \mathrm{d}\mathcal{V} \tag{2.63}$$

The resulting (discrete) quantity $\mathbf{U}_{i,j,k}$ is assumed to be "concentrated" in the cell *centroid*, defined as

$$\mathbf{x}^c_{i,j,k} = \frac{1}{\mathcal{V}_{i,j,k}} \int_{\mathcal{V}_{i,j,k}} \mathbf{x} \, \mathrm{d}\mathcal{V} \tag{2.64}$$

We assume always to have a two-dimensional grid in the (x, y) plane, which can be extrapolated in the third dimension. Most grid quantities can thus be obtained by reasoning in two dimensions. Assuming that each face with normal lying in the (x, y) plane is also a plane surface, it can be shown that the (x, y) components of the centroid $\mathbf{x}^c_{i,j,k}$ can be exactly computed with the formula

$$\mathbf{x}^c_{i,j,k} = \frac{1}{3} \sum_{v=1}^{4} \overline{\mathbf{x}}_{v+1/2} [(\mathbf{x}_v \wedge \mathbf{x}_{v+1}) \cdot \hat{\mathbf{z}}] \tag{2.65}$$

where the fractional subscripts such as $v + 1/2$ will be widely used to denote quantities at the cell interfaces. The line above the half-indexed symbols denotes the arithmetic mean

$$\overline{\varphi}_{l+1/2} = \frac{1}{2}(\varphi_l + \varphi_{l+1}) \tag{2.66}$$

and $\mathbf{x}_v$ is a redefinition of $\mathbf{x}^v_{i+1/2,j+1/2,k+1/2}$ (coordinate of the grid vertices, also called nodes) used for compactness of the formula, such that

$$\begin{aligned}
&\mathbf{x}_{v=1} = \mathbf{x}^v_{i-1/2,j-1/2,k-1/2} && \mathbf{x}_{v=2} = \mathbf{x}^v_{i+1/2,j-1/2,k-1/2} \\
&\mathbf{x}_{v=3} = \mathbf{x}^v_{i+1/2,j+1/2,k-1/2} && \mathbf{x}_{v=4} = \mathbf{x}^v_{i-1/2,j+1/2,k-1/2} \\
&\mathbf{x}_{v=5} = \mathbf{x}_{v=1}
\end{aligned}$$

i.e. for increasing v, $\mathbf{x}_v$ identify sequentially all the vertex of cell i, j, k in the (x, y) plane, counterclockwise. In $\hat{\mathbf{z}}$ direction things are much easier, since we just consider an equispaced extrapolation in that direction. As such, the centroid third component can be computed as the mean of the third component of vertices. We shall now describe the approximations used to write the fluxes.

2.4.2 Discretization of convective terms

The convective fluxes (also named Eulerian fluxes) on the cell faces can be approximated in a straightforward way with formula (6.2.8) of (Hirsch, 1988). Considering as an example the generic face $i + 1/2$, we have

$$\mathbf{F}'_{i+1/2,j} = \frac{1}{2} \left(\mathbf{F}'_{i,j} + \mathbf{F}'_{i+1,j} \right) \tag{2.67}$$

(as shown later, we will not use this expression, though). Having directly expressed the flux on each face, the resulting scheme is conservative, as already stressed previously. As such, the discrete conservation of conserved quantities is guaranteed

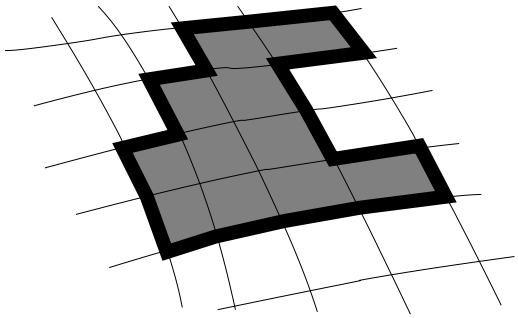

Figure 2.2: *Two-dimensional sketch of the compound volume used to illustrate the discrete conservation property. The filled area is* $\bigcup \mathcal{V}_{i,j,k}$*. The thick solid line is* $\partial(\bigcup \mathcal{V}_{i,j,k})$*.*

also at a discrete level, that is, no artificial source terms are added numerically, and the temporal variation of the discrete $\mathbf{U}$ is only due to the fluxes on the boundary of the considered volume. Referring to Fig. 2.2, if we consider a volume composed by the union of different discrete cells, the definition of the integral mean on that volume is easily seen to bring the volume-weighted average of the discrete $\mathbf{U}_{i,j,k}$ on the cell composing the new control volume, that is

$$\int_{\bigcup \mathcal{V}_{i,j,k}} \mathbf{U} \, \mathrm{d}\mathcal{V} = \sum_{cells} \int_{\mathcal{V}_{i,j,k}} \mathbf{U} \, \mathrm{d}\mathcal{V} = \sum_{cells} \mathcal{V}_{i,j,k} \mathbf{U}_{i,j,k} \tag{2.68}$$

and from equation (2.62)

$$\frac{\mathrm{d}}{\mathrm{d}t} \int_{\bigcup \mathcal{V}_{i,j,k}} \mathbf{U} \, \mathrm{d}\mathcal{V} + \sum_{cells} \sum_{\text{faces}} \left[\mathbf{F}'_f \, S_f \right] = \sum_{cells} \sum_{\text{faces}} \left[\mathbf{G}'_f \, S_f \right] \tag{2.69}$$

Now, each face belongs to two adjacent cells, and a flux contributing in a negative way in a cell contribute in a positive way in the other cell (quantities exiting a cell are entering the other cell), so that the sums $\sum_{cells} \sum_{\text{faces}}$ cancel out to be just $\sum_{\partial(\bigcup \mathcal{V}_{i,j,k})}$, i.e. the time variation of the integral mean quantities over the compound volume depends just on the fluxes on the edge faces of the compound volume itself, without the appearance of artificial internal sources.

Since the integral formulation is able to handle discontinuities, the conservative formulation, which resemble the integral formulation at a discrete level, is also able to handle them. In this respect, the Lax-Wendroff theorem holds (Hirsch, 1988):

***Theorem* 1** (Lax-Wendroff)**.** *If the solution of the discretized system* (2.62) *converges boundedly almost everywhere to some function* $\mathbf{x}, \mathbf{t}$ *when* $\Delta\mathbf{x}$, Δt *tend to zero, then* $\mathbf{u}(\mathbf{x}, t)$ *is a* weak solution *of* (2.34)

This property is related to the conservation of the first integrals at a discrete level. One can expect that the conservation of also higher order integrals at a discrete level could be beneficial for the numerical solution. Indeed, Pirozzoli (2010, 2011a) show that the discretization of a particular form of the equations brings a conservative

scheme, which also conserves a quadratic integral, the kinetic energy, in the limit of inviscid, incompressible fluid. Codes fulfilling these conservation properties also at a discrete level gain a non-linear stability which enables them to run without the addition of artificial, numerical viscosity. This property is very important in a code which is used for DNS. Although in his papers Pirozzoli uses the Finite Difference approach, it can be shown the equivalence between FD and FV approaches until the first is formulate in conservative form on a Cartesian, uniform grid (Hirsch, 1988), that is (considering a two-dimensional example)

$$\frac{1}{\mathcal{V}_{i,j,k}} \oint_S \mathbf{F} \cdot \hat{\mathbf{n}} = \frac{1}{\mathcal{V}_{i,j,k}} \oint_S (f \ \mathrm{d}y - g \ \mathrm{d}x) \simeq \tag{2.70}$$

$$\simeq \frac{1}{\Delta x \Delta y}(f_{i+1/2,j}\Delta y + g_{i,j+1/2}\Delta x - f_{i-1/2,j}\Delta y - g_{i,j-1/2}\Delta x) = \tag{2.71}$$

$$= \frac{f_{i+1/2,j} - f_{i-1/2,j}}{\Delta x} + \frac{g_{i,j+1/2} - g_{i,j-1/2}}{\Delta y} \tag{2.72}$$

i.e., starting from the FV discretization we found a FD formula.

In Appendix A we show in the Finite Difference framework that an SBP operator, satisfying properties (A.2), applied to the equations in split-form naturally lead to an energy conserving scheme. In Appendix A we also show that the conservative formulas given by Pirozzoli (2010, 2011a) can be generalized leaving undefined the splitting parameter. However it is also shown that only the values of the parameters used by Pirozzoli lead to an energy conserving scheme. These considerations made us to choose an approximation for the convective fluxes slightly different than (2.67)

$$\mathbf{F}'_{i+1/2,j} = \overline{u'}_{i+1/2,j} \begin{Bmatrix} \overline{\rho}_{i+1/2,j} \\ (\overline{\rho \mathbf{u}})_{i+1/2,j} \\ (\overline{\rho H})_{i+1/2,j} \end{Bmatrix} + \overline{p}_{i+1/2,j} \begin{Bmatrix} 0 \\ \hat{\mathbf{n}}_{i+1/2,j} \\ 0 \end{Bmatrix} \tag{2.73}$$

$$\mathbf{F}'_{i,j+1/2} \quad \text{obtained by considering increments on } j \text{ rather than } i \tag{2.74}$$

where $\overline{u'}_{i+1/2,j} = \overline{\mathbf{u}}_{i+1/2,j} \cdot \hat{\mathbf{n}}_{i+1/2,j}$, and $\hat{\mathbf{n}}_{i+1/2,j}$ is exactly computed on each face, and the normal $\hat{\mathbf{n}}_{i+1/2,j}$ is always assumed to point towards greater i, so that for cell i the external normal on face $i+1/2$ is $\hat{\mathbf{n}}_{i+1/2,j}$, and on face $i-1/2$ is $-\hat{\mathbf{n}}_{i-1/2,j}$ (Fig. 2.3). In particular the latter assumption let us rewrite (2.62) as

$$\begin{aligned} \frac{\mathrm{d}\mathbf{U}_{i,j,k}}{\mathrm{d}t} &+ \frac{1}{\mathcal{V}_{i,j,k}} \left(\mathbf{F}'_{i+1/2,j} S_{i+1/2,j} - \mathbf{F}'_{i-1/2,j} S_{i-1/2,j}\right) + \\ &+ \frac{1}{\mathcal{V}_{i,j,k}} \left(\mathbf{F}'_{i,j+1/2} S_{i,j+1/2} - \mathbf{F}'_{i,j-1/2} S_{i,j-1/2}\right) = \\ &= \frac{1}{\mathcal{V}_{i,j,k}} \left(\mathbf{G}'_{i+1/2,j} S_{i+1/2,j} - \mathbf{G}'_{i-1/2,j} S_{i-1/2,j}\right) + \\ &+ \frac{1}{\mathcal{V}_{i,j,k}} \left(\mathbf{G}'_{i,j+1/2} S_{i,j+1/2} - \mathbf{G}'_{i,j-1/2} S_{i,j-1/2}\right) \end{aligned} \tag{2.75}$$

This expression perhaps reveals even better the equivalence between FD and FV methods.

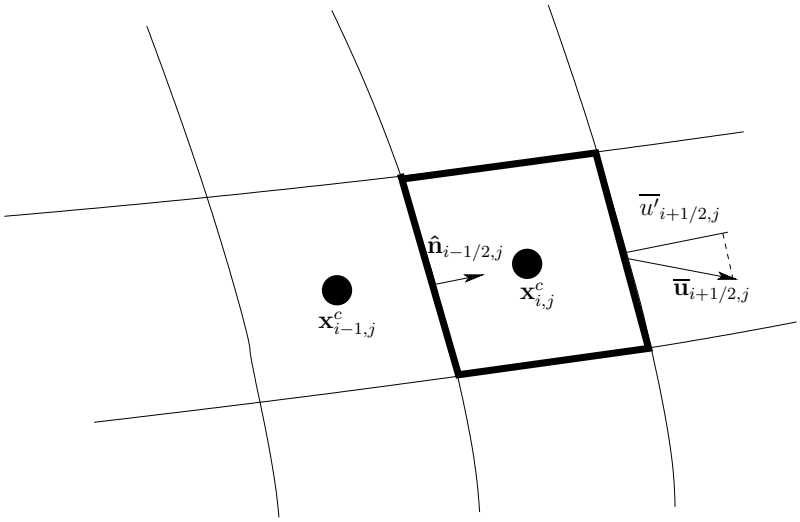

Figure 2.3: *Sketch to illustrate the convention used for normal on faces.*

Choice (2.73) for the fluxes is the analogous of the Blaisdell et al. (1996) splitting in the Finite Difference framework, and the same advantages may be expected when used in the Finite Volume approach. In fact, this form of the flux is retrieved by (A.33) and (A.35), if we consider the second order expansion in a periodic domain (focusing our attention just for the flux of the continuity equation for the sake of clarity)

$$h_{i+1/2} = 2 \sum_{k=1}^{r} \sum_{l=1}^{k} A_{i-k+l,\, i+l} \frac{\rho_{i+l} + \rho_{i-k+l}}{2} \frac{u'_{i+l} + u'_{i-k+l}}{2} \tag{2.76}$$

and for second order we have $r = 1$ and $A_{i,i+1} = 1/2$, thus yielding

$$h_{i+1/2} = \frac{\rho_{i+1} + \rho_i}{2} \frac{u'_{i+1} + u'_i}{2} \tag{2.77}$$

The choice of using the Blaisdell et al. (1996) splitting is due to the fact that in this work the results where almost coincident with the ones obtained with the Kennedy and Gruber (2008) splitting, but at a lower computational cost. Note that, as reported also by Pirozzoli, Blaisdell et al. (1996) splitting does not increase the stability through the conservation of the kinetic energy, but through the minimization of the aliasing error.

The use of centered stencils leads to a second order accurate, non-dissipative scheme on Cartesian meshes. These property are maintained for sufficiently smooth varying mesh sizes (Hirsch, 1988). However, flow traveling through a discontinuity such as a shock must encounter some dissipation, also in the limit of vanishing viscosity, thus the use of the formula (2.73) alone is conceptually wrong in presence of a shock, since no dissipation is added through the shock. We overcome this problem by using formula (2.73) alone in regions of the flow where there are no shocks, and by correcting this flux by adding an artificial diffusion derived by the WENO scheme (Weighted-Essentially Non-Oscillatory, (Jiang and Shu, 1996)) only

in regions with shocks. The shocks are located through a modified Ducros sensor (Ducros et al., 1999)

$$\Theta = \max\left(-\frac{\nabla\cdot\mathbf{u}}{\sqrt{(\nabla\cdot\mathbf{u})^2+(\nabla\times\mathbf{u})^2+\varepsilon}},\,0\right) \tag{2.78}$$

$$\varepsilon = \left(\frac{u_\infty}{c}\right)^2 \tag{2.79}$$

which is defined on each computational cell. On the faces the value representing the sensor is chosen to be

$$\Theta_{i+1/2,j} := \max(\Theta_{i,j},\,\Theta_{i+1,j}) \tag{2.80}$$

$$\Theta_{i,j+1/2} \quad \text{obtained by considering increments on } j \text{ rather than } i \tag{2.81}$$

and the discontinuity is located assuming a threshold value for Θ. The one used throughout this work is $\overline{\Theta} = 0.05$, unless otherwise stated. When the value across a face is greater then the threshold $\overline{\Theta}$, a dissipative flux is added. Little variants of the approach are also used, but unless otherwise stated we follow the approach described below.

2.4.3 WENO dissipation

To build the dissipative artificial fluxes, we follow the approach described in (Shu, 2003), where the WENO reconstruction is applied to the conserved variables, and the reconstructed values are inserted in the Lax-Friedrichs flux, whose expression for the one-dimensional model problem reads

$$F(U(x_{i+1/2},t)) \simeq \frac{F(U^-_{i+1/2},t)+F(U^+_{i+1/2},t)}{2} - \frac{\alpha}{2}(U^+_{i+1/2}-U^-_{i+1/2}) \tag{2.82}$$

$$\alpha = \max_U \frac{\partial F}{\partial U} \tag{2.83}$$

Here, the right-hand-side is an approximation for flux on face $i+1/2$, $U^-_{i+1/2}$ and $U^+_{i+1/2}$ are the WENO reconstructed variables on each side of face $i+1/2$. The first term on RHS is clearly an approximation for $F_{i+1/2}$, while the second term, which vanishes for a smooth converged solution, represents the artificial diffusion. In our implementation, we retain the expression (2.73) for the approximation of $F_{i+1/2}$ in all the domain, while only taking into account the dissipative term appearing in (2.82), where instead of taking the maximum over all U_i, we only take the maximum between cells $(i, i+1)$ to decrease artificial dissipation (local Lax-Friedrichs Scheme); that is, in the shocked region we use the expression

$$F(U(x_{i+1/2},t)) \simeq \frac{F(U_i,t)+F(U_{i+1},t)}{2} + F^{d,WENO}_{i+1/2} \tag{2.84}$$

$$F^{d,WENO}_{i+1/2} = -\frac{\alpha}{2}(U^+_{i+1/2}-U^-_{i+1/2})\,, \qquad \alpha = \max_{(U_i,U_{i+1})}\frac{\partial F}{\partial U} \tag{2.85}$$

The order of the WENO reconstruction may be decided in input, but unless otherwise stated, we use a third-order reconstruction throughout this work. As should be clear from (2.85), we reconstruct dimension by dimension, that is, on each face we consider a one dimensional problem. This fact, together with the coupling with (2.73), leads to an overall second order accuracy. The treatment of the artificial diffusion term on the one-dimensional model problem equation is exported in the one-dimensional equations system by diagonalizing the problem. To achieve the diagonal form of the system, we use a property of the Eulerian flux to be a homogeneous function of degree one in $\mathbf{U}$, as such, we can express $\mathbf{F}' = \mathbf{A}'\mathbf{U}$ (Beam and Warming, 1976, 1978), where $\mathbf{A}' = \partial\mathbf{F}'/\partial\mathbf{U}$. In particular, to retrieve the numerical diffusion term, we linearize the problem around face $i+1/2$, obtaining the (linear) flux

$$\mathbf{F}' \simeq \mathbf{A}'_{i+1/2}\mathbf{U} \tag{2.86}$$

which can be diagonalized (since the Euler system of equations is an hyperbolic system) introducing matrix $\mathbf{L}'_{i+1/2}$ of the normalized left eigenvectors of $\mathbf{A}'$ and matrix $\mathbf{R}'_{i+1/2} = {\mathbf{L}'_{i+1/2}}^{-1}$ of the normalized right eigenvectors

$$\mathbf{F}' \simeq \mathbf{R}'_{i+1/2}\mathbf{\Lambda}'_{i+1/2}\mathbf{L}'_{i+1/2}\mathbf{U} \tag{2.87}$$

where $\mathbf{\Lambda}'_{i+1/2}$ is the diagonal matrix of the eigenvalues. Pre-multiplying for $\mathbf{L}'_{i+1/2}$

$$\left(\mathbf{L}'_{i+1/2}\mathbf{F}'\right) \simeq \mathbf{\Lambda}'_{i+1/2}\left(\mathbf{L}'_{i+1/2}\mathbf{U}\right) \tag{2.88}$$

It is easy to apply the flux (2.85) to this form

$$\left(\mathbf{L}'_{i+1/2}\mathbf{F}'^{d,WENO}_{i+1/2}\right) = -\frac{1}{2}\underset{max}{\mathbf{\Lambda}'_{i,i+1}}\left(\mathbf{L}'_{i+1/2}\mathbf{U}^{+}_{i+1/2} - \mathbf{L}'_{i+1/2}\mathbf{U}^{-}_{i+1/2}\right) \tag{2.89}$$

and finally, pre-multiplying for $\mathbf{R}'_{i+1/2}$

$$\mathbf{F}'^{d,WENO}_{i+1/2} = -\frac{1}{2}\mathbf{R}'_{i+1/2}\underset{max}{\mathbf{\Lambda}'_{i,i+1}}\mathbf{L}'_{i+1/2}\left(\mathbf{U}^{+}_{i+1/2} - \mathbf{U}^{-}_{i+1/2}\right) \tag{2.90}$$

In this procedure we didn't break symmetry with respect the face $i+1/2$; as such, the overall second order accuracy for the approximation of the convective fluxes is maintained. Until now we did not properly define an intermediate state for matrices in $i+1/2$. Common choices are the Roe's state (Roe, 1981) between $(i, i+1)$, or, for a less diffusive scheme, Roe's state between $(i+1/2^-, i+1/2^+)$, such that the **final form of the WENO dissipative fluxes** is

$$\mathbf{F}'^{d,WENO}_{i+1/2} = -\frac{1}{2}\mathbf{R}'_{i+1/2}\underset{max}{\mathbf{\Lambda}'_{i,i+1}}\mathbf{L}'_{i+1/2}\left(\mathbf{U}^{+}_{i+1/2} - \mathbf{U}^{-}_{i+1/2}\right) \tag{2.91}$$

$$\mathbf{R}'_{i+1/2},\ \mathbf{L}'_{i+1/2} \text{ evaluated in Roe's state between } (i, i+1) \text{ or } (i+1/2^{\pm}) \tag{2.92}$$

$$\underset{max}{\mathbf{\Lambda}'_{i,i+1}} = \mathrm{diag}(\Lambda'_l)\,, \quad \Lambda'_l = \max_{i,i+1}\lambda'_l\,, \quad \lambda'_l \text{ eigenvalue of } \frac{\partial\mathbf{F}'}{\partial\mathbf{U}} \tag{2.93}$$

$$\mathbf{U}^{+}_{i-1/2},\ \mathbf{U}^{-}_{i-1/2} \text{ right and left WENO reconstructed variables} \tag{2.94}$$

2.4.4 Viscous fluxes

In the previous subsection we derived an artificial diffusion term. Here, we provide the discretization procedure for the physical ones. Recalling equations (2.59) and (2.60), $\mathbf{G}'_f$ is an approximation for

$$\begin{aligned}\mathbf{G}_j n_j = \sqrt{\gamma}\frac{M_\infty}{Re_c}\begin{Bmatrix} 0 \\ \mu\frac{\partial u_i}{\partial n} \\ \frac{1}{Pr}\frac{\gamma}{\gamma-1}K\frac{\partial T}{\partial n}\end{Bmatrix} + \\ + \sqrt{\gamma}\frac{M_\infty}{Re_c}\begin{Bmatrix} 0 \\ \mu\frac{\partial u_j}{\partial x_i}n_j - \frac{2}{3}\mu\frac{\partial u_k}{\partial x_k}n_i \\ \mu u_i\frac{\partial u_i}{\partial n} + \mu u_i\frac{\partial u_j}{\partial x_i}n_j - \frac{2}{3}\mu\frac{\partial u_k}{\partial x_k}u_n\end{Bmatrix}\end{aligned} \tag{2.95}$$

The normal derivatives in (2.95) are computed applying second order accurate Finite

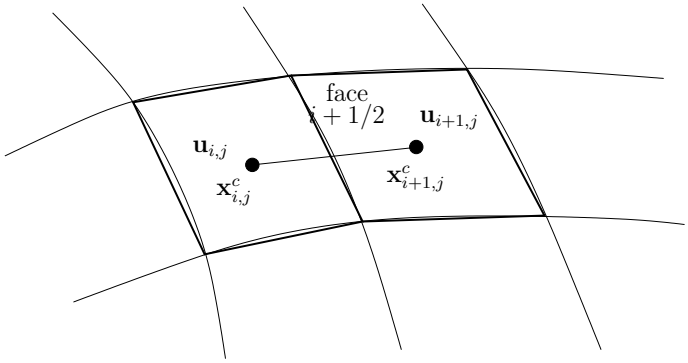

Figure 2.4: *Cells involved in the evaluation of $\partial\varphi/\partial n$ appearing in viscous fluxes on face $i+1/2$.*

Differences. Referring to Fig. 2.4, we have, for example for the term contributing to the momentum equations

$$\mu\left.\frac{\partial u_i}{\partial n}\right|_f \simeq \overline{\mu}_{i+1/2,j,k}\,\frac{u_{i+1,j,k}-u_{i,j,k}}{|\mathbf{x}^c_{i+1,j,k}-\mathbf{x}^c_{i,j,k}|} \tag{2.96}$$

The other derivatives appearing in the second row of (2.95) are first computed in each cell center by the gradient theorem

$$\frac{\partial\varphi}{\partial x_i} := \frac{1}{\mathcal{V}}\int_{\mathcal{V}}\frac{\partial\varphi}{\partial x_i}\,\mathrm{d}\mathcal{V} = \frac{1}{\mathcal{V}}\oint_{\partial\mathcal{V}}\varphi n_i\,\mathrm{d}S \tag{2.97}$$

where, as usual, the value of φ on faces is taken as the average value between adjacent cells in order to maintain second order accuracy. The obtained gradients refers to the cell-centroids. To obtain the values on faces, to be inserted in (2.95), we again consider the average values between adjacent cells.

In (2.95) we have split the content of vector $\mathbf{G}_j n_j$ in two vectors, in that, as will be explained, only the first, which has a greater importance for stability, will be dealt with also implicitly.

2.4.5 Runge-Kutta time-integration

With all the previous step we have been able to define a set of Ordinary Differential Equations (ODE), of the kind $\mathrm{d}\mathbf{U}_{i,j,k}/\mathrm{d}t = \mathbf{RHS}$, which can be efficiently solved with a Runge-Kutta algorithm. In this work, unless otherwise stated, we will use a three stages Runge-Kutta algorithm. To explain the algorithm used we refer to Orlandi (2012), considering separately linear and non-linear terms appearing in the semi-discrete system of equations

$$\frac{\partial \mathbf{U}_i}{\partial t} = [\mathbf{N}(\mathbf{U})]_i + (\mathbf{L}\mathbf{U})_i \tag{2.98}$$

Here $\mathbf{N}$ represents the non-linear terms, and $\mathbf{L}$ contains the linear terms that are to be treated implicitly. The latter is meant to increase the stability of the scheme. Denoting with superscripts n and $n+1$ the discretized times, and with superscripts L_1, L_2 the intermediate Runge-Kutta stages, we have

$$\mathbf{U}_i^{L_1} = \mathbf{U}_i^n + \gamma_1 \Delta t \mathbf{N}_i^n + \rho_1 \Delta t \mathbf{N}_i^{-L_2} + \alpha_1 \Delta t[\theta(\mathbf{L}\mathbf{U})_i^{L_1} + (1-\theta)(\mathbf{L}\mathbf{U})_i^n] \tag{2.99a}$$

$$\mathbf{U}_i^{L_2} = \mathbf{U}_i^{L_1} + \gamma_2 \Delta t \mathbf{N}^{L_1} + \rho_2 \Delta t \mathbf{N}^n + \alpha_2 \Delta t[\theta(\mathbf{L}\mathbf{U})_i^{L_2} + (1-\theta)(\mathbf{L}\mathbf{U})_i^{L_1}] \tag{2.99b}$$

$$\mathbf{U}_i^{n+1} = \mathbf{U}_i^{L_2} + \gamma_3 \Delta t \mathbf{N}^{L_2} + \rho_3 \Delta t \mathbf{N}^{L_1} + \alpha_3 \Delta t[\theta(\mathbf{L}\mathbf{U})_i^{n+1} + (1-\theta)(\mathbf{L}\mathbf{U})_i^{L_2}] \tag{2.99c}$$

where Δt is the discretized time interval $\Delta t = t^{n+1} - t^n$, the superscript $-L_2$ denotes the equivalent of L_2 but at time level $n-1$ and

$$\begin{aligned} &\gamma_1 = 8/15\,, && \gamma_2 = 5/12\,, && \gamma_3 = 3/4\,, \\ &\rho_1 = 0\,, && \rho_2 = -17/60\,, && \rho_3 = -5/12\,, \\ &\alpha_i = \rho_i + \gamma_i\,, && && \theta = \begin{cases} 1 & \text{Implicit Euler} \\ 1/2 & \text{Crank-Nicolson} \end{cases} \end{aligned} \tag{2.100}$$

Each of the (2.99) is a time integration on a fractional step $\alpha_i \Delta t$, as can be easily seen by expanding in Taylor series for example the terms of (2.99a) around time level n. The $\mathbf{L}$ terms are treated implicitly by using an Implicit Euler type of integration ($\theta = 1$, first order) or a Crank-Nicolson one ($\theta = 1/2$, second order). Each of the (2.99) may be recast in the so called *delta form*, as

$$(\mathbf{U}_i^{L_1} - \mathbf{U}_i^n) = \gamma_1 \Delta t \mathbf{N}_i^n + \rho_1 \Delta t \mathbf{N}_i^{-L_2} + \alpha_1 \Delta t (\mathbf{L}\mathbf{U})_i^n + \alpha_1 \theta \Delta t[(\mathbf{L}\mathbf{U})_i^{L_1} - (\mathbf{L}\mathbf{U})_i^n] \tag{2.101a}$$

$$(\mathbf{U}_i^{L_2} - \mathbf{U}_i^{L_1}) = \gamma_2 \Delta t \mathbf{N}_i^{L_1} + \rho_2 \Delta t \mathbf{N}_i^n + \alpha_2 \Delta t (\mathbf{L}\mathbf{U})_i^{L_1} + \alpha_2 \theta \Delta t[(\mathbf{L}\mathbf{U})_i^{L_2} - (\mathbf{L}\mathbf{U})_i^{L_1}] \tag{2.101b}$$

$$(\mathbf{U}_i^{n+1} - \mathbf{U}_i^{L_2}) = \gamma_3 \Delta t \mathbf{N}_i^{L_2} + \rho_3 \Delta t \mathbf{N}_i^{L_1} + \alpha_3 \Delta t (\mathbf{L}\mathbf{U})_i^{L_2} + \alpha_3 \theta \Delta t[(\mathbf{L}\mathbf{U})_i^{n+1} - (\mathbf{L}\mathbf{U})_i^{L_2}] \tag{2.101c}$$

so that the choice of the implicit integration method between Implicit Euler and Crank-Nicolson only affects a coefficient of the terms that go on the left-hand-side during the solving procedure. However, it must be remarked that when the computations are not fully explicit, the order of the time integration is the same

of the implicit scheme, and the Runge-Kutta third order is retrieved only for fully explicit computations. It is however still a convenient approach for the enhanced stability we achieve. Another advantage of the approach is the coefficient $\rho_1 = 0$, since this way no information from previous steps is required for the time integration from time level n to time level $n+1$. It is perhaps worth mentioning that the temporal integration does not alter the conservative nature of the scheme.

2.4.6 Implicit treatment of j fluxes

In the description of the Runge-Kutta algorithm we did not define the terms $\mathbf{N}$ and $\mathbf{L}$. For reference purposes, lets recall one of the (2.101), for example (2.101c)

$$(\mathbf{U}_i^{n+1} - \mathbf{U}_i^{L_2}) = \gamma_3 \Delta t \mathbf{N}_i^{L_2} + \rho_3 \Delta t \mathbf{N}_i^{L_1} + \alpha_3 \Delta t (\mathbf{L}\mathbf{U})_i^{L_2} + \alpha_3 \theta \Delta t [(\mathbf{L}\mathbf{U})_i^{n+1} - (\mathbf{L}\mathbf{U})_i^{L_2}]$$

When run in full-explicit mode, then $\mathbf{L} = 0$ (representative of the linear terms to be treated implicitly) and $\mathbf{N}$ is given by taking into account all the previous spatial discretized terms. It is useful to rewrite the expression with all the previous discretized terms, remembering that overbars denote arithmetic averages and the prime retains informations about the orientation of the surface

$$\frac{\mathrm{d}\mathbf{U}_{i,j}}{\mathrm{d}t} = \mathbf{RHS}_{i,j} = \mathbf{N}_{i,j} \quad \Rightarrow \tag{2.102}$$

$$\begin{aligned} \Rightarrow \quad \mathbf{N}_{i,j} = & -\frac{1}{\mathcal{V}_{i,j}} \left(\mathbf{F}'_{i+1/2,j} S_{i+1/2,j} - \mathbf{F}'_{i-1/2,j} S_{i-1/2,j} \right) + \\ & -\frac{1}{\mathcal{V}_{i,j}} \left(\mathbf{F}'_{i,j+1/2} S_{i,j+1/2} - \mathbf{F}'_{i,j-1/2} S_{i,j-1/2} \right) + \\ & +\frac{1}{\mathcal{V}_{i,j}} \left(\mathbf{G}'_{i+1/2,j} S_{i+1/2,j} - \mathbf{G}'_{i-1/2,j} S_{i-1/2,j} \right) + \\ & +\frac{1}{\mathcal{V}_{i,j}} \left(\mathbf{G}'_{i,j+1/2} S_{i,j+1/2} - \mathbf{G}'_{i,j-1/2} S_{i,j-1/2} \right) \end{aligned} \tag{2.103}$$

$$\begin{aligned} \mathbf{F}'_{i+1/2,j} = & \overline{u'}_{i+1/2,j} \begin{Bmatrix} \overline{\rho}_{i+1/2,j} \\ (\overline{\rho \mathbf{u}})_{i+1/2,j} \\ (\overline{\rho H})_{i+1/2,j} \end{Bmatrix} + \overline{p}_{i+1/2,j} \begin{Bmatrix} 0 \\ \hat{\mathbf{n}}_{i+1/2,j} \\ 0 \end{Bmatrix} + \\ & + f(\Theta_{i+1/2,j}) \mathbf{F}'^{d,WENO}_{i+1/2,j} \\ & f(\Theta_{i+1/2,j}) = \begin{cases} 0 & \text{for } \Theta_{i+1/2,j} < \overline{\Theta} \\ 1 & \text{for } \Theta_{i+1/2,j} \geq \overline{\Theta} \end{cases} \\ & \mathbf{F}'^{d,WENO}_{i+1/2} = -\frac{1}{2} \mathbf{R}'_{i+1/2} \underset{max}{\mathbf{\Lambda}'_{i,i+1}} \mathbf{L}'_{i+1/2} \left(\mathbf{U}^+_{i+1/2} - \mathbf{U}^-_{i+1/2} \right) \end{aligned} \tag{2.104}$$

$\mathbf{F}'_{i,j+1/2}$ obtained by considering increments on j rather than i

$$
\begin{aligned}
\mathbf{G}'_{i+1/2,j} =& \mathbf{G}'^{1}_{i+1/2,j} + \mathbf{G}'^{2}_{i+1/2,j} + \mathbf{G}'^{3}_{i+1/2,j} \\
\mathbf{G}'^{1}_{i+1/2,j} =& \sqrt{\gamma}\frac{M_\infty}{Re_c}\begin{Bmatrix} 0 \\ \overline{\mu}_{i+1/2,j}\frac{\mathbf{u}_{i+1,j}-\mathbf{u}_{i,j}}{|\mathbf{x}^c_{i+1,j}-\mathbf{x}^c_{i,j}|} \\ \frac{1}{Pr}\frac{\gamma}{\gamma-1}\overline{K}_{i+1/2,j}\frac{T_{i+1,j}-T_{i+1,j}}{|\mathbf{x}^c_{i+1,j}-\mathbf{x}^c_{i,j}|} \end{Bmatrix} \\
\mathbf{G}'^{2}_{i+1/2,j} =& \sqrt{\gamma}\frac{M_\infty}{Re_c}\begin{Bmatrix} 0 \\ \overline{\mu}_{i+1/2,j}\overline{\left(\frac{\partial \mathbf{u}}{\partial x_i}\right)}_{i+1/2,j}\cdot\hat{\mathbf{n}}_{i+1/2,j} \\ \overline{\mu}_{i+1/2,j}\mathbf{u}\cdot\frac{\mathbf{u}_{i+1}-\mathbf{u}_i}{|\mathbf{x}^c_{i+1,j}-\mathbf{x}^c_{i,j}|} + \overline{\mu}_{i+1/2,j}\overline{(u_i)}_{i+1/2,j}\overline{\left(\frac{\partial \mathbf{u}}{\partial x_i}\right)}_{i+1/2,j}\cdot\hat{\mathbf{n}}_{i+1/2,j} \end{Bmatrix} \\
\mathbf{G}'^{3}_{i+1/2,j} =& \sqrt{\gamma}\frac{M_\infty}{Re_c}\begin{Bmatrix} 0 \\ -\frac{2}{3}\overline{\mu}_{i+1/2,j}\overline{\left(\frac{\partial u_k}{\partial x_k}\right)}_{i+1/2,j}\hat{\mathbf{n}}_{i+1/2,j} \\ -\frac{2}{3}\overline{\mu}_{i+1/2,j}\overline{\left(\frac{\partial u_k}{\partial x_k}\right)}_{i+1/2,j}\overline{u'}_{i+1/2,j} \end{Bmatrix} \\
\mathbf{G}'_{i,j+1/2} \quad & \text{obtained by considering increments on } j \text{ rather than } i
\end{aligned}
\tag{2.105}
$$

Further definitions can be found in the previous subsections. So for full-explicit computations $\mathbf{N}$ and $\mathbf{L}$ are well defined, and we achieve second order in space and third order in time. When run in semi-implicit mode, we treat implicitly some of the terms including fluxes in the j direction, both for the convective and the viscous parts. As such, terms that in the explicit part go forming $\mathbf{N}$, now go form $\mathbf{L}$, such that

$$
\mathbf{N}^L_{expl} = \mathbf{N}^L_{impl} + (\mathbf{LU})^L \tag{2.106}
$$

For what concerns the viscous part, since it is already an almost linear term, we can easily deal with it. As such we shall describe it first, then we will describe what we do with the convective part, and finally put all together.

Semi-implicit treatment of viscous terms. As we stated, the time-integration of some of the fluxes in j direction will be treated implicitly. We start by the viscous fluxes, so that from (2.103) and (2.105) we have, in matrix form and only considering $\mathbf{G}'^{1}$

$$
(\mathbf{L}^{\mathbf{v}}\mathbf{U})_{i,j} = \frac{1}{\mathcal{V}_{i,j}}\left(\mathbf{G}'^{1}_{i,j+1/2}S_{i,j+1/2} - \mathbf{G}'^{1}_{i,j-1/2}S_{i,j-1/2}\right) \tag{2.107}
$$

$$
\mathbf{G}'^{1}_{i,j+1/2} = \mathbf{A}^{\mathbf{v}}{}_{i,j+1/2}(\mathbf{V_T}_{i,j+1} - \mathbf{V_T}_{i,j}), \qquad \mathbf{V_T}_{i,j} = \begin{Bmatrix} \rho_{i,j} \\ \mathbf{u}_{i,j} \\ T_{i,j} \end{Bmatrix} \tag{2.108}
$$

$$
\mathbf{A}^{\mathbf{v}}{}_{i,j+1/2} = \sqrt{\gamma}\frac{M_\infty}{Re_c}\begin{bmatrix} 0 & 0 & 0 \\ 0 & \frac{\overline{\mu}_{i,j+1/2}}{|\mathbf{x}^c_{i+1,j}-\mathbf{x}^c_{i,j}|}\mathbf{I} & 0 \\ 0 & 0 & \frac{1}{Pr}\frac{\gamma}{\gamma-1}\frac{\overline{K}_{i,j+1/2}}{|\mathbf{x}^c_{i+1,j}-\mathbf{x}^c_{i,j}|} \end{bmatrix} \tag{2.109}
$$

We want to solve the implicit part by solving for the conservative variables $\mathbf{U}$, while in this formula there are the primitive variables $\mathbf{V_T}$. In the continuous case they are linked by the Jacobian matrix $\mathbf{P_T} = (\partial\mathbf{U})/(\partial\mathbf{V_T})$. Here the subscript T stands for the fifth component of $\mathbf{V_T}$ being the temperature, to distinguish them from $\mathbf{V_p}$, $\mathbf{P_p}$ where instead pressure is considered. Considering a similar relation for the discrete case, we have

$$\Delta\mathbf{V_T}_{i,j} = \mathbf{P_T}_{i,j}\Delta\mathbf{U}_{i,j} \tag{2.110}$$

where the Δ refers to temporal variations, for example $\Delta U^{L_2}_{i,j} = (U^{n+1}_{i,j} - U^{L_2}_{i,j})$. So we rewrite (2.107) for a $\Delta\mathbf{V}$ as

$$(\mathbf{L^v}\Delta\mathbf{U})_{i,j} = \frac{1}{\mathcal{V}_{i,j}}\left[S_{i,j+1/2}\mathbf{A^v}_{i,j+1/2}(\mathbf{P_T}_{i,j+1}\Delta\mathbf{U}_{i,j+1} - \mathbf{P_T}_{i,j}\Delta\mathbf{U}_{i,j}) + \right. \tag{2.111}$$

$$\left. - S_{i,j-1/2}\mathbf{A^v}_{i,j-1/2}(\mathbf{P_T}_{i,j}\Delta\mathbf{U}_{i,j} - \mathbf{P_T}_{i,j-1}\Delta\mathbf{U}_{i,j-1})\right] \tag{2.112}$$

Defining the matrices $\mathbf{L^A}$, $\mathbf{L^B}$, $\mathbf{L^C}$ as

$$\mathbf{L^A}_{i,j} = \frac{S_{i,j-1/2}}{\mathcal{V}_{i,j}}\,\mathbf{A^v}_{i,j-1/2}\mathbf{P_T}_{i,j-1}\,, \qquad \mathbf{L^C}_{i,j} = \frac{S_{i,j+1/2}}{\mathcal{V}_{i,j}}\mathbf{A^v}_{i,j+1/2}\mathbf{P_T}_{i,j+1} \tag{2.113}$$

$$\mathbf{L^B}_{i,j} = -\frac{1}{\mathcal{V}_{i,j}}\left[S_{i,j+1/2}\mathbf{A^v}_{i,j+1/2} + S_{i,j-1/2}\mathbf{A^v}_{i,j-1/2}\right]\mathbf{P_T}_{i,j} \tag{2.114}$$

Thus we can write

$$(\mathbf{L^v U})_{i,j} = \mathbf{L^A}_{i,j}\mathbf{U}_{i,j-1} + \mathbf{L^B}_{i,j}\mathbf{U}_{i,j} + \mathbf{L^C}_{i,j}\mathbf{U}_{i,j+1} \tag{2.115}$$

To fix the ideas, let see how the equations for the Runge-Kutta time-integration reads when only the viscous j fluxes are to be implicit. We have:

$$\begin{aligned}
\mathbf{N^v}_{i,j} = &- \frac{1}{\mathcal{V}_{i,j}}\left(\mathbf{F'}_{i+1/2,j}S_{i+1/2,j} - \mathbf{F'}_{i-1/2,j}S_{i-1/2,j}\right) + \\
&- \frac{1}{\mathcal{V}_{i,j}}\left(\mathbf{F'}_{i,j+1/2}S_{i,j+1/2} - \mathbf{F'}_{i,j-1/2}S_{i,j-1/2}\right) + \\
&+ \frac{1}{\mathcal{V}_{i,j}}\left(\mathbf{G'}_{i+1/2,j}S_{i+1/2,j} - \mathbf{G'}_{i-1/2,j}S_{i-1/2,j}\right) + \\
&+ \frac{1}{\mathcal{V}_{i,j}}\left(\mathbf{G'^2}_{i,j+1/2}S_{i,j+1/2} - \mathbf{G'^2}_{i,j-1/2}S_{i,j-1/2}\right) + \\
&+ \frac{1}{\mathcal{V}_{i,j}}\left(\mathbf{G'^3}_{i,j+1/2}S_{i,j+1/2} - \mathbf{G'^3}_{i,j-1/2}S_{i,j-1/2}\right)
\end{aligned} \tag{2.116}$$

which differs from (2.103) for the absence of the viscous j fluxes $\mathbf{G'^1}$. Then we have (2.115), and inserting both in (2.101c) yields, conveniently setting $(\mathbf{U}^{n+1}_{i,j} - \mathbf{U}^{L_2}_{i,j}) =: \Delta\mathbf{U}^{L2}_{i,j}$

$$\begin{aligned}
\Delta\mathbf{U}^{L2}_{i,j} = &\,\gamma_3\Delta t\mathbf{N^v}^{L_2}_{i,j} + \rho_3\Delta t\mathbf{N^v}^{L_1}_{i,j} + \\
&+ \alpha_3\Delta t\left(\mathbf{L^A}^{L_2}_{i,j}\mathbf{U}^{L_2}_{i,j-1} + \mathbf{L^B}^{L_2}_{i,j}\mathbf{U}^{L_2}_{i,j} + \mathbf{L^C}^{L_2}_{i,j}\mathbf{U}^{L_2}_{i,j+1}\right) + \\
&+ \alpha_3\theta\Delta t\left(\mathbf{L^A}^{L_2}_{i,j}\Delta\mathbf{U}^{L_2}_{i,j-1} + \mathbf{L^B}^{L_2}_{i,j}\Delta\mathbf{U}^{L_2}_{i,j} + \mathbf{L^C}^{L_2}_{i,j}\Delta\mathbf{U}^{L_2}_{i,j+1}\right)
\end{aligned} \tag{2.117}$$

The unknowns we have to solve for are the vectors $\Delta\mathbf{U}^{L_2}$, so we can rewrite, in block-matrix form

$$\begin{bmatrix} \ddots & \ddots & \ddots & \ddots & \ddots \\ 0 & -\alpha_3\theta\Delta t\mathbf{L}^{\mathbf{A}}{}^{L_2}_{i,j} & \mathbf{I}-\alpha_3\theta\Delta t\mathbf{L}^{\mathbf{B}}{}^{L_2}_{i,j} & -\alpha_3\theta\Delta t\mathbf{L}^{\mathbf{C}}{}^{L_2}_{i,j} & 0 \\ \ddots & \ddots & \ddots & \ddots & \ddots \end{bmatrix} \begin{Bmatrix} \vdots \\ \Delta\mathbf{U}^{L_2}_{i,j-1} \\ \Delta\mathbf{U}^{L_2}_{i,j} \\ \Delta\mathbf{U}^{L_2}_{i,j+1} \\ \vdots \end{Bmatrix} = \begin{Bmatrix} \vdots \\ \mathbf{RHS}_{i,j-1} \\ \mathbf{RHS}_{i,j} \\ \mathbf{RHS}_{i,j+1} \\ \vdots \end{Bmatrix}$$

where at the left-hand-side we have a block-tridiagonal matrix, and $\mathbf{RHS}_{i,j}$ is given by the first two rows at the right-hand-side of (2.117), so the system may be efficiently solved to get the increments $\Delta\mathbf{U}$.

Some notes about the linearization procedure:

1. Relation (2.110) introduces an approximation, so that the implicit viscous j fluxes are not exactly equal to the explicit viscous j fluxes. However, using both does not introduce any inconsistency in the equations. As such, for convenience we compute the "implicit fluxes" that appears in $\mathbf{RHS}_j$ in the "explicit" way, that is, at the right-hand-side we compute the flux using the primitive variables rather than the conservative ones, which must be however used at the left-hand-side.

2. The unavoidable approximation intrinsic to the (2.101), and which has been used in (2.117), is that the $\mathbf{L}$ linear term must be known. As such, they can only be evaluated at previous times, even if, conceptually, the ones multiplying $\mathbf{U}^{n+1}$ should have been evaluated at time level $n+1$.

Overall, they don't affect the order of accuracy of the semi-implicit scheme, which remains one for Implicit Euler ($\theta = 1$) and two for Crank-Nicolson ($\theta = 1/2$).

Semi-implicit treatment of convective terms. As done with the viscous j fluxes, we treat implicitly also the convective j fluxes. Since the convective part is non-linear, before proceeding we need to linearize them. From (2.103) and (2.104) we have

$$(\mathbf{L}^{\mathbf{c}}\mathbf{U})_{i,j} = -\frac{1}{\mathcal{V}_{i,j}}\left(\mathbf{F}'_{i,j+1/2}S_{i,j+1/2} - \mathbf{F}'_{i,j-1/2}S_{i,j-1/2}\right) \tag{2.118}$$

$$\mathbf{F}'_{i,j+1/2} \simeq \mathbf{F}\left(\mathbf{U}_{i,j+1/2}\right) + f(\Theta_{i,j+1/2})\mathbf{F}'^{d,WENO}_{i,j+1/2} \tag{2.119}$$

The approximation symbol in (2.119) is due to the fact that here we do not split the operator, as instead we do in the explicit part. This is a crucial assumption, since the kinetic energy is no more conserved in the implicit integration. However, the grids we will use present a shock almost aligned to faces $i+1/2$, and the treatment in the i direction still uses the split-convective approach. This is not the only approximation, since our final goal is to linearize the equations to solve a block-tridiagonal linear system. We now consider a property of the Eulerian flux to be a homogeneous

function of degree one in $\mathbf{U}$, as such, we can express $\mathbf{F}' = \mathbf{A}'\mathbf{U}$ (we can move the Jacobian $\mathbf{A}' = (\partial\mathbf{F}'/(\partial\mathbf{U}))$ inside or outside the derivative operator) (Beam and Warming, 1976, 1978). In particular, we can also write

$$\mathbf{F}'_{i,j+1/2} \simeq \mathbf{A}'_{i,j+1/2}\mathbf{U}_{i,j+1/2} + f(\Theta_{i,j+1/2})\mathbf{F}'^{d,WENO}_{i,j+1/2} \tag{2.120}$$

The artificial diffusion term is not easy to linearize; furthermore, the WENO reconstruction involves a larger stencil, so that the resulting system would involve no more the inversion of a block-tridiagonal matrix. As such, we substitute the WENO diffusion with the (more dissipative) Lax-Friedrichs one. In practice, we apply the local Lax-Friedrichs numerical flux to $\mathbf{A}'\mathbf{U}$ to only have the artificial diffusion fluxes, so it is better to explain the method in detail. Matrix $\mathbf{A}'_{i,j+1/2}$ contains informations about the wave system on face $j+1/2$, with waves propagating both on positive and negative direction. The Lax-Friedrichs method consists in splitting the flux to deal separately with waves propagating in positive *or* in negative direction. Lets deal first with the classical scheme applied to the linearized system $\mathbf{F} = \mathbf{A}_{j+1/2}\mathbf{U}$. We split the flux function as the sum of positive and negative fluxes, defined as follows

$$\begin{aligned}
\mathbf{A}_{j+1/2}\mathbf{U} &= \mathbf{A}^{+}_{j+1/2}\mathbf{U} + \mathbf{A}^{-}_{j+1/2}\mathbf{U} \\
\mathbf{A}^{\pm}_{j+1/2} &= \frac{1}{2}\left(\mathbf{A}_{j+1/2} \pm \underset{max}{\mathbf{A}_{j,j+1}}\right) \\
\underset{max}{\mathbf{A}_{j,j+1}} &= \mathbf{R}_{j+1/2}\underset{max}{\mathbf{\Lambda}_{j,j+1}}\mathbf{L}_{j+1/2}
\end{aligned} \tag{2.121}$$

With the above splitting, matrix $\mathbf{A}^{+}_{j+1/2}$ describes waves on face $j+1/2$ propagating only in the positive direction, while matrix $\mathbf{A}^{-}_{j+1/2}$ describes waves on face $j+1/2$ propagating only in the negative direction. We can now find the exact solution of the linearized problem, since positive waves will convect unchanged $\mathbf{U}_j$ in $j+1/2$, while negative waves will convect unchanged $\mathbf{U}_{j+1}$ in $j+1/2$. So we can write

$$\begin{aligned}
\mathbf{F}_{j+1/2} &= \mathbf{A}^{+}_{j+1/2}\mathbf{U}_j + \mathbf{A}^{-}_{j+1/2}\mathbf{U}_{j+1} = \\
&= \frac{1}{2}\left(\mathbf{A}_{j+1/2} + \underset{max}{\mathbf{A}_{j,j+1}}\right)\mathbf{U}_j + \frac{1}{2}\left(\mathbf{A}_{j+1/2} - \underset{max}{\mathbf{A}_{j,j+1}}\right)\mathbf{U}_{j+1} = \\
&= \mathbf{A}_{j+1/2}\overline{\mathbf{U}}_{j+1/2} - \frac{1}{2}\underset{max}{\mathbf{A}_{j,j+1}}\left(\mathbf{U}_{j+1} - \mathbf{U}_j\right)
\end{aligned} \tag{2.122}$$

so that

$$\mathbf{F}_{j+1/2} = \mathbf{A}_{j+1/2}\overline{\mathbf{U}}_{j+1/2} + \mathbf{F}^{d,LF}_{j+1/2}\,, \qquad \mathbf{F}^{d,LF}_{j+1/2} = -\frac{1}{2}\underset{max}{\mathbf{A}_{j,j+1}}\left(\mathbf{U}_{j+1} - \mathbf{U}_j\right) \tag{2.123}$$

A common choice is to define the matrix $\mathbf{A}_{j+1/2}$ in Roe's intermediate state between j and $j+1$. Substituting the Lax-Friedrichs dissipation (right equation of (2.123)) to the WENO one in (2.120), and identifying also $\mathbf{U}_{i,j+1/2}$ as $\overline{\mathbf{U}}_{i,j+1/2}$ (left equation of (2.123)), we obtain

$$\mathbf{F}'^{impl}_{i,j+1/2} = \frac{1}{2}\mathbf{A}'_{i,j+1/2}\left(\mathbf{U}_{i,j+1} + \mathbf{U}_{i,j}\right) - f(\Theta_{i,j+1/2})\frac{1}{2}\underset{max}{\mathbf{A}'_{j,j+1}}\left(\mathbf{U}_{i,j+1} - \mathbf{U}_{i,j}\right) \tag{2.124}$$

so defining

$$\mathbf{A}'^{\pm}_{i,j+1/2} := \frac{1}{2}\left(\mathbf{A}'_{i,j+1/2} \pm f(\Theta_{i,j+1/2})\mathbf{A}'_{\substack{j,j+1 \\ max}}\right) \tag{2.125}$$

we obtain

$$\mathbf{F}'^{impl}_{i,j+1/2} = \mathbf{A}'^{+}_{i,j+1/2}\mathbf{U}_{i,j} + \mathbf{A}'^{-}_{i,j+1/2}\mathbf{U}_{i,j+1} \tag{2.126}$$

and substituting in (2.118)

$$\begin{aligned}(\mathbf{L^c U})_{i,j} = -\frac{1}{\mathcal{V}_{i,j}} \Big[& S_{i,j+1/2}\left(\mathbf{A}'^{+}_{i,j+1/2}\mathbf{U}_{i,j} + \mathbf{A}'^{-}_{i,j+1/2}\mathbf{U}_{i,j+1}\right) + \\ & -S_{i,j-1/2}\left(\mathbf{A}'^{+}_{i,j-1/2}\mathbf{U}_{i,j-1} + \mathbf{A}'^{-}_{i,j-1/2}\mathbf{U}_{i,j}\right)\Big]\end{aligned} \tag{2.127}$$

As done when dealing with the viscous fluxes, also here we define the matrices $\mathbf{L^D}$, $\mathbf{L^E}$, $\mathbf{L^F}$, as

$$\mathbf{L^D}_{i,j} = \frac{S_{i,j-1/2}}{\mathcal{V}_{i,j}}\,\mathbf{A}'^{+}_{i,j-1/2}\,, \qquad \mathbf{L^F}_{i,j} = -\frac{S_{i,j+1/2}}{\mathcal{V}_{i,j}}\mathbf{A}'^{-}_{i,j+1/2} \tag{2.128}$$

$$\mathbf{L^E}_{i,j} = -\frac{1}{\mathcal{V}_{i,j}}\left[S_{i,j+1/2}\mathbf{A}'^{+}_{i,j+1/2} - S_{i,j-1/2}\mathbf{A}'^{-}_{i,j-1/2}\right] \tag{2.129}$$

The matrices $\mathbf{L^D}$, $\mathbf{L^E}$, $\mathbf{L^F}$, are the analogous of, respectively, $\mathbf{L^A}$, $\mathbf{L^B}$, $\mathbf{L^C}$ for the viscous fluxes, so that an analogous block-tridiagonal system can be defined. As explained in note 1 at the end of the previous paragraph, all the manipulations to fluxes, for convenience, will be used just on terms that go at the left-hand-side of the system, while terms appearing at the right-hand-side will be deal with as in the explicit part of the code. Just to be clear, at the right-hand-side we will use the WENO dissipative fluxes also in the j direction, while on the left-hand-side we will use the Lax-Friedrichs one.

Final semi-implicit scheme. We put together the results of the two previous paragraphs, to obtain the time increment at each l-th stage of the Runge-Kutta algorithm by solving the block-tridiagonal system:

$$\begin{bmatrix} \ddots & \ddots & \ddots \\ -\alpha_l\theta\Delta t\left(\mathbf{L^A}^l_{i,j} + \mathbf{L^D}^l_{i,j}\right) & \mathbf{I} - \alpha_l\theta\Delta t\left(\mathbf{L^B}^l_{i,j} + \mathbf{L^E}^l_{i,j}\right) & -\alpha_l\theta\Delta t\left(\mathbf{L^C}^l_{i,j} + \mathbf{L^F}^l_{i,j}\right) \\ \ddots & \ddots & \ddots \end{bmatrix} \begin{Bmatrix} \vdots \\ \vdots \\ \Delta\mathbf{U}^l_{i,j-1} \\ \Delta\mathbf{U}^l_{i,j} \\ \Delta\mathbf{U}^l_{i,j+1} \\ \vdots \\ \vdots \end{Bmatrix} = \begin{Bmatrix} \vdots \\ \vdots \\ \mathbf{RHS}^l_{i,j-1} \\ \mathbf{RHS}^l_{i,j} \\ \mathbf{RHS}^l_{i,j+1} \\ \vdots \\ \vdots \end{Bmatrix}$$

with matrices $\mathbf{L^A}$, $\mathbf{L^B}$, $\mathbf{L^C}$, $\mathbf{L^D}$, $\mathbf{L^E}$, $\mathbf{L^F}$ defined in (2.113), (2.114), (2.128), (2.129),

$$
\begin{aligned}
\mathbf{RHS}^l_{i,j} &= \gamma_l \Delta t \mathbf{N}^l_{i,j} + \rho_l \Delta t \mathbf{N}^{l-1}_{i,j} + \alpha_l \Delta t \mathbf{L^e}^l_{i,j} \\
\mathbf{N}_{i,j} &= -\frac{1}{\mathcal{V}_{i,j}} \left(\mathbf{F}'_{i+1/2,j} S_{i+1/2,j} - \mathbf{F}'_{i-1/2,j} S_{i-1/2,j} \right) + \\
&\quad + \frac{1}{\mathcal{V}_{i,j}} \left(\mathbf{G}'_{i+1/2,j} S_{i+1/2,j} - \mathbf{G}'_{i-1/2,j} S_{i-1/2,j} \right) + \\
&\quad + \frac{1}{\mathcal{V}_{i,j}} \left(\mathbf{G}'^2_{i,j+1/2} S_{i,j+1/2} - \mathbf{G}'^2_{i,j-1/2} S_{i,j-1/2} \right) + \\
&\quad + \frac{1}{\mathcal{V}_{i,j}} \left(\mathbf{G}'^3_{i,j+1/2} S_{i,j+1/2} - \mathbf{G}'^3_{i,j-1/2} S_{i,j-1/2} \right) \\
\mathbf{L^e}_{i,j} &= -\frac{1}{\mathcal{V}_{i,j}} \left(\mathbf{F}'_{i,j+1/2} S_{i,j+1/2} - \mathbf{F}'_{i,j-1/2} S_{i,j-1/2} \right) + \\
&\quad + \frac{1}{\mathcal{V}_{i,j}} \left(\mathbf{G}'^1_{i,j+1/2} S_{i,j+1/2} - \mathbf{G}'^1_{i,j-1/2} S_{i,j-1/2} \right)
\end{aligned}
$$

and

$$
\begin{aligned}
\mathbf{F}'_{i+1/2,j} =& \overline{u'}_{i+1/2,j} \begin{Bmatrix} \overline{\rho}_{i+1/2,j} \\ (\overline{\rho \mathbf{u}})_{i+1/2,j} \\ (\overline{\rho H})_{i+1/2,j} \end{Bmatrix} + \overline{p}_{i+1/2,j} \begin{Bmatrix} 0 \\ \hat{\mathbf{n}}_{i+1/2,j} \\ 0 \end{Bmatrix} + \\
&+ f(\Theta_{i+1/2,j}) \mathbf{F}'^{d,WENO}_{i+1/2,j} \\
& f(\Theta_{i+1/2,j}) = \begin{cases} 0 & \text{for } \Theta_{i+1/2,j} < \overline{\Theta} \\ 1 & \text{for } \Theta_{i+1/2,j} \geq \overline{\Theta} \end{cases} \\
& \mathbf{F}'^{d,WENO}_{i+1/2} = -\frac{1}{2} \mathbf{R}'_{i+1/2} \underset{max}{\mathbf{\Lambda}'_{i,i+1}} \mathbf{L}'_{i+1/2} \left(\mathbf{U}^+_{i+1/2} - \mathbf{U}^-_{i+1/2} \right)
\end{aligned}
$$

$\mathbf{F}'_{i,j+1/2}$ obtained by considering increments on j rather than i

$$
\begin{aligned}
\mathbf{G}'_{i+1/2,j} =& \mathbf{G}'^1_{i+1/2,j} + \mathbf{G}'^2_{i+1/2,j} + \mathbf{G}'^3_{i+1/2,j} \\
\mathbf{G}'^1_{i+1/2,j} =& \sqrt{\gamma} \frac{M_\infty}{Re_c} \begin{Bmatrix} 0 \\ \overline{\mu}_{i+1/2,j} \frac{\mathbf{u}_{i+1,j} - \mathbf{u}_{i,j}}{|\mathbf{x}^c_{i+1,j} - \mathbf{x}^c_{i,j}|} \\ \frac{1}{Pr} \frac{\gamma}{\gamma - 1} \overline{K}_{i+1/2,j} \frac{T_{i+1,j} - T_{i+1,j}}{|\mathbf{x}^c_{i+1,j} - \mathbf{x}^c_{i,j}|} \end{Bmatrix} \\
\mathbf{G}'^2_{i+1/2,j} =& \sqrt{\gamma} \frac{M_\infty}{Re_c} \begin{Bmatrix} 0 \\ \overline{\mu}_{i+1/2,j} \overline{\left(\frac{\partial \mathbf{u}}{\partial x_i} \right)}_{i+1/2,j} \cdot \hat{\mathbf{n}}_{i+1/2,j} \\ \overline{\mu}_{i+1/2,j} \mathbf{u} \cdot \frac{\mathbf{u}_{i+1} - \mathbf{u}_i}{|\mathbf{x}^c_{i+1,j} - \mathbf{x}^c_{i,j}|} + \overline{\mu}_{i+1/2,j} \overline{(u_i)}_{i+1/2,j} \overline{\left(\frac{\partial \mathbf{u}}{\partial x_i} \right)}_{i+1/2,j} \cdot \hat{\mathbf{n}}_{i+1/2,j} \end{Bmatrix} \\
\mathbf{G}'^3_{i+1/2,j} =& \sqrt{\gamma} \frac{M_\infty}{Re_c} \begin{Bmatrix} 0 \\ -\frac{2}{3} \overline{\mu}_{i+1/2,j} \overline{\left(\frac{\partial u_k}{\partial x_k} \right)}_{i+1/2,j} \hat{\mathbf{n}}_{i+1/2,j} \\ -\frac{2}{3} \overline{\mu}_{i+1/2,j} \overline{\left(\frac{\partial u_k}{\partial x_k} \right)}_{i+1/2,j} \overline{u'}_{i+1/2,j} \end{Bmatrix}
\end{aligned}
$$

$\mathbf{G}'_{i,j+1/2}$ obtained by considering increments on j rather than i

The resulting order of accuracy in time results lowered to first order when Implicit Euler integration ($\theta = 1$) is used, to second order when Crank-Nicolson ($\theta = 1/2$) is used, and we recover the full third order only for explicit calculations.

2.5 Numerical boundary conditions

In the Finite Volume approach, boundary conditions enter the domain only in the evaluation of fluxes near the boundary. A major problem in the enforcement of correct boundary conditions is due to the fact that we deal with a bounded domain, while in fact some of the conditions are known at infinity. As such, the enforcement of free-stream conditions on the bounded domain may cause spurious wave reflections, which may also lead to instability. A classic way to deal with this problem is to apply non-reflective boundary conditions (Poinsot and Lele, 1992), which on each boundary face linearizes the problem in the normal direction. The resulting system of equations is then cast in characteristic variables, which diagonalize the problem. As a result, one obtains a system of equations, with each equation describing a linear convection problem. One can then identify waves entering and leaving the domain, and enforce the correct boundary conditions to avoid, or at least minimize, numerical reflection. This remains an approximation, since we are anyway dealing with a bounded domain. However, such approach guarantees good accuracy and stability.

However, FV approach appears to be somehow intrinsically non-reflective. Instead of explicitly use the characteristic approach to enforce the boundary conditions, we use the so called *ghost cells* approach, in which cells outside the computational domain are introduced and which contain the boundary conditions. Using ghost cells has the advantage to let one use the same scheme also on the boundary, i.e. we continue using the same formulas for the evaluation of fluxes also on boundaries. The introduction of ghost cells is also convenient, since they are needed for the parallelization of the code, on the virtual boundaries which define the mesh part on which a single processor works.

As already stressed, our way of enforcing the boundary conditions is not based on the characteristic approach. As such, it is expected that a larger domain is required with respect the characteristic approach in order to obtain the same quality of the solution. The strength of our approach lies in its simplicity. We shall now describe the different sets of boundary conditions used in this work.

Subsonic Inlet Boundary - Far Boundary. We simply impose the free-stream values for all the conserved variables. Strictly speaking, this is a supersonic inlet condition, and the resulting mathematical problem is ill-posed, since for subsonic inlet not all the informations travels from the outside to the inside of the domain. However, this very simple approach works well when the domain edge on which it is applied is far from the airfoil and no strong variation of the solution is encountered. This is particularly true when the (subsonic) Mach number is increased, and for transonic problems it does not bring to any issues

even if the inlet boundary is close to the airfoil (see for example sec. 3.3.2, in which the inlet boundary is located only 2.5 chords ahead of the airfoil).

Wall Boundary. We use the *reflecting boundary conditions* (Hirsch, 1988). With this method, we simply reflect the velocity at the wall, such that the sum of velocity in the ghost cell and in the first inner cell (for fixed i) is zero. With this condition, the non-linear part of the Eulerian fluxes is automatically zero. We extrapolate at zero-order the other conservative variables. In particular, for the pressure this is aligned with the usual boundary layer assumption, while this condition on temperature translates in an adiabatic wall.

Subsonic Outlet Boundary. We use a zero order extrapolation for all the conservative variables, except for the total energy per unit mass, which is instead computed assuming a pressure equal to the free-stream one. As explained by LeVeque (2002), a zero-order extrapolation in the ghost cell of a Finite Volume scheme often gives a reasonable set of absorbing boundary conditions. As outlined by Pirozzoli and Colonius (2013), the straightforward application of non-reflecting boundary conditions for subsonic outlet may lead to numerical drift, since the free-stream value of pressure is not necessarily preserved. The explicit imposition of the free-stream pressure in our method is a simple fix for this problem.

Periodic boundary conditions are instead always applied in the $\hat{\mathbf{z}}$ direction. Setting the values in the ghost cells closes both the explicit and implicit parts of the scheme. The explicit fluxes closure is automatic since the fluxes can be all evaluated without any difference with respect the inner fluxes. For the implicit part, it is less automatic, but still the approach remains straightforward. Recalling the resulting discrete system

$$\begin{bmatrix} \ddots & & \\ -\alpha_l\theta\Delta t\left(\mathbf{L}^{\mathbf{A}^l}_{i,j}+\mathbf{L}^{\mathbf{D}^l}_{i,j}\right) & \mathbf{I}-\alpha_l\theta\Delta t\left(\mathbf{L}^{\mathbf{B}^l}_{i,j}+\mathbf{L}^{\mathbf{E}^l}_{i,j}\right) & -\alpha_l\theta\Delta t\left(\mathbf{L}^{\mathbf{C}^l}_{i,j}+\mathbf{L}^{\mathbf{F}^l}_{i,j}\right) \\ & \ddots & \end{bmatrix} \begin{Bmatrix} \vdots \\ \Delta\mathbf{U}^l_{i,j-1} \\ \Delta\mathbf{U}^l_{i,j} \\ \Delta\mathbf{U}^l_{i,j+1} \\ \vdots \end{Bmatrix} = \begin{Bmatrix} \vdots \\ \mathbf{RHS}^l_{i,j-1} \\ \mathbf{RHS}^l_{i,j} \\ \mathbf{RHS}^l_{i,j+1} \\ \vdots \end{Bmatrix}$$

we have to include in the vectors also the component on the ghost cells. For example, considering the boundary $j=1$, the resulting first block equation reads

$$\begin{aligned} -\alpha_l\theta\Delta t\left(\mathbf{L}^{\mathbf{A}^l}_{i,1}+\mathbf{L}^{\mathbf{D}^l}_{i,1}\right)\Delta\mathbf{U}^l_{i,0}+ \\ +\left[\mathbf{I}-\alpha_l\theta\Delta t\left(\mathbf{L}^{\mathbf{B}^l}_{i,1}+\mathbf{L}^{\mathbf{E}^l}_{i,1}\right)\right]\Delta\mathbf{U}^l_{i,1}+ \\ -\alpha_l\theta\Delta t\left(\mathbf{L}^{\mathbf{C}^l}_{i,1}+\mathbf{L}^{\mathbf{F}^l}_{i,1}\right)\Delta\mathbf{U}^l_{i,2}=\mathbf{RHS}^l_{i,1} \end{aligned}$$

We can express $\Delta\mathbf{U}^l_{i,0}$ from the boundary conditions, as

$$\Delta\mathbf{U}^l_{i,0}=\mathbf{A}_{BC}\Delta\mathbf{U}^l_{i,1} \tag{2.130}$$

with $\mathbf{A}_{BC}$ readily obtained for the different boundary conditions.

Subsonic Inlet Boundary - Far Boundary.

$$\mathbf{A}_{BC} = \begin{bmatrix} 0 & 0 & 0 \\ 0 & 0 & 0 \\ 0 & 0 & 0 \end{bmatrix} \tag{2.131}$$

since we have steady boundary conditions.

Wall Boundary.

$$\mathbf{A}_{BC} = \begin{bmatrix} 1 & 0 & 0 \\ 0 & -\mathbf{I} & 0 \\ 0 & 0 & 1 \end{bmatrix} \tag{2.132}$$

since we reflect the velocity components.

Subsonic Outlet Boundary. This condition is less immediate, but still straightforward. We have to state this condition in terms of primitive variables, since we extrapolate all variables except pressure, for which we assume the free-stream fixed value.

$$\Delta \mathbf{V}_{\mathbf{p}_{i,0}}{}^{l} = \begin{bmatrix} 1 & 0 & 0 \\ 0 & \mathbf{I} & 0 \\ 0 & 0 & 0 \end{bmatrix} \Delta \mathbf{V}_{\mathbf{p}_{i,1}}{}^{l}, \qquad \Delta \mathbf{V}_{\mathbf{p}}{}^{l} = \mathbf{P}_{\mathbf{p}} \Delta \mathbf{U}^{l},$$

$$\mathbf{P}_{\mathbf{p}_{i,0}} \Delta \mathbf{U}_{i,0}^{l} = \begin{bmatrix} 1 & 0 & 0 \\ 0 & \mathbf{I} & 0 \\ 0 & 0 & 0 \end{bmatrix} \mathbf{P}_{\mathbf{p}_{i,1}} \Delta \mathbf{U}_{i,1}^{l},$$

$$\Delta \mathbf{U}_{i,0}^{l} = \mathbf{P}_{\mathbf{p}_{i,0}}^{-1} \begin{bmatrix} 1 & 0 & 0 \\ 0 & \mathbf{I} & 0 \\ 0 & 0 & 0 \end{bmatrix} \mathbf{P}_{\mathbf{p}_{i,1}} \Delta \mathbf{U}_{i,1}^{l}$$

Since $\mathbf{P}_{\mathbf{p}}$ (and $\mathbf{P}_{\mathbf{p}}{}^{-1}$) only depends on ρ and $\mathbf{u}$, for a subsonic outlet we have $\mathbf{P}_{\mathbf{p}_{i,0}} = \mathbf{P}_{\mathbf{p}_{i,1}}$, thus obtaining

$$\mathbf{A}_{BC} = \mathbf{P}_{\mathbf{p}_{i,1}}^{-1} \begin{bmatrix} 1 & 0 & 0 \\ 0 & \mathbf{I} & 0 \\ 0 & 0 & 0 \end{bmatrix} \mathbf{P}_{\mathbf{p}_{i,1}} \tag{2.133}$$

We illustrate first the procedure in the case of $j = 1$. Expressing $\Delta \mathbf{U}_{i,0}^{l}$ as just explained, we obtain the modified first block equation

$$\left[\mathbf{I} - \alpha_l \theta \Delta t \left(\mathbf{L}^{\mathbf{B}}{}_{i,1}^{l} + \mathbf{L}^{\mathbf{A}}{}_{i,1}^{l} \mathbf{A}_{BC} + \mathbf{L}^{\mathbf{E}}{}_{i,1}^{l} + \mathbf{L}^{\mathbf{D}}{}_{i,1}^{l} \mathbf{A}_{BC}\right)\right] \Delta \mathbf{U}_{i,1}^{l} + \\ - \alpha_l \theta \Delta t \left(\mathbf{L}^{\mathbf{C}}{}_{i,1}^{l} + \mathbf{L}^{\mathbf{F}}{}_{i,1}^{l}\right) \Delta \mathbf{U}_{i,2}^{l} = \mathbf{RHS}_{i,1}^{l}$$

A similar procedure for $j = N$ yields

$$-\alpha_l \theta \Delta t \left({\mathbf{L}^{\mathbf{A}}}^l_{i,N} + {\mathbf{L}^{\mathbf{D}}}^l_{i,N} \right) \Delta \mathbf{U}^l_{i,N-1} +$$
$$+ \left[\mathbf{I} - \alpha_l \theta \Delta t \left({\mathbf{L}^{\mathbf{B}}}^l_{i,N} + {\mathbf{L}^{\mathbf{C}}}^l_{i,N} \mathbf{A}_{BC} + {\mathbf{L}^{\mathbf{E}}}^l_{i,N} + {\mathbf{L}^{\mathbf{F}}}^l_{i,N} \mathbf{A}_{BC} \right) \right] \Delta \mathbf{U}^l_{i,N} = \mathbf{RHS}^l_{i,N}$$

Thus we can solve the block-tridiagonal system in the N unknowns $\Delta \mathbf{U}^l_{i,j}$.

The applied boundary conditions do not lower the order of accuracy of the scheme, which results second order accurate in space and up to third order accurate in time, depending on if we run explicit or implicit calculations.

Chapter 3

Verification and validation

In this chapter we deal with a fundamental part of a work based on numerical simulations: the code validation. The aim of this chapter is to understand if the error introduced by numerics is small enough, as to obtain valid results. The code validation has to be effectuated through test cases, referring to experimental results and/or to previous, reliable, numerical simulations. First the code is verified using the lid-driven cavity flow as test case, then the validation is performed through a NASA test case on RAE-2822 airfoil to see the behaviour of the code in a steady case, then comparisons are made with a well documented, experimental test case on transonic buffet of first kind, to see the ability of the code to handle an oscillating shock.

3.1 Introduction

Following Roache (1997), we make the fundamental distinction between verification and validation, that is, by verification we mean "solving the equations right" and by validation we mean "solving the right equations". In the same spirit, the distinction is made between numerical errors and model errors. Numerical errors are due fundamentally to two causes - rounding errors and truncation errors - while model errors depend on the mathematical model we are using. Rounding errors are due to the use of a finite number of decimal digits in the representation of a number during the computations. One can overcome this problem through the adoption of double precision computations. Truncation errors are due to the discretization of the equations, or in other words, to the fact that it is no more solved the exact system of equations, but an approximation of it, so those are errors tied to the code itself. It is possible to reduce those errors by increasing the resolution. In addition to considering the numerical errors themselves, it is necessary to consider their evolution during the computations: the various numerical operations may amplify also an initially little error, i.e. the code must be stable. From the previous considerations, one may guess that using a stable code, operating in double precision and with a fine enough mesh, good results can always be obtained. Lax theorem assures that this is indeed true for a linear case: in a linear case, a consistent and

stable code converges towards the exact solution. Unfortunately, in general the theorem hypothesis are not satisfied.

In the present case, the mathematical model consists of the Navier-Stokes equations, thus many of the required hypothesis don't hold. First of all, the equations are non-linear, for the presence of the convective terms. To describe the other complications, it is better to talk first of the inviscid case: when we consider the zero viscosity case, the flow may present discontinuities, and, for a physically relevant solution, quantities to the two sides of it must be linked by specific laws (weak solutions of the problem, which satisfy the Rankine-Hugoniot jump relations). At a mathematical level, extending the admissible solutions also to the weak solutions leads to the lost of the uniqueness properties which one expects from the experimental evidences (at a mathematical level this property has never been demonstrated for the Navier-Stokes equations). Considering the numerical schemes, Lax theorem does not hold in this context, but holds the Lax-Wendroff theorem, which states that if a conservative and consistent scheme converges, than it converges towards a weak solution of the conservation laws. We emphasize that convergence is a hypothesis of the theorem, not a consequence. In general, even if the scheme converges, it may not converge towards the correct weak solution of the problem (entropy solution, the only one, one hopes, obtainable as the limit of the viscous solution, as viscosity tends to zero). In the real, viscous case, there won't be real discontinuities, but only high gradients. Unfortunately, in the discrete case it is difficult to appreciate the difference between a discontinuous solution and one with a very high gradient, so that the problems affecting the numerical schemes in presence of a discontinuity may also affect the numerical simulations of real flows.

To evaluate the adequacy of the code, we consider the lid-driven cavity flow in order to verify the code. Then to evaluate the adequacy of the code in presence of shocks on a profile, we consider a steady NASA test case on RAE-2822 airfoil and an unsteady transonic case on a 18% thick circular-arc airfoil, comparing with a well documented experiment.

3.2 Verification

Here we verify the code with a convergence study, i.e. we try to recover the formal convergence order by estimating numerical errors as the difference between the computed solution and Richardson extrapolation (Roache, 1997). If the solution is converging, the estimated errors should behave in a predictable way, linked to the effective convergence order. If the code is bug-free, the effective convergence order and the formal order of accuracy should be very close. The procedure is straightforward once the numerical solution is provided in a fixed point on three different meshes, in which for simplicity the grid spacing is halved each time; following Roache (1997), the estimated convergence order is

$$\tilde{n} = \log\left(\frac{f_3 - f_2}{f_2 - f_1}\right) \Big/ \log 2\,, \tag{3.1}$$

where subscript 1 denotes the finest grid. The obtained value of $\tilde{n}$ should be close to the formal order of accuracy. This is a quite powerful tool in order to verify the code, since also a minor bug is able to invalidate the procedure, not letting the formal convergence order to be recovered.

3.2.1 Lid-driven cavity

The lid-driven cavity problem has long been used as a test case for new codes or new solution methods. The geometry is simple, and so are the boundary conditions. The standard case is fluid contained in a square domain, with three steady sides and one moving side (with velocity tangent to the side). The considered Reynolds number is $Re = 200$, based on lid velocity and size, corresponding to steady flow.

The grid spacing is uniform in both space directions, and in order to assess the convergence order three meshes are considered, namely $N_x \times N_y = 128 \times 128$, 256×256, 512×512. In order to facilitate the convergence analysis, results on finer grids have to be transferred to the coarsest grid. Recalling the definition (2.63), the

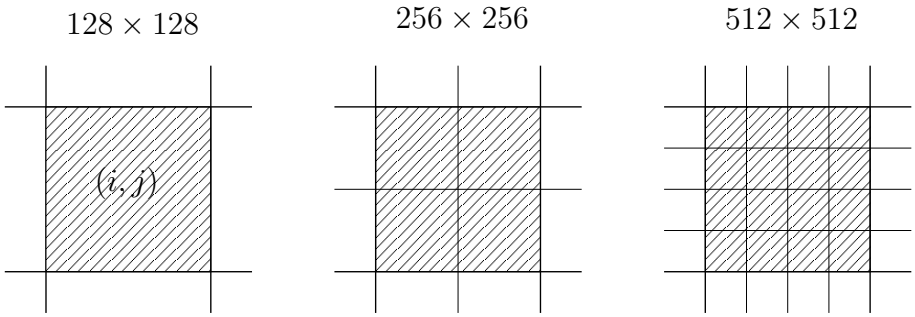

Figure 3.1: *Procedure to obtain solution on the coarsest mesh from the finer meshes results. Once cell (i, j) is chosen, the equivalent value from the finer grids are recovered by volume-weighted averaging on the shaded volumes.*

equivalent values on the coarse mesh are computed from the results on the finer meshes by a volume-weighted average, on the same volume identified by each cell composing the coarsest grid. The conversion procedure is graphically explained in Fig. 3.1. Hence for grid 256, the results are transferred to grid 128 by averaging on the four cells corresponding to cell (i, j) of grid 128, and for grid 512 the same is obtained by averaging on the 16 cells shaded in Fig. 3.1. Figure 3.2 (a) shows a comparison between contours of the conserved variable ρu_1 obtained transferring all the results to the coarsest grid. The three results are indistinguishable in figure. Panel b) also shows streamlines obtained on the finest grid.

Using formula (3.1) in each point of the equivalent solutions, it is possible to estimate the convergence order pointwise, and the resulting convergence order is shown in Fig. 3.3. Similar to Bonfiglioli and Paciorri (2014), tab. 3.1 shows the percentage of monotonically converging grid points, the averaged measured order $< \tilde{n} >$ and its standard deviation $\sigma(\tilde{n})$ computed only within this subset of grid points. The results are comparable to those shown by Bonfiglioli and Paciorri (2014)

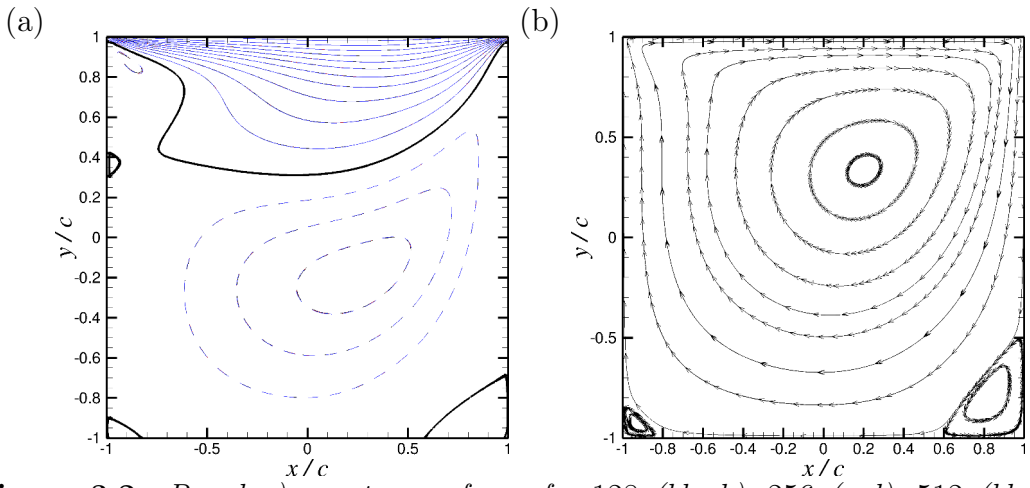

Figure 3.2: *Panel a): contours of ρu_1 for 128 (black), 256 (red), 512 (blue) grids. Results on finer grids are converted to the coarsest grid through the volume-weighted average procedure (Fig. 3.1). Solid line denotes positive values, whereas dashed lines negative ones. Panel b): streamlines obtained on the finest grid.*

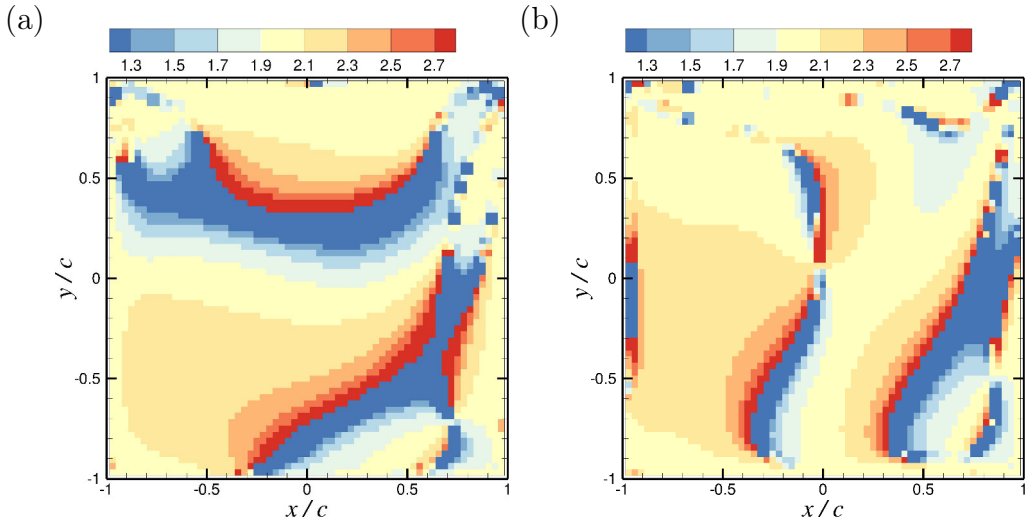

Figure 3.3: *Pointwise estimated convergence order on ρu_1 (a) and on ρu_2 (b).*

Table 3.1: *Convergence statistics for lid-driven cavity flow.*

Variable	Decreasing error	$< \tilde{n} >$	$\sigma(\tilde{n})$
ρu_1	93.7%	2.071	0.634
ρu_2	96.5%	2.075	0.511

and indeed the second order accuracy is attained.

The results shown above were obtained without the addition of WENO artificial diffusion, not needed for smooth flow. For that purpose, we set

$$f(\Theta_{i+1/2,j}) = 1\,,$$

so that WENO diffusion is activated within the whole field. This time differences

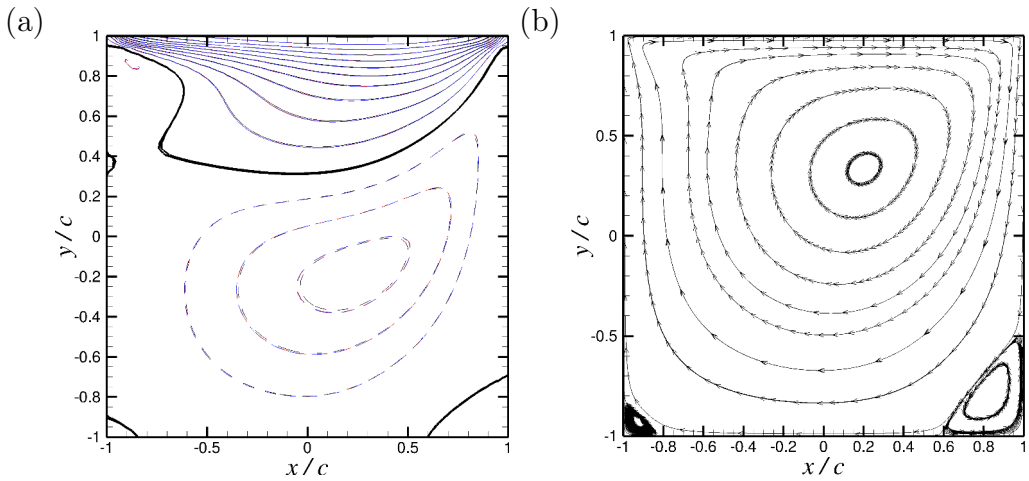

Figure 3.4: *Panel a): contours of ρu_1 for 128 (black), 256 (red), 512 (blue) grids. Results on finer grids are converted to the coarsest grid through the volume-weighted average procedure (Fig. 3.1). Panel b): streamlines obtained on the finest grid. WENO diffusion activated in the whole field.*

between the three solutions are more evident, and in Fig. 3.4 (a) some of the iso-contours are clearly distinct. The convergence order is shown in Fig. 3.5. Table

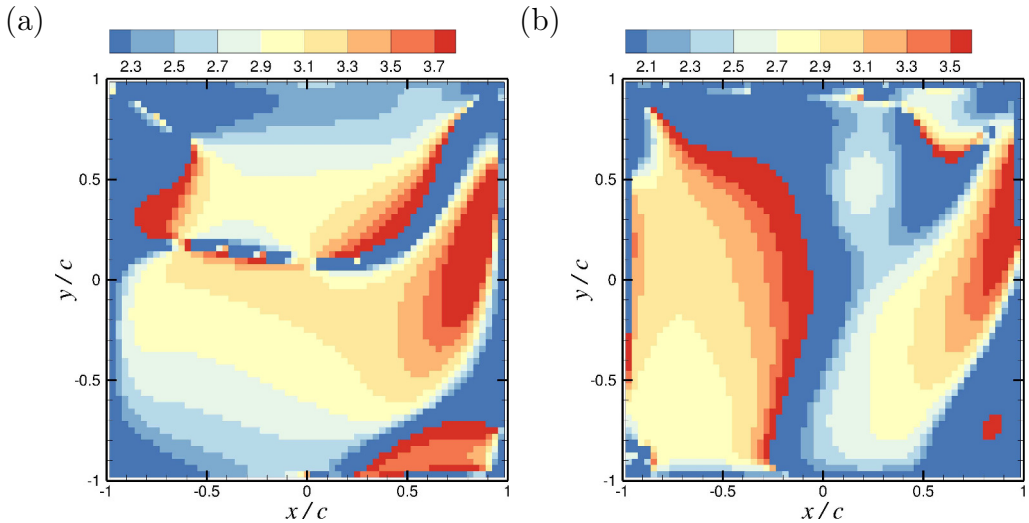

Figure 3.5: *Pointwise estimated convergence order on ρu_1 (a) and on ρu_2 (b). WENO diffusion activated in the whole field.*

3.2 shows again the statistics related to convergence. Again the percentage of

monotone convergent points and standard deviation are similar to previous results, but convergence order is now three.

Table 3.2: *Convergence statistics for lid-driven cavity flow, with WENO diffusion activated.*

Variable	Decreasing error	$< \tilde{n} >$	$\sigma(\tilde{n})$
ρu_1	93.6%	2.916	0.784
ρu_2	87.9%	2.770	0.989

This conclude the verification part of the work, and we start now with the validation, in order to see if the physics is captured by the scheme.

3.3 Validation

The aim of this part of the work is to verify the ability of the code in the description of the flow physics, with particular attention devoted to the correct tracking of the shock motion. The first test case will relate to steady transonic flow on an airfoil, while more emphasis will be put on the second test, which will be compared with experimental data obtained for an oscillating shock.

3.3.1 Flow around RAE-2822, $Re_c = 6.5 \times 10^6$

In this section we use the test case available at `https://www.grc.nasa.gov/www/wind/valid/raetaf/raetaf01/raetaf01.html`. The grid is exactly the same as used in the reference calculations, in order to have a fair comparison, with a number of cells in the longitudinal direction of $N_x = 368$ and of $N_y = 64$ in the wall normal direction. The flow conditions are: $M_\infty = 0.729$, $Re_c = 6.5 \times 10^6$, $\alpha = 2.31°$, and the Spalart-Allmaras turbulence model is used. Figure 3.6 offers a qualitative comparison between Mach number contours. A more quantitative comparison is offered by Fig. 3.7, which shows the comparison between the pressure coefficients. The only apparent difference is in the shock position, which is slightly shifted upstream in our computations.

3.3.2 Numerical simulation of buffet on circular-arc airfoil

Since the code has to be used for transonic buffet description, the fundamental test we perform now is to verify the ability of the code of describing the shock motion. A well documented case on a circular-arc airfoil with 18% thickness is considered (McDevitt, 1979). The most detailed test case is for Reynolds number $Re_c = 11 \times 10^6$, $M_\infty = 0.76$, at zero incidence. Under these flow conditions shock motion of type C is present, with shocks only moving in the upstream direction, both on the suction and the pressure side, with relative phase lag of 180°. The most useful quantities for comparison are the reduced frequency $k_r \simeq 0.49$, the shock position

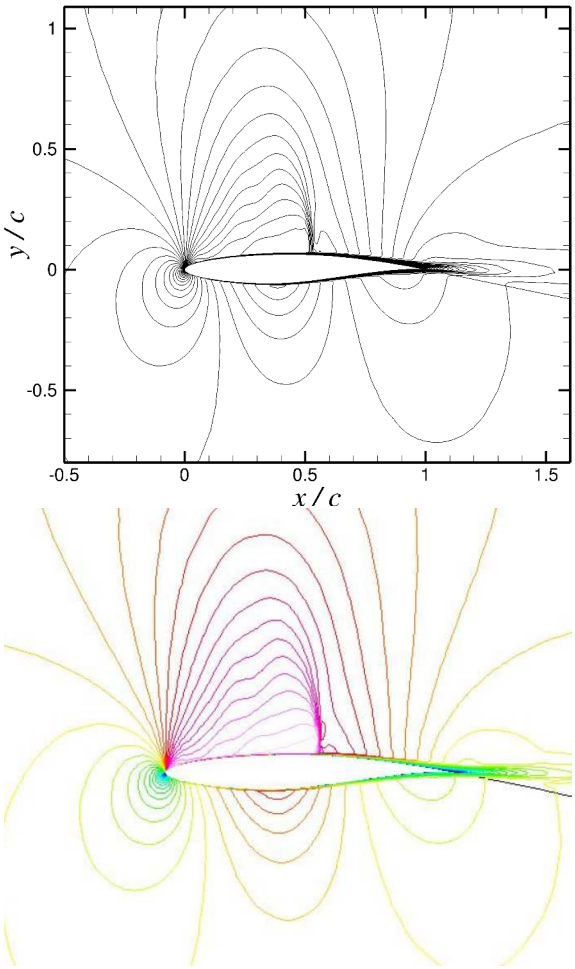

Figure 3.6: *Qualitative comparison between Mach number contours of reference computations and the ones of the present work. Upper panel: present work. Lower panel: reference.*

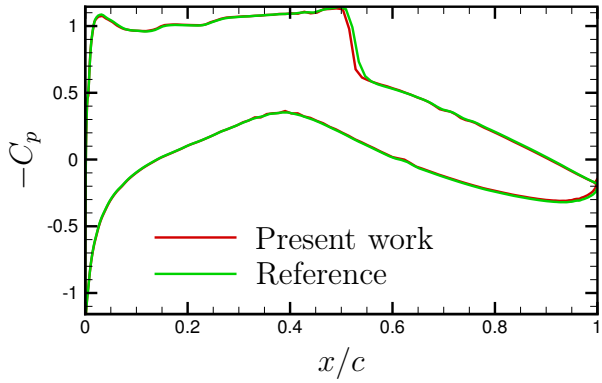

Figure 3.7: *Comparison between pressure coefficients obtained by reference computations and in the present work.*

Table 3.3: *Details of the grid used for simulation of the circular-arc airfoil.*

N_x	N_y	L_x/c	L_y/c
265	128	8.5	30
$N_{x_{suction}}$	$\Delta y_w/c$	L_l/c	L_r/c
142	5×10^{-5}	2.5	5

during the buffet cycle, the averaged pressure coefficient, the pressure coefficient in discrete intervals in the buffet cycle, and the pressure signal at four stations along the airfoil.

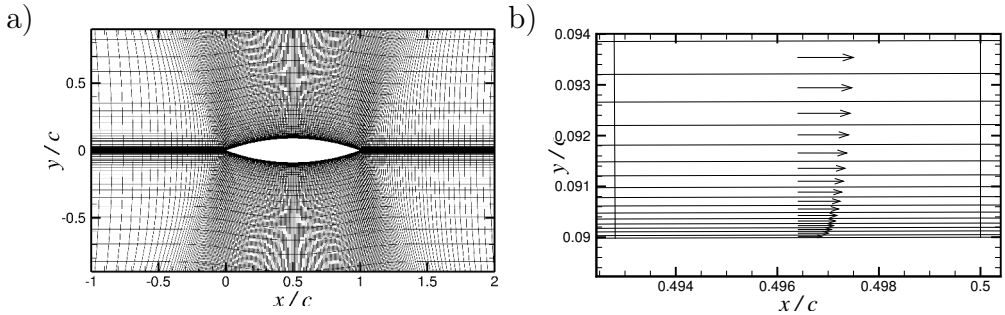

Figure 3.8: *Sketch of the grid used for buffet of first kind (a), and velocity profile at the middle of the chord (b). Details of the grid can be found in tab. 3.3.*

The chosen grid is an H type mesh, shown in Fig. 3.8. Details of the grid can be found in tab. 3.3, where $N_x = 265$ is the total number of cells in the i direction, $N_y = 128$ is the total number of cells in j direction, $L_x/c = 8.5$ and $L_y/c = 30$ are the lengths of the edges of the external box delimiting the computational domain, parallel to x and y axes respectively. $L_l/c = 2.5$ is the distance of the left edge of the domain from the leading edge, while $L_r/c = 5$ is the distance of the right edge of the domain from the trailing edge; on these two edges, nodes are distributed exponentially in i direction. To complete the description of the grid, we have 142 cells on suction side wall, and 142 on pressure side wall, for a total of 284 cells at the wall, homogeneously distributed. $\Delta y_w = 5 \times 10^{-5}$ is the distance of the first cell-center from the wall, and as can be seen in panel b) of Fig. 3.8, it is barely sufficient to have a description of the viscous region of the boundary layer.

The time history of the lift coefficient and its frequency spectrum are shown in Fig. 3.9. The Strouhal number associated with buffet is $St = fc/u_\infty \simeq 0.153$, corresponding to a reduced frequency $k_r = \pi cf/u_\infty \simeq 0.482$, bringing to a fair comparison with the experimental value $k_r = 0.49$.

Next we compare the shock location vs. time with the one obtained experimentally by McDevitt (1979). In our results the shock positions are identified by looking at the shock sensor Θ, assuming a threshold value $\Theta = 0.99$. The comparison with McDevitt (1979) results is shown in Fig. 3.10. The comparison is very good for $0.5 < x/c < 0.8$, whereas for $x/c < 0.5$ shocks are no longer detected

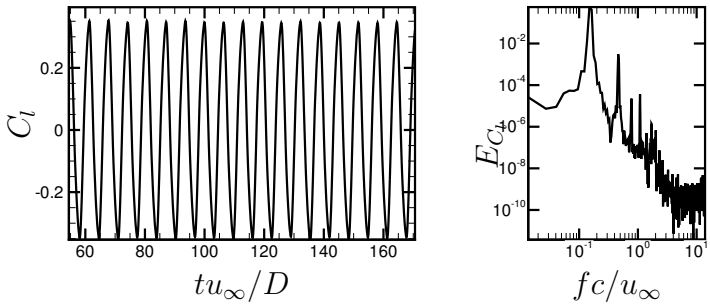

Figure 3.9: *Time history and frequency spectrum of the lift coefficient.*

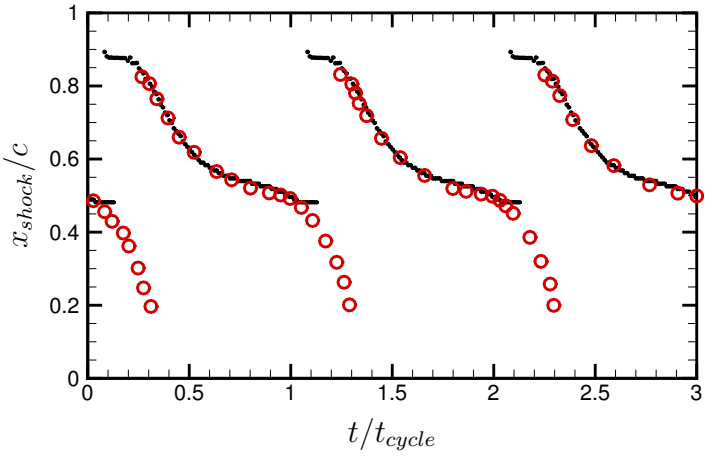

Figure 3.10: *Shock locations on suction side vs. time. Time is normalized with buffet period (t_{cycle}). Black dots: shocks detected on the boundary layer edge. Red circles: data from McDevitt (1979).*

at the boundary layer edge in our simulation. However, shocks are still present away from the wall, as can be seen in Fig. 3.11, which shows the value of the sensor Θ at time $t/t_{cycle} \simeq 0.9$ and $t/t_{cycle} \simeq 1$, a time where Fig. 3.10 would suggest only a steady shock located in $x/c \simeq 0.5$. As can be seen in Fig. 3.11 (b), indeed a shock

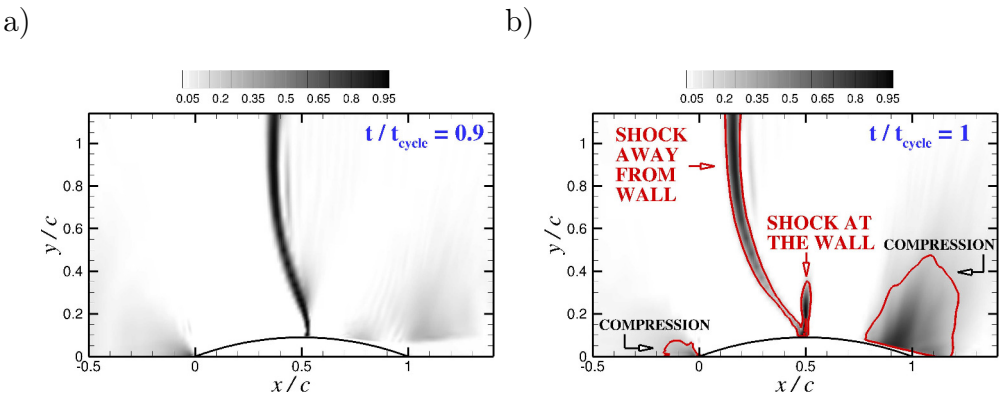

Figure 3.11: *Contours of sensor Θ. White lines corresponds to isoline $\Theta = 0.2$.*

is present at the wall, located in $x/c \simeq 0.5$, but there is also a shock away from the wall which is still propagating towards the leading edge, and whose effects are still felt by the boundary layer, as shown by the isoline $\Theta = 0.2$ in panel b) with a compression wave reaching the boundary layer. In order to improve the comparison, we recompute the shock location with a threshold value $\Theta = 0.2$, as suggested by Fig. 3.11 (b), and the results are shown in Fig. 3.12. Panel a) includes also points

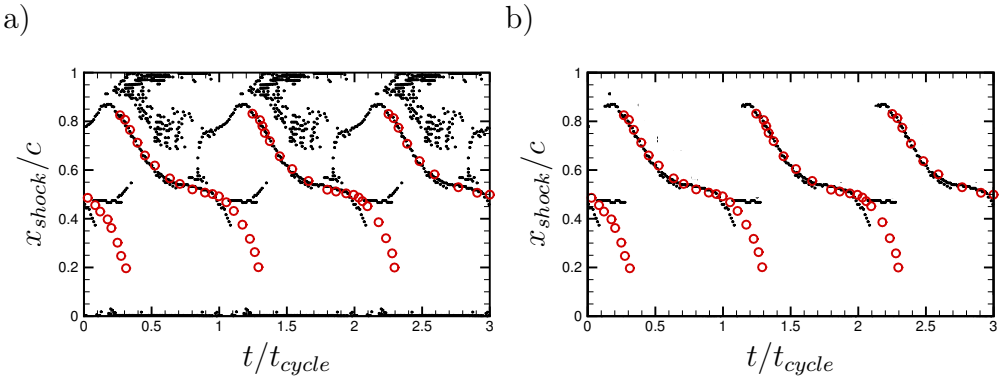

Figure 3.12: *Shock locations on suction side vs. time. Time is normalized with buffet period (t_{cycle}). Black dots: shocks located by $\Theta = 0.2$ on the boundary layer edge. Red circles: data from McDevitt (1979). Panel a) includes compression zones unaffected by shocks, which have been removed in panel b) with the help of visualizations like Fig. 3.11.*

which correspond to compressions. With the help of visualizations like Fig. 3.11, we removed those compression regions obtaining the result shown in panel b). As can be seen, we achieve a little improvement, since we are able to see the shock motion also for $0.37 < x/c < 0.5$, however the agreement in this region is less satisfactory, still fair.

Further comparisons are made in terms of the pressure coefficients, whose values on suction side are shown at ten instants of time within the buffet cycle in Fig. 3.13. Each panel shows good agreement with the experimental data for the stations from the leading edge to the shock, with the exception of panels c), d), since the experimental shock continues his upstream propagation while the computed shock stops in $x/c \simeq 0.5$, with only a compression wave continuing to move upstream, clearly discernible in panel b) ahead of the shock. Downstream of the shock, the agreement is less satisfactory, still is fair considering that the turbulence model has some problems in perfectly capturing separated regions (see for example (Menter, 1996)), especially from panel d) to panel j). Instead, in panels from a) to c), differences in the rear part of the airfoil are clearly visible, due to the slower formation of the new shock in the computations with respect the sudden shock appearance detected experimentally. The overall agreement is however good, as also shown by Fig. 3.14 a), which shows the comparison between the time-averaged pressure coefficients. This time the agreement is very good for all the region $x/c < 0.6$, while only small deviations are seen for $x/c > 0.6$. The differences may be attributed to the presence of a weak shock in our computation, located in $x/c \simeq 0.87$, which survives the time-averaging procedure, and which is not present in McDevitt (1979) results. The shock may be also seen in panel b), which shows pressure contours, with the associated trailing edge separation highlighted by the lines $u = 0$. Nevertheless, the overall agreement is good.

Finally in fig. 3.15 we compare the pressure signal at four stations along the wall. Apparently the largest deviations are seen in panel a) for $x/c = 0.25$, whereas 3.13 showed a good agreement for the pressure coefficient in all the region $x < 0.6$. However the figures are not drawn with the same y scale, as such the differences in panel a) result magnified, while the maximum differences are for the most rearward station, in panel d). Nevertheless, the agreement is good, even at the latter location.

As a side note, we have also considered the same test case with a different turbulent Prandtl number $Pr_T = 0.9$ and with a different boundary condition on the model variable $\hat{\nu}$, namely:

- We initialized the field with $\hat{\nu} = 5\tilde{\nu}_\infty$, where $\tilde{\nu}_\infty$ is the kinematic viscosity at the free-stream, in order to activate the turbulence model
- We assigned a low free-stream value to it, $\hat{\nu}_\infty = \frac{1}{100}\hat{\nu}_\infty$, in order to not change the effective Reynolds number.

Exactly the same shock dynamics was found, without any apparent difference in the solution with respect the case with $\hat{\nu}_\infty = 5\tilde{\nu}_\infty$ and $Pr_T = 0.6$.

We can thus conclude that the code may successfully be employed for transonic buffet description, and the results that we will show during the thesis work can be considered meaningful.

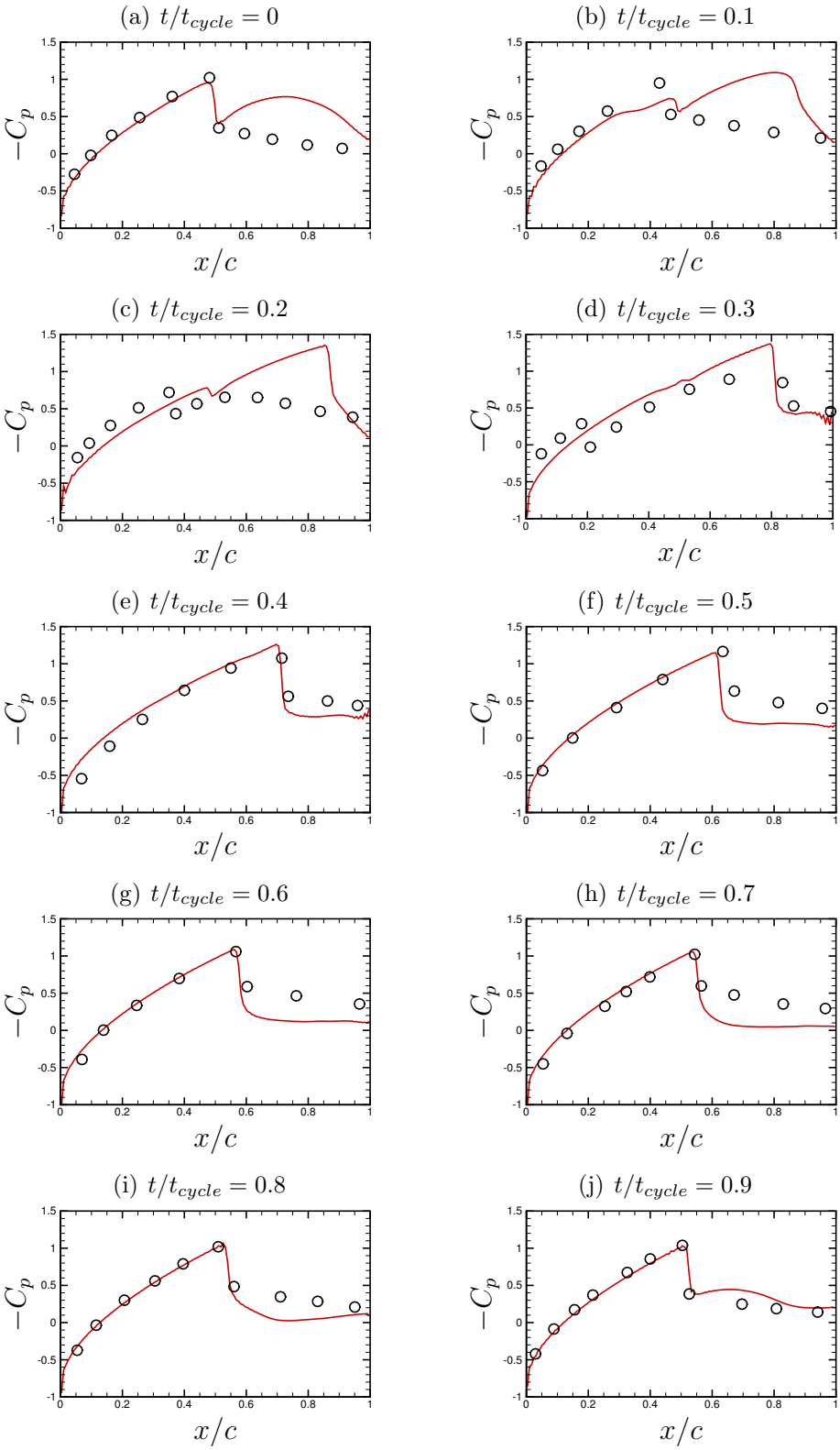

Figure 3.13: *Instantaneous pressure coefficients within a buffet cycle. Empty circles are taken by McDevitt (1979).*

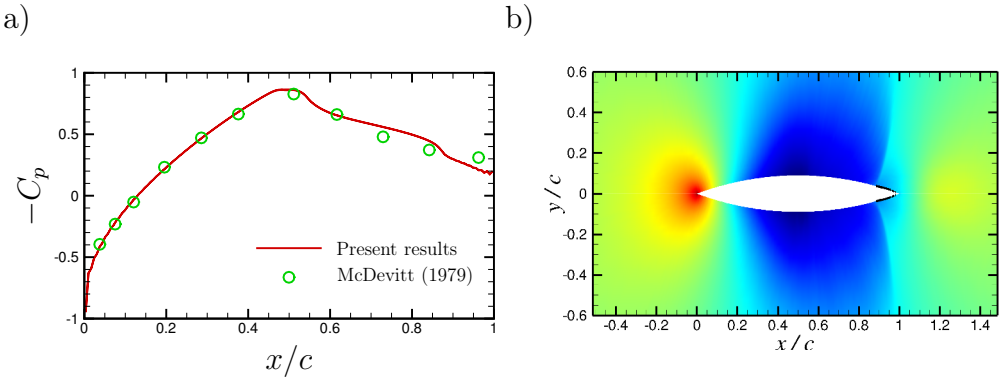

Figure 3.14: *Time-averaged pressure coefficients (a) and mean pressure field (b). Black lines in panel b) identify separated regions.*

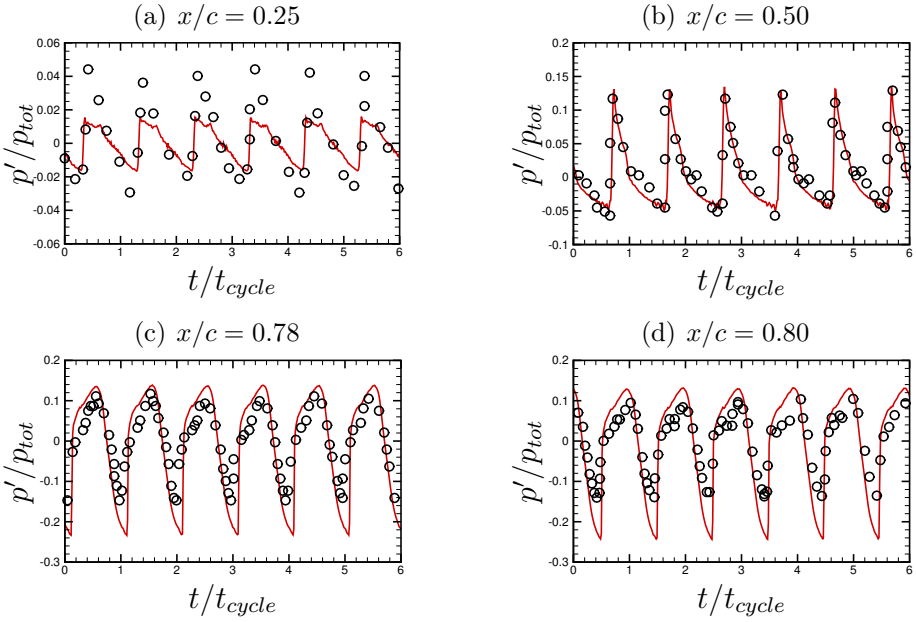

Figure 3.15: *Comparison of pressure time-signal. t_{cycle} is the buffet period, p' are the pressure fluctuations, p_{tot} is the total pressure ahead of the shock. Empty circles are taken by McDevitt (1979).*

Chapter 4

Results with turbulence modeling

4.1 Objectives and operational conditions

We consider flow conditions established during the European project TFAST (`http://tfast.eu/`, in which the effect of the boundary layer state on the shock wave/boundary layer interaction was studied), with a chord Reynolds number $Re_c = 3 \times 10^6$. Numerical simulations have been carried out for the V2C airfoil, a supercritical laminar wing designed by Dassault Aviation during TFAST. A range of transonic Mach numbers and angle of incidence are considered, but the bulk of the analysis is carried out for flow conditions at free-stream Mach number $M_\infty = 0.7$ and angle of incidence $\alpha = 7°$, which shows well-established buffet. Most of the following results are also published in (Memmolo et al., in press).

The aim of this part of the work is to elucidate the mechanisms responsible for transonic buffet of second kind (only one oscillating shock on the lifting surface), referring our analysis to the V2C supercritical laminar airfoil, and to assess the effect of the boundary layer state on the shock oscillations.

Simulations are carried out with physical models of different complexity, namely (i) unsteady Reynolds-averaged Navier-Stokes simulations (URANS), (ii) delayed detached-eddy simulations (DDES) and (iii) implicit large-eddy simulations (ILES). The Spalart-Allmaras turbulence model is used for both URANS and DDES. ILES does not require additional (turbulence) modeling, in that the numerical dissipation inherent to the WENO part of the numerical flux serves as a subgrid scale (SGS) model. It is important to note that the incoming boundary layer state is turbulent for URANS and DDES, whereas it may be laminar for ILES. We also run ILES with forced transition of the boundary layer, where the transition is forced by a simple two-dimensional obstacle. We also perform a numerical experiment on Unsteady RANS, to highlight the role of waves travelling on pressure side. Estimates of the propagation velocities of coherent disturbances are obtained, to check the validity of mechanisms based on acoustic feedback from the trailing edge.

To complete the description of the mathematical model used, we only apply adiabatic wall boundary conditions, as also anticipated in the chapter on the numerical method. The scheme is the one described in that chapter, with the

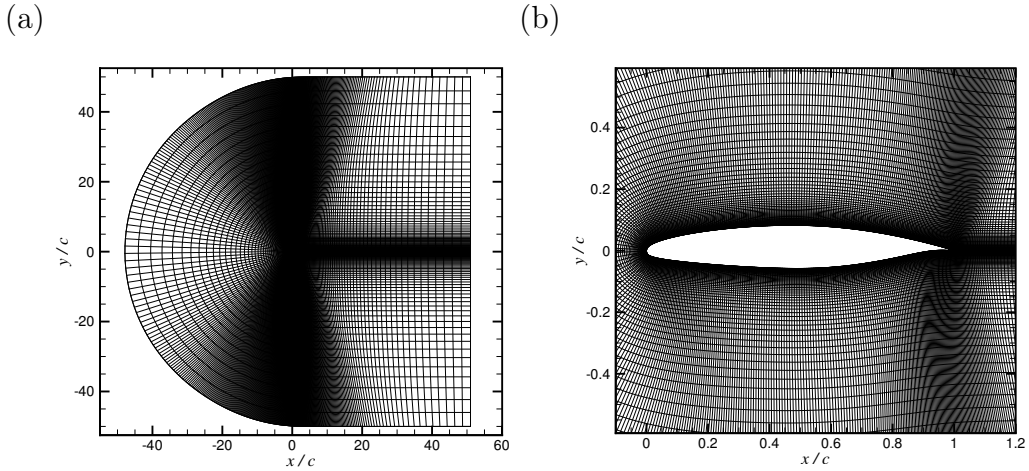

Figure 4.1: *Sample computational mesh for the V2C airfoil. The full mesh is shown in panel (a), and a zoom in the airfoil region is shown in panel (b).*

simulations run semi-implicitly for both the viscous and the convective j fluxes, with first order in time, and with the WENO dissipation (which is active only near shocks and at the leading edge for $\overline{\Theta} = 0.05$) which is computed with matrices evaluated in the $(i, i+1)$ cells rather than in the left and right states. Also, the function controlling the amount of dissipation is here defined in a different way, namely

$$f(\Theta_{i+1/2,j}) = \begin{cases} 0.1 & \text{for } \Theta_{i+1/2,j} < \overline{\Theta} \\ 1 & \text{for } \Theta_{i+1/2,j} \geq \overline{\Theta} \end{cases}$$

rather than

$$f(\Theta_{i+1/2,j}) = \begin{cases} 0 & \text{for } \Theta_{i+1/2,j} < \overline{\Theta} \\ 1 & \text{for } \Theta_{i+1/2,j} \geq \overline{\Theta} \end{cases}$$

for enhanced stability.

Three meshes were tested for URANS, generated with a hyperbolic meshing tool. The chosen mesh is generated by placing the external boundary of the computational domain at a distance of around 25 chords from the airfoil surface and with mesh spacing at the wall of $\Delta y/c \simeq 2 \times 10^{-6}$, corresponding to $\Delta y^+_{max} \simeq 0.6$ at the wall, where the plus symbol is used to denote wall units. The URANS mesh includes $N_x \cdot N_y = 896 \cdot 144$ cells, where N_x, N_y are the number of points in the airfoil tangential and wall-normal direction, respectively. A sample C-type mesh used for URANS is shown in Fig. 4.1. The same mesh was used for DDES, upon extrusion in the spanwise direction over a span $L_z = 0.5\,c$, along which $N_z = 96$ cells are placed. The computational mesh for ILES consists of $N_x \cdot N_y \cdot N_z = 2560 \cdot 384 \cdot 512$ cells. ILES with natural transition was run for a time-span $tU_\infty/c \simeq 100$, corresponding to ten buffet periods, whereas much longer time integration intervals are used for RANS and DDES.

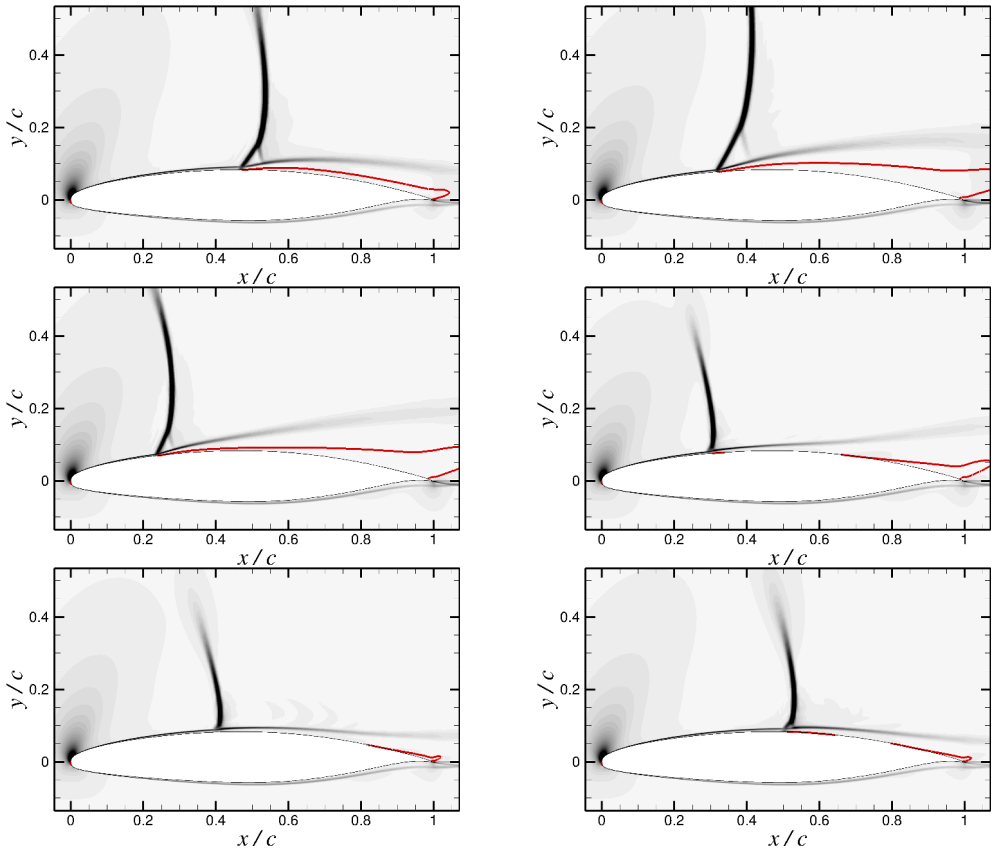

Figure 4.2: *Numerical schlieren in a buffet period, equispaced in time, as obtained by Unsteady RANS at* $M_\infty = 0.7$, $\alpha = 7°$, $Re_c = 3 \times 10^6$. *Red lines:* $u_1 = 0$. *Time advances from left to right.*

4.2 Results

In this section first we show an example of the shock motion on the airfoil, then we show the buffet onset map, as obtained by simulations run with turbulence modeling in the $M - \alpha$ plane, which is used to chose the operational conditions, and next we analyze the effect of the turbulence models themselves on the solution behaviour in presence of well-established buffet.

4.2.1 Buffet envelope

In order to introduce the phenomenon, we show an example of buffeted flow in Fig. 4.2 as obtained by Unsteady RANS at $M_\infty = 0.7$, $\alpha = 7°$, $Re_c = 3 \times 10^6$, showing the shock, highlighted by numerical schlieren contours (gradient of density), in a buffet cycle. The red lines ($u_1 = 0$) also highlight separated regions on the airfoil. As can be seen, during the upstream motion of the shock the boundary layer separates, while it reattaches during its downstream motion. Also the shear layer motion (the shaded line near the edge of the boundary layer) is highly coupled with the shock motion. As the shock moves, the aerodynamic coefficients vary considerably, since

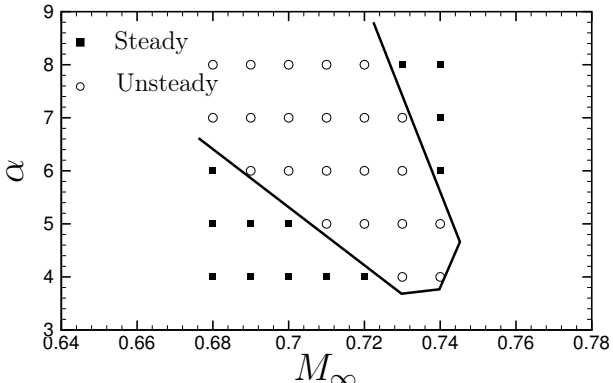

Figure 4.3: *Buffet envelope for the V2C airfoil at* $Re_c = 3 \times 10^6$ *as obtained with URANS.*

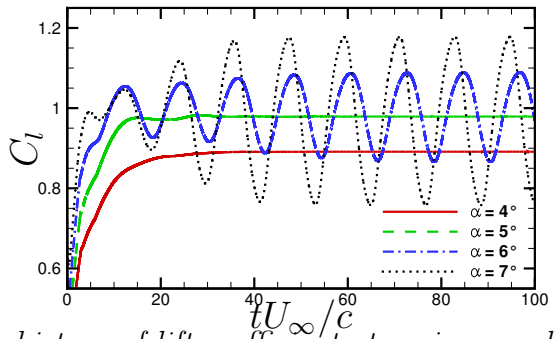

Figure 4.4: *Time history of lift coefficient at various angles of incidence* ($\alpha = 4 - 7°$)*, at* $M_\infty = 0.7$*,* $Re_c = 3 \times 10^6$*.*

the pressure jump due to the shock moves and so does the separated region. As such, they can be used to detect buffet, as done in the following study.

A series of URANS have been carried out to determine the buffet limits of the V2C airfoil at a chord Reynolds number $Re_c = 3 \times 10^6$, in the $\alpha - M_\infty$ plane (α being the angle of incidence, M_∞ the free-stream Mach number). The buffet envelope is sketched in Fig. 4.3, where open circles indicate unsteady flow conditions, and solid squares correspond to steady configurations, as judged based on the time evolution of the lift coefficient. For illustration, in Fig. 4.4 we show the lift coefficient versus time for $M_\infty = 0.7$ at various angles of incidence, suggesting the onset of oscillations at $5° \leq \alpha \leq 6°$. The black line in Fig. 4.3 is an attempt to draw the stability boundary for the V2C airfoil which is found to comprise an upper and a lower branch, similar to what obtained for a NACA0012 airfoil (Crouch et al., 2009). DDES was also applied and found to deliver the same buffet boundary as URANS. However, as shown later, the quantitative prediction of the two methods is quite different in the presence of well-established buffet.

4.2.2 Comparison among URANS, DDES, ILES

Three-dimensional visualizations of the instantaneous flow fields provided by ILES and DDES at $\alpha = 7°$, $M_\infty = 0.7$, $Re_c = 3 \times 10^6$ are shown in Fig. 4.5, where

(a)

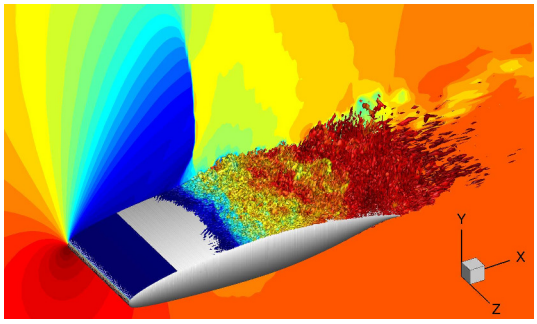

(b)

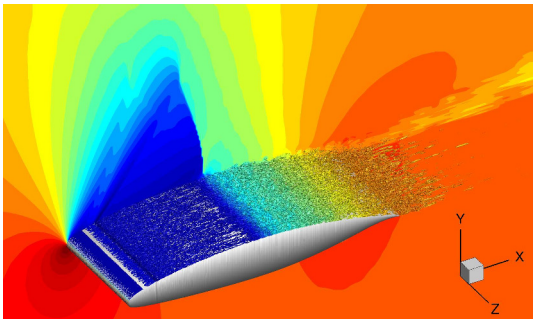

(c)

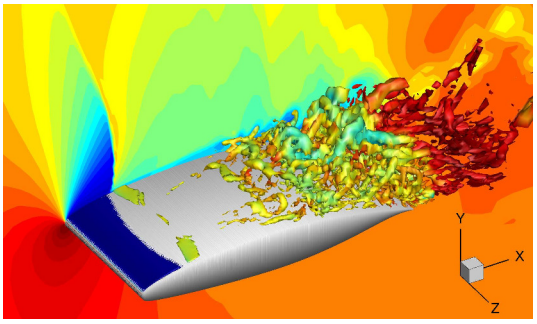

Figure 4.5: *Iso-surfaces of swirling strength for ILES with natural (a) and forced (b) transition, and DDES (b), colored with local pressure. Density isolines are shown in the $x-y$ slice. $M_\infty = 0.7$, $Re_c = 3 \times 10^6$, $\alpha = 7°$.*

vortical structures are detected as iso-surfaces of the swirling strength. It is evident that in ILES much finer flow scales are resolved than in DDES. Fig. 4.5(a) also shows the capability of ILES of describing the main features of the interaction, including the extremely thin incoming laminar boundary layer which undergoes transition in the proximity of the shock foot as a consequence of the associated strong adverse pressure gradient. The figure also shows density contours in a $x - y$ slice, which allows to identify by their abrupt color change the lambda shock which is formed. The shock motion for ILES with natural transition appears (surprisingly) to be quite localized about its mean position, as can be seen in Fig. 4.6, as opposed to DDES which predicts much larger excursion, with the shock almost reaching the leading edge in its most upstream position (visible in Fig. 4.5(c)). Bruce and Babinsky (2008) describe accurately, although for internal flow, the effects of the shock motion on the interaction with the boundary layer, with the leading shock leg of the lambda shock getting stronger during its upstream traveling, with subsequent thickening of the boundary layer. In the transonic external flow field, the interaction is also affected by the acoustic waves able to reach the front of the shock. Acoustic waves propagating outside the separated boundary layer from the trailing edge toward the shock are also clearly seen in this visualization. A better visualization of the acoustic propagation and of the shock motion is offered by the numerical schlieren shown in Fig. 4.6. These are some snapshots of a movie we generated from the data. The left column shows numerical schlieren for ILES with natural transition, and one can see that the shock motion remains quite localized about its mean position. Acoustic waves are seen traveling towards the shock from the downstream flow, and even if not particularly evident from the snapshots, they are also able to circumvent the shock tip, reaching the supersonic region from the top, as it is evident in the movie. The oblique wave which is seen starting at the wall at $x/c \simeq 0.3$ is due to the fact that the laminar boundary layer reacts to the adverse pressure gradient encountered at the shock in a much upstream location then the actual shock location. The boundary layer then undergoes transition after the interaction with the shock, as highlighted by the schlieren images. The transition allows the boundary layer to stay only mildly separated, as shown by the friction coefficients in Fig. 4.7 (a). For what concerns ILES with forced transition, there are two apparent differences: first, the shock excursion is much stronger, even if it never reaches the leading edge of the airfoil, and second, there is a wave system which originates at the obstacle on the wall used to force transition. Part of this waves go interacting directly with the shock, whose lambda structure is more evident in this case, while the most external undergoes a reflection on the (relative) sonic line. Another difference with respect the natural transition is the boundary layer dynamics, which during the upstream motion of the shock experiences massive separation, and during the shock downstream motion reattaches to the wall. However, the mean friction coefficient shows again a mean flow which is mildly separated, as can be seen in Fig. 4.7 (a). Figure 4.7 (b) shows instead that the dynamics on pressure side is substantially identical for the two cases, with the boundary layer that separates at $x/c \simeq 0.7$ and then reattaches after undergoing transition. The fact that the dynamics on pressure

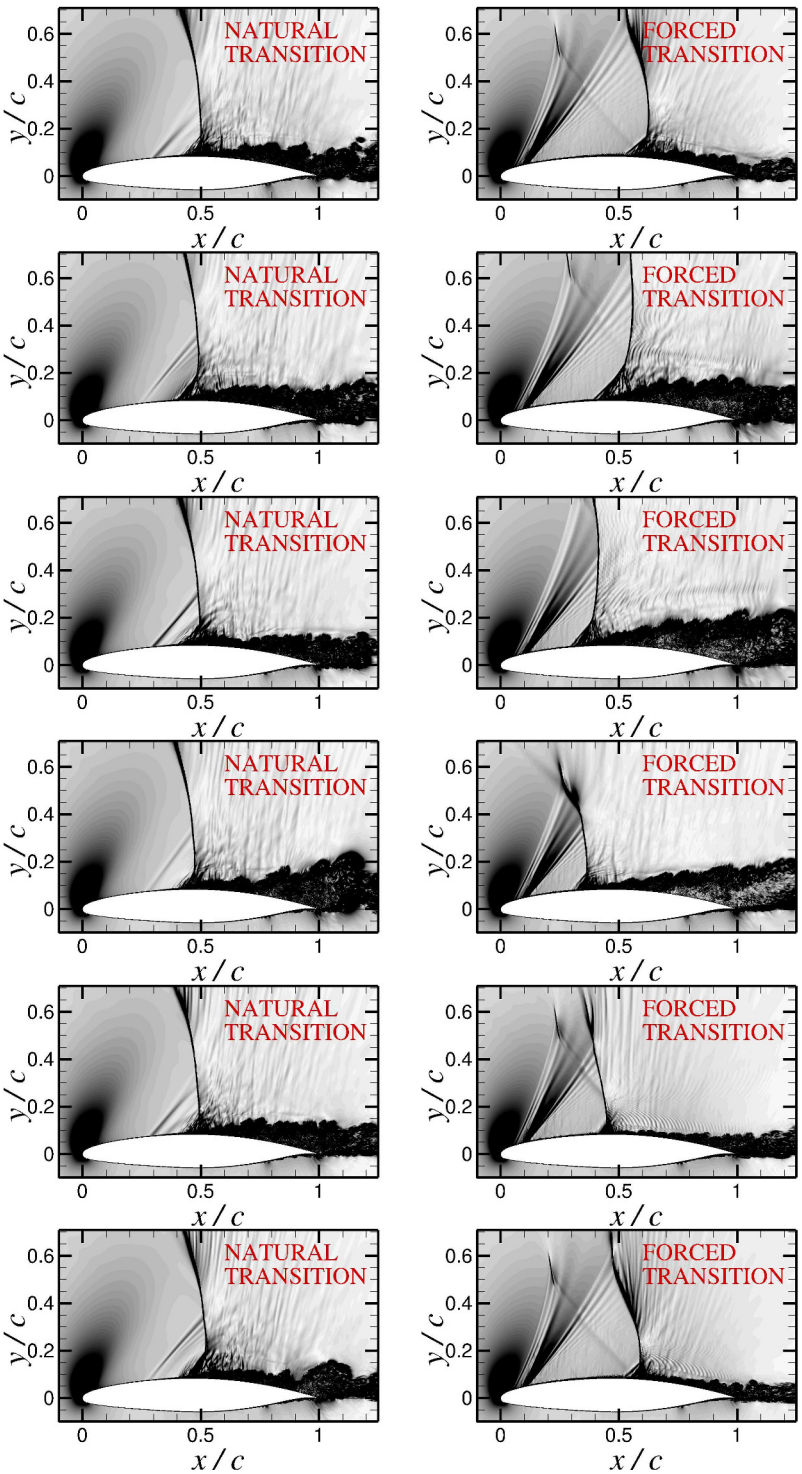

Figure 4.6: *Numerical schlieren visualizations for ILES with natural and forced transition within a buffet cycle. Time advances from top to bottom.*

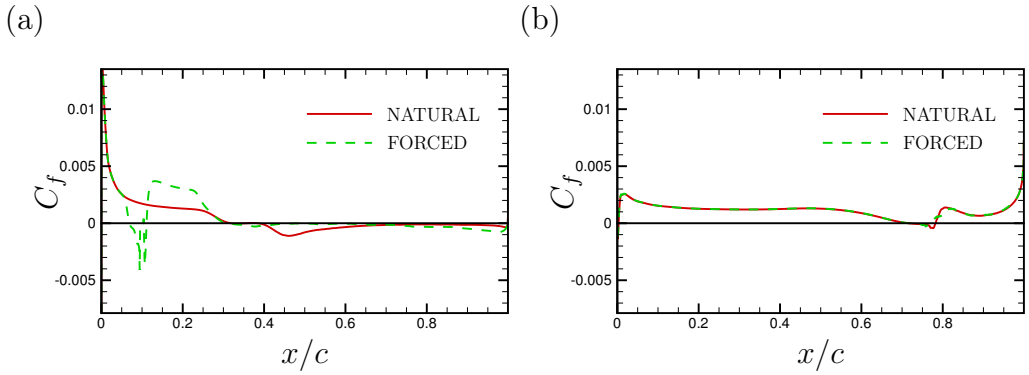

Figure 4.7: *Mean friction coefficients for ILES with laminar and forced transition, on suction (a) and pressure (b) sides.* $M_\infty = 0.7$, $Re_c = 3 \times 10^6$, $\alpha = 7°$.

side is identical in both cases suggests that waves propagation on pressure side only plays a marginal role in the unsteady phenomenon.

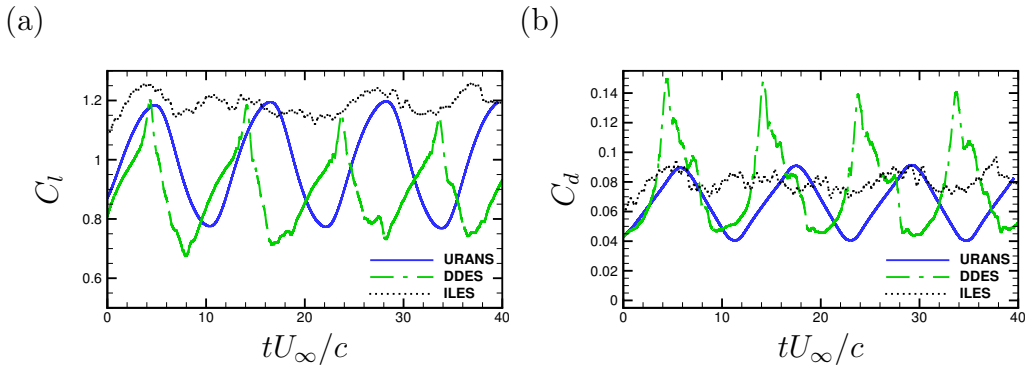

Figure 4.8: *Evolution of lift (a) and drag (b) coefficients from URANS, DDES and ILES with natural transition.* $M_\infty = 0.7$, $Re_c = 3 \times 10^6$, $\alpha = 7°$.

The consequences of shock motion can be appreciated in Fig. 4.8, which shows the time evolution of lift and drag coefficients. URANS and especially DDES both show large shock excursion, whereas ILES with laminar incoming boundary layer appears to yield much more limited oscillations, and higher mean lift coefficient, whereas the mean drag coefficient is similar across all computations. ILES with forced transition gives results quite similar to Unsteady RANS, as can be seen in Fig. 4.9. DDES and URANS both predict a large shock motion. Substantial differences are also observed between URANS and DDES, including: (i) the shape of the $C_l - t$ curve, which exhibits a saw-tooth profile in DDES, with sharper extrema; (ii) mean value of the lift coefficient, which is lower in DDES; (iii) more broad-banded range of excited frequencies in DDES. Similar differences were also pointed out in other recent studies (Szubert et al., 2016).

A comparison of the mean wall pressure coefficient from URANS and DDES is shown in Fig. 4.10 for a steady flow case ($M_\infty = 0.7$, $\alpha = 4°$) and for a case with buffet ($M_\infty = 0.7$, $\alpha = 7°$). Experimental data are also shown for comparison.

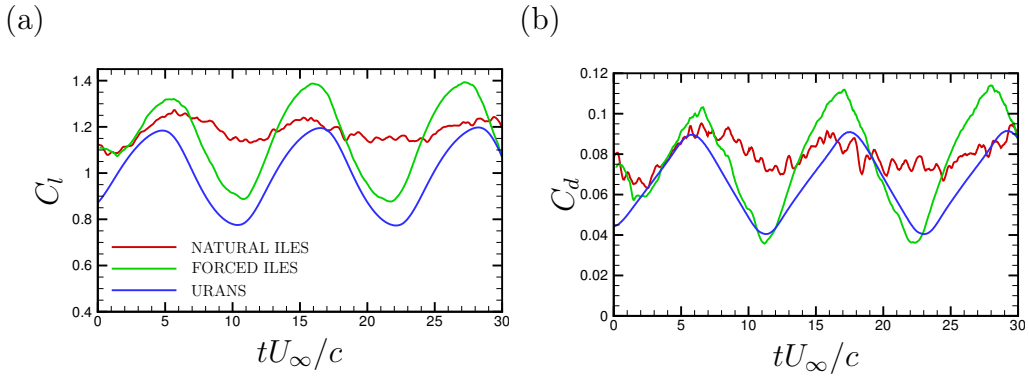

Figure 4.9: *Evolution of lift (a) and drag (b) coefficients from URANS, and ILES with natural and forced transition.* $M_\infty = 0.7$, $Re_c = 3 \times 10^6$, $\alpha = 7°$.

At $\alpha = 4°$ the numerical results are relatively close, except for the mean shock position, with DDES closer to experiments. At $\alpha = 7°$ the reverse trend is observed, and the URANS results are closer to experiments. The smoothed shape of the DDES pressure coefficient on the suction side clearly indicates the presence of unnaturally large shock excursions, almost reaching the leading edge. The mean pressure coefficient for ILES is shown in Fig. 4.10(c), which achieves fair agreement with experiments, although deviations are observed especially in the aft part of the airfoil.

We should mention that we also run RANS with transitional boundary layer, but almost no differences were found with respect the fully turbulent simulation. We show in Fig. 4.11 a comparison between ILES with forced transition and transitional Unsteady RANS, showing again the great similarity between the two results. They differ mostly for the mean shock position, while from figure it can be argued that the shock excursion has similar amplitude in both cases.

The spectral signature of buffet is clearly visible in Fig. 4.12, where we show the frequency spectrum of wall pressure obtained with ILES with natural transition all along the suction side of the airfoil. Two main peaks are identified, including: (i) a low-frequency peak at $St_c \simeq 0.10$ where $St_c = fc/U_\infty$ is the Strouhal number), concentrated around the mean shock position ($x/c = 0.47$), associated with buffet; and (ii) a secondary peak at higher frequency ($St_c \simeq 1$), which spans a wider range of x, and is likely traced to boundary layer separation (see below). Similar buffet frequencies are also found for DDES ($St_c \simeq 0.09$) and URANS ($St_c \simeq 0.08$). Figure 4.12 has been shown in particular to identify the cut-off frequencies which will be used for signal processing in the analysis of the next section for the case of ILES with natural transition.

4.3 Buffet Mechanisms

As pointed out in the first thesis chapter, buffet of second kind is frequently connected with an acoustic feedback mechanism, whereby scattered waves from the

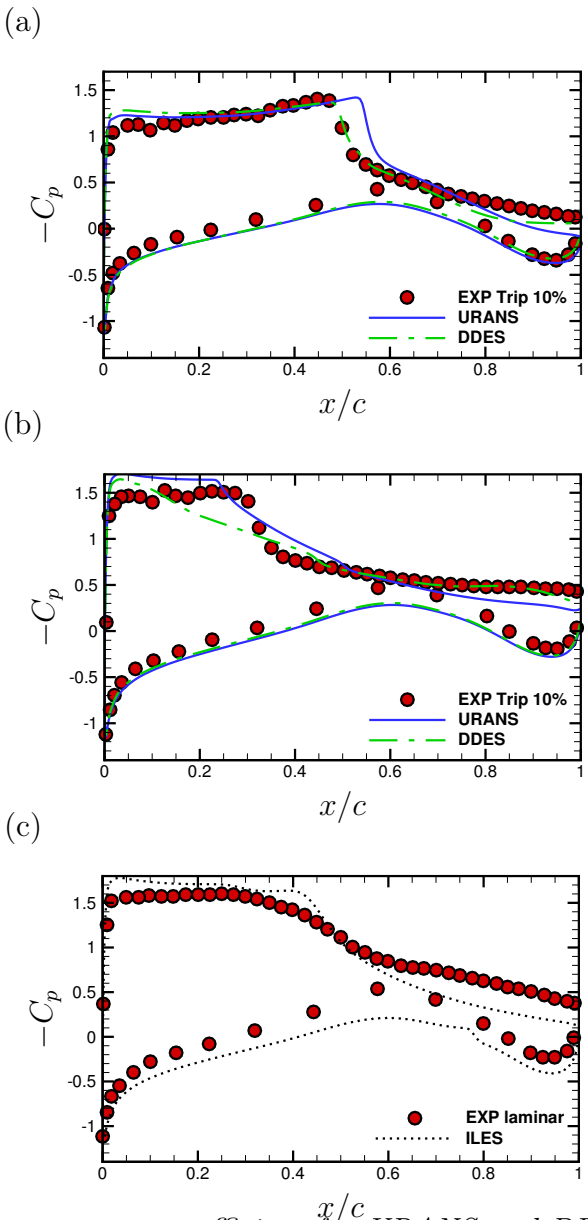

Figure 4.10: *Mean pressure coefficient for URANS and DDES at $\alpha = 4°$ (a) and $\alpha = 7°$ (b), and for ILES at $\alpha = 7°$ (c). $M_\infty = 0.7$, $Re_c = 3 \times 10^6$. Experiments from the Institute of Aviation, Warsaw, Poland.*

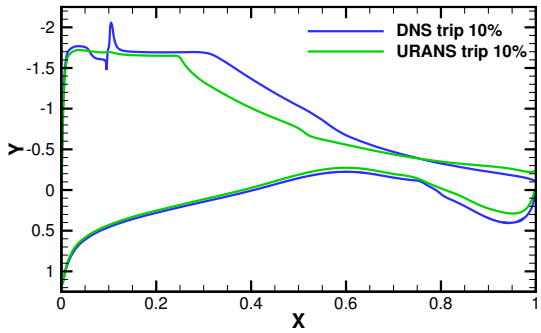

Figure 4.11: *Mean pressure coefficient for ILES with forced transition and URANS at $\alpha = 7°$.*

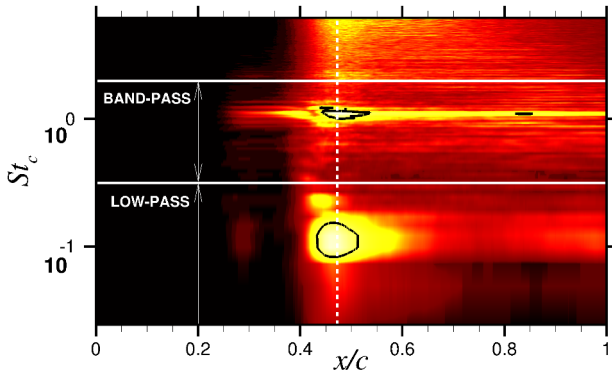

Figure 4.12: *Frequency spectrum of wall pressure at various streamwise stations on the suction side from ILES with natural transition at $M_\infty = 0.7$, $\alpha = 7°$, $Re_c = 3 \times 10^6$. $St_c = fc/U_\infty$ is the Strouhal number. Bright shades denote higher values. The white dashed line indicates the mean shock location. The black iso-lines identify the two main peaks. The horizontal solid lines mark the cut-off frequencies used for signal filtering.*

trailing edge information travel upstream either on the suction or on the pressure side of the airfoil, which is the physical mechanism which sustains the global instability characterizing this buffet type. The discussion that follows is aimed to separately scrutinize these alleged paths to buffet.

4.3.1 Downstream convection

The main mechanism for downstream propagation of disturbances from the shock foot to the trailing edge is the unsteady shedding of large vortical structures associated with shock-induced flow separation (Pirozzoli et al., 2010b). The convection velocity (U_d) of those downstream traveling disturbances is here determined as follows (see Fig. 4.13):

1. the fluctuating pressure signals (black lines in Fig. 4.13(a)) are cross-correlated with a reference signal (grey in the same figure), chosen half-way between the mean shock position and the trailing edge;

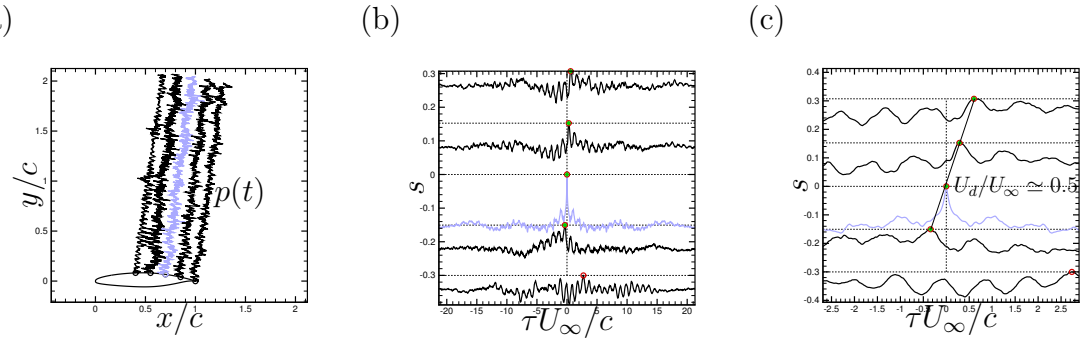

Figure 4.13: *Illustration of the procedure followed to estimate the downstream convection velocity of pressure disturbances: (a) the pressure signals (black) are cross-correlated with a reference signal (grey); (b) cross-correlation curves (circles: absolute maxima); (c) resulting convection velocity. Here, s is the distance between the two cross-correlated signals, $p(t)$ (at the generic x/c on suction side) and $p_0(t)$ (reference signal, at $x_0/c = 0.7$ on suction side), and τ is the time shift.*

Table 4.1: *Typical values of downstream convection velocity (U_d) of coherent pressure disturbances from previous studies.*

Author	Airfoil	Re_c	M_∞	α (deg)	U_d/U_∞
Hartmann et al. (2013)	DRA2303	3×10^6	0.73	3.5	0.08
Deck (2005)	OAT15A	3×10^6	0.73	3.5	0.06
Jacquin et al. (2009)	OAT15A	3×10^6	0.73	3.5	0.07

2. the cross-correlation coefficients (Fig. 4.13(b)) show absolute maxima which identify the time delay and the relative position of the coherent disturbances with respect to the reference (grey) pressure signal;

3. the slope of the line connecting the maxima of the cross-correlation yields the propagation velocity (Fig. 4.13(c)).

Typical values of the convection velocity quoted in previous experimental works are listed in Tab. 4.1. Carrying out this procedure at several x stations for given reference signal (grey bullet), results in the map of Fig. 4.14(a). The maximum of the cross-correlation is (of course) attained for zero time delay and probe distance, corresponding to the maximum value of the auto-correlation coefficient, whereas the maxima which identify coherent disturbances approximatively lie on a single line. The resulting estimate for the downstream velocity is $U_d \simeq 0.4U_\infty$, much higher than the values given in Tab. 4.1, which probably suggests that we are detecting different disturbances than experiments. To explain this apparent inconsistency we have repeated the same procedure on the low-pass filtered pressure signals, with cut-off frequency $St_c \simeq 0.3$, (see Fig. 4.12 for reference). This way we correlated pressure signals which contains only the low frequency related to buffet, without the contamination of high frequencies. The result is shown in Fig. 4.14(b), in

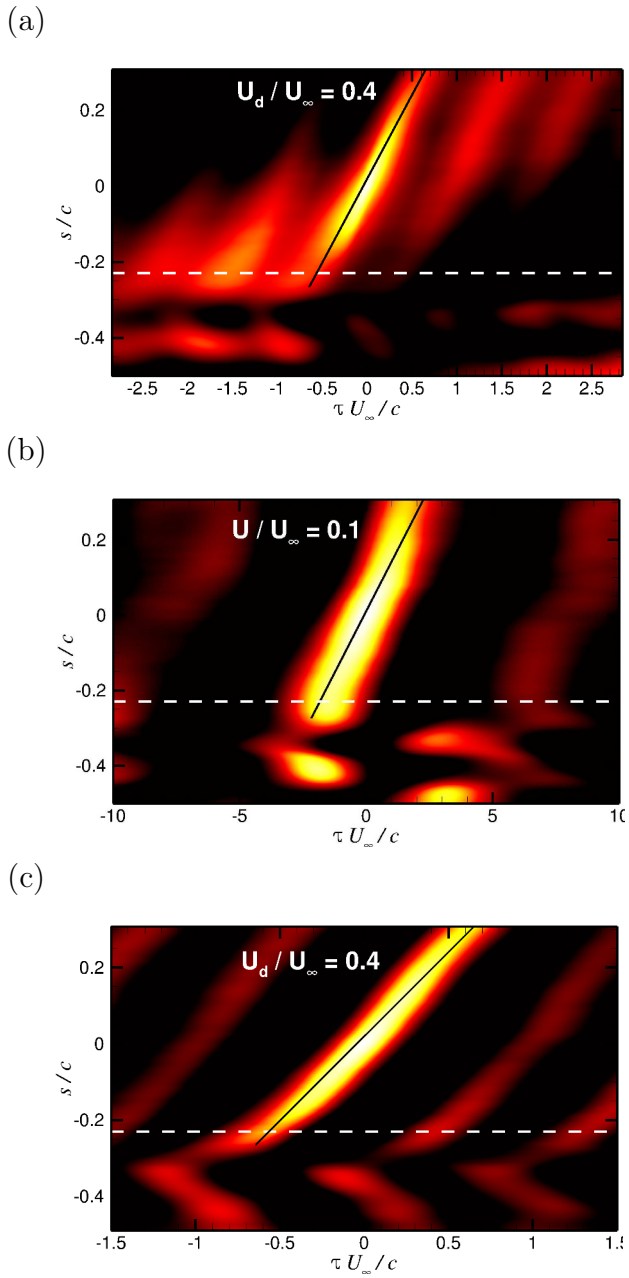

Figure 4.14: *Cross-correlation map of pressure signals for ILES (a), low-pass filtered signals (b), and band-pass filtered signals (c). Solid line: constant velocity line for the estimated downstream propagation velocity (U_d) from the shock foot to the trailing edge of the coherent pressure disturbances. Dashed line: mean shock location. Bright shades denote higher values.*

which the strong correlation again indicates coherent disturbances propagating at nearly constant velocity downstream of the shock. However, the convection speed

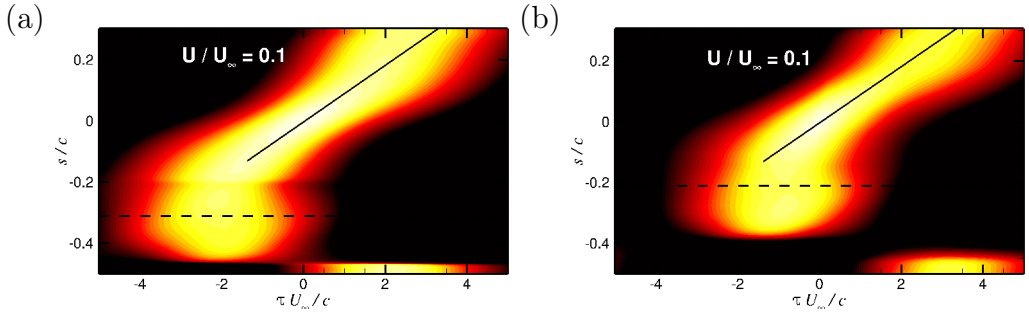

Figure 4.15: *Downstream convection velocity obtained for filtered ILES with forced transition and unfiltered Unsteady RANS.*

is now $U_d/U_\infty \simeq 0.1$, much closer to the values listed in Tab. 4.1, and to the value obtained with URANS and (unfiltered) ILES with forced transition (Fig. 4.15). The same analysis was also performed for band-pass filtered pressure signals, by retaining the frequency range $0.3 \leq St_c \leq 2.4$ (the secondary peak in the spectra, see Fig. 4.12), confirming that the convection velocity retrieved for the unfiltered pressure signal is associated with the disturbances with higher frequency than buffet. It is noteworthy that their convection velocity ($U_d \simeq 0.4U_\infty$) is comparable to the expected convection velocity in a fully separated shear layer, somewhere between the free-stream velocity and the average velocity in the separated region, which is essentially zero. This also justifies the previous interpretation given in Fig. 4.12 of the secondary peak as resulting from a Kelvin-Helmholtz vortex shedding process (Babinsky and Harvey, 2011).

The obtained convection velocities are consistent with the analysis of Roos (1980), who uses a similar procedure to determine the convection velocity, finding that the disturbances associated with higher frequencies are convected downstream more rapidly than low-frequency pressure variations. The initial discrepancy with the values of Tab. 4.1 could thus be related to the higher sampling frequency used in ILES than in the experiments.

Finally, we would like to point out that no upstream disturbance can be traced in Fig. 4.14, which is contrary to inferences of some experiments (Hartmann et al., 2013).

4.3.2 Upstream acoustic propagation on suction side

In order to analyze upstream acoustic propagation we use the methods of geometrical acoustics (see, for example, (Pierce et al., 1981)) applied to the mean field computed with ILES with natural transition, since in this case the mean field is representative of the instantaneous fields. Briefly, the disturbances are assumed to travel following Huygens' principle, i.e. each point of a wavefront acts as an acoustic

source. One can thus derive the following equations

$$\frac{\mathrm{d}x_i}{\mathrm{d}t} = \frac{as_i}{|\mathbf{s}|} + v_i \ , \qquad i = 1, 2 \ , \tag{4.1}$$

$$\frac{\mathrm{d}s_i}{\mathrm{d}t} = -|\mathbf{s}|\frac{\partial a}{\partial x_i} - \sum_{j=1}^{2} s_j \frac{\partial v_j}{\partial x_i} \ , \quad i = 1, 2 \ , \tag{4.2}$$

where $\mathbf{x}$ is the path followed by an acoustic disturbance (acoustic ray), $\mathbf{s} = \mathbf{n}/(a + \mathbf{v} \cdot \mathbf{n})$ is the wave-slowness vector (parallel to $\mathbf{n}$), $\mathbf{v}$ is the ambient medium velocity, $\mathbf{n}$ is the normal to the wavefront and a is the sound speed. Providing the starting point $\mathbf{x_0}$ and the local shape of the wavefront, one can follow any acoustic disturbance along its path. We note that Huygens' principle is only valid for uniform flow, whereas it only approximatively applies to our non-uniform mean flow, only giving reliable predictions for high-frequency disturbances. However, as shown by pressure correlations and as also shown by other studies (Crouch et al., 2009; Hartmann et al., 2013), no low-frequency waves are scattered at the trailing edge on suction side, hence the simplified approach is applicable in the present case.

Figure 4.16 shows the computed acoustic rays, along with the time it takes for a disturbance to travel through. These acoustic rays must be seen in the same spirit as one sees the light propagation from a point source, and in this sense they are the trajectory followed by an acoustic disturbance originating at the trailing edge (the point source) in order to hit a specific point of the field, which feels the disturbance after a certain time interval from its generation. Note that to avoid some problems related to the high shear present in the boundary layer, the initial conditions to be enforced to equations (4.1), (4.2) are not taken at the trailing edge, but are taken along a circular line (dashed in Fig. 4.16), representing a wavefront artificially propagated in a uniform flow at free-stream conditions with point source located at the trailing edge. Starting the computations from different points on this circular line, one obtains the different rays generated at the trailing edge. Fig. 4.16 clearly brings out high-frequency waves traveling upstream on the pressure and on the suction side of the airfoil. The waves propagating on the upper side may either hit directly the aft part of the shock or turn around its edge and penetrate the sonic zone, hitting the shock at its front.

The model of Lee (2001) predicts the buffet frequency resulting from acoustic feedback from the trailing edge as follows,

$$f_{Lee} = \left(\frac{L_s}{U_d} + t_u \right)^{-1} \ , \tag{4.3}$$

where L_s is the distance of the trailing edge from the mean shock position, U_d is the downstream convection velocity of the coherent pressure disturbances, and t_u is the time the acoustic waves scattered at the trailing edge take to reach the shock. In non-dimensional form

$$St_{c,\,Lee} = \left(\frac{L_s/c}{U_d/U_\infty} + t_u U_\infty / c \right)^{-1} \ . \tag{4.4}$$

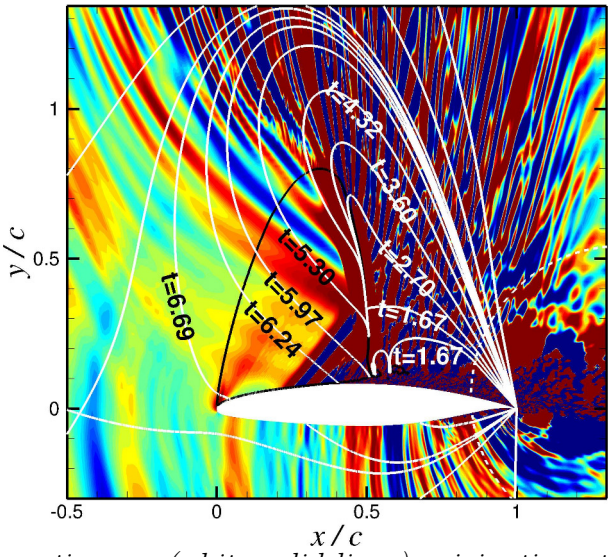

Figure 4.16: *Acoustic rays (white solid lines) originating at the trailing edge, superimposed to contours of the divergence of the velocity disturbances. The labels refer to the travel through times (made nondimensional by c/U_∞). The white dashed line denotes the initial wavefront effectively used, and the sonic line is marked in black.*

In ILES, upstream traveling disturbances are found to hit the shock in its aft part after $t_u U_\infty/c \simeq 1.7$ (see Fig. 4.16), which (also assuming $L_s/c \simeq 0.5$, $U_d/U_\infty \simeq 0.1$) yields $St_c \simeq 0.15$, 50% higher than the computed buffet frequency ($St_c \simeq 0.10$). Alternatively, disturbances may hit the shock at its front by traveling over its tip. Considering this modification to Lee's model, the time taken to hit the shock foot by circumventing the shock tip is (again, see Fig. 4.16) $t_u U_\infty/c \leq 6.0$, and the estimated buffet frequency is $St_c \geq 0.09$, yielding a better agreement with the computed frequency. The best agreement is however recovered by setting $t_c U_\infty/c \simeq 5.0$, which is the travel time of a ray hitting the front of the shock halfway of the sonic line, which actually yields the 'correct' buffet frequency $St_c \simeq 0.10$. It should be remarked that the same attempts are unsuccessful if the convection speed of the unfiltered disturbances (namely $U_d/U_\infty \simeq 0.4$) is inserted into eq. 4.4, in which case substantial overestimate of the buffet frequency is always achieved.

If we apply the same procedure also to ILES with forced transition and Unsteady RANS, we obtain conclusions similar to what obtained for ILES with natural transition (Fig. 4.17), with the best agreement between estimated and computed frequency obtained considering acoustic waves penetrating the supersonic region by circumventing the shock tip (the figure shows only this "optimum" ray).

4.3.3 Upstream acoustic propagation on pressure side

Crouch et al. (2009) considers a symmetrical airfoil at nonzero angle of incidence, finding waves originating at the shock foot that propagate along the suction side toward the trailing edge, turning around it and reaching the opposite side of the

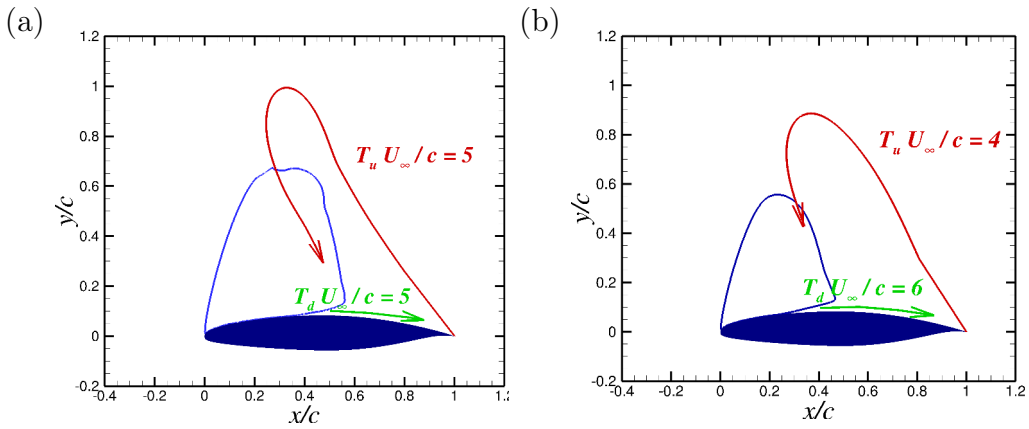

Figure 4.17: *Synthesis of dynamics on suction side for ILES with forced transition (a) and Unsteady RANS (b).*

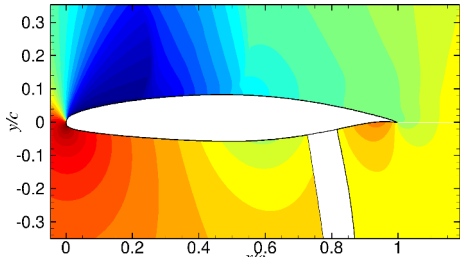

Figure 4.18: *Sponge zone (blanked) for URANS experiments, with superposed pressure contours. In the sponge zone, the solution cannot advance in time.*

shock propagating along the pressure side. Indeed, waves traveling on pressure side are visible in Fig. 4.16, which is yet another possible mechanism for shock oscillation due to acoustic feedback. Following Jacquin et al. (2009), we have then attempted to add the contribution of these waves to the buffet frequency estimate of Lee's original model, thus obtaining

$$f_{Lee} = \left(\frac{L_s}{U_d} + t_u + t_s \right)^{-1} , \tag{4.5}$$

where t_s is the time it takes for an acoustic disturbance originated at the trailing edge to reach the shock traveling along the pressure side. The acoustic path on pressure side is better followed looking at the pressure correlation. As confirmed by this procedure, t_s is nearly equal to the time it takes to a disturbance moving in an undisturbed medium to travel from the trailing edge to the leading edge, and then to the mean shock location, hence $t_u U_\infty / c \simeq 2.5$. Inserting this estimate into (4.5) gives $St_c \simeq 0.11$, again close to the buffet frequency.

To further judge on the actual relevance of acoustic wave propagation along the pressure side in buffet, we have carried out numerical experiments with URANS, whereby we have zeroed the time variation of the solution in a sponge zone near the trailing edge (see Fig. 4.18), thus posing a barrier to any possible upstream traveling wave. Contrary to what the figure may suggest, the sponge zone is not a wall, in

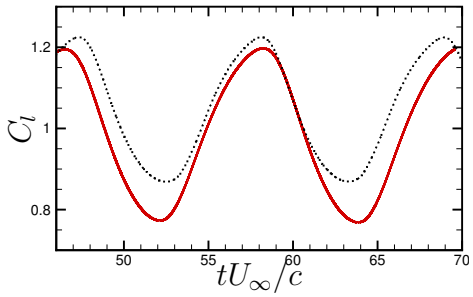

Figure 4.19: *Evolution of the lift coefficient of URANS with sponge zone (dots) and without sponge zone (solid line).*

the sense that non-zero fluxes are allowed to cross that region. What is avoided is their temporal variation, which would be the way propagating disturbances are felt: a disturbance crossing that region would generate a variation of the solution, and if such variation is inhibited, it means that the region remains unaffected by that disturbance, or in other words, the disturbance is not able to enter the sponge region. We stress again that the sponge region is not to be intended as a wall, since non-zero velocity are imposed within it. Inspecting the evolution of the lift coefficient (see Fig. 4.19), it appears that both the amplitude and the frequency of the force coefficients associated with buffet are very similar, even if the effect on the amplitude is stronger than expected, probably due to the different intermittence reaching the shock. This is sufficient to rule out any influence of waves propagating on the pressure side on the buffet mechanism, thus supporting models which only consider the dynamics of the suction side (Hartmann et al., 2013). Waves on pressure side have an effect, though, since the lift coefficients are not equal in the two cases. However what they show is that the primary cause of buffet must be searched on suction side dynamics, while pressure side upstream communication only appears to play a role in the modified intermittence reaching the shock foot in its front.

4.4 Conclusion

Numerical simulations of flow around a supercritical airfoil have been performed using URANS, DDES, and ILES turbulence modeling. All models are found to yield consistent predictions of the buffet frequency, which as in previous experiments is of the order of $St_c \approx 0.1$. The numerical simulations suggest strong influence of the upstream boundary layer state, and quite surprisingly a laminar boundary layer seems to yield more limited shock excursions than the fully turbulent case, with similar buffet frequency. This counterintuitive result may be strongly dependent on the considered Reynolds number, since as will be shown in the following chapter the same result does not hold for DNS computations at a lower Reynolds number. The numerical database has been used to detect/rule out potential mechanisms responsible for buffet. All building block typically advocated in previous experimental and numerical studies are here recovered, including downstream

convecting disturbances in the separated shear layer past the shock foot, and upstream-traveling acoustic disturbances on the suction and on the pressure side of the airfoil. Lee's predictive model for buffet frequency with contributions also from upstream traveling acoustic waves on the pressure side is found to be roughly consistent with the measured value. However, numerical simulations carried out with an artificial sponge on the pressure side to cancel acoustic feedback waves would tend to rule out the former mechanism, as the effect on the buffet frequency is minimal. Surveying only the dynamics on suction side, we found agreement between estimated and measured frequency by considering downstream traveling low-frequency disturbances from the shock foot to the trailing edge, and upstream traveling high-frequency acoustic disturbances circumventing the shock tip. In summary, it appears that the only acoustic feedback loop mechanism compatible with transonic buffet is the one involving upstream traveling acoustic waves on suction side penetrating the sonic region.

Chapter 5

DNS results

5.1 Objectives and operational conditions

A Reynolds number of $Re_c = 3 \times 10^6$, the same of the previous chapter, is still prohibitive for DNS computations. As such, we switch in this chapter to a lower Reynolds number $Re_c = 3 \times 10^5$. The problem in lowering the Reynolds number is mostly related to the possibility for the boundary layer of reaching a turbulent state. We also use Unsteady RANS for comparison.

We run four DNS cases, considering both natural and forced transition at two different angles of incidence, $\alpha = 4°$ and $\alpha = 7°$. We force transition both on suction and pressure sides. Also when we run the natural transition cases, the pressure side will be tripped anyway, for reasons that will be clarified in section 5.2. As already stressed, the Reynolds number is lowered to $Re_c = 3 \times 10^5$, while the free-stream Mach number is $M_\infty = 0.7$. These conditions are chosen as a natural continuation of the work described in the previous chapter.

The simulations are started from a two-dimensional Unsteady RANS, which is also used to assess the grid, which is the same for the four DNS. An *a posteriori* check is later performed on all simulations.

As in the previous chapter, here the different simulations are run semi-implicitly for both the viscous and the convective j fluxes, with second order in time, with the WENO dissipation (which is active only near shocks and at the leading edge for $\overline{\Theta} = 0.05$) which is computed with matrices evaluated in the $(i, i+1)$ cells rather than in the left and right states (sec. 2.4.3). Also, the function controlling the amount of dissipation is the default

$$f(\Theta_{i+1/2,j}) = \begin{cases} 0 & \text{for } \Theta_{i+1/2,j} < \overline{\Theta} = 0.05 \\ 1 & \text{for } \Theta_{i+1/2,j} \geq \overline{\Theta} = 0.05 \end{cases}$$

The grid, chosen after a RANS based calibration, has $N_x = 4096$, $N_y = 512$, $N_z = 256$ cells. The domain span size is taken as $L_z/c = 0.1$. A wider domain would have been too expensive. The size of the domain is larger than the one used by Garnier and Deck (2010).

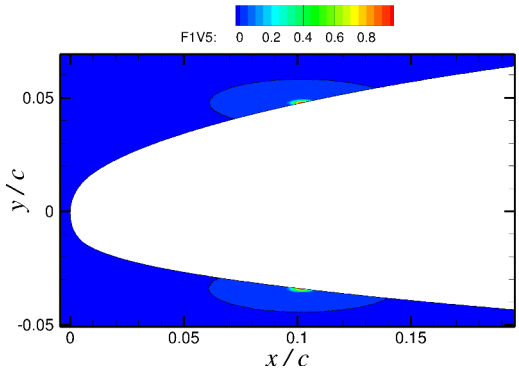

Figure 5.1: *Navier-Stokes equations modified in the two zones included between the two black lines. The figure shows the amplitude of function $F_2(x, y)$, which is the factor which measures the relative strength of the tripping force.*

Also, the nature of the boundary layer trip used for DNS is different than the one used for ILES. We use the tripping force described in (Schlatter and Örlü, 2012), and the description of the trip and the reasons we switched from the two-dimensional obstacle to a more sophisticated approach deserve a section by themselves to be explained.

We perform a similar analysis as done in the previous chapter. As anticipated, the interesting but counterintuitive result of a stabilizing effect on the shock motion of the laminar incoming boundary layer is not retrieved in DNS computations at lower Reynolds number. The mechanism previously illustrated appears instead to hold.

5.2 Boundary layer tripping

As anticipated, for the DNS computations we force transition using the method described by Schlatter and Örlü (2012). Instead of a physical device, a volume force is introduced to perturb the boundary layer. As such, we are modifying the Navier-Stokes to also include, at the right-hand-side, the term $F_2(x, y)g(z, t)$. $F_2(x, y)$ is defined as

$$F_2(x, y) = \exp\left[\left(\frac{x - x_0}{l_x}\right)^2 - \left(\frac{x}{l_y}\right)^2\right] \tag{5.1}$$

It is just a "Gaussian blob" which defines the regions of the (x, y) plane where the tripping force should act. Figure 5.1 shows contours of $F_2(x, y)$ for the chosen x_0, y_0, l_x, l_y, whose values will be given in the following. As can be seen in figure, we consider a forced transition also on pressure side, and we will explain the reason for this in the following. Function $g(z, t)$ is the one which permits the imposition of temporal frequencies and in the span

$$g(z, t) = A_t\{[1 - b(t)]h^i(z) + b(t)h^{i+1}(z)\} \tag{5.2}$$

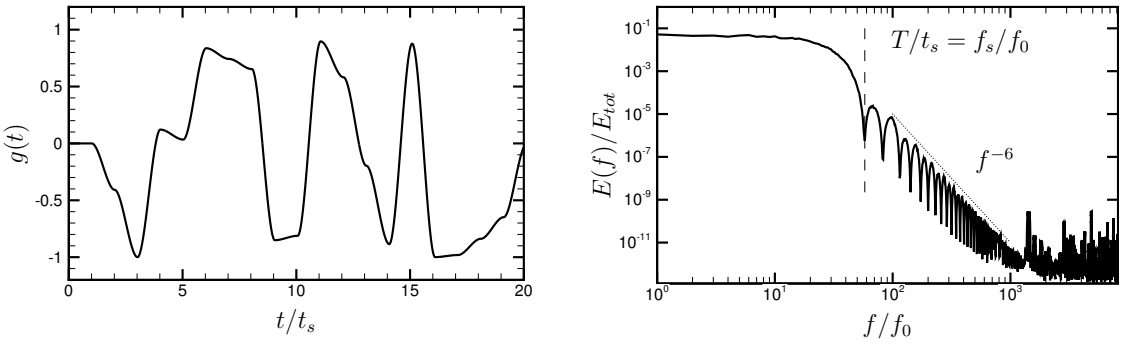

Figure 5.2: *$g(z,t)$ vs. time and frequency for fixed z.*

where $b(t) = 3p^2 - 2p^3$, $p = t/t_s - i$, $i = \text{int}(t/t_s)$, with $\text{int}(\cdot)$ denoting the integer part of the argument. t_s denotes the time scale, as shown in Fig. 5.2. For fixed z, $g(z,t)$ vs. time and frequency is sketched in fig 5.2. In z direction, $g(z,t)$ is given by the sum of two sinusoidal functions, with random phases and frequencies, given by

$$h^i(z) = \sin\left(\frac{2\pi}{\lambda^i}z + 2\pi r_p^i\right), \quad \text{where } \frac{1}{\lambda^i} = \frac{r^i}{z_s}, \quad 0 < r^i < 1 \tag{5.3}$$

z_s defines λ^i, i.e. the maximum considered wave number $k_{z,max}$, and r^i is a random number. Moreover, we correct the relation to have a perfectly periodic forcing in the z direction, that is, we enforce $n\lambda^i = L_z$, where n is an integer number. The correction simply reads

$$\frac{1}{\lambda^i} = \frac{1}{L_z} int\left(\frac{r^i}{z_s}L_z\right) \tag{5.4}$$

Moreover, the correction does not alter the value of λ^i_{min}

$$\frac{1}{\lambda^i} < \frac{1}{L_z}\left(\frac{r^i}{z_s}L_z\right) = \frac{r^i}{z_s} < \frac{1}{z_s} = \frac{1}{\lambda^i_{min}} \;\Rightarrow \lambda^i_{min} \text{ is not changed}$$

A tripping force defined in this way allows smooth restarts, even if random numbers are involved. The direction of the volume force is normal to the wall, and so we must add the term $F_2 g \hat{\mathbf{n}}_{wall}$ to the momentum equations, and the term $F_2 g u_n$ to the total energy equation.

Now we shall explain why we considered this forcing method. As a first attempt, we tried the tripping device already used for the ILES described in the previous chapter. Trying different heights and shapes of the device had only two outcomes: a laminar boundary layer or a transitional one, but with shock locked near the tripping device. The use of the Schlatter and Örlü (2012) tripping force, instead, resulted anyway in a transitional boundary layer, without the shock-locking.

Figure 5.3 shows on the first row the two-dimensional obstacle tripping, with the minimal height which induced transition, and not with a rectangular shape, but with a wedge shape, in an attempt to unlock the shock from the tripping device. It did not

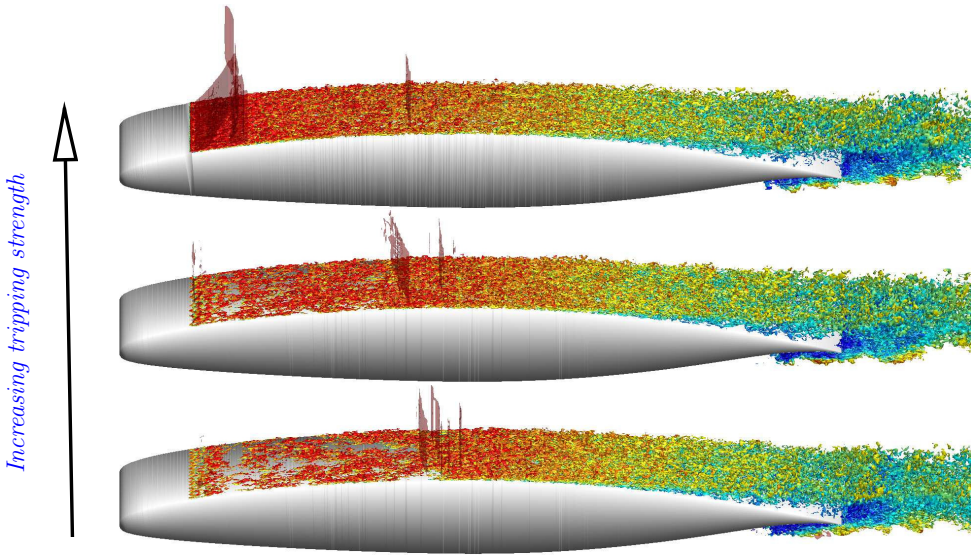

Figure 5.3: *Effects of different tripping on suction side. Swirling strength isosurfaces are used to highlight forced transition effects, while shock are located through contours of the velocity divergence.* $Re_c = 3 \times 10^5$, $M_\infty = 0.7$, $\alpha = 4°$.

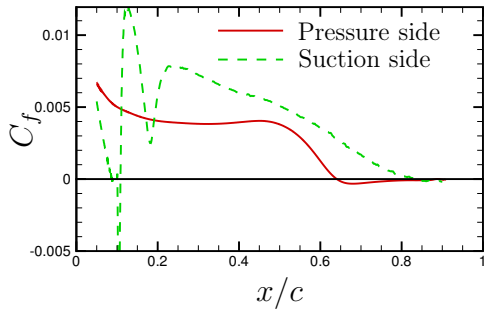

Figure 5.4: *Skin friction coefficient for top case of Fig. 5.3 (wedge).* $M_0 = 0.7$, $Re_c = 3 \cdot 10^5$, $\alpha = 4°$.

work. The second and the third rows feature both the volume force tripping, with different strengths. We can see that the second row features a transitional boundary layer, without the shock-locking. The flow undergoes separation on pressure side starting from $x/c \simeq 0.65$, as can be seen in Fig. 5.4, due to the strong adverse pressure gradient in the pressure recovery region on pressure side. Since the flow is laminar on pressure side, and the Reynolds number is not high enough to promote a natural transition in that zone soon after separation, a large separation region is unavoidable, unless we force transition also on pressure side. For consistency, we force transition on pressure side also when we run the "laminar" simulations, so that the terms "laminar" (natural transition) and "tripped" (forced transition) only distinguish the different states of the incoming boundary layer on suction side.

The missing details of the trip are given in tab. 5.1, but first a point has to be made:

- The center of the Gaussian blob $F_2(x,t)$ is $x_0 = 0.1$, correspondent to $Re_x =$

Table 5.1: *Details of the volume force tripping. δ_0^* is the boundary layer thickness in the tripping center $x_0/c = 0.1$.*

l_x	l_y	t_s	z_s
$4\delta_0^*$	δ_0^*	$4\delta_0^*/u_\infty$	$1.7\delta_0^*$

30000. Schlatter and Örlü (2012) use the tripping force for a boundary layer on a flat plate, and to define the various parameter involved in the tripping method they use values relative to the inlet boundary layer thickness δ_0^*. Since here we are dealing with a boundary layer on an airfoil, we have to assume a different reference quantity, which we choose to be the boundary layer thickness at x_0. The quantities listed in tab. 5.1, are all taken from (Schlatter and Örlü, 2012), assuming for δ_0^* the boundary layer thickness in the tripping center

- Schlatter and Örlü (2012) does not report the maximum amplitude given to A_t. After a calibration procedure, we have chosen the value $100u_\infty^2$, which corresponds to second row of Fig. 5.3.

5.3 DNS at $\alpha = 4°$

Lets first deal with the laminar and tripped simulations at $\alpha = 4°$. The *a posteriori* check is reported in Fig. 5.5, in terms of wall units. Both respect Hosseini

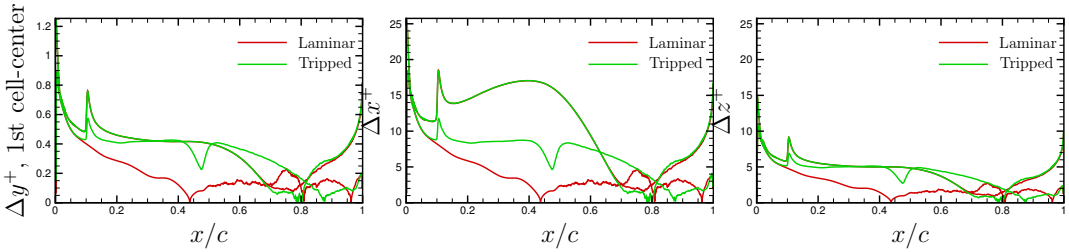

Figure 5.5: *Wall spacing in wall units: distance of the first cell-center from the wall (left column), Δx^+ (middle column) and Δz^+ (right column) at $M_0 = 0.7$, $Re_c = 3 \cdot 10^5$, $\alpha = 4°$.*

et al. (2016) recommendations: $\Delta x^+ < 10$, $\Delta y^+ < 0.5$, $\Delta z^+ < 5$.

Figure 5.6 shows the temporal behaviour of the two DNS, in terms of lift and drag coefficients, and of aerodynamic efficiency. As can be seen, the tripped simulation behaves as expected, showing no buffet, in accordance with the results of the previous chapter (Fig. 4.3), even if they refer to a higher Reynolds number. The laminar incoming boundary layer, instead, shows clearly the shock buffeting. As will be shown, the dynamics in this case is really complicated, since there are multiple shocks interacting with each other. The same analysis performed in the previous chapter is thus not performed in this case, we only extract some characteristic, as the downstream disturbances convection velocity, for compare them with the simpler

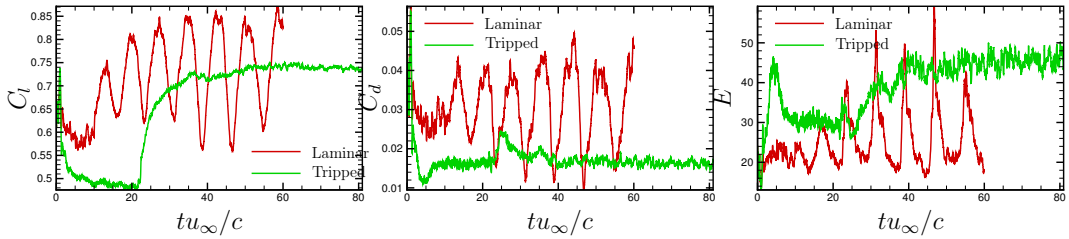

Figure 5.6: *Time history of lift (left column) and drag coefficient (middle column), and aerodynamic efficiency (right column) at* $M_0 = 0.7$, $Re_c = 3 \times 10^5$, $\alpha = 4°$.

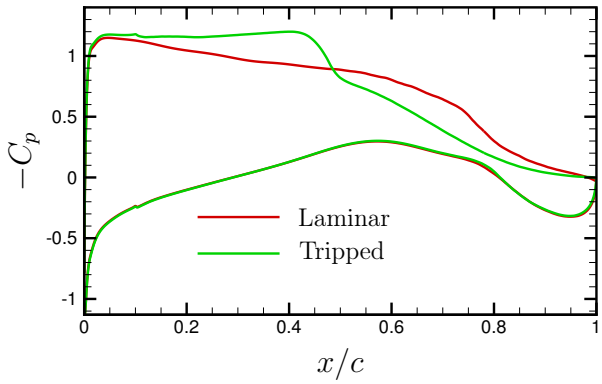

Figure 5.7: *Pressure coefficients of the mean fields at* $M_0 = 0.7$, $Re_c = 3 \cdot 10^5$, $\alpha = 4°$.

case showing a single shock. Anyway, the figures clearly show superior performances of the tripped boundary layer with respect the laminar one in these flow conditions.

The pressure coefficients of both simulations are shown in Fig. 5.7. The figure shows quantities averaged both in the span and in time. The time interval to be used in the averaging procedure is chosen looking at the temporal evolution of the lift coefficients, and is chosen as $24.8 < tu_\infty/c < 58.8$ for the laminar simulation and as $tu_\infty/c > 49.7$ for the tripped one. We can see that on pressure side the two curves almost coincide, while on suction side the shock is clearly visible in the tripped simulation, whereas its effects are spread on a much longer part of the suction side in the laminar simulation, due to its large motion in this case.

Figure 5.8 shows friction coefficient (first column), displacement boundary layer thickness (second column) and the incompressible shape factor (third column), both on suction (first row) and pressure (second row) sides. The friction coefficient on suction side for the tripped simulation, and on pressure side for both the simulation, shows a peak at $x_0 = 0.1$, which corresponds to the trip. Focusing first on quantities on suction side, we can see that in the tripped boundary layer case, the shock is not strong enough to induce separation. The flow is decelerated in correspondence of the shock, and this is reflected in the local minimum generated in C_f, then the flow accelerates again, and the separation is delayed to $x/c \simeq 0.85$. This is also reflected in the pressure coefficient (Fig. 5.7): in the separated region, for $0.85x/c < 1$, the pressure coefficient is nearly equal zero, and for lower x it smoothly converges to the

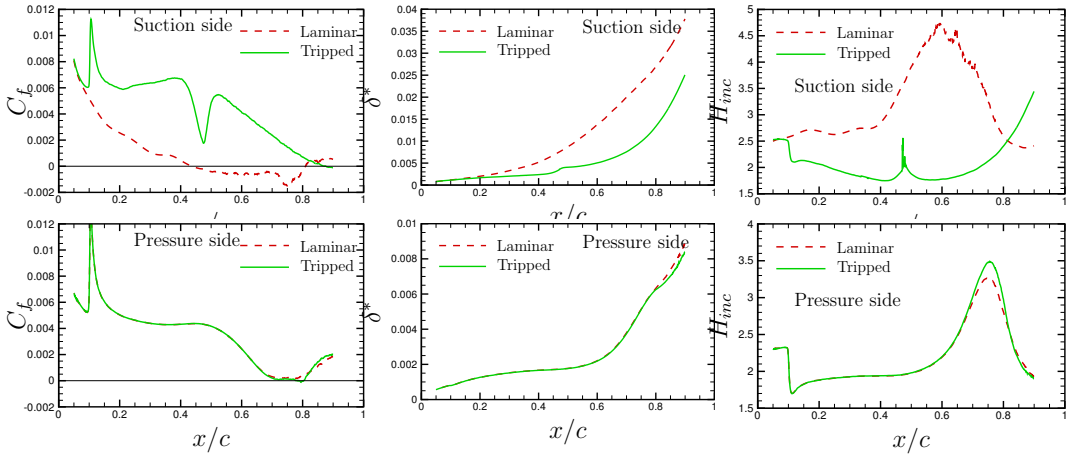

Figure 5.8: *Skin friction coefficient (left column), displacement b.l. thickness (middle column), incompressible shape factor (right column) on suction side (first row) pressure side (second row) at* $M_0 = 0.7$, $Re_c = 3 \cdot 10^5$, $\alpha = 4°$.

experimental one, which is however referring to an attached boundary layer, since the Reynolds number is higher. The laminar boundary layer is instead separated, in average, over more than half of the airfoil chord. The average separation point for the laminar case is close to the shock location in the tripped case. Focusing on pressure side, we notice that it is mildly influenced by the state of the boundary layer on suction side, even if as already stated, the laminar case is highly unsteady. The friction coefficient shows that from $x/c \simeq 0.7$ on, the flow is close to separation, and in fact, as explained in section sec. 5.2, if the boundary layer on pressure side is laminar, it would undergoes separation from $x \simeq 0.65$. The tripping is effective in delaying the separation, and, together with the strong adverse pressure gradient, to drive a flow transition, as shown by the incompressible shape factor, which increases in the region where the flow tends to separate, but suddenly decrease again, indicating an attached, transitional boundary layer. We can also notice that the initial value of the incompressible shape factor, close to 2.5 - with 2.6 being the typical value for zero-pressure gradient laminar boundary layer - is lowered after the interaction with the trip-force, indicating an effective trip. The trip is thus effective in its fundamental tasks. Figure 5.10 shows the velocity tangential to the wall vs. the wall distance, in plus units. Only the tripped simulation is taken into account in this figure, since on pressure side the results were almost coincident for laminar and tripped cases, while on suction side the laminar simulation is already expected to not follow any log-law. Instead, we tried to see if a Blasius-like self-similarity still exists for the velocity on suction side for the laminar case, but this is not the case, as shown by Fig. 5.9. The first row of Fig. 5.10 refers to suction side, while second row refers to pressure side. First column shows the tangential velocity in wall units vs. distance from the wall also expressed in wall units. Second column shows a derived quantity which is constant for a logarithmic behaviour of u^+.We observe that the Reynolds number is too low to obtain the high-Reynolds number behavior in the logarithmic overlap region, and that a more prominent wake region

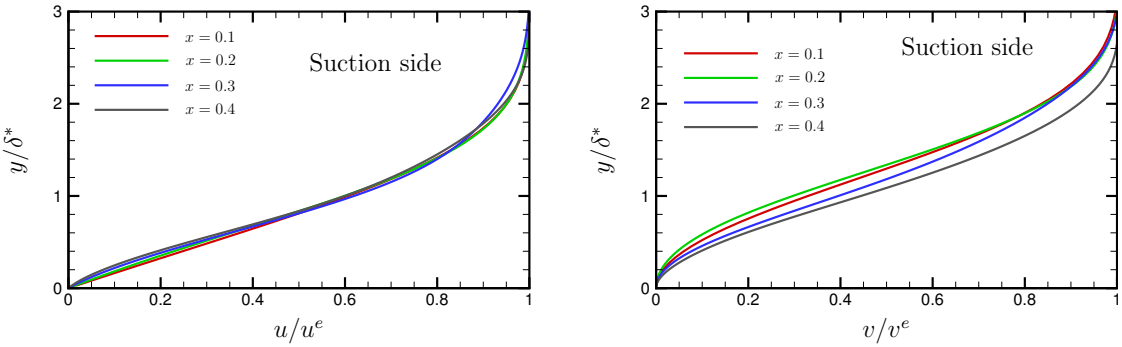

Figure 5.9: *Tangential and normal to the wall velocities on suction side scaled for self-similarity at $M_0 = 0.7$, $Re_c = 3 \cdot 10^5$, $\alpha = 4°$ for laminar case on suction side.*

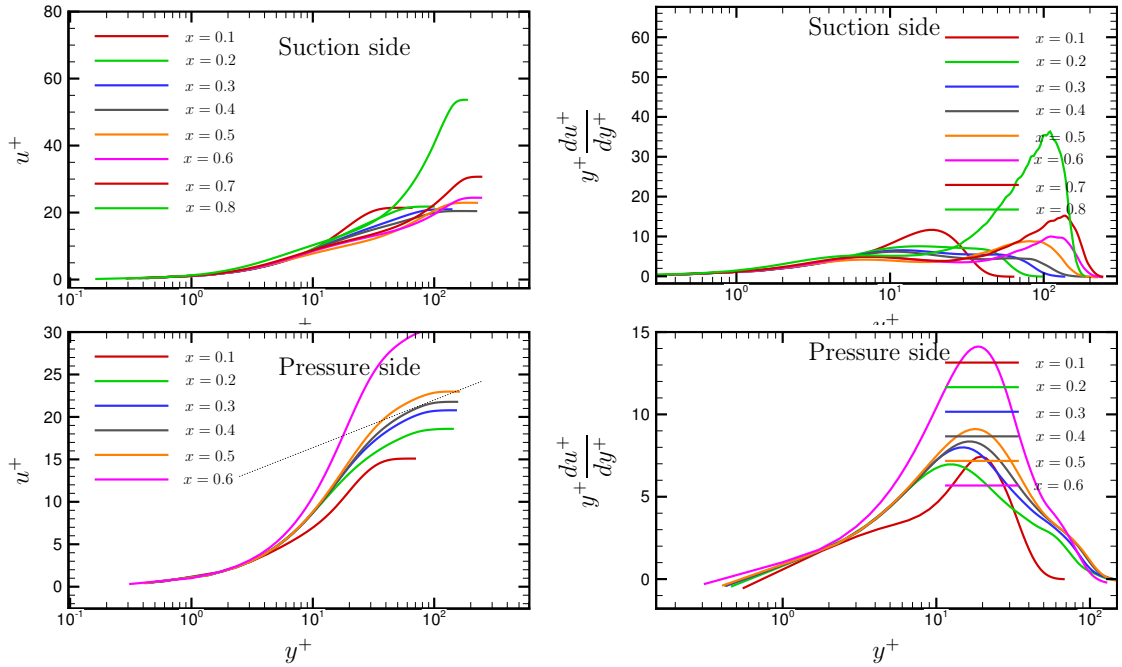

Figure 5.10: *Tangential velocity on pressure side in wall units and a check for the log-law (right) at $M_0 = 0.7$, $Re_c = 3 \cdot 10^5$, $\alpha = 4°$ for tripped boundary layer on suction (first row) and pressure (second row) sides. The black dotted line is the correct slope for the log-law region.*

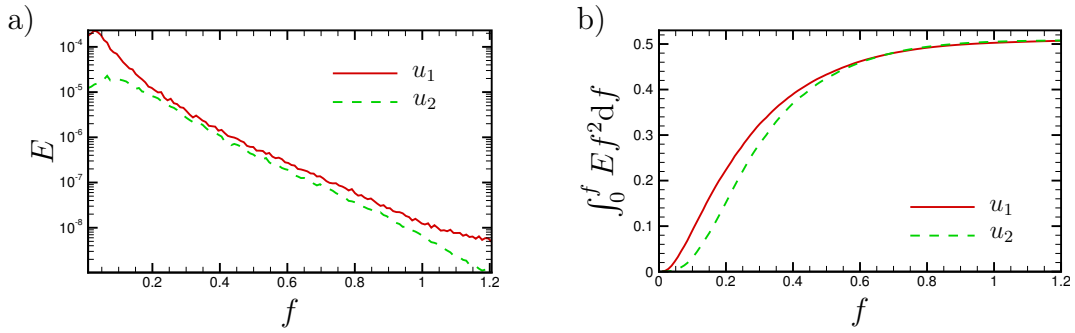

Figure 5.11: *Spectra along the span of longitudinal and transversal velocity at* $y^+ = 11.6$ *(a) and partial sum of the 1-D dissipation.* $M_0 = 0.7$*,* $Re_c = 3 \cdot 10^5$*,* $\alpha = 4°$*, suction side, tripped boundary layer.*

is observed, connected to the presence of the adverse pressure gradient. The same behavior is also found by Vinuesa et al. (2017).

Figure 5.16 shows in panel a) the spectra along the span of the longitudinal and transversal velocities, whereas panel b) shows the partial sum of the one-dimensional dissipation. The exponential decay of the first and the constant value attained by the second prove that the resolution is adequate and the simulation can be considered a DNS.

5.3.1 Buffet analysis

As can be seen in Fig. 5.12, buffet is of type C of Tijdeman (1977) classification, with shocks moving only in the upstream direction. As also discussed in the introduction of the thesis, it is not unusual for the flow on an airfoil with a laminar boundary layer to show multiple shocks. The figure shows the flow averaged in the span, in ten different, equispaced instants. The number of the shocks varies during the buffet cycle, and the dynamics is really complicated to describe. In the description of the mechanisms in the Introduction of the thesis, we were able to associate the strength of the shock to its position and its velocity. The presence of various rarefaction waves interacting with shocks makes the evaluation of the shock strength less straightforward. So there is a varying number of shocks, of varying strength during the cycle, which also interact with each other. Acoustic waves are also seen in figure, and it appears that the shocks weakened by the interaction with the rarefaction waves tends to follows the same behaviour. This makes also a little more evident the entrainment of acoustic waves in the supersonic regions. There are no clearly defined triple points. The figure also shows, in red, the line $u_1 = 0$ representative of separation. One can see that a fully attached boundary layer is never present during the whole buffet cycle. Separation follows the complicated dynamics of the shocks, but it is evident that during part of the cycle it is separated on a great part of the airfoil, while in subsequent times it only shows some separation patches. Incipient separation on pressure side was shown by the time averaged friction coefficient. We can see that during part of the cycle, separation is present

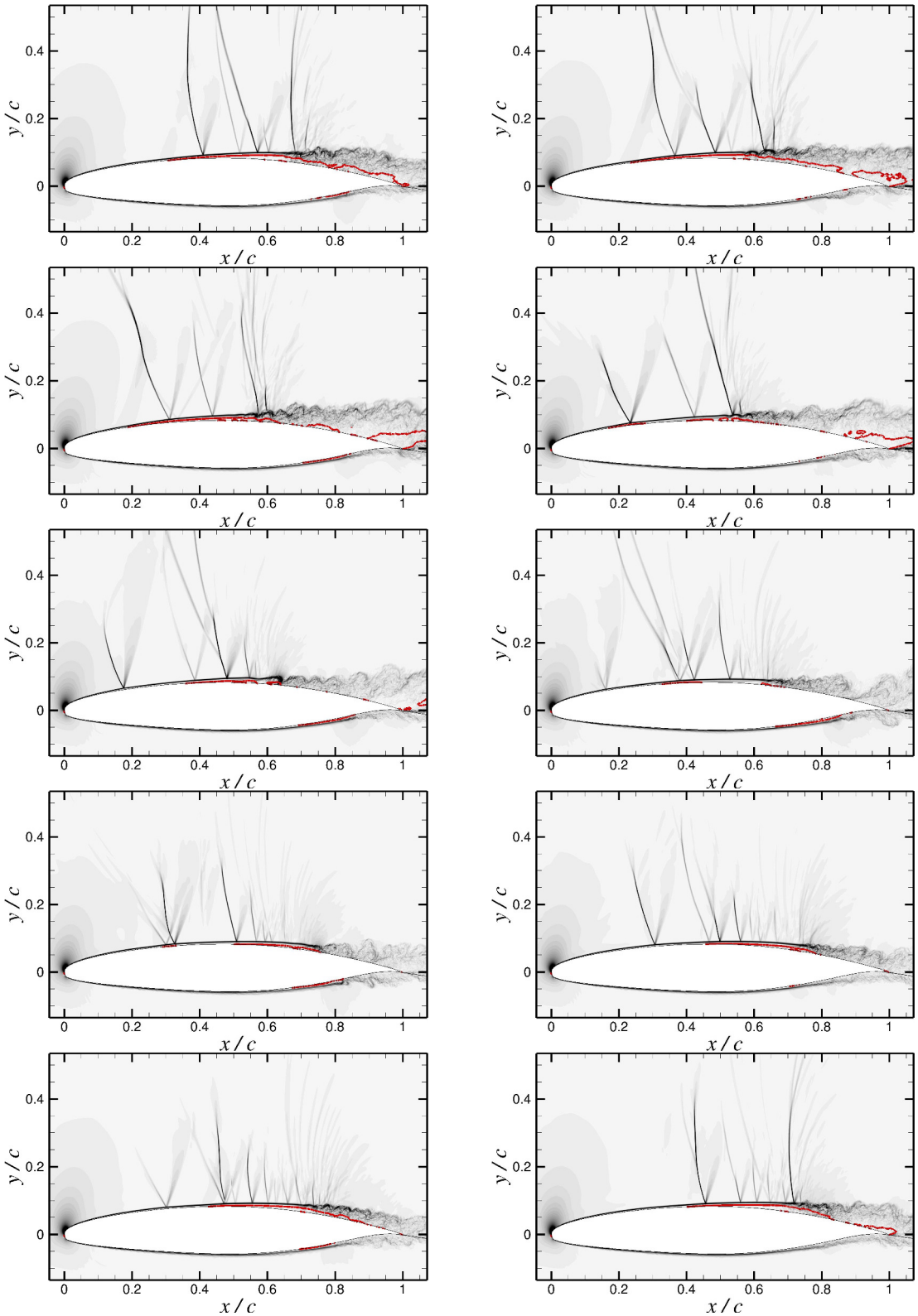

Figure 5.12: *Numerical Schlieren contours within a buffet period at* $M_0 = 0.7$, $Re_c = 3 \cdot 10^5$, $\alpha = 4°$ *(DNS LAM). Instantaneous fields averaged in the span. Red lines:* $U = 0$.

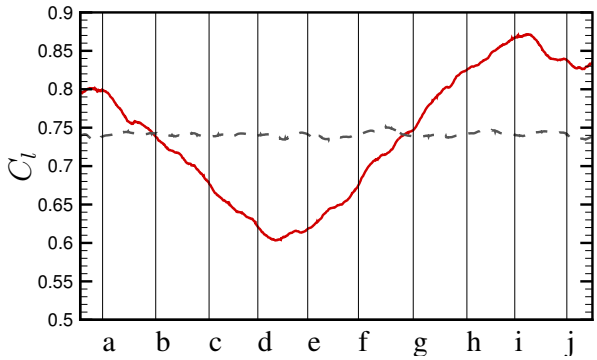

Figure 5.13: *Lift coefficient in a buffet period for the laminar simulation at $\alpha = 4°$. The intersection of the vertical lines with the red curve identify the instants shown in Fig. 5.12. It is also reported for comparison the lift coefficient of the tripped suction side case (dashed line).*

on pressure side, depending on the effective angle seen by the flow near the trailing edge: when the flow is not separated at the trailing edge on suction side, there are more chances that the flow separates on pressure side. Times corresponding to Fig. 5.12 are shown in Fig. 5.13. The figure also shows the lift coefficient of the tripped simulation, for comparison. The laminar, unsteady C_l seems to oscillate around the (statistically) steady one of the tripped simulation. The time denoted with (a) is the figure at the left-top corner of Fig. 5.12. There is a phase delay corresponding to the maximum separation extension and the minimum of the lift coefficient. Separation is better illustrated by looking at the friction coefficient. We show it just for the suction side, in Fig. 5.14. Starting from the first panel of the figure, we see that the separation starting in $x/c \simeq 0.3$ is moving downstream. When the separation point reaches the middle chord, a separation bubble appears also near $x/c \simeq 0.3$ again. Both moves downstream, and another separation bubble appears, this time in the most upstream location where it is detected, in $x \simeq 0.2$. This separation bubbles starts increasing, with the separation continuing to start in $x \simeq 0.2$. Then the bubble merges with the other bubbles, and the separation starting in $x/c \simeq 0.2$ extends almost until the trailing edge, and the separation point starts moving, and the cycle repeats again.

As already stressed, here we do not attempt the same mechanism analysis done in the previous chapter, simply because there is no mean shock. Instead, we plan to perform the same analysis for $\alpha = 7°$, where simulations are run for a longer time span. For $\alpha = 4°$ we just extract some useful informations to be compared with the $\alpha = 7°$ case. We start by computing the spectrum, shown in Fig. 5.15. The left panel shows the premultiplied spectrum, while the right one shows again the lift coefficient, highlighting the temporal range used in the spectrum computation. As abscissa in the spectra figures we use the curvilinear abscissa s, with origin in the trailing edge, and positive variation of it denotes clockwise spatial variation along the airfoil. The leading edge corresponds to $s/c \simeq 1$. So $0 < s/c < 1$ identifies the pressure side, with upstream direction corresponding to positive s variations, while $1 < s/c < 2$ identifies suction side, with downstream direction corresponding

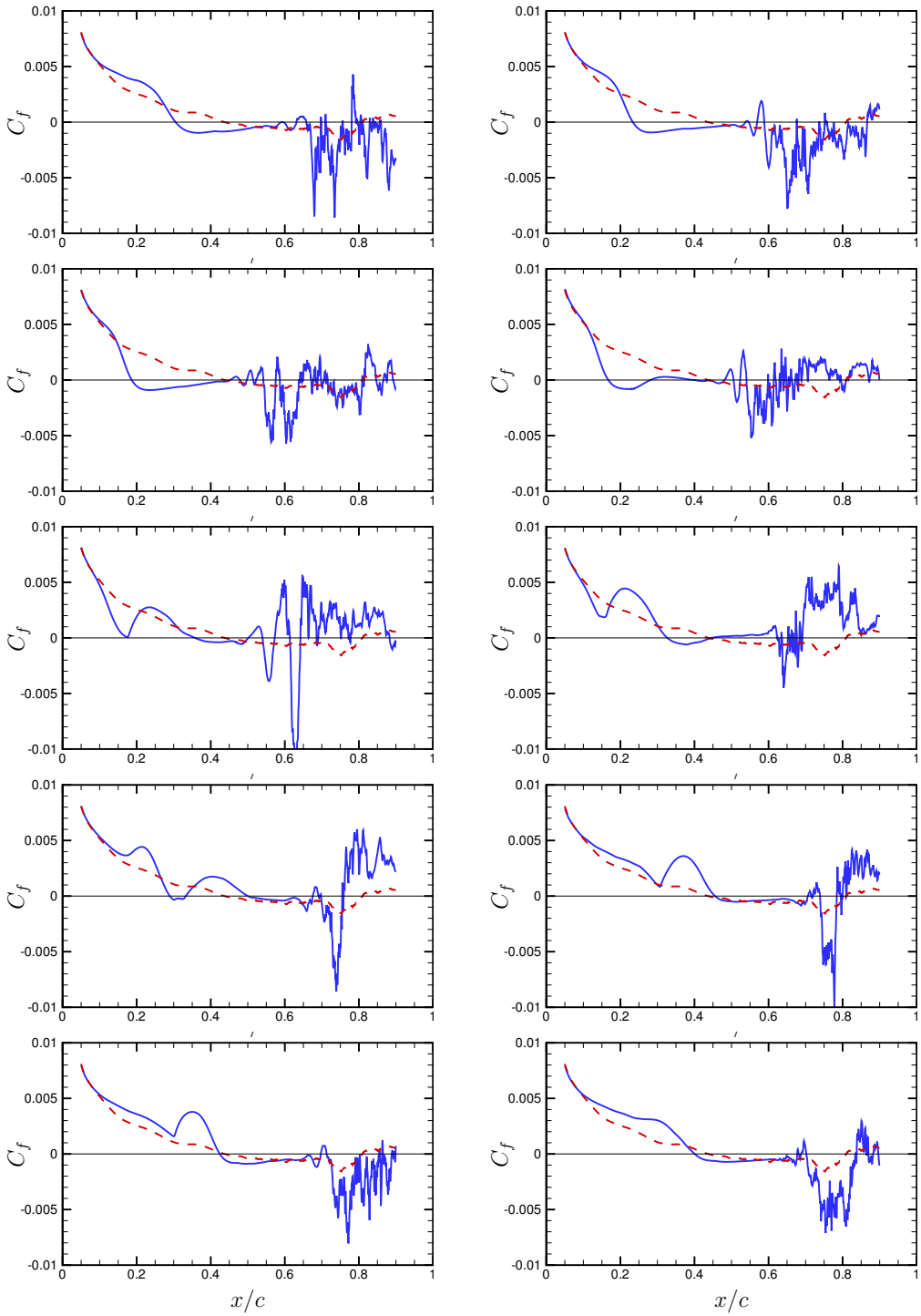

Figure 5.14: *Skin friction coefficients averaged in the span within a buffet period at* $M_0 = 0.7$, $Re_c = 3 \cdot 10^5$, $\alpha = 4°$ *for the laminar simulation. Red lines: time averaged* C_f.

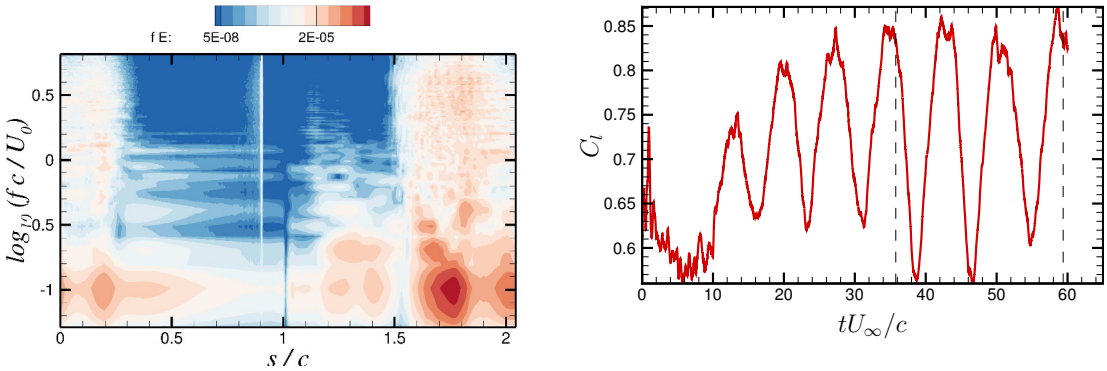

Figure 5.15: *Premultiplied spectrum of wall pressure at various streamwise stations on the suction side for laminar suction side at $M_0 = 0.7$, $Re_c = 3{\cdot}10^5$, $\alpha = 4°$. s is the curvilinear abscissa, as defined in Fig. 5.16. Dashed lines delimit time interval used.*

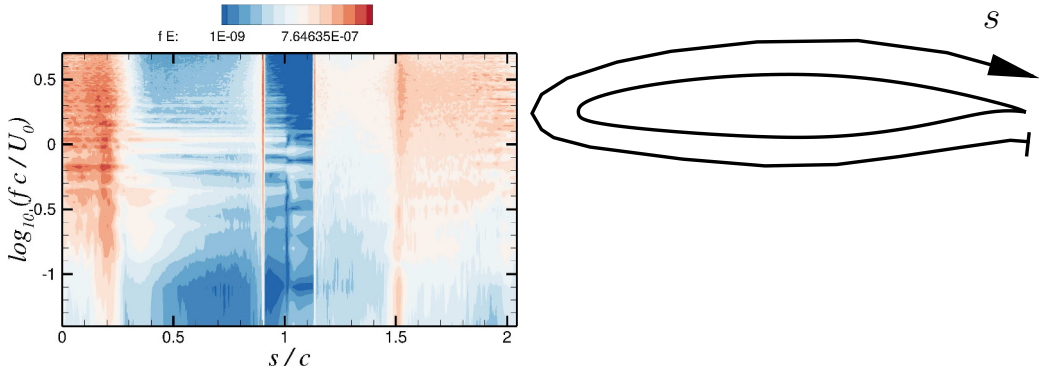

Figure 5.16: *Premultiplied spectrum of wall pressure at various streamwise stations on the suction side for tripped suction side at $M_0 = 0.7$, $Re_c = 3 \cdot 10^5$, $\alpha = 4°$. s is the curvilinear abscissa, as defined in the right panel.*

to positive s variations. Buffet frequencies are dominating the spectrum, with the maximum of the premultiplied spectrum being $St \simeq 0.1$, which may be also used to identify the shock oscillation frequency (Délery and Dussauge, 2009). By comparing the laminar premultiplied spectrum with the corresponding one for the tripped simulation (Fig. 5.16), we may also locate the frequency range which corresponds to the large-scale unsteadiness. In particular, the value $St \leq 0.5$ will be used as a discriminant during the spectral filtering operations. Figure 5.17 shows pressure disturbances signals in different streamwise stations as a function of time, similar to what has also been done by Brouwer (2016). These graphs allow us to gain some insight on disturbances propagation. The curvilinear abscissa s (see right panel of Fig. 5.16) has been used, which permits a spatial periodic extension, and the chosen s interval starts from the leading edge ($s/c \simeq 1$), travel two times around the airfoil, and ends at the trailing edge ($s/c \simeq 2 - 4$). First row corresponds to z averaged unfiltered signals, second row to z averaged low-pass filtered signals, third row to z averaged high-pass filtered signals. Left column corresponds to the laminar suction side, while second column to the tripped one. Also superimposed

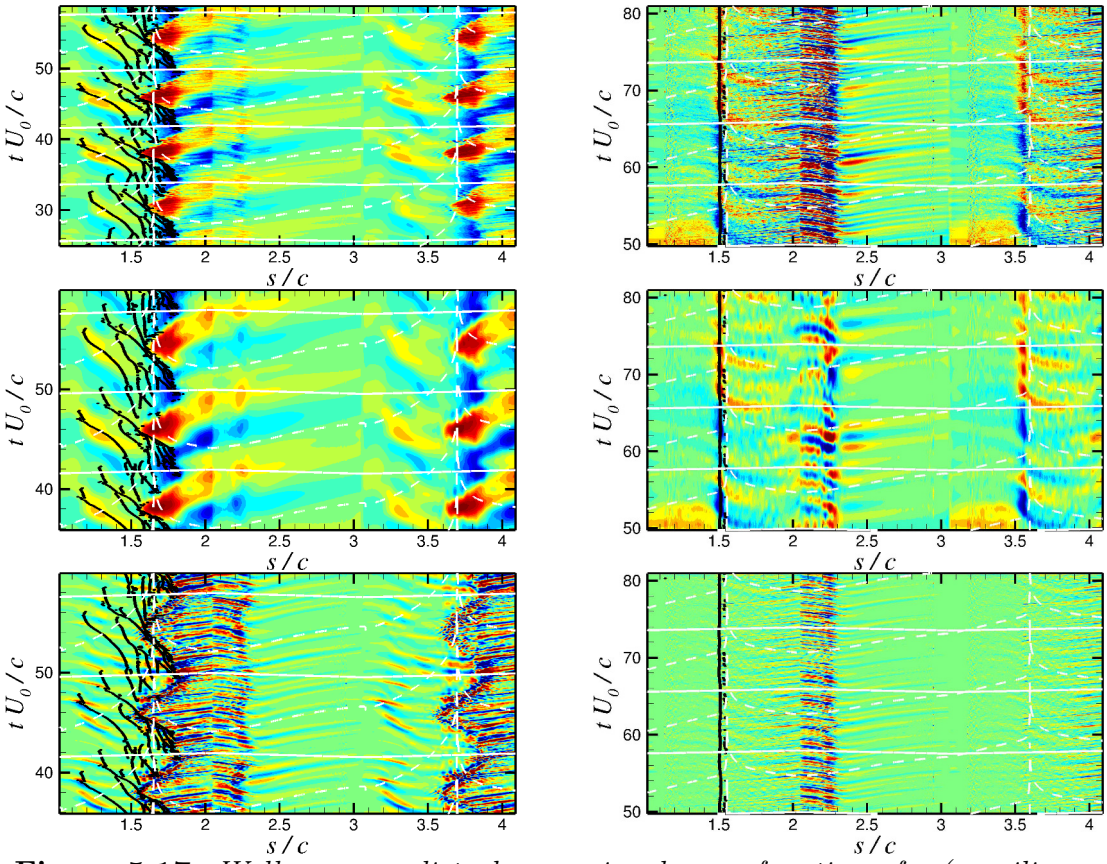

Figure 5.17: *Wall-pressure disturbances signals as a function of s (curvilinear abscissa) and time for laminar simulation (left column) and tripped simulation (right column) at $\alpha = 4°$. Black dots denotes shocks. White lines are representative of acoustic disturbances associated with the mean field. First row: unfiltered signals. Second row: low-pass filtered ($St < 0.5$) signals. Third row: high-pass filtered signals ($St > 0.5$).*

to each panel there are the shock locations (black dots) and the estimated acoustic disturbances path (white lines). Shocks are located by looking at the shock sensor Θ. Assuming a threshold value of $\Theta = 0.99$, one can identify the shocks. The black dots represent approximatively the intersection of the shocks identified this way with the boundary layer edge. Acoustic disturbances paths are evaluated by assuming acoustic velocity estimates based upon one-dimensional results, assuming zero losses. In the laminar case, the shocks are moving only upstream, while in the tripped case the shock is steady. For the tripped simulation, no significant differences exist between filtered and unfiltered fields, with the propagation velocities of pressure disturbances always having the same values. $2 < s/c < 2.3$, which corresponds to $1 > x > 0.7$ on pressure side, shows the clear signature of separation, with disturbances convected towards the trailing edge rather than upstream, as acoustic disturbances, as on the rest of the pressure side. The same happens also for the laminar simulation, even if in this case the separation point shows some time dependence tied to the large-scale motion. The same signature is found on the high-pass filtered signal for the laminar simulation, downstream of the shocks. As shown in the previous chapter, this is linked to the Kelvin-Helmholtz vortex shedding dynamics (and the same is true for the pressure side). This dynamics starts as a consequence of the shock induced separation, as confirmed by the strong correlation with the shock location. On suction side, between leading edge and shocks, a quasi periodic shock waves system is seen, with shocks interacting with each other, and with only a single shock at a time reaching almost the leading edge. The shock trajectory matches well with the positive pressure variations for the low-pass filtered signal. However, similar signature for pressure near the leading edge on suction side are also found in the high-pass filtered signals, which means that upstream propagating high-frequency waves are able to reach the leading edge. These waves must be originated by the shock itself or they must reach the boundary layer from the wall normal direction, with their origin outside the boundary layer itself. More insight can be offered by the cross-correlation. The procedure is the same as the one used in the previous chapter (Fig. 4.13 on page 88), with the solely exception that we vary the point location where the reference pressure signal is taken. Varying the location of the reference signal has very low influence on the outcome of the cross-correlation operations if we consider the laminar case, only having some incidence (especially if we take the reference point near shock induced separation) on the maximum values of the cross-correlation, not on the resulting convection velocities. Figure 5.18 shows the cross-correlations for the low-pass (left panel) and high-pass (right panel) filtered pressure signals for the laminar suction side. The reference signals are taken respectively in $x_{ref} = 0.7$ and $x_{ref} = 0.3$, with the solely reason that correlation appeared to be max in that points. However, as already stressed, the same informations contained in figure could be obtained using any other reference point. The figure shows also the shocks, with the only purpose of comparing the slopes of the curves, and to have a better feeling on which are the shocked regions. An estimate of the propagation velocity of instability waves is attempted with the white line in the left panel. We obtain a value close to the value

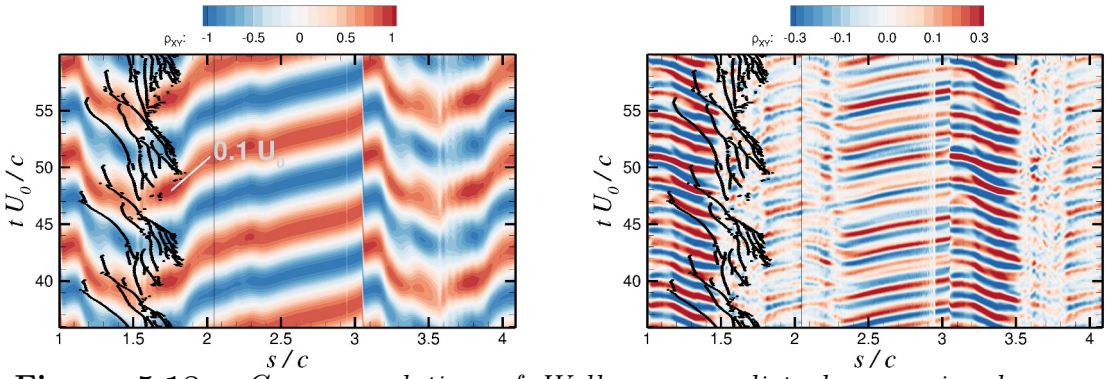

Figure 5.18: *Cross-correlation of Wall-pressure disturbances signals as a function of s (curvilinear abscissa) and time delay for laminar simulation at $\alpha = 4°$. Left column: low-pass filtered signals ($St < 0.5$), $x_{ref} = 0.7$. Right column: high-pass filtered signals ($St > 0.5$), $x_{ref} = 0.3$. Black dots denotes shocks. White line is an estimate of the convection velocity of instability waves downstream of the shock.*

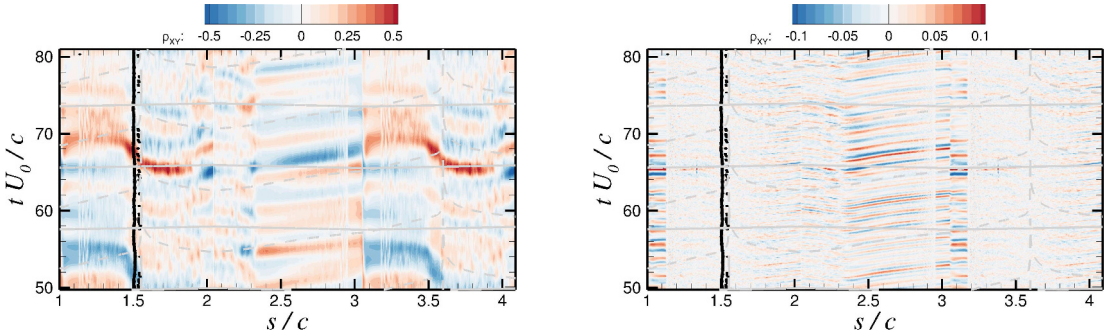

Figure 5.19: *Cross-correlation of Wall-pressure disturbances signals as a function of s (curvilinear abscissa) and time delay for tripped simulation at $\alpha = 4°$. Left column: low-pass filtered signals ($St < 0.5$), $x_{ref} = 0.7$. Right column: high-pass filtered signals ($St > 0.5$), $x_{ref} = 0.3$. Black dots denotes shocks. White line is an estimate of the convection velocity of instability waves downstream of the shock.*

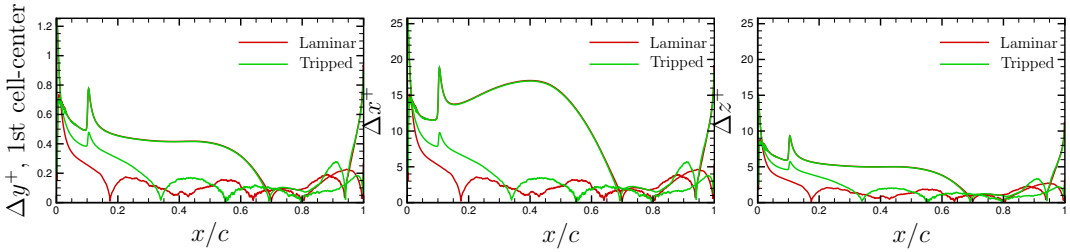

Figure 5.20: *Wall spacing in wall units: distance of the first cell-center from the wall (left column), Δx^+ (middle column) and Δz^+ (right column) at $M_0 = 0.7$, $Re_c = 3 \cdot 10^5$, $\alpha = 7°$.*

obtained in the last chapter, where we used turbulence modeling and considered a higher Re_c and α. Lets focus now on the right panel, describing the high-pass filtered signals. Contours range from -0.3 to 0.3, since the high-frequency waves can be considered as noise for what concerns the correlation, disturbing the signals. However, we can clearly see a strong, regular correlation. In particular, lets focus our attention near $s/c \simeq 3$ (leading edge): looking at the left, we are looking at the downstream direction on pressure side, looking at the right, we are looking at the downstream direction on suction side. The white vertical strip which is visible at the left corresponds to the pressure side trip, which introduces noise, lowering the correlation. We can see that there is a strong correlation near the leading edge of pressure disturbances travelling toward the leading edge both on pressure and on suction sides. This means that the upstream travelling disturbances on suction side are not originated at the shock, but reach the boundary layer from the external flow. Since they refer to frequencies an order of magnitude higher than the large-scale unsteadiness, the shock motion cannot be the direct cause, but they must be the signature of acoustic disturbances circumventing the shock tips. It has been stressed that on pressure side, the upstream communication only happens through acoustic waves. Since the correlation is strong, the disturbances on the two sides near the leading edge must have a common origin, that must be searched at the trailing edge or in the wake. Correlation in the tripped case is much less strong, as shown in Fig. 5.19. The same parameters used for the laminar case are also used for the tripped simulation. There is no additional information provided by correlation: on pressure side, we have acoustic upstream propagation, until the flow undergoes separation, then information is propagated downstream. On suction side, downstream of the shock cannot be traced any downstream propagating disturbance. From the high-pass filtered signals, one can also observe the upstream propagation of disturbances generated by the tripping on suction side.

5.4 DNS at $\alpha = 7°$

Lets now deal with the laminar and tripped simulations at $\alpha = 7°$. In these conditions, buffet is expected for both simulations, as for ILES results. We will see however that the behaviour in the laminar case is much different than the one

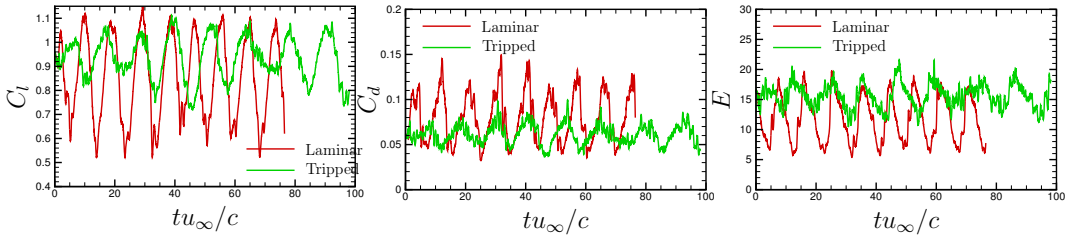

Figure 5.21: *Time history of lift (left column) and drag coefficient (middle column), and aerodynamic efficiency (right column) at* $M_0 = 0.7$, $Re_c = 3 \times 10^5$, $\alpha = 7°$.

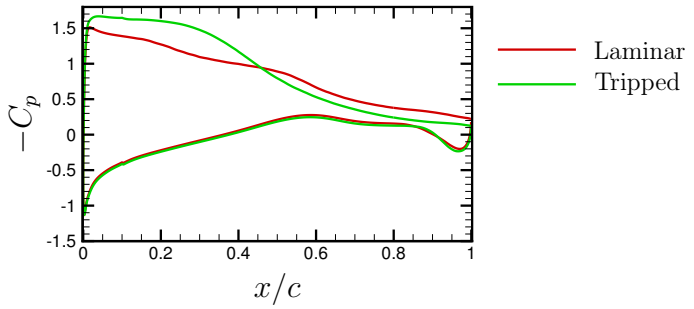

Figure 5.22: *Pressure coefficients of the mean fields at* $M_0 = 0.7$, $Re_c = 3 \cdot 10^5$, $\alpha = 7°$. *Pressure averaged both in the span and in time* ($tu_\infty/c > 13$ *for the laminar case and* $tu_\infty/c > 24$ *for the tripped one).*

provided by laminar ILES. The *a posteriori* check is reported in Fig. 5.20, in terms of wall units. In this case Δy^+ and Δz^+ respect Hosseini et al. (2016) recommendations ($\Delta y^+ < 0.5$, $\Delta z^+ < 5$), while $\Delta x^+ < 10$ is not respected for the first half of the airfoil on pressure side, to save some computational resource, since separation on pressure side is expected to start in the second half, and because we already demonstrated that pressure side does not play a major role in the phenomenon (the effects of disturbances propagating on pressure side are retained, as will be shown by pressure signal analysis). Figure 5.21 shows the temporal behaviour of the two DNS, in terms of lift and drag coefficients, and of aerodynamic efficiency. As can be seen, both simulation behaves as expected, showing buffet. In contrast with ILES results at higher Reynolds number, laminar simulation behaves worse than the tripped one, with larger excursion of the lift coefficient, a higher mean drag coefficient, and with an overall efficiency lower than in the tripped case. Also this time, as will be shown, the laminar simulation presents a system of multiple shocks. Fig. 5.22 shows the mean pressure coefficients of the two DNS. Also in this case, as for the 4° case, on pressure side the two curves almost coincide, whereas they clearly differ on suction side. On the latter, the laminar simulation shows an almost continuous compression, due to the shocks motion which involves the entire suction side such that no mean shock arises, while the tripped simulation only has a limited compression region, corresponding to the mean shock. Figure 5.23 shows friction coefficient (first column), displacement boundary layer thickness (second column) and the incompressible shape factor (third column), both on suction (first row) and

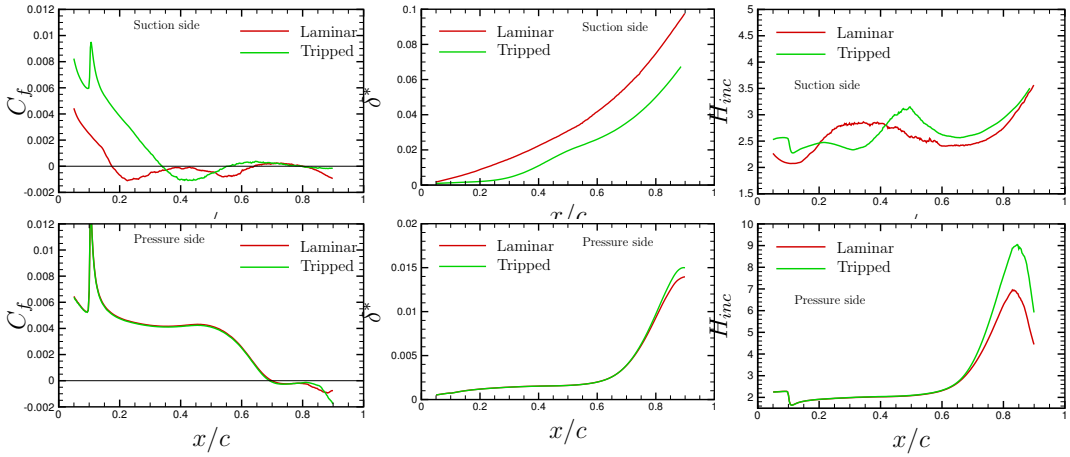

Figure 5.23: *Skin friction coefficient (left column), displacement b.l. thickness (middle column), incompressible shape factor (right column) on suction side (first row) pressure side (second row) at* $M_0 = 0.7$, $Re_c = 3 \cdot 10^5$, $\alpha = 7°$.

pressure (second row) sides. The friction coefficient on suction side for the tripped simulation, and on pressure side for both the simulations, shows a peak at $x_0 = 0.1$, which corresponds to the trip. Focusing first on quantities on suction side, we can see that in the tripped boundary layer case, the mean flow shows only a recirculating bubble for $0.35 < x/c < 0.55$ as a consequence of the shock interaction with the boundary layer, followed by a region of incipient separation and by separation in the region near the trailing edge, for $x/c > 0.8$. The laminar boundary layer has a much higher tendency to separation, which for the averaged flow starts at $x/c \simeq 0.2$ and extends to the trailing edge, with only two regions of incipient separation. As shown by the statistics reported in Fig. 5.23, the separated boundary layer in the laminar case behaves in a more irregular way with respect the tripped case, showing some noise in the region of mild separation at $x/c \simeq 0.4$ and of stronger separation for $x/c > 0.8$. Focusing now on pressure side, also this time the influence of the flow on the upper side of the surface is very low, and concentrated near the trailing edge. Separation at the trailing edge on pressure side shows an opposite behaviour of separation on suction side, with stronger separation for the tripped case than for the laminar one. However, differences in the statistics can be seen only in the separated region. The friction coefficient shows that from $x/c \simeq 0.7$ on, the flow separates, so that the tripping device at this Reynolds number and at this angle of incidence is not so effective. However, there is not a massive separation, since the friction coefficients stay close to zero until $x/c \simeq 0.8$ is reached. The same is also shown by the incompressible shape factor, which does not recover to low values neither near the trailing edge. Figure 5.24 does not show any self-similarity for the laminar case. Figure 5.25 shows the velocity tangential to the wall vs. the wall distance, in plus units. Only the tripped simulation is taken into account in this figure, since on pressure side the results were almost coincident for laminar and tripped cases, while on suction side the laminar simulation is already expected to not follow any log-law. The first row of Fig. 5.25 refers to suction side, while second row refers to

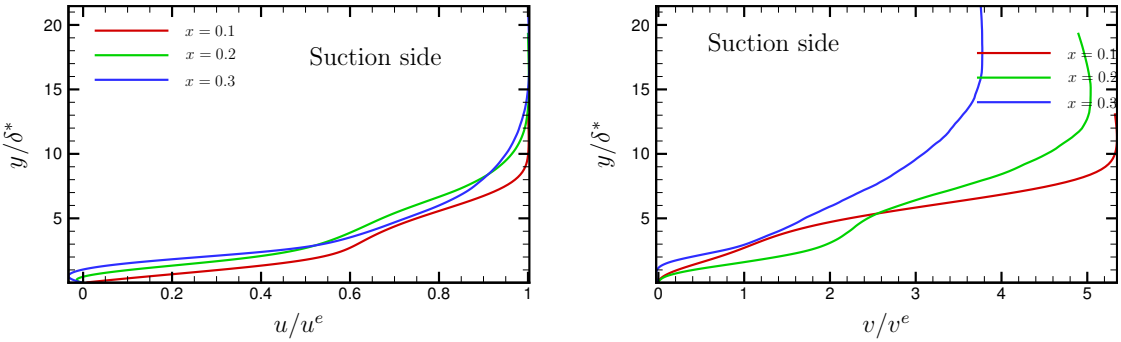

Figure 5.24: *Tangential and normal to the wall velocities on suction side scaled for self-similarity at $M_0 = 0.7$, $Re_c = 3{\cdot}10^5$, $\alpha = 7°$ for laminar case on suction side.*

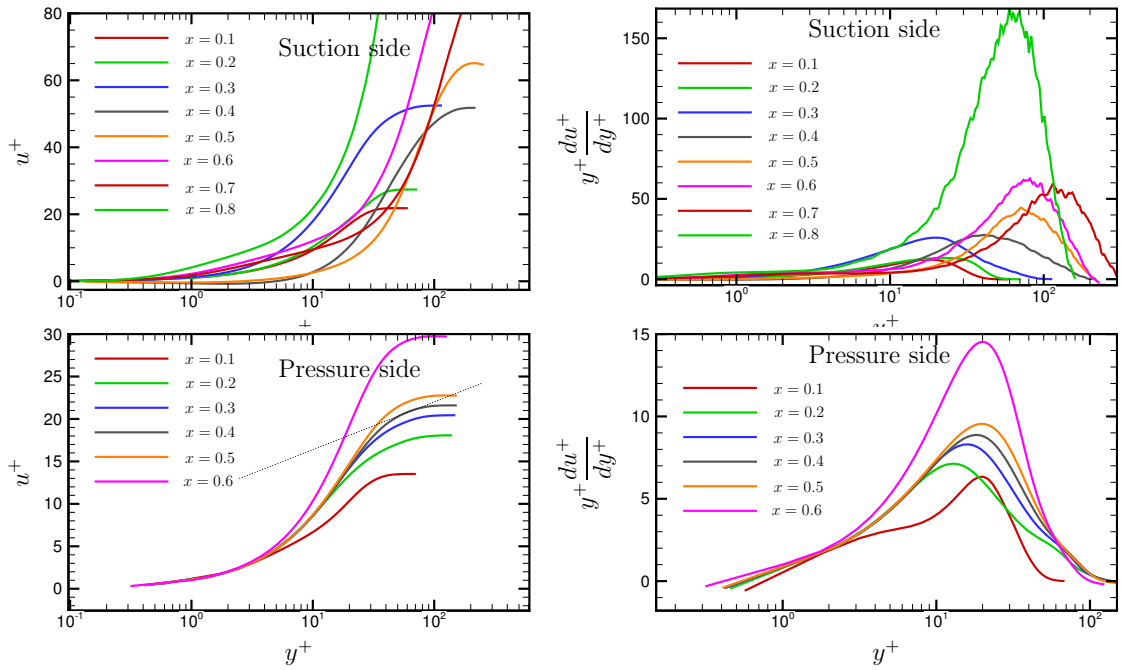

Figure 5.25: *Tangential velocity on pressure side in wall units and a check for the log-law (right) at $M_0 = 0.7$, $Re_c = 3 \cdot 10^5$, $\alpha = 7°$ for tripped boundary layer on suction (first row) and pressure (second row) sides. The black dotted line is the correct slope for the log-law region.*

pressure side. First column shows the tangential velocity in wall units vs. distance from the wall also expressed in wall units. Second column shows a derived quantity which is constant for a logarithmic behaviour of u^+. We can see that there is no well established log-law in this case either, and the same conclusions can be drawn as for the $\alpha = 4°$ case.

5.4.1 Buffet analysis

As can be seen in Fig. 5.26, which shows the dynamics in a buffet cycle for the laminar case through numerical Schlieren, also for $\alpha = 7°$ the flow presents multiple shocks, with a complicated dynamics. This time the shocks dynamics resembles an hybrid type A-C of Tijdeman (1977) classification (Sec. 1.2.5), with the most upstream shock leaving the airfoil, and the most downstream one forming by coalescence of acoustic waves coming from the downstream flow, but with shocks also moving in the downstream direction. Figure 5.26 reports ten frames of a movie we generated and which is here used to describe the dynamics. Referring to the third row-right panel, also using Fig. 5.27 to help identify the separation regions and the nature of the boundary layer, and reading the figures from left to right: the boundary layer separates at $x/c \simeq 0.2$, and the separation extends practically until the trailing edge. At the separation point, compression waves are generated by the external flow deviation, which tend to coalesce to form the former leg (shock A) of a big lambda shock, with the second leg being the well defined shock which reflects on the boundary layer edge at $x/c \simeq 0.45$ (shock B). The laminar boundary layer apparently starts a natural transition downstream of shock B. The same panel also figures another well defined shock, located at $x/c \simeq 0.6$ (shock C) with shocklets in the relative supersonic tongue and on top of it, the latter apparently deriving from coalescence of compression waves coming from the flow downstream. The first lambda shock becomes taller, with shock A moving towards the leading edge, shock B towards the trailing edge, and the triple point moving even more away from the wall. The boundary layer still undergoes transition near shock B. While shock B moves, the shocklets which were located at the top of shock C move towards it, and are still visible in the subsequent panel. Also shock C is moving towards shock B, and with compression waves originating from the transitional boundary layer forms another lambda shock, with the triple point close to the wall. Switching to the sequent panel, the first lambda shock is still continuing the same dynamics, with shock A very close to the leading edge now, with the triple point outside the frame, and with shock B which stops moving to the right, but starts to move to the left after the coalescence with the shocklets. The boundary layer is now transitional also inside the first lambda shock, and the generated waves interact with both shocks B and C. Shock C is no more the second leg of a lambda shock, but merges with shock B in a Mach interaction. Both are moving to the left, with the relative triple point moving at a constant distance from the wall. Meanwhile, shock A becomes weaker and leave the airfoil as waves. Now at the leading edge shocklets appear, originating from the coalescence of compression waves, which in turn originate from the reflection of the

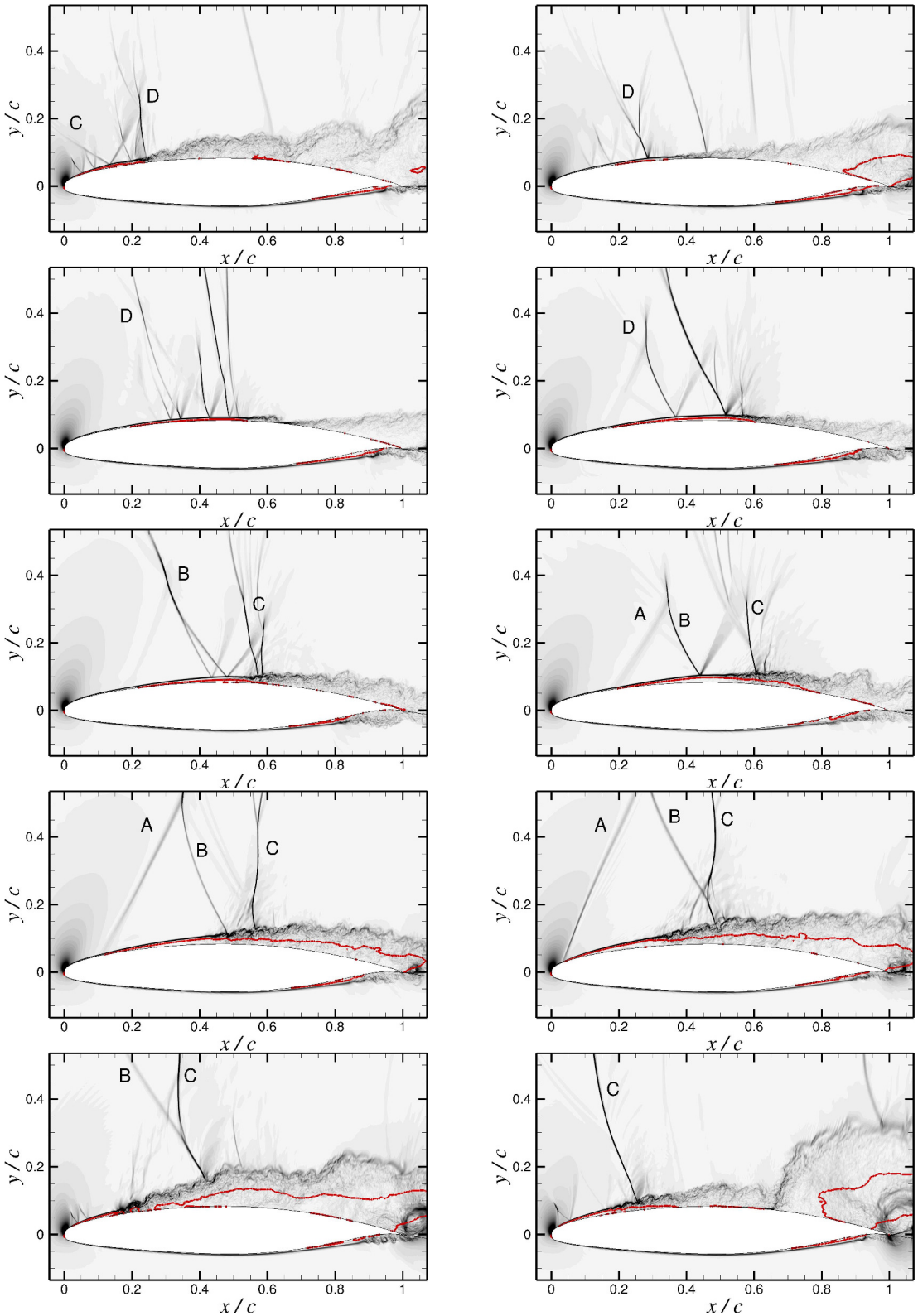

Figure 5.26: *Numerical Schlieren contours within a buffet period at* $M_0 = 0.7$, $Re_c = 3 \cdot 10^5$, $\alpha = 7°$ *(DNS LAM). Instantaneous fields averaged in the span. Time increase from left to right. Red lines:* $U = 0$.

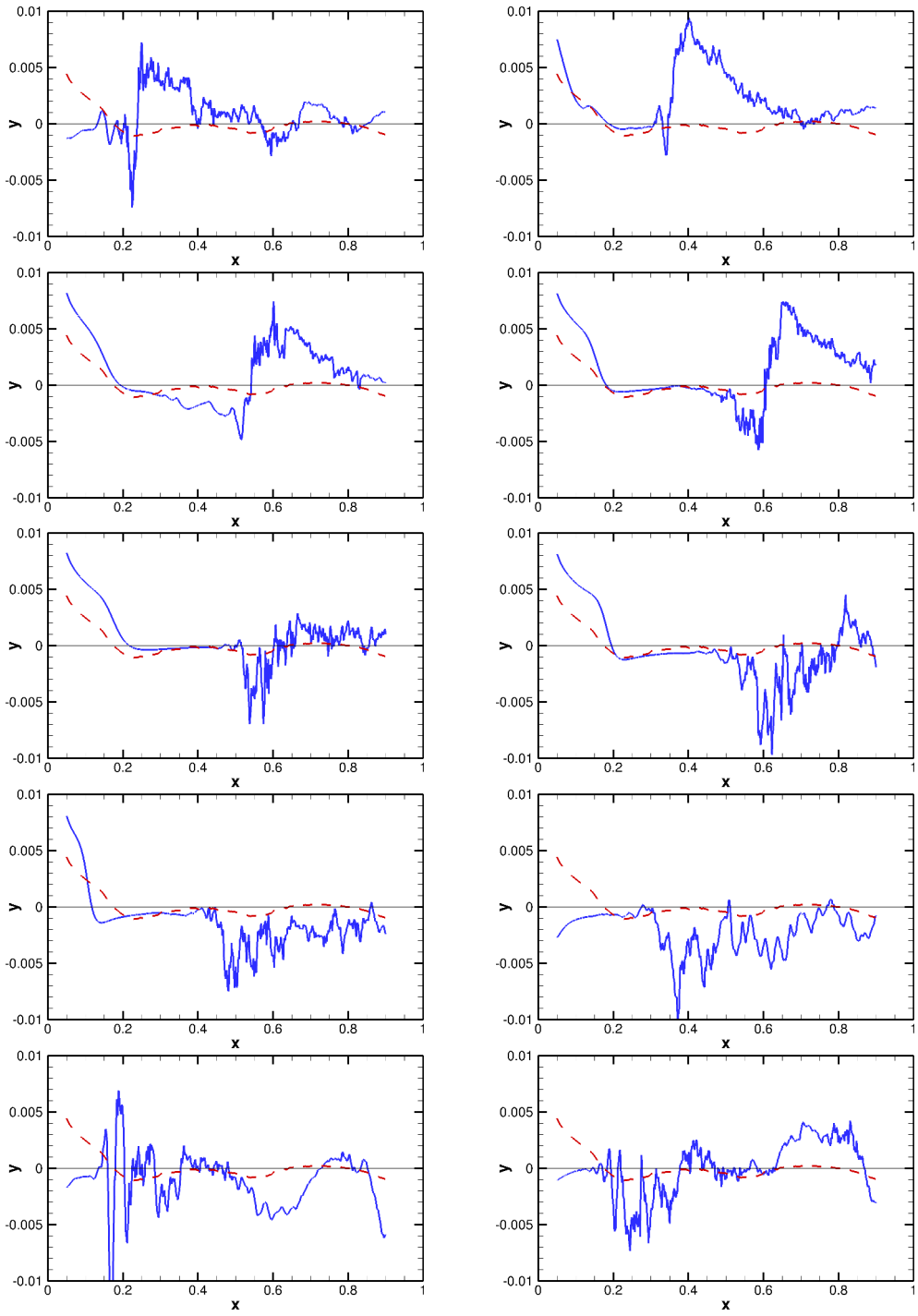

Figure 5.27: *Skin friction coefficients averaged in the span within a buffet period at $M_0 = 0.7$, $Re_c = 3 \cdot 10^5$, $\alpha = 7°$ for the laminar simulation. Time increases from left to right. Red lines: time averaged C_f.*

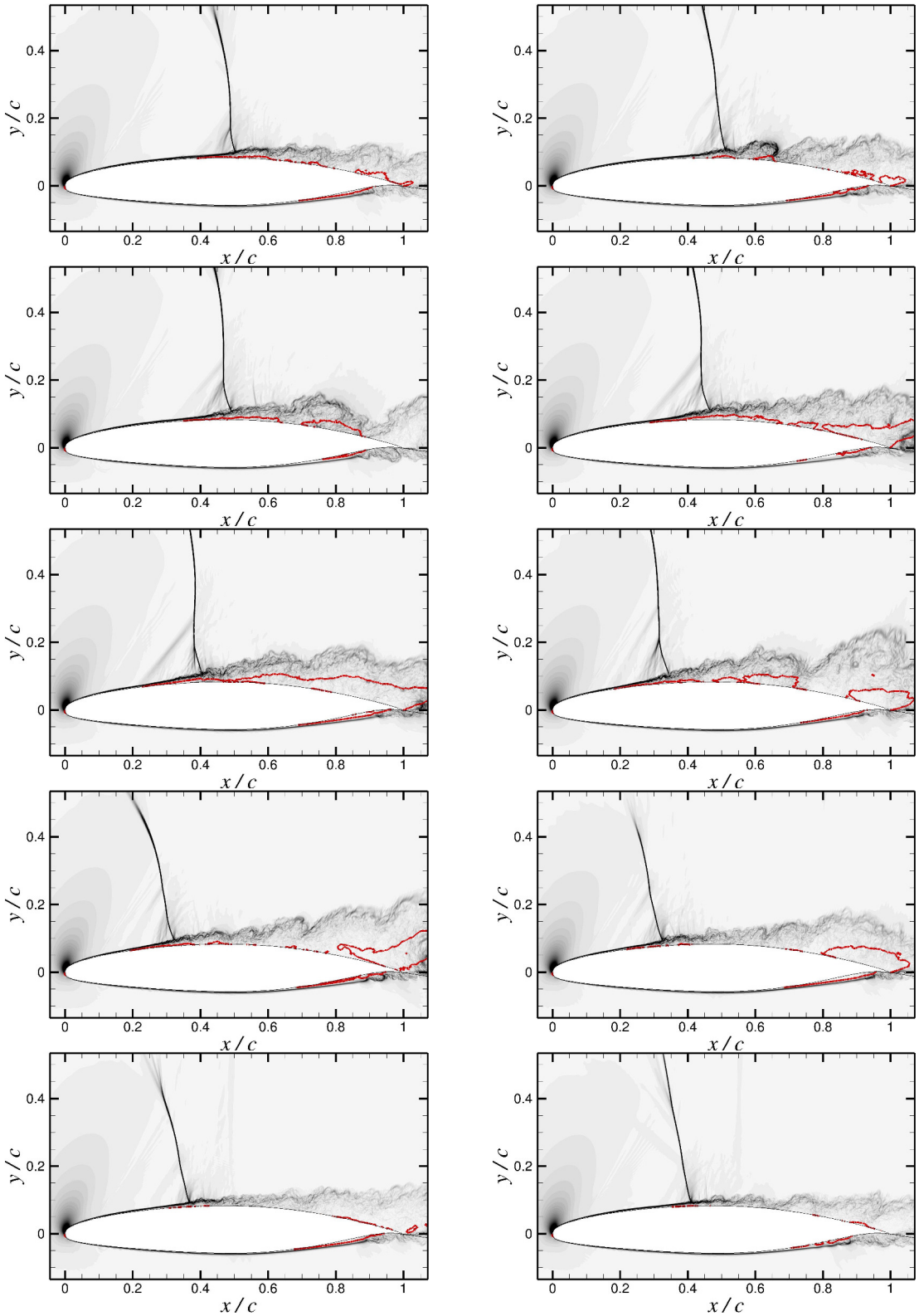

Figure 5.28: *Numerical Schlieren contours within a buffet period at* $M_0 = 0.7$, $Re_c = 3 \cdot 10^5$, $\alpha = 7°$ *(DNS TRIP). Instantaneous fields averaged in the span. Time increases from left to right. Red lines:* $U = 0$.

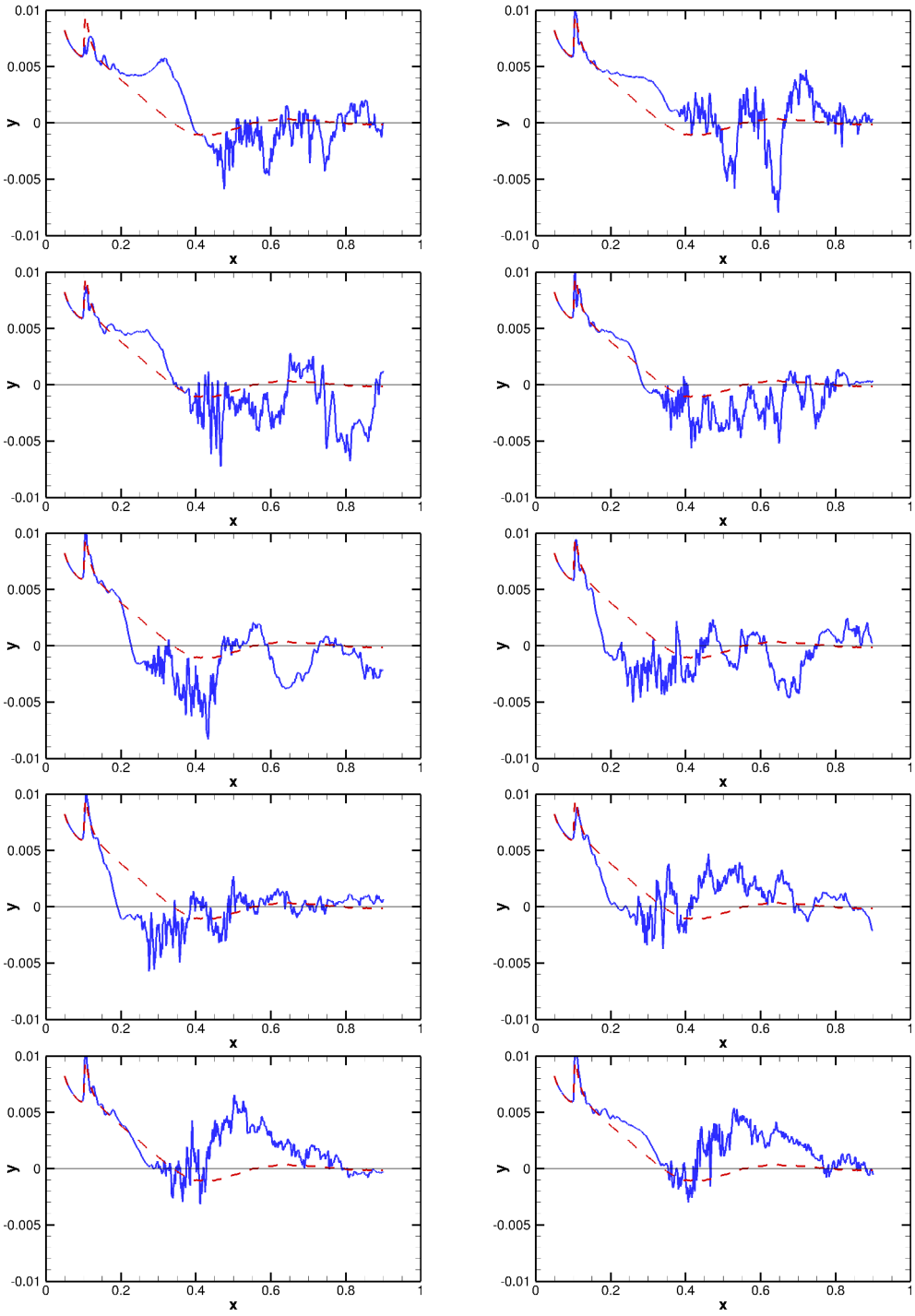

Figure 5.29: *Skin friction coefficients averaged in the span within a buffet period at $M_0 = 0.7$, $Re_c = 3 \cdot 10^5$, $\alpha = 7°$ for the tripped simulation. Red lines: time averaged C_f. Time advances from left to right.*

expansion waves at the leading edge. This shock train is moving in a non-monotone direction, but basically is moving to the right. Now the transition region is at the middle of the new shocklets and shock B, and generates a new coalescence shock, which interacts with shock B, weakening it. Shock B then leaves the airfoil as waves, while the new shock merges with shock C. Other shocklets are generated by the transitional boundary layer behind shock C, and are moving to the left. Of the original shocks, only shock C survived, and separation is concentrated in its neighborhood. The perturbations of the shear layer have traveled downstream, and the strongest perturbations at the trailing edge are now visible. Those perturbations are very intense, and flow with positive vorticity is also entrained on suction side from pressure side. Such perturbations generates a strong acoustic field, with also a new coalescence shock, which propagates in the leading edge direction. This occurs when the shear layer is in its farthermost location from the wall in the trailing edge region. From Fig. 5.27, we can also see that this scattering is not related to separation, but to the shear layer dynamics, which is in phase with the large scale motion. This led us think that the downstream instability waves associated with the shock motion are the signature of the shear layer low-frequency dynamics, which is the one which affects the acoustic production at the trailing edge. The acoustic waves then interact with the shock both to increase the sound pressure level in its aft part, as depicted by Hartmann et al. (2013), and also circumventing the shocks and penetrating the sonic region, being also able to reach the shear layer in front of the shock. Returning to the flow description: Shock C is still moving to the left, and it is now leaving the domain, weakened by passing through the low-pressure region at the leading edge. In the top-left panel it is still possible to see a part of shock C, with a much higher inclination, at $x/c \simeq 0.15$. When it is leaving the airfoil, separation starts at the leading edge, and ends at the foot of a new coalescence shock (shock D), visible too in the top-left panel at $x/c \simeq 0.25$. Shock D starts moving at the right, together with the shock train formed previously at the leading edge. Meanwhile, weak shocks produced by the strong disturbances at the trailing edge are now located in the middle between trailing edge and shock D. When they start to interact, flow is already separated again on most of the airfoil suction side. Similar to the flow description depicted by Hartmann et al. (2013), the strongest modification happens at the tips of the shocks, with the foot of shock C which is still moving to the right, while its tip to the left. Here a complicated interaction starts, which results in the flow configuration visible in the second row-right panel of Fig. 5.26, where shock D is the shock to the left, still moving to the right, and a new shock at the right, formed by the coalescence of the strong disturbances previously formed at the trailing edge, which is moving to the left. The merging of this two shocks produces again shock B. Some of the strong perturbations which contribute to produce shock B continue travelling to the left, and are seen to reach the shear layer between shock A and B. Then the cycle starts again.

Times corresponding to Fig. 5.26, 5.27, 5.28, 5.29 are shown in Fig. 5.30. The time denoted with (a) is the figure at the left-top corner of the figures.

Now we attempt the same description for the tripped case, as can be seen in

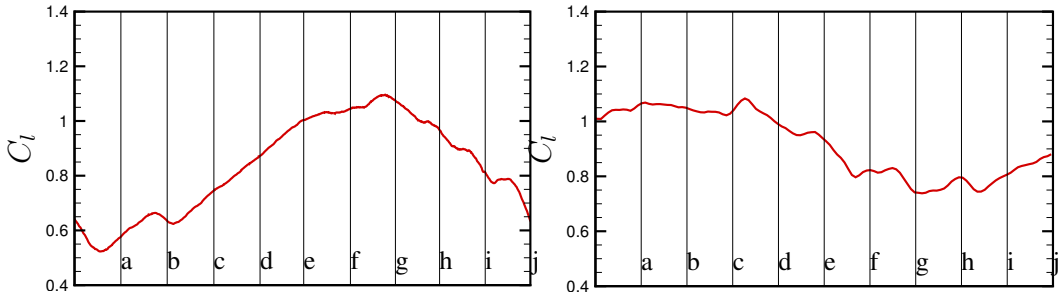

Figure 5.30: *Lift coefficient in a buffet period for laminar (left) and tripped (right) simulations at $\alpha = 7°$. The intersection of the vertical lines with the curves identify the instants shown in Fig. 5.26, 5.27, 5.28, 5.29.*

Fig. 5.28 and 5.29, starting again from the third row-right panel. The flow structure is simpler this time, with only one shock which undergoes a type A buffet. The shock is close to its most upstream position and the shear layer at the trailing edge is at its farthermost distance from the wall. As for the laminar case, the strongest disturbances at the trailing edge are produced now. Strong, almost discrete, pulse are generated close to the trailing edge. When these waves are produced, the shock is still moving to the left. When the shock is in its most upstream position, these waves have not yet reached the shock, which is however reached by weaker waves which are anyway produced downstream. These weaker waves are also capable of circumventing the shock tip and interact with the shear layer. The shock starts moving to the right, and a first strong pulse reaches its tip. Each pulse interacting with the shock during its downstream motion tends to coalesce behind the shock, increasing their strength, and then tends to circumvent the shock tip, with part of the pulse reaching the front of the shock. Strong waves entering this supersonic region are seen propagating towards the wall (shear layer) when the shock is moving downstream, while during the upstream motion of the shock, much weaker perturbations reach the wall, both because the strong disturbances are already gone, and because the shock tip gets further away from the wall. As such, it appears that the model depicted by (Hartmann et al., 2013), with the whole shock reacting to strong perturbations to its tip, may explain the shock movement. Such a feedback mechanism would not involve non-linear mechanisms to start, and would agree with the global instability results of Crouch et al. (2009).

To understand what is the frequency range associated with the large-scale motions, we compute the wall-pressure premultiplied spectra for the laminar and the tripped simulations. The results are shown in Fig. 5.31, which also shows the initial time used for the spectra computation, represented by the dashed lines in the lift coefficients, also shown in figure. The left column refers to the laminar simulation, while the right one to the tripped suction side. Again, as abscissa in the spectra figures we use the curvilinear abscissa s, with origin in the trailing edge, and positive variation of it denotes clockwise spatial variation along the airfoil. The leading edge corresponds to $s/c \simeq 1$. So $0 < s/c < 1$ identifies the pressure side, with upstream direction corresponding to positive s variations, while $1 < s/c < 2$ identifies suction

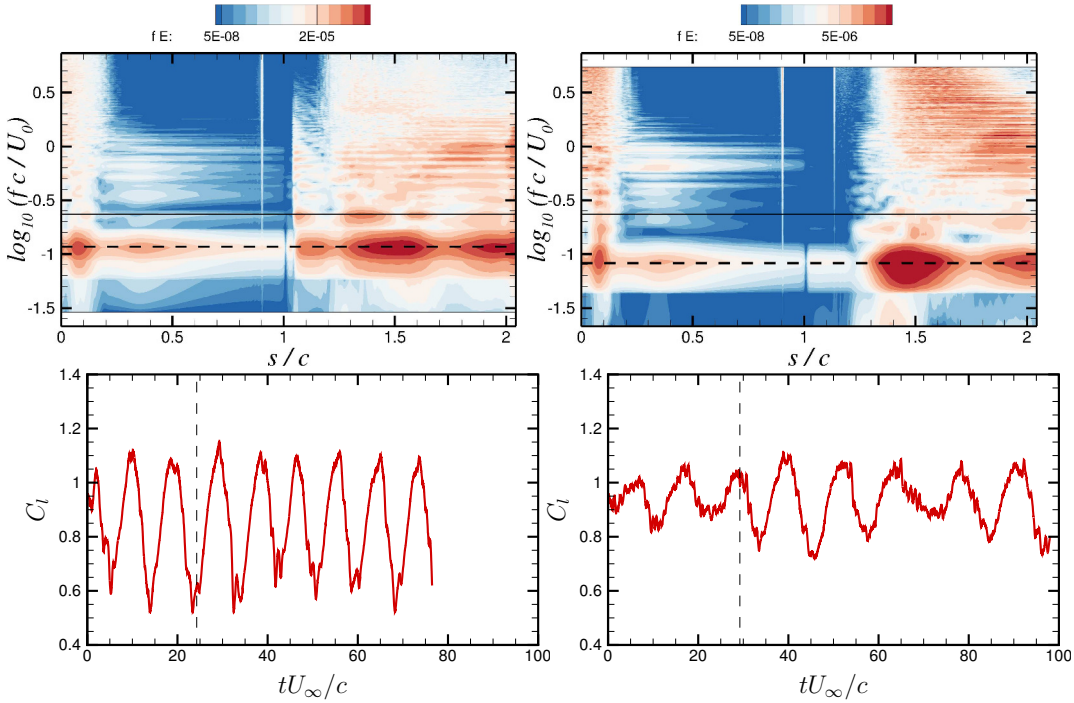

Figure 5.31: *First row: premultiplied spectrum of wall pressure at various streamwise stations. Dashed lines identify buffet frequency as obtained by C_l spectra. Solid lines are the cutoff frequency used in the low-pass filtering procedures. Second row: lift coefficients, where dashed lines delimit time interval used. Left column: laminar suction side. Right column: tripped suction side. $M_0 = 0.7$, $Re_c = 3 \cdot 10^5$, $\alpha = 7°$.*

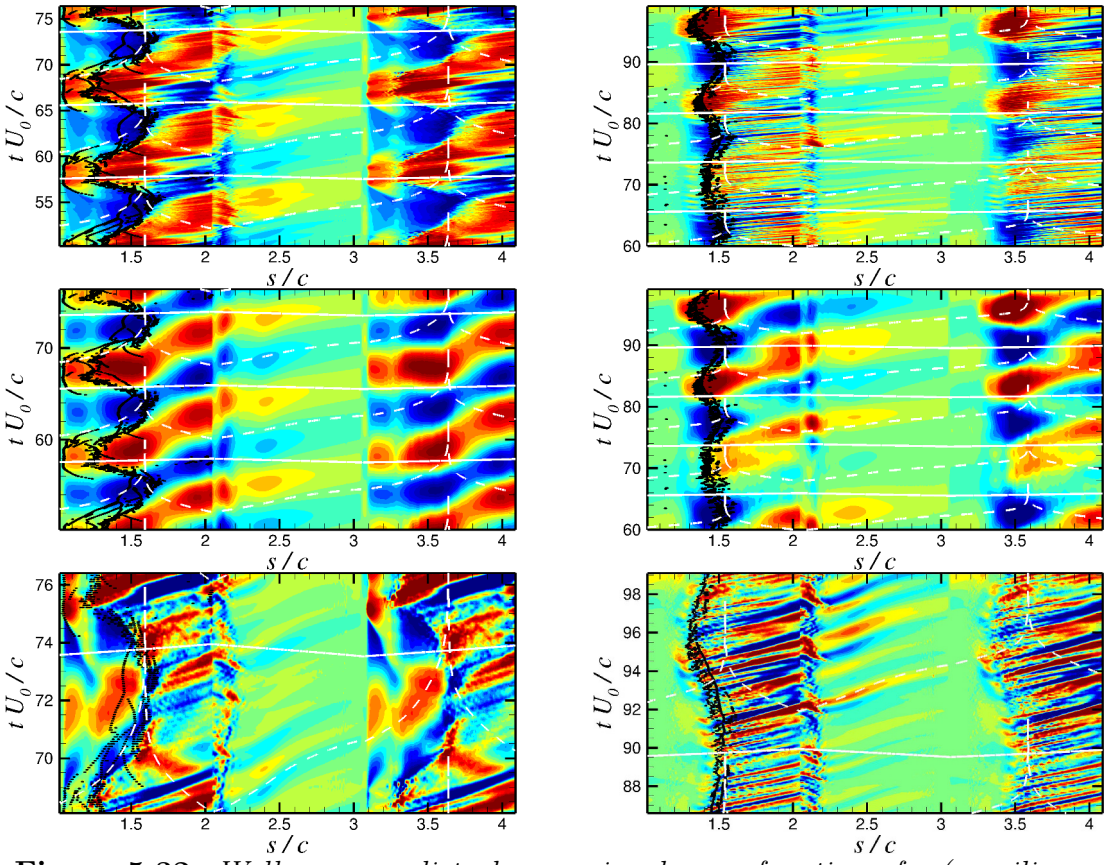

Figure 5.32: *Wall-pressure disturbances signals as a function of s (curvilinear abscissa) and time for laminar simulation (left column) and tripped simulation (right column) at $\alpha = 7°$. Black dots denotes shocks. White lines are representative of acoustic disturbances associated with the mean field. First row: unfiltered signals. Second row: low-pass filtered ($St < 0.19$) signals. Third row: high-pass filtered signals ($St > 0.19$).*

side, with downstream direction corresponding to positive s variations. The black dashed lines in the spectra denotes the buffet frequency as obtained by computing the lift coefficient spectra, $St_{lam} = 0.12$ and $St_{trip} = 0.08$. The figure also shows the cutoff frequency used in the low-pass filtering procedures, represented by solid lines. In fact, the buffet low-frequency range is all contained below the solid lines in both cases.

Figure 5.32 shows pressure disturbances signals in different streamwise stations as a function of time. The curvilinear abscissa has been used which permits a spatial periodic extension, and the chosen interval starts from the leading edge ($s/c \simeq 1$), travel two times around the airfoil, and ends at the trailing edge ($s/c \simeq 2 - 4$). First row corresponds to z averaged unfiltered signals, second row to z averaged low-pass filtered signals, third row to z averaged high-pass filtered signals. Left column corresponds to the laminar suction side, while second column to the tripped one. Also superimposed to each panel there are the shock locations (black dots) and the estimated acoustic disturbances path (white lines). Shocks are located by

looking at the shock sensor Θ just as explained when dealing with the simulation at $\alpha = 4°$. The unfiltered signals carry information at the different frequencies, however the dominant behaviour is brought by low-frequency information. Looking at the low-pass filtered signals, the two simulations share similar features downstream of the shocks, with coherent pressure disturbances propagating downstream to the trailing edge. The strength of these disturbances is related to the shock movement amplitude. As such, the shocks must be seen as the source of these disturbances, which affect the shear layer dynamics, as discussed in the description of Fig. 5.26 and 5.28. As can be seen, the stronger pressure disturbances are produced when the shocks move upstream, and reach the trailing edge when the shock is in its most downstream position. As shown before, when the shock moves upstream, the shear moves away from the wall. Hence when these strong disturbances reach the trailing edge, the distance from the wall of the shear is maximum, leading to the strongest acoustic production. In the laminar case, there is a well defined shock pattern, which during the upstream motion corresponds to shock C. However, as described before, this pattern is not representative of a unique well defined shock, but is the result of a complex interaction between shocks and waves. However, the resulting shock motion causing the pressure disturbances is surprisingly well defined. The same comments hold true for the tripped simulation, even if in this case there is a single well defined shock, as shown by Schlieren visualizations. On pressure side, the dynamics does not offer any significance difference with respect the case at $\alpha = 4°$, with the great part of pressure side only affected by acoustic disturbances, with the exception of the separation region near the trailing edge, which reacts to the pressure disturbances reaching the trailing edge. As shown when describing the dynamics through Schlieren visualizations, separated flow from pressure side is entrained at the trailing edge on suction side as the strongest disturbances reach the trailing edge, and contribute to the generation of even wider disturbances. Looking at the high-pass filtered signals for the tripped simulation, we can see again the Kelvin-Helmholtz instability signature downstream of the shock, and on the separation region on pressure side. Also, in front of the shock are seen perturbations to the boundary layer coming from the external flow, as depicted for the laminar simulation at $\alpha = 4°$, and as will be shown by looking at the correlation. These disturbances appear to propagate mostly in the upstream direction, but also to interact with the shock, modulating the Kelvin-Helmholtz instability. The same does not hold true for the laminar simulation this time, with the high frequency disturbances at the trailing edge which are associated with the shocks located in that area, as can be seen in the bottom-left panel, focusing around time $tu_\infty/c \simeq 74$: the line dividing the negative and positive disturbances appear to be generated by coalescing waves which form the shock visible in the most upstream location. In the region comprised between this shock and the main shock, there is yet another dynamics, apparently associated with the boundary layer detachment (red patch visible at time $tu_\infty/c \simeq 72$, which follows the acoustic white dashed line). Behind the main shock, it also seen the Kelvin-Helmholtz signature, again, but this time also upstream propagating disturbances are seen, faster then the acoustic disturbances, and which may be the signature of

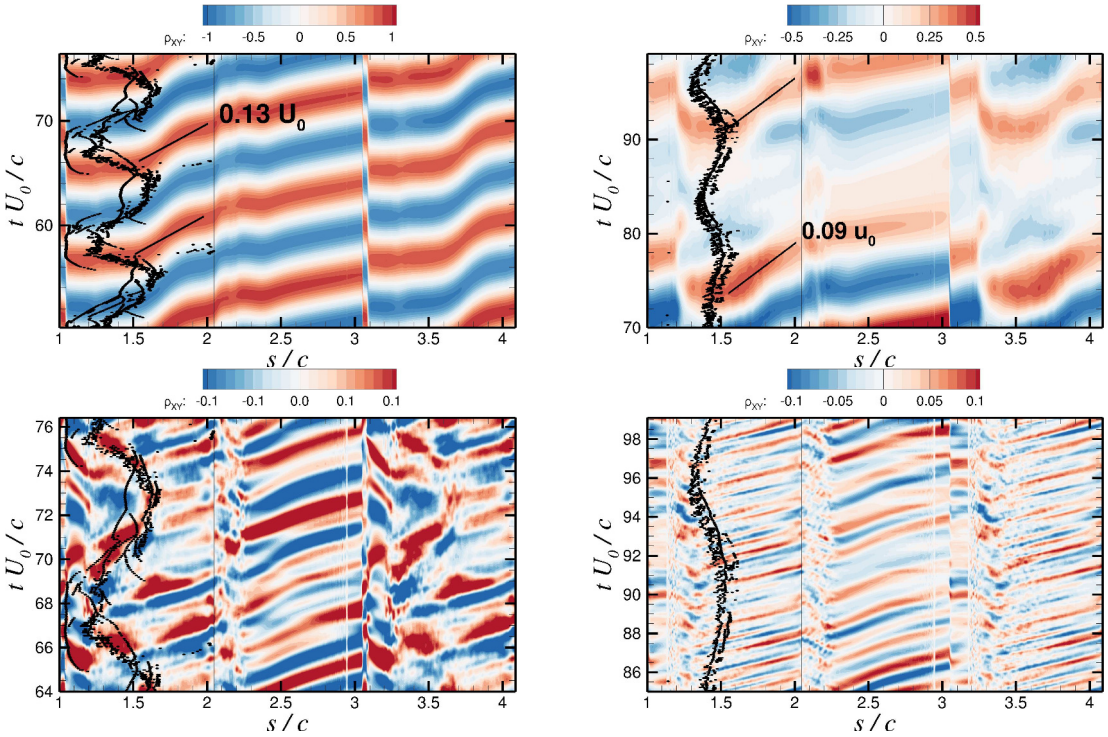

Figure 5.33: *Cross-correlation of wall-pressure disturbances signals as a function of s (curvilinear abscissa) and time delay for laminar (left column) and tripped (right column) simulations at $\alpha = 7°$. First row: low-pass filtered signals ($St < 0.23$), $x_{ref} = 0.7$. Second row: high-pass filtered signals ($St > 0.23$), $x_{ref} = 0.7$. Black dots denotes shocks. Solid black lines are estimates of convection velocities of instability waves downstream of the shock.*

external undetected shocks which are forming in the trailing edge region.

More insight can be offered by the cross-correlation. The procedure is the same as the one used previously (Fig. 4.13 on page 88). Figure 5.33 shows the cross-correlations for the low-pass (top row) and high-pass (bottom row) filtered pressure signals for the laminar (left column) and tripped (right column) suction side. The reference signals are taken in $x_{ref} = 0.7$, with the only reason that correlation appeared to be high in that points. However, as previously stressed, the same informations contained in figure could be obtained using any other reference point. The figure shows also the shocks, with the only purpose of comparing the slopes of the curves, and to have a better feeling on which are the shocked regions. An estimate of the propagation velocity of instability waves is attempted with the black solid lines for the low-pass filtered signals. The convection velocities appear to share the same order, irrespectively of the incoming boundary layer nature and of the incidence angle. Also, the value is close to that obtained with turbulence modeling at a higher Re_c. The high-pass filtered signals do not offer new, additional informations. Correlations offered the downstream propagation velocities of the instability waves. We can then try to use again the geometrical acoustics method to find the acoustic path in the mean field.

5.4.2 Geometrical acoustics

Here we apply geometrical acoustics again, as done in the ILES case. Geometrical acoustics gives an idea of which the path of the acoustic disturbances should be. It only works for high-frequency sound waves, but we stressed already that the instability waves only generate high-frequency scattering at the trailing edge. As such geometrical acoustics is an appropriate tool in this case. The inconvenient is that we apply it to the mean field, and each time the mean field differs considerably from the instantaneous one, the acoustic path we find has no meaning. This means that this approach cannot be used in the description of the acoustic propagation properties for the laminar incoming boundary layer, since the flow structure is very complicated, and mean and instantaneous fields differ considerably. However, when we described the shock dynamics for the tripped case, we outlined that the most energetic acoustic disturbances reach the shock when it is close to its mean position during its downstream motion. As such, we expect the geometrical method to be reliable enough to understand where is the feeding region of the acoustic disturbances. As shown in Fig. 5.34, the method already employed on the

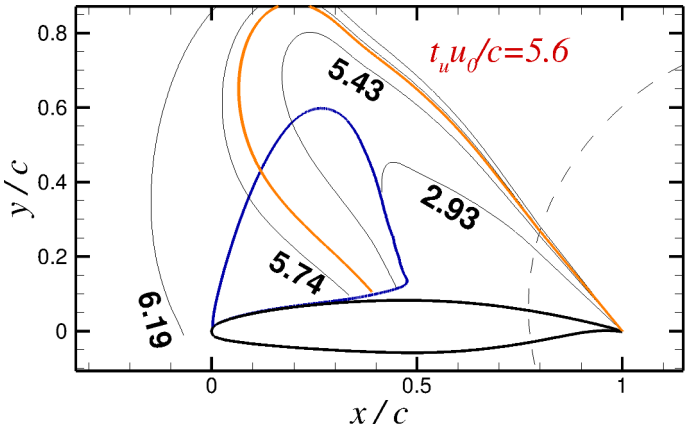

Figure 5.34: *Acoustic rays as obtained for the tripped simulation using the mean field.*

simulations run with turbulence modeling at a higher Reynolds number, predicts again the same interaction region between acoustic waves and shock, with acoustic waves circumventing the shock tip. In fact, as done in the ILES case, we assume that the buffet period is given by the sum of the time needed by the instability waves to reach the trailing edge, plus the time needed by the acoustic waves to reach the shock. Assuming known the buffet period - the inverse of the frequency as obtained by lift coefficient spectrum ($St = 0.083$) - and the downstream travel time - distance between mean shock (located at $x/c = 0.42$ as obtained by the maximum of the wall-pressure RMS) over downstream convection velocity $u_d/u_\infty = 0.09$ - one can retrieve the travel time needed by the acoustic disturbances to reach the shock, obtaining

$$t_u u_\infty / c = 1/0.083 - (1. - 0.42)/0.09 = 5.6$$

This time corresponds to the red acoustic ray depicted in Fig. 5.34. We can see again that Hartmann et al. (2013) model is the one which appears to be closer to this result. The picture also suggests that the interaction region between shock and acoustic waves may be the front of the shock. However, considering that the main field is anyway something different than the instantaneous fields, this figure cannot be used to prove that, and should only be used to support Hartmann et al. (2013) flow picture.

Chapter 6

Buffet control

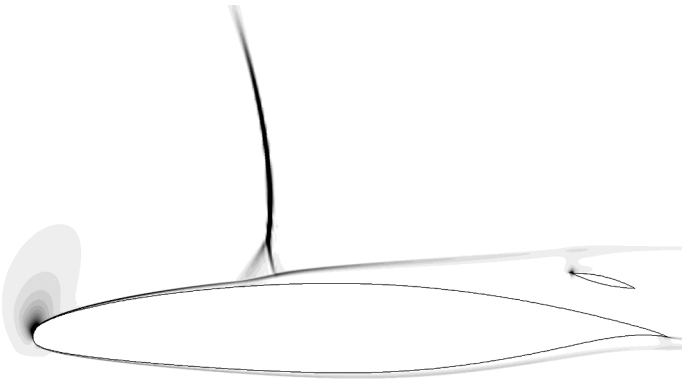

Figure 6.1: *Sketch of the passive control device.*

The aim of this chapter is the development of a new, passive control strategy. In the previous chapters we have shown that the acoustic feedback loop mechanism gives a picture which is consistent with all of our simulations. It describes buffet as being composed of two separate patterns: i) eddies originating at the shock foot and propagating towards the trailing edge, ii) acoustic waves originating at the trailing edge and propagating towards the shock. The novel passive control device tries to act on both the buffet building blocks. The design is similar to LEBU (Large-Eddy Break-Up), with a thin circular-arc airfoil placed on suction side. A sketch is visible in Fig. 6.1. Placing the device between trailing edge and shock, on suction side, it may have a twofold beneficial effect: i) breaking the eddies propagating towards the trailing edge, ii) manipulating the acoustic field originating at the trailing edge.

6.1 Numerical implementation

The LEBU device is introduced as a cut of the domain, as can be seen in Fig. 6.2. Thanks to this approach, we can avoid the use of a multi-block code, since from the cell-center perspective there is no discontinuity introduced by the device (we have a single row of cell-centers both at the top and at the bottom of LEBU, as in the

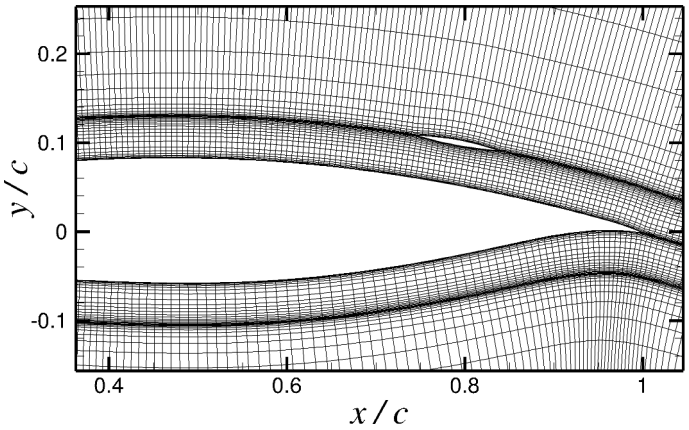

Figure 6.2: *Example of the computational mesh used for implementation of LEBU device.*

case without domain cut). As such, the numerical implementation is a relatively easy task: if the face $j + 1/2$ belongs to LEBU, we redefine the numerical fluxes on it, with different values if we are at the top or at the bottom of the device. Also the fluxes on the opposite face of the physical cell "touched" by LEBU are changed, since the WENO, which may be active near the leading edge of the device, uses cells which come across the new boundary. Also for the application of the numerical boundary conditions on the new boundary defined by LEBU, we define two ghost rows. Following the same definitions for the fluxes using the new set of ghost cells, the numerical implementation does not offer additional difficulties with respect the code described in the second chapter of the thesis. Also, to minimize the risk of bug insertion in the implementation phase, we did not modify the old subroutines, we just add other subroutines which correct the fluxes where needed, with the solely exceptions of the subroutines used to define the grid and the block-matrices for the semi-implicit treatment.

The technique only permits the implementation of devices with a small angle at the leading edge. The domain cut is generated by manipulation of an initial mesh without any domain cut (with the exception of the airfoil wall and wake). Then a line at constant j is selected, and is deformed to obtain two lines, defining the device shape. Than the generated lines can be used to build a grid with standard techniques.

6.2 Unsteady RANS of uncontrolled case

We aim to use Unsteady RANS for the calibration of the control device. First we must assess the capability of RANS to describe the flow at $Re_c = 3 \times 10^5$, by comparing the results for the uncontrolled case with the DNS results. Only fully turbulent RANS are considered, since apparently the tripped RANS (SA-Ia) gives very similar results, only more irregular than the fully turbulent counterpart.

We consider first the steady flow at $Re_c = 3 \times 10^5$, $M_\infty = 0.7$, $\alpha = 4°$, performing

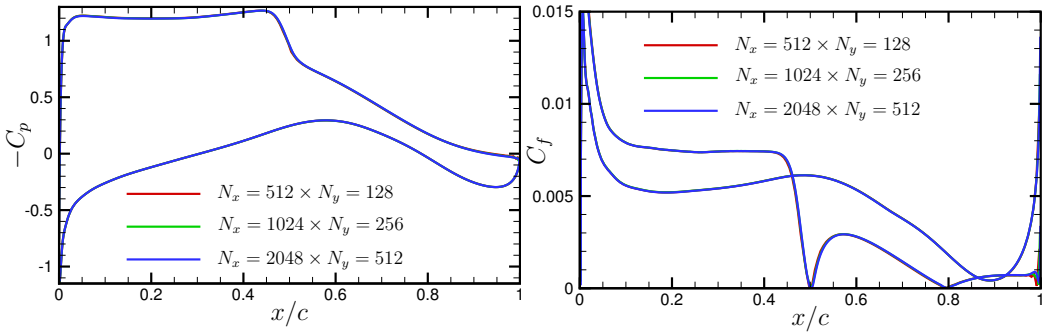

Figure 6.3: *Grid refinement for Unsteady RANS at* $Re_c = 3 \times 10^5$, $M_\infty = 0.7$, $\alpha = 4°$. *Left panel: pressure coefficient. Right panel: absolute value of the friction coefficient.*

the grid assessment shown in Fig. 6.3. There is a very good agreement between all the three tried grids. Even if the solutions were already expected to be steady, we run the simulation in the Unsteady RANS mode, until the steady state was reached. Figure 6.4 shows a comparison with results of DNS with forced transition. The top-left panel shows numerical Schlieren of the (statistically) steady flow relative to the DNS, with a weak shock located at the middle-chord. The comparison between the lift coefficients is good. One can then expect a good agreement between the pressure coefficients, too. Indeed, the only remarkable differences are found in the shock position, which is slightly more downstream for the Unsteady RANS with respect the DNS, and on a little region on the pressure side, where the DNS shows a tendency of the flow to separate, while RANS does not. The drag coefficients, not shown in figure, differ much more, and the explanation is found by looking at the friction coefficients: RANS overestimates friction on the whole pressure side, and on suction side until the shock (which is a little more downstream of the DNS) is reached, then underestimates it for the remaining part. There is, however, a fair overall agreement, considering the low Reynolds number we are applying the RANS modeling to, and we conclude that Unsteady RANS is able to predict with sufficient accuracy the statistically steady flows, especially for what concerns the pressure field. Now we want to asses the adequacy of Unsteady RANS also to conditions where an unsteady flow is expected. A similar comparison in the unsteady case is less satisfactory, as shown in Fig. 6.5. The Schlieren refers to a shock position close to its maximum upstream position, during the phase of the cycle in which the boundary layer experiences massive separation induced by the strong shock on suction side. By comparing the lift coefficients, we can see that the DNS is much more irregular than the corresponding RANS, and that the shock excursion is underestimated by RANS during most of the time span used for DNS. This is also reflected in the pressure coefficients, where we can see a steeper profile for RANS, denoting a more regular and narrow shock motion. However, the biggest difference in the mean pressure distribution is found on pressure side, where the flow separates for DNS, while remains attached for RANS, allowing a greater pressure recovery. The friction coefficient this time is overestimated by RANS over the whole profile. The overall

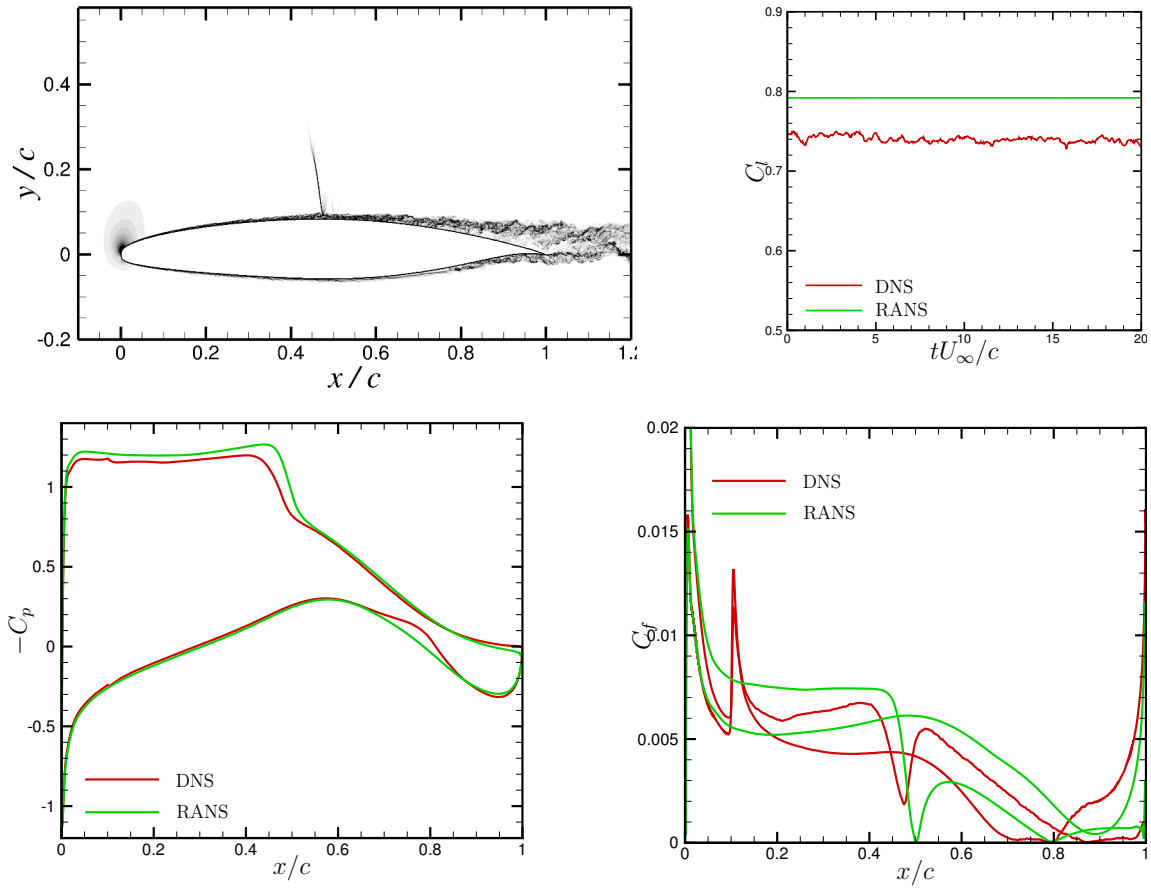

Figure 6.4: *Comparison of Unsteady RANS and DNS with forced transition results at $Re_c = 3 \times 10^5$, $M_\infty = 0.7$, $\alpha = 4°$. Top-left: numerical Schlieren for DNS. Top-right: comparison of lift coefficients. Bottom-left: comparison of pressure coefficients. Bottom-right: comparison of absolute value of friction coefficients.*

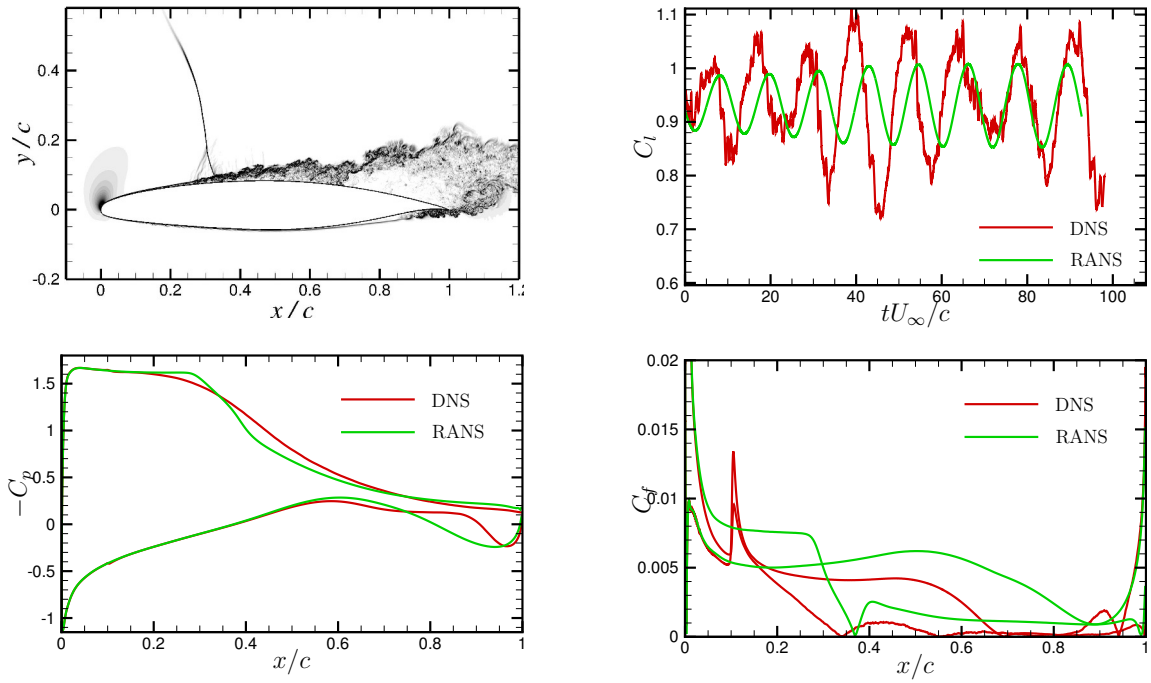

Figure 6.5: *Comparison of Unsteady RANS and DNS with forced transition results at $Re_c = 3 \times 10^5$, $M_\infty = 0.7$, $\alpha = 7°$. Top-left: numerical Schlieren for DNS. Top-right: comparison of lift coefficients. Bottom-left: comparison of pressure coefficients. Bottom-right: comparison of absolute value of friction coefficients.*

agreement between DNS and Unsteady RANS is fair, and again, the mean pressure distribution appears to be more than satisfactory, with the only exception of the separated region on pressure side.

In conclusion, Unsteady RANS appears to be a reasonable tool for testing the control device and finding an optimal configuration. However, once chosen, the configuration has to be tested with a DNS to obtain confident results.

6.3 Parametric study

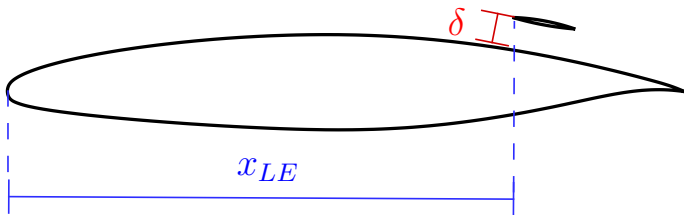

Figure 6.6: *Varying parameters in the study.*

Now we assess the efficacy of the control device, by trying different configurations. During the parametric study, we keep constant the length and the relative thickness of the circular-arc flap, respectively at $L_{LEBU} = 0.1c$ and $h_{max}/L_{LEBU} = 0.06$, unless otherwise stated. We vary the distance of the device from the airfoil surface (δ), and the relative position of its leading edge with respect the leading edge of the airfoil (x_{LE}). We choose to vary these parameters because it is expected that they are the most influencing ones. We run again the grid convergence study for the controlled

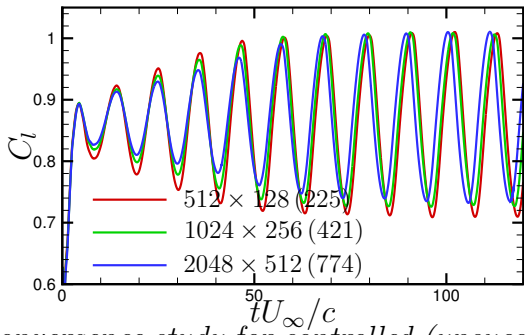

Figure 6.7: *Grid convergence study for controlled (unsuccessfully) case. $x_{LE} = 0.75c$, $\delta = 0.05c$. The number of cells refer to the grid without control device, uses as starting point for the construction of the grid with device. The effective N_y used is listed in parenthesis.*

case. Fig. 6.7 shows the outcome. The number of cells listed in figure refer to the initial (uncontrolled) grid: the N_y cells are concentrated in the boundary layer of the airfoil. Now we also have the boundary layer on the device. As such, we need more N_y to resolve the flow. Our solution was the use of the same Δy_{wall} both for airfoil and flap, while to decide the new number of cells in the transversal direction

we just kept constant the Δy_∞. The result was that the number of cells N_y nearly doubles for each grid. The effective total N_y used is listed in parenthesis in figure. We can see that $N_x = 1024$ and $N_y = 256\,(421)$ offers a good resolution. Since the total number of cells N_y, found as just explained, would depend on the distance of the device from the airfoil (δ), we simply decided to double the starting N_y and to take that value for all δ values. As such, the grids we used for the parametric study share the same $N_x = 1024$, $N_y = 512$ (effective).

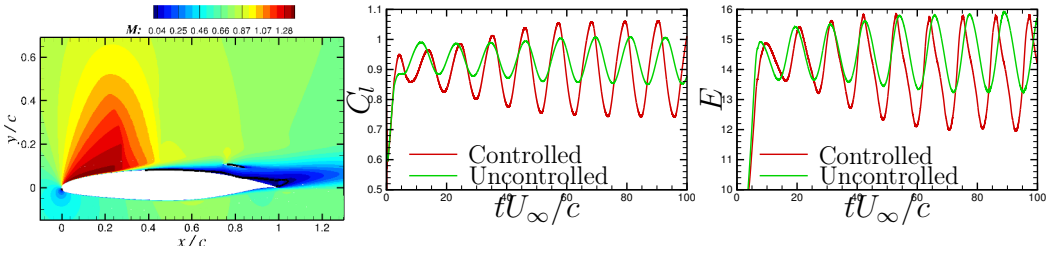

Figure 6.8: *Unsuccessfully controlled case. $x_{LE} = 0.75c$, $\delta = 0.05c$. Left panel: Mach contours and line $u_1 = 0$ (black). Middle panel: lift coefficients. Right panel: efficiency. Buffet is stronger for the controlled case.*

As already shown by Fig. 6.7, misplacing the device does not bring any advantage with respect the uncontrolled counterpart. Instead, as shown by Fig. 6.8, the control device degrades the performances, bringing stronger oscillations and a lower mean efficiency. However, as shown by Fig. 6.9, a correct positioning of the device appears

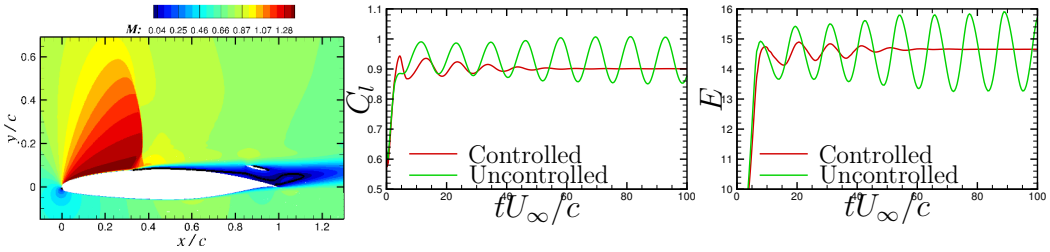

Figure 6.9: *Successfully controlled case. $x_{LE} = 0.85c$, $\delta = 0.075c$, thickness in this particular case was increased to 12%. Left panel: Mach contours and line $u_1 = 0$ (black). Middle panel: lift coefficients. Right panel: efficiency. Buffet eliminated with no efficiency losses.*

to be able to eliminate the instability, as shown by the lift coefficient. As can be seen in the right panel, efficiency does not degrade with respect the uncontrolled case. This appeared to be very promising. Before starting the parametric study, we checked the behaviour of the flow when the successful control device is added to a solution already showing buffet. Figure 6.10 indeed shows a solution slowly approaching a steady state, indicating that the control device is effective not only in the prevention of buffet, but also in the post-onset control. We then run a campaign of simulations, varying x_{LE} and δ, to see in which configuration the control was effective. The resulting map (Fig. 6.11) describes a very robust control, effective

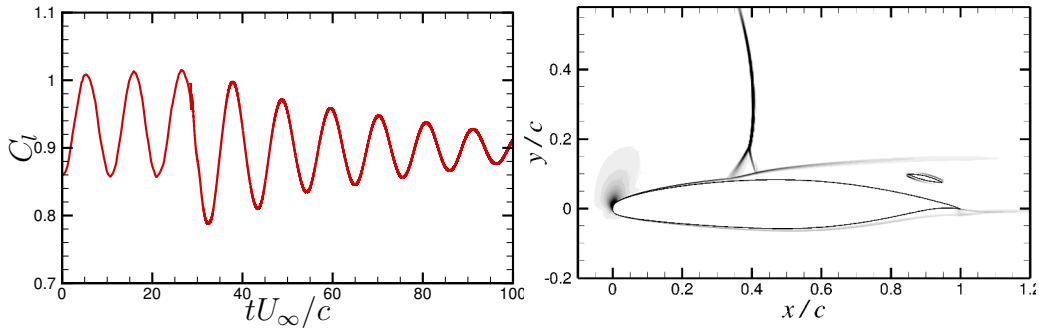

Figure 6.10: *Control device added to a solution already showing buffet (at $tu_\infty/c \simeq 28$). Left panel: lift coefficient. Right panel: numerical Schlieren.*

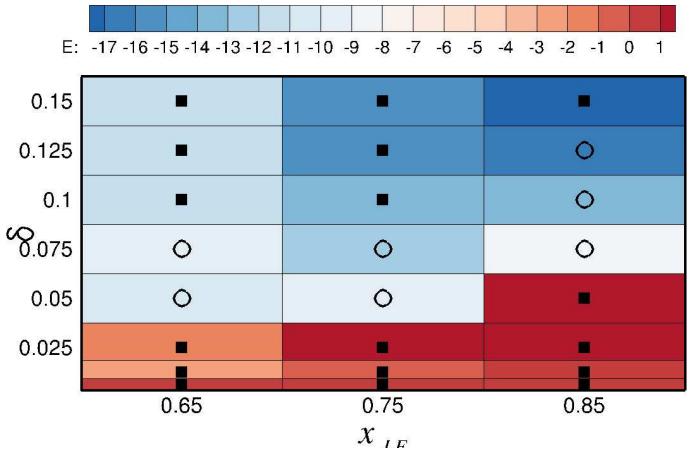

Figure 6.11: *Buffet envelope with superimposed mean efficiency. Empty circles refer to unsuccessfully controlled cases, solid squares to successful control. Colors refer to mean efficiency relative variations with respect the uncontrolled case. Red: no losses. Blue: high losses.*

in a range of parameters values. Empty circles denotes unsteady solutions, while solid squares indicate effective control. The colours denote the relative variation respect the uncontrolled case of the total mean efficiency, defined as the total mean lift coefficient over the total mean drag coefficient. The map indicates that there are two distinct configurations in which the control is effective: a high configuration, which is able to stabilize the flow at the price of a high loss of efficiency, and a low configuration, which is able to eliminate the unsteadiness without losses. The two configurations are separated by a region of the parameter space where the control is not effective, and in which buffet worsens, as shown before. The fact that the low configuration is effective is interesting, since the implementation on a real wing comports a lower additional weight and less complexity. Also, we tried configurations very close to the airfoil surface, which were anyway effective in the control. As a

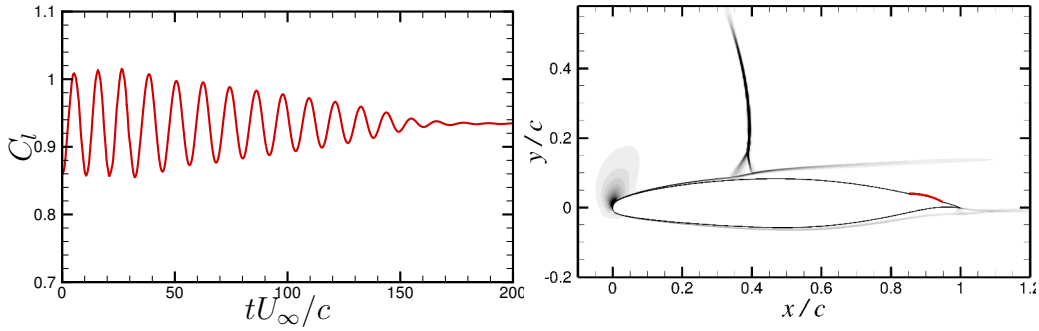

Figure 6.12: *Effect of a bump near the trailing edge, as a degenerated case of the control device. Bump is highlighted in red.*

degenerated case we tried then also a bump, in a region close to the trailing edge, shown in Fig. 6.12. It was also successful in the control of the unsteadiness. Here we restarted again from a buffeted solution, and slowly a steady state is attained.

6.3.1 DNS test of the control device

By looking at the lift coefficient time behaviour for Unsteady RANS, we selected the configuration which appeared to bring the steady state in the minimum time. The choice fell on $x_{LE} = 0.85c$ and $\delta = 0.025c$, and we tested the device with a DNS. The result is shown in Fig. 6.13. The time behaviour with respect the Unsteady RANS was so different, without the expected benefits gained from the control device, that we stopped the simulation after two periods, since this was a very expensive DNS, as $N_x = 4096$, $N_y = 695$, $N_z = 256$. The control is added to DNS at the time identified by the dotted line. The red line is the solution without control, while the green line corresponds to the controlled case. As can be seen, the control appears to be able to reduce buffet intensity, but not to eliminate the instability in the chosen test configuration. Since RANS showed the control to be very promising, further DNS tests are needed in order to assess the effectiveness of the passive control.

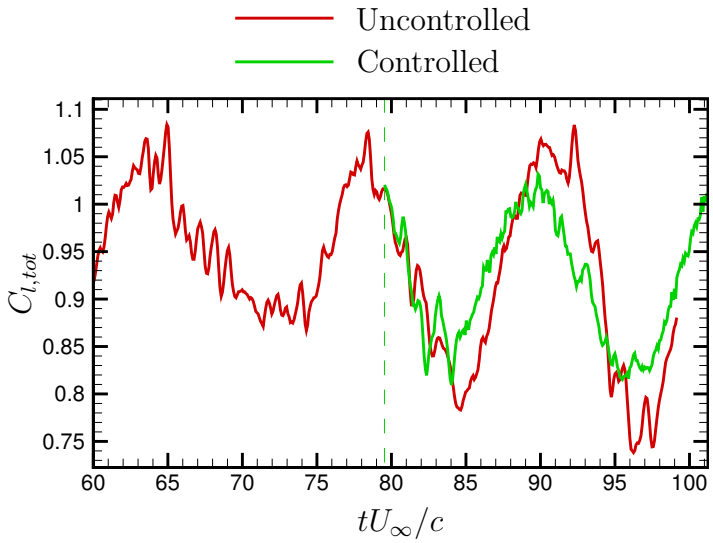

Figure 6.13: *DNS test of the control device. The device is applied to an already buffeted solution. The device appears to be able to lower buffet intensity, but not to eliminate the unsteadiness.*

Chapter 7

Conclusions and outlook

Transonic buffet over airfoils may be of different kinds: i) with oscillating shocks on both sides of the airfoil, ii) with one oscillating shock over the suction side of the lifting surface. The low-frequency characterizing the phenomenon appears to be able to discriminate the two different kinds of buffet, with a typical frequency associated with buffet of the first kind (two oscillating shocks) which is the double of the typical one associated with the second kind (one oscillating shock). By putting together the pieces of the puzzle during the bibliographic research, we were able to show that buffet of first and second kind are two distinct objects: the first, mostly tied to separation dynamics of the boundary layer on both suction and pressure sides and not amenable of a linear description neither at onset conditions, the second, being the result of a global instability of the flow, which is fed by an acoustic feedback loop. In particular, the assumption of the two kinds of buffet being two distinct objects is able to explain Crouch et al. (2009) wrong results: they obtained a global instability map by using the RANS approach, which fits very well the buffet stability limits for the lower Mach/higher alpha boundary, demonstrating quite conclusively that buffet of second kind is a modal phenomenon, at least at the onset. However, their instability map shows the wrong behavior for the higher Mach/lower alpha boundary, where buffet of first kind is more likely to appear. The same analysis applied to closed (channel) environments appears to fail (Sartor et al., 2015); by comparing the global stability analysis results for closed (channel) and open (airfoil) environments, we were also able to anticipate that waves reaching the shock from the front circumventing the shock tip or traveling along pressure side play an important role as to feed the global instability for buffet of second kind, which is the focus of our numerical study.

We performed a parametric study at Reynolds number $Re_c = 3 \times 10^6$ with turbulence modeling (Unsteady RANS and DDES), identifying a "stability map" for transonic buffet on the V2C airfoil, a supercritical laminar wing designed by Dassault Aviation in the context of the European research program TFAST. The stability map as obtained by URANS and DDES is the same, but the unsteady behaviour of the flow offered by the two approaches is different in nature, with DDES giving a less reliable flow description with respect the (cheaper) Unsteady

RANS with Spalart-Allmaras turbulence model.

We used the obtained map to choose the flow conditions in which to investigate transonic buffet with more sophisticated approaches, namely Implicit LES and DNS, the latter at a lower Reynolds number ($Re_c = 3 \times 10^5$). For both the approaches, different incoming boundary layer states are considered, namely tripped and untripped boundary layer near the leading edge. ILES predicts a stronger stability of the shock for the laminar incoming boundary layer with respect its turbulent counterpart, at a Reynolds number $Re_c = 3 \times 10^6$. This was a very interesting result, since a laminar boundary layer brings superior performances than a turbulent one in terms of efficiency and fuel consumption, and the results also showed a stronger stability of the shock, suggesting a twofold beneficial effect of the laminar incoming boundary layer. DNS computations at a lower Reynolds number have shown an opposite trend, with a shock which is much less stable for laminar boundary layer than its turbulent counterpart, showing shock motion also in cases where the tripped boundary layer brings a steady shock. In particular, the DNS database shows that the untripped boundary layer undergoes a strong large-scale unsteadiness also for an angle of incidence of 4°, which is not present when a tripped boundary layer is considered. As such, the ILES results may either be a numerical artifact, or the stability of the laminar incoming boundary layer may strongly depend on the considered Reynolds number. However, ILES with forced transition yields very similar results as those obtained with Unsteady RANS, encouraging the idea that the counterintuitive result obtained by ILES may indeed be correct for sufficiently high Reynolds number.

We used the databases furnished by DNS and by the various turbulence models to check whether the acoustic feedback-loop mechanisms used to explain buffet of second kind holds or not for our simulations. We performed an Unsteady RANS experiment to check the importance of disturbances propagating upstream along the pressure side in buffet of second kind. In this experiment we put an acoustic barrier near the trailing edge, on pressure side, applied to flow conditions showing buffet of second kind when no numerical barrier exists. The barrier doesn't stabilize the unsteadiness, and has a minor effect on buffet frequency, which throughout this work is used as the target value to be obtained in order to check the validity of a model of the large-scale unsteadiness mechanism. As such, we concluded that disturbances propagating along the pressure side, circumventing the leading edge and reaching the front of the shock should not be regarded as an important ingredient of the fundamental mechanism. An effect of the barrier has however been noticed on the buffet amplitude, which is lower when the barrier is active. We speculated that this behavior is a consequence of the different level of intermittence reaching the shock, which is higher when the upstream propagation along the pressure side is not inhibited. The acoustic feed-back loop mechanism in all the tested configurations appears to hold, with low-frequency coherent pressure disturbances - tied to the low-frequency dynamics of the shear layer - propagating towards the trailing edge, and high-frequency acoustic waves scattered at the trailing edge which propagate towards the tip of the shock, also circumventing the shock and reaching the supersonic

region ahead of the shock itself. Assuming such a model brings fair agreement between buffet frequency estimates and measurements. Among the classical acoustic feedback-loop models proposed to explain buffet, our results are closer to Hartmann et al. (2013) picture of the flow, where the interaction region between acoustic waves and shock is assumed to be the shock tip region. In our flow picture, however, it appears that waves entering the supersonic region ahead of the shock also play a role in the unsteady phenomenon, and further research is needed in order to assess their importance. All simulations showing buffet share the same downstream convection velocity for the low-frequency coherent pressure disturbances.

A novel passive control device has been developed: a LEBU placed between the shock and the trailing edge, on suction side. A parametric study based on Unsteady RANS computations has shown it to be effective in two configurations: a high configuration (LEBU far away from the airfoil wall), which stabilizes the flow at the price of a high efficiency drop, and a low configuration (LEBU close to the airfoil wall), which stabilizes the flow without efficiency losses. The parametric study has been effectuated at fixed flow conditions, with the size and the shape of LEBU fixed, and by only varying its position. The fact that the lower configuration works without efficiency losses has also the advantage of bringing a lighter structure, if implemented on a vehicle. After the assessment, a preliminary DNS test of a suitable configuration has been made. The choice fell on the case which RANS showed to bring flow stability in the shortest time, in order to save some computational time. The DNS test showed that the control device has the potential for weakening the shock oscillations, but no evidence of a complete stabilization of the unsteadiness was found in the chosen test configuration. More DNS tests are needed in order to assess the effectiveness of the developed control device.

Appendix A

SBP operators applied to split-form

We show here that SBP (Summation By Parts) operators applied to split forms may give rise to conservative schemes, which also conserve kinetic energy. Fisher et al. (2013) proved the conservativeness of the scheme for the double split. Here we give an alternative proof of the conservativeness of the resulting scheme, which we will use for proving that the same applies also for the triple split, provided a suitable choice of the coefficients arising in the Kennedy and Gruber (2008) split is chosen. The same proof can be applied to the triple split with no additional difficulty with respect the double split, however in literature we could not find any reference for it.

A.1 Proof in the case of Feiereisen et al. (1981) splitting

Fisher et al. (2013) state and prove that, given any diagonal-norm SBP operator $\mathcal{D}_{sbp}$, satisfying the properties

$$\mathcal{D}_{sbp} = \mathcal{P}^{-1}\mathcal{Q}\,, \qquad \mathcal{Q} + \mathcal{Q}^T = \mathrm{diag}(-1, 0, \ldots, 0, 1) \tag{A.1}$$

$$\mathcal{P} = \mathrm{diag}(P_1, \ldots, P_N)\,, \qquad P_i > 0 \tag{A.2}$$

the split form of $\frac{\partial fg}{\partial x}$

$$\alpha\frac{\partial fg}{\partial x} + (1-\alpha)\left(f\frac{\partial g}{\partial x} + g\frac{\partial f}{\partial x}\right) \tag{A.3}$$

discretized with $\mathcal{D}_{sbp}$ leads to a conservative approximation in the norm $\mathcal{P}$, i.e. the approximation can be cast in the form

$$\alpha\mathcal{D}_{sbp}(fg) + (1-\alpha)\left(f\mathcal{D}_{sbp}(g) + g\mathcal{D}_{sbp}(f)\right) = \mathcal{P}^{-1}\left(h_{i+1/2} - h_{i-1/2}\right) \tag{A.4}$$

and the expression for $h_{i+1/2}$ has compact support and is consistent with the original flux (fg), so that the Lax-Wendroff theorem holds.

The proof is divided in three parts. We have to:

- Prove the conservativeness of the discretization of the split-form in the $\mathcal{P}$ norm

- Retrieve the fluxes $h_{i+1/2}$
- Verify the consistency.

Conservativeness in the $\mathcal{P}$ norm. Before proceed with the demonstration, it is convenient to better illustrate the SBP property. The discrete counterpart of $\int_{x_1}^{x_N} f\frac{\partial g}{\partial x}\,\mathrm{d}x$ in the SBP framework is the $\mathcal{P}$ inner product

$$\int_{x_1}^{x_N} f\frac{\partial g}{\partial x}\,\mathrm{d}x \simeq (f,\mathcal{D}g)_{\mathcal{P}} = \mathbf{f}^T\mathcal{P}\mathcal{D}_{sbp}\mathbf{g} = \mathbf{f}^T\mathcal{Q}_{sbp}\mathbf{g} \tag{A.5}$$

Then we have

$$\begin{aligned}\int_{x_1}^{x_N} f\frac{\partial g}{\partial x}\,\mathrm{d}x + \int_{x_1}^{x_N} g\frac{\partial f}{\partial x}\,\mathrm{d}x &\simeq \mathbf{f}^T\mathcal{Q}\mathbf{g} + \mathbf{g}^T\mathcal{Q}\mathbf{f} = \\ &= \mathbf{f}^T\mathcal{Q}\mathbf{g} + \mathbf{f}^T\mathcal{Q}^T\mathbf{g} = \\ &= \mathbf{f}^T(\mathcal{Q}+\mathcal{Q}^T)\mathbf{g} = \\ &= \mathbf{f}^T\mathrm{diag}(-1,0,\ldots,0,1)\mathbf{g} = \\ &= f_N g_N - f_1 g_1\end{aligned} \tag{A.6}$$

Thus, with the SBP operator, the $\mathcal{P}$ inner product depends only on the boundary values, as the continuous counterpart. Now we apply the same principle to the split form, also introducing the vector notation, for convenience

$$\begin{aligned}&\alpha\int_{x_1}^{x_N}\frac{\partial(fg)}{\partial x}\,\mathrm{d}x + (1-\alpha)\left(\int_{x_1}^{x_N} f\frac{\partial g}{\partial x}\,\mathrm{d}x + \int_{x_1}^{x_N} g\frac{\partial f}{\partial x}\,\mathrm{d}x\right) \simeq \\ &\simeq \alpha\mathbf{1}^T\mathcal{P}\mathcal{D}(\mathbf{fg}) + (1-\alpha)(\mathbf{f}^T\mathcal{P}\mathcal{D}\mathbf{g} + \mathbf{g}^T\mathcal{P}\mathcal{D}\mathbf{f})\end{aligned} \tag{A.7}$$

where $\mathbf{1}$ is the vector whose components are all ones, $\mathcal{D}$ is the matrix representing the SBP operator, $\mathcal{D}\mathbf{fg}$ "=" $D_{il}(f_l g_l)$, and $\mathbf{f}$, $\mathbf{g}$ are the discretized vectors. To recover symmetry, we can add the term $(\mathbf{fg})^T\mathcal{P}\mathcal{D}\mathbf{1}$, since $\mathcal{D}\mathbf{1} = 0$, as for a polynomial of degree zero we always recover the exact derivative when we apply the discrete operator. Thus we can write

$$\begin{aligned}&\alpha\int_{x_1}^{x_N}\frac{\partial(fg)}{\partial x}\,\mathrm{d}x + (1-\alpha)\left(\int_{x_1}^{x_N} f\frac{\partial g}{\partial x}\,\mathrm{d}x + \int_{x_1}^{x_N} g\frac{\partial f}{\partial x}\,\mathrm{d}x\right) \simeq \\ &\simeq \alpha[(\mathbf{fg})^T\mathcal{P}\mathcal{D}\mathbf{1} + \mathbf{1}^T\mathcal{P}\mathcal{D}(\mathbf{fg})] + (1-\alpha)(\mathbf{f}^T\mathcal{P}\mathcal{D}\mathbf{g} + \mathbf{g}^T\mathcal{P}\mathcal{D}\mathbf{f}) = \\ &= \alpha[(fg)_N 1 - (fg)_1 1] + (1-\alpha)(f_N g_N - f_1 g_1) = \\ &= f_N g_N - f_1 g_1\end{aligned} \tag{A.8}$$

where the first equality arises from (A.6), so that the $\mathcal{P}$ norm conservativeness is proved for any α.

Expression of local fluxes $h_{i+1/2}$. In indices formulation, but *without* using Einstein's convention, we are looking for $h_{i+1/2}$ such that (since $\mathcal{D} = \mathcal{P}^{-1}\mathcal{Q}$)

$$\frac{\alpha}{P_i}\sum_l Q_{il} f_l g_l + \frac{1-\alpha}{P_i}\sum_l Q_{il}(f_i g_l + f_l g_i) = \frac{1}{P_i}(h_{i+1/2} - h_{i-1/2}) \tag{A.9}$$

i.e.

$$\alpha\sum_l Q_{il} f_l g_l + (1-\alpha)\sum_l Q_{il}(f_i g_l + f_l g_i) = (h_{i+1/2} - h_{i-1/2}) \tag{A.10}$$

The expression for $h_{i+1/2}$ may be found recursively. If we assume

$$h_{1-1/2} = f_1 g_1 \tag{A.11}$$

then

$$\begin{aligned} h_{i+1/2} &= h_{1-1/2} + \sum_{k=1}^{i}(h_{k+1/2} - h_{k-1/2}) = \\ &= f_1 g_1 + \sum_{k=1}^{i}\left[\alpha\sum_l Q_{kl} f_l g_l + (1-\alpha)\sum_l Q_{kl}(f_k g_l + f_l g_k)\right] \end{aligned} \tag{A.12}$$

where the first equality is obvious for the telescopic property, while the second one follow from (A.10). If the expressions (A.11), (A.12) are correct then we must retrieve $h_{N+1/2} = f_N g_N$:

$$h_{N+1/2} = f_1 g_1 + \sum_{k=1}^{N}\left[\alpha\sum_l Q_{kl} f_l g_l + (1-\alpha)\sum_l Q_{kl}(f_k g_l + f_l g_k)\right] \tag{A.13}$$

and the sum is coincident with (A.8), i.e. the starting discretization where we apply $\mathbf{1}^T\mathcal{P}$, and we have already shown that its evaluation brings $f_N g_N - f_1 g_1$, thus proving that the expression (A.12) is indeed correct.

Lax-Wendroff consistency. We must prove that $h_{i+1/2}(f_l = f, g_k = g) = h(f,g) = fg$:

$$h_{i+1/2} = fg + \sum_{k=1}^{i}\sum_l Q_{kl}(2-\alpha)fg = fg\left[1 + (2-\alpha)\sum_{k=1}^{j-1}\sum_l Q_{kl}\right] \tag{A.14}$$

and this is fg since $\sum_l Q_{kl} = 0$. In fact

$$\mathcal{D}_{sbp}\mathbf{1} = 0 \quad \Rightarrow \quad P_i^{-1}\sum_l Q_{il} 1 = 0 \tag{A.15}$$

$$\sum_l Q_{kl} = 0 \tag{A.16}$$

since $\mathcal{P} \neq 0$.

Compact expression. Lets start from the observation that for any antisymmetric matrix $\mathcal{A}$ we have

$$\mathbf{g}^T\mathcal{A}\mathbf{f} + \mathbf{f}^T\mathcal{A}\mathbf{g} = 0 \tag{A.17}$$

We define $\mathcal{A}$ to be

$$\mathcal{A} = \mathcal{Q} - \text{diag}(Q_{11}, 0, \ldots, 0, Q_{NN}) = \mathcal{Q} - \text{diag}(-1/2, 0, \ldots, 0, 1/2) \tag{A.18}$$

so that we can rewrite the fluxes $h_{i+1/2}$ as

$$h_{i+1/2} = \frac{\alpha}{2} f_1 g_1 + \sum_{k=1}^{i} \left[\alpha \sum_l A_{kl} f_l g_l + (1-\alpha) \sum_l A_{kl}(f_k g_l + f_l g_k) \right] \tag{A.19}$$

for $1 \leq i < N$. Here we are considering $i < N$, since for $i = N$ (and $i = 1$) we already dispose of the compact expression $h_{N+1/2} = f_N g_N$ ($h_{1-1/2} = f_1 g_1$).

$\mathcal{A}$ is a banded matrix, with the same half-width of $\mathcal{Q}$, which in turn has the same half-width of $\mathcal{D}_{sbp}$, which is limited, since $\mathcal{D}_{sbp}$ is an approximation of a FD explicit derivative. Thus, $\mathcal{A}$ is of the kind (here we represent a matrix with half-width $r = 3$):

$$\mathcal{A} = \begin{array}{c|cccccccccc}
 & 1 & 2 & \ldots & i-1 & i & \ldots & \text{N-3} & \text{N-2} & \text{N-1} & \text{N} \\ \hline
1 & * & * & * & * & & & & & & \\
2 & * & * & * & * & * & & & & & \\
\vdots & * & * & * & * & * & * & & & & \\
i-1 & * & * & * & * & * & * & * & & & \\
i & & * & * & * & * & * & * & * & & \\
\vdots & & & * & * & * & * & * & * & * & \\
\text{N-3} & & & & * & * & * & * & * & * & * \\
\text{N-2} & & & & & * & * & * & * & * & * \\
\text{N-1} & & & & & & * & * & * & * & * \\
\text{N} & & & & & & & * & * & * & *
\end{array}$$

Lets deal separately with the sums appearing in (A.19)

"Non-conservative" sum. Lets deal first with:

$$h^e_{i+1/2} := \sum_{k=1}^{i} \sum_{l} A_{kl}(f_k g_l + f_l g_k) \tag{A.20}$$

We split the sum in l such that we have the same indices in the first part (in the sense that $\sum_{k=1}^{i}\sum_{l=1}^{N} = \sum_{k=1}^{i}\sum_{l=1}^{i} + \sum_{k=1}^{i}\sum_{l=i+1}^{N}$):

$$h^e_{i+1/2} = \sum_{k=1}^{i} \sum_{l=1}^{i} A_{kl}(f_k g_l + f_l g_k) + \sum_{k=1}^{i} \sum_{l=i+1}^{N} A_{kl}(f_k g_l + f_l g_k) \tag{A.21}$$

The first sum of (A.21) is zero. In fact

$$\begin{aligned} \sum_{k=1}^{i} \sum_{l=1}^{i} A_{kl}(f_k g_l + f_l g_k) &= \sum_{l=1}^{i} \sum_{k=1}^{i} A_{lk}(f_l g_k + f_k g_l) = \\ &= -\sum_{k=1}^{i} \sum_{l=1}^{i} A_{kl}(f_k g_l + f_l g_k) \end{aligned} \tag{A.22}$$

(we used the fact that $\mathcal{A}$ is antisymmetric) and since it must equal its opposite, it must be zero. This means that the first square block of $\mathcal{A}$ (red) does not contribute to the sum

$$\mathbf{A} = \left[\begin{array}{ccccc|ccccccc} 1 & + & + & + & + & & & & & & & \\ 2 & + & + & + & + & * & & & & & & \\ \vdots & + & + & + & + & * & * & & & & & \\ i & + & + & + & + & * & * & * & & & & \\ \hline & 1 & 2 & \dots & i & i+1 & \dots & \text{N-3} & \text{N-2} & \text{N-1} & \text{N} \end{array}\right]$$

(we are just considering the first i rows of $\mathcal{A}$, since the sum extends only to it).

Considering that $\mathcal{A}$ is a banded matrix, with half-width r, the sum (A.20) is just to be extended on the "blue triangle" which is left, and which in the matrix has its three vertices in $(i, i+1)$, $(i, i+r)$, $(i+1-r, i+1)$. If we describe this triangle traveling parallel to the diagonal of the matrix, we can write

$$h^e_{i+1/2} = \sum_{k=1}^{r} \sum_{l=1}^{k} A_{i-k+l,\, i+l}(f_{i-k+l} g_{i+l} + g_{i-k+l} f_{i+l}) \tag{A.23}$$

where k selects the distance from the main diagonal of the matrix (and the number of terms which belongs to that segment), and l "travels" along such diagonal parallel.

This way of expressing the fluxes resembles the one of Fisher et al. (2013). Some care is needed when we are near the edge, but here we just wanted to prove the compactness of the flux expression, and graphically it is clear that the stencil is still compact.

"Conservative" sum.

$$h^c_{i+1/2} := \sum_{k=1}^{i} \sum_{l} A_{kl}(f_l g_l) \tag{A.24}$$

To symmetrize the expression, we sum and subtract $A_{kl} f_k g_k$ inside the sum

$$h^c_{i+1/2} = \sum_{k=1}^{i} \sum_{l} A_{kl}(f_l g_l + f_k g_k) - \sum_{k=1}^{i} \sum_{l} A_{kl}(f_k g_k) \tag{A.25}$$

Lets focus on the second sum

$$\sum_{k=1}^{i} \sum_{l} A_{kl}(f_k g_k) = \sum_{k=1}^{i} f_k g_k \sum_{l} A_{kl} \tag{A.26}$$

and from the definition of $\mathcal{A}$ (A.18) and (A.16)

$$0 = \sum_{l} Q_{kl} \text{ "=" } \mathcal{Q}\mathbf{1} = \mathcal{A}\mathbf{1} + \text{diag}(-1/2, 0, \ldots, 0, 1/2)\mathbf{1} \text{ "=" } \tag{A.27}$$

$$\text{"=" } \sum_{l} A_{kl} - 1/2\delta_{k1} + 1/2\delta_{kN} \tag{A.28}$$

and since, as already stated, $i \neq N$, we obtain

$$\sum_{k=1}^{i} \sum_{l} A_{kl}(f_k g_k) = \sum_{k=1}^{i} f_k g_k (1/2\delta_{k1} - 1/2\delta_{kN}) = 1/2 f_1 g_1 \tag{A.29}$$

Thus

$$h^c_{i+1/2} = \sum_{k=1}^{i} \sum_{l} A_{kl}(f_l g_l + f_k g_k) - \frac{1}{2} f_1 g_1 \tag{A.30}$$

Now we can apply the same methodology applied for the "non-conservative" part

$$h^c_{i+1/2} = \sum_{k=1}^{i} \sum_{l=1}^{i} A_{kl}(f_l g_l + f_k g_k) + \sum_{k=1}^{i} \sum_{l=i+1}^{N} A_{kl}(f_l g_l + f_k g_k) - \frac{1}{2} f_1 g_1$$

As for the "non-conservative" part, we have that the first sum is zero, thus

$$h^c_{i+1/2} = \sum_{k=1}^{i} \sum_{l=i+1}^{N} A_{kl}(f_l g_l + f_k g_k) - \frac{1}{2} f_1 g_1 \tag{A.31}$$

so that the terms which contribute to the sum are the ones with the same indices as the "non-conservative" contribution

$$h^c_{i+1/2} = -\frac{1}{2} f_1 g_1 + \sum_{k=1}^{r} \sum_{l=1}^{k} A_{i-k+l,\, i+l}(f_{i+l} g_{i+l} + f_{i-k+l} g_{i-k+l}) \tag{A.32}$$

Complete flux. Reassembling all together

$$\begin{aligned} h_{i+1/2} = &\cancel{\frac{\alpha}{2} f_1 g_1} + \\ &+ \alpha \left[\cancel{-\frac{1}{2} f_1 g_1} + \sum_{k=1}^{r} \sum_{l=1}^{k} A_{i-k+l,\, i+l} (f_{i+l} g_{i+l} + f_{i-k+l} g_{i-k+l}) \right] + \\ &+ (1-\alpha) \left[\sum_{k=1}^{r} \sum_{l=1}^{k} A_{i-k+l,\, i+l} (f_{i-k+l} g_{i+l} + g_{i-k+l} f_{i+l}) \right] \end{aligned}$$

and finally

$$\begin{aligned} h_{i+1/2} = \sum_{k=1}^{r} \sum_{l=1}^{k} A_{i-k+l,\, i+l} [&\alpha (f_{i+l} g_{i+l} + f_{i-k+l} g_{i-k+l}) + \\ &+ (1-\alpha)(f_{i-k+l} g_{i+l} + g_{i-k+l} f_{i+l})] \end{aligned} \tag{A.33}$$

Alternative expression for the flux. The square bracket in the sum (A.33) may be cast in a different form observing that

$$\begin{aligned} &\frac{1}{\alpha} \left[(1-\alpha) f_m + \alpha f_n \right] \left[(1-\alpha) g_m + \alpha g_n \right] = \\ =&\alpha f_n g_n + \frac{(1-\alpha)^2}{\alpha} f_m g_m + (1-\alpha)(f_m g_n + f_n g_m) = \\ =&\alpha (f_n g_n + f_m g_m) + \frac{1-2\alpha}{\alpha} f_m g_m + (1-\alpha)(f_m g_n + f_n g_m) \end{aligned}$$

thus

$$\begin{aligned} &\alpha (f_m g_m + f_n g_n) + (1-\alpha)(f_m g_n + f_n g_m) = \\ =&\frac{1}{\alpha} \left[(1-\alpha) f_m + \alpha f_n \right] \left[(1-\alpha) g_m + \alpha g_n \right] - \frac{1-2\alpha}{\alpha} f_m g_m \end{aligned} \tag{A.34}$$

and for the particular value of the splitting parameter $\alpha = 1/2$

$$\alpha (f_m g_m + f_n g_n) + (1-\alpha)(f_m g_n + f_n g_m) = 2 \frac{f_m + f_n}{2} \frac{g_m + g_n}{2} \tag{A.35}$$

which is the same expression provided by Pirozzoli (2010), if we consider a periodic domain. In fact, for a periodic domain the diagonal norm operators have the properties $\mathcal{A} = \mathcal{Q} = \mathcal{D}_{sbp} = \mathcal{D}_{central}$ (the first equality follow from the fact that $\mathcal{A}$ and $\mathcal{Q}$ differ only on the edges, the second follows from considering that the diagonal norm $P_i = 1$ in the inner part (Strand, 1994). $\mathcal{D}_{sbp} = \mathcal{D}_{central}$ is a property also used by Pirozzoli (2011a)).

A.2 Energy conservation only for $\alpha = 1/2$

Following Pirozzoli (2011a), we discard the pressure and viscous contributions, that is

$$\frac{\partial \rho}{\partial t} + \frac{\partial (\rho u_j)}{\partial x_j} = 0 \tag{A.36}$$

$$\frac{\partial (\rho u_i)}{\partial t} + \frac{\partial (\rho u_i u_j)}{\partial x_j} = 0 \tag{A.37}$$

Multiplying (A.37) by u_i and subtracting (A.36) multiplied by $(u_i u_i/2)$

$$u_i \frac{\partial (\rho u_i)}{\partial t} - \frac{u_i u_i}{2} \frac{\partial \rho}{\partial t} + u_i \frac{\partial (\rho u_i u_j)}{\partial x_j} - \frac{u_i u_i}{2} \frac{\partial (\rho u_j)}{\partial x_j} = 0 \tag{A.38}$$

Each time that u_i appears inside a derivative operation, we use the rule of the derivative of a product, considering u_i as one of the factors, thus yielding

$$\frac{u_i u_i}{2} \frac{\partial \rho}{\partial t} + \rho u_i \frac{\partial u_i}{\partial t} + \frac{u_i u_i}{2} \frac{\partial (\rho u_j)}{\partial x_j} + \rho u_j u_i \frac{\partial u_i}{\partial x_j} = 0 \tag{A.39}$$

If now we rewrite the products like $u_i \mathrm{d}u_i = \mathrm{d}(u_i u_i/2)$, we have

$$\frac{u_i u_i}{2} \frac{\partial \rho}{\partial t} + \rho \frac{\partial (u_i u_i/2)}{\partial t} + \frac{u_i u_i}{2} \frac{\partial (\rho u_j)}{\partial x_j} + \rho u_j \frac{\partial (u_i u_i/2)}{\partial x_j} = 0 \tag{A.40}$$

and finally

$$\frac{\partial k}{\partial t} + \frac{\partial k u_j}{\partial x_j} = 0 \tag{A.41}$$

Thus we obtain a conservation equation also for the kinetic energy $k = \rho u_i u_i/2$. What we now want to prove is that this conservation equation is retrieved also from the discretization of the equations written in split-form, assumed suitable split-form and discretization are used.

Feiereisen et al. (1981) splitting We start from the equations

$$\frac{\partial \rho}{\partial t} + \frac{\partial (\rho u_j)}{\partial x_j} = 0 \tag{A.42}$$

$$\frac{\partial (\rho u_i)}{\partial t} + \alpha \frac{\partial (\rho u_j u_i)}{\partial x_j} + (1-\alpha)(\rho u_j \frac{\partial u_i}{\partial x_j} + u_i \frac{\partial (\rho u_j)}{\partial x_j}) = 0 \tag{A.43}$$

The semi-discretized version is

$$\frac{\partial \rho_N}{\partial t} + \mathcal{D}_j (\rho u_j)_N = 0 \tag{A.44}$$

$$\begin{aligned} \frac{\partial (\rho u_i)_N}{\partial t} + \alpha \mathcal{D}_j (\rho u_j u_i)_N + \\ + (1-\alpha)((\rho u_j)_N \mathcal{D}_j (u_i)_N + (u_i)_N \mathcal{D}_j (\rho u_j)_N) = 0 \end{aligned} \tag{A.45}$$

We proceed just as before, by multiplying (A.45) by $(u_i)_N$ and subtracting (A.44) multiplied by $(u_i u_i)_N/2$. The sum in N does not follow Einstein convention. Thus we have

$$\frac{\partial k_N}{\partial t} = \left(\frac{1}{2} - \alpha\right)(u_i u_i)_N D_j(\rho u_j)_N + \tag{A.46}$$

$$+\alpha(u_i)_N D_j(\rho u_j u_i)_N + \tag{A.47}$$

$$+(1-\alpha)(\rho u_j u_i)_N D_j(u_i)_N \tag{A.48}$$

hence the conservation in the $\mathcal{P}$ norm follows immediately if we select $\alpha = 1/2$

$$\sum_N \frac{\partial(P_N k_N)}{\partial t} = \frac{1}{2}\sum_N (u_i)_N P_N D_j(\rho u_j u_i)_N + \tag{A.49}$$

$$+\frac{1}{2}\sum_N (\rho u_j u_i)_N P_N D_j(u_i)_N = \tag{A.50}$$

$$=\frac{1}{2}\sum_N (\rho u_j u_i)_N (Q_j + Q_j^T)(u_i)_N = \tag{A.51}$$

$$=(u_N k_N - u_1 k_1) \tag{A.52}$$

This is the same result reported by Pirozzoli (2010, 2011a) if we consider a periodic domain.

A.3 Triple splitting

Now we extend what has been done for the double splitting to the Kennedy and Gruber (2008) splitting, which is

$$\begin{aligned}\frac{\partial(\rho u\varphi)}{\partial x} = &\alpha\frac{\partial(\rho u\varphi)}{\partial x} + \\ &+\beta\left(u\frac{\partial(\rho\varphi)}{\partial x} + \rho\frac{\partial(u\varphi)}{\partial x} + \varphi\frac{\partial(\rho u)}{\partial x}\right) + \\ &+(1-\alpha-2\beta)\left(\rho u\frac{\partial\varphi}{\partial x} + \rho\varphi\frac{\partial u}{\partial x} + u\varphi\frac{\partial\rho}{\partial x}\right)\end{aligned} \tag{A.53}$$

Now we want to perform the discretization with the SBP operator $\mathcal{D}$. We have to proceed as already done for the double splitting.

Conservativeness in the $\mathcal{P}$ norm. In the same spirit of (A.8), we write

$$\begin{aligned}
&\alpha \int_{x_1}^{x_N} \frac{\partial(\rho u\varphi)}{\partial x}\, \mathrm{d}x + \\
&+ \beta \int_{x_1}^{x_N} \left(u\frac{\partial(\rho\varphi)}{\partial x} + \rho\frac{\partial(u\varphi)}{\partial x} + \varphi\frac{\partial(\rho u)}{\partial x} \right) \mathrm{d}x + \\
&+ (1-\alpha-2\beta) \int_{x_1}^{x_N} \left(\rho u\frac{\partial\varphi}{\partial x} + \rho\varphi\frac{\partial u}{\partial x} + u\varphi\frac{\partial\rho}{\partial x} \right) \mathrm{d}x \simeq \\
&\simeq \alpha \left[\mathbf{1}^T\mathcal{P}\mathcal{D}(\rho\mathbf{u}\varphi) + (\rho\mathbf{u}\varphi)^T\mathcal{P}\mathcal{D}\mathbf{1} \right] + \\
&+ \beta \left[\mathbf{u}^T\mathcal{P}\mathcal{D}(\rho\varphi) + \rho^T\mathcal{P}\mathcal{D}(\mathbf{u}\varphi) + \varphi^T\mathcal{P}\mathcal{D}(\rho\mathbf{u}) \right] + \\
&+ (1-\alpha-2\beta) \left[(\rho\mathbf{u})^T\mathcal{P}\mathcal{D}\varphi + (\rho\varphi)^T\mathcal{P}\mathcal{D}\mathbf{u} + (\mathbf{u}\varphi)^T\mathcal{P}\mathcal{D}\rho \right]
\end{aligned} \tag{A.54}$$

where we also added the term equal to zero $(\rho\mathbf{u}\varphi)^T\mathcal{P}\mathcal{D}\mathbf{1}$. Thus, we recover the Summation By Parts property if we select a particular value for β, such that

$$\beta = 1-\alpha-2\beta \qquad \Rightarrow \qquad \beta = \frac{1-\alpha}{3} \tag{A.55}$$

thus having

$$\begin{aligned}
&\alpha \int_{x_1}^{x_N} \frac{\partial(\rho u\varphi)}{\partial x}\, \mathrm{d}x + \\
&+ \beta \int_{x_1}^{x_N} \left(u\frac{\partial(\rho\varphi)}{\partial x} + \rho\frac{\partial(u\varphi)}{\partial x} + \varphi\frac{\partial(\rho u)}{\partial x} \right) \mathrm{d}x + \\
&+ (1-\alpha-2\beta) \int_{x_1}^{x_N} \left(\rho u\frac{\partial\varphi}{\partial x} + \rho\varphi\frac{\partial u}{\partial x} + u\varphi\frac{\partial\rho}{\partial x} \right) \mathrm{d}x \simeq \\
\simeq &\alpha \left[\mathbf{1}^T\mathcal{P}\mathcal{D}(\rho\mathbf{u}\varphi) + (\rho\mathbf{u}\varphi)^T\mathcal{P}\mathcal{D}\mathbf{1} \right] + \\
&+ \frac{1-\alpha}{3} \left[\mathbf{u}^T\mathcal{P}\mathcal{D}(\rho\varphi) + (\rho\varphi)^T\mathcal{P}\mathcal{D}\mathbf{u} \right] + \\
&+ \frac{1-\alpha}{3} \left[\rho^T\mathcal{P}\mathcal{D}(\mathbf{u}\varphi) + (\mathbf{u}\varphi)^T\mathcal{P}\mathcal{D}\rho \right] + \\
&+ \frac{1-\alpha}{3} \left[\varphi^T\mathcal{P}\mathcal{D}(\rho\mathbf{u}) + (\rho\mathbf{u})^T\mathcal{P}\mathcal{D}\varphi \right] = \\
= &\alpha[1\rho_N u_N\varphi_N - 1\rho_1 u_1\varphi_1] + \\
&+ \frac{1-\alpha}{3}[u_N\rho_N\varphi_N - u_1\rho_1\varphi_1] + \\
&+ \frac{1-\alpha}{3}[\rho_N u_N\varphi_N - \rho_1 u_1\varphi_1] + \\
&+ \frac{1-\alpha}{3}[\varphi_N u_N\rho_N - \varphi_1 u_1\rho_1] = \\
= &\rho_N u_N\varphi_N - \rho_1 u_1\varphi_1
\end{aligned} \tag{A.56}$$

Thus showing the conservativeness of the discretization of the triple split. Just for the sake of clarity, we are performing the discretization in the following way

($\mathcal{D} = \mathcal{P}^{-1}\mathcal{Q}$):

$$\begin{aligned}\left.\frac{\partial(\rho u\varphi)}{\partial x}\right|_{x_i} \simeq\ & \alpha\frac{1}{P_i}\sum_l Q_{il}(\rho_l u_l\varphi_l)+\\ &+\frac{1-\alpha}{3}\frac{1}{P_i}\sum_l Q_{il}[u_i(\rho_l\varphi_l)+u_l(\rho_i\varphi_i)]+\\ &+\frac{1-\alpha}{3}\frac{1}{P_i}\sum_l Q_{il}[\rho_i(u_l\varphi_l)+\rho_l(u_i\varphi_i)]+\\ &+\frac{1-\alpha}{3}\frac{1}{P_i}\sum_l Q_{il}[\varphi_i(\rho_l u_l)+\varphi_l(\rho_i u_i)]\end{aligned} \tag{A.57}$$

Expression of local fluxes $h_{i+1/2}$. We are trying again to write the derivative approximation as $\mathcal{P}^{-1}(h_{i+1/2} - h_{i-1/2}$. In indices formulation, we are looking for $h_{i+1/2}$ such that

$$\begin{aligned}h_{i+1/2} - h_{i-1/2} =\ & \alpha\sum_l Q_{il}(\rho_l u_l\varphi_l)+\\ &+\frac{1-\alpha}{3}\sum_l Q_{il}[u_i(\rho_l\varphi_l)+u_l(\rho_i\varphi_i)]+\\ &+\frac{1-\alpha}{3}\sum_l Q_{il}[\rho_i(u_l\varphi_l)+\rho_l(u_i\varphi_i)]+\\ &+\frac{1-\alpha}{3}\sum_l Q_{il}[\varphi_i(\rho_l u_l)+\varphi_l(\rho_i u_i)]\end{aligned} \tag{A.58}$$

We proceed exactly as done for the double splitting, assuming

$$h_{1-1/2} = \rho_1 u_1\varphi_1 \tag{A.59}$$

and

$$\begin{aligned}h_{i+1/2} =\ & \rho_1 u_1\varphi_1 + \alpha\sum_{k=1}^{i}\sum_l Q_{kl}(\rho_l u_l\varphi_l)+\\ &+\frac{1-\alpha}{3}\sum_{k=1}^{i}\sum_l Q_{kl}[u_k(\rho_l\varphi_l)+u_l(\rho_k\varphi_k)]+\\ &+\frac{1-\alpha}{3}\sum_{k=1}^{i}\sum_l Q_{kl}[\rho_k(u_l\varphi_l)+\rho_l(u_k\varphi_k)]+\\ &+\frac{1-\alpha}{3}\sum_{k=1}^{i}\sum_l Q_{kl}[\varphi_k(\rho_l u_l)+\varphi_l(\rho_k u_k)]\end{aligned} \tag{A.60}$$

Again, we have to prove that this expression yields $h_{N+1/2} = \rho_N u_N \varphi_N$.

$$\begin{aligned} h_{N+1/2} = \rho_1 u_1 \varphi_1 &+ \alpha \sum_{k=1}^{N} \sum_{l} Q_{kl}(\rho_l u_l \varphi_l) + \\ &+ \frac{1-\alpha}{3} \sum_{k=1}^{N} \sum_{l} Q_{kl}[u_k(\rho_l \varphi_l) + u_l(\rho_k \varphi_k)] + \\ &+ \frac{1-\alpha}{3} \sum_{k=1}^{N} \sum_{l} Q_{kl}[\rho_k(u_l \varphi_l) + \rho_l(u_k \varphi_k)] + \\ &+ \frac{1-\alpha}{3} \sum_{k=1}^{N} \sum_{l} Q_{kl}[\varphi_k(\rho_l u_l) + \varphi_l(\rho_k u_k)] \end{aligned} \tag{A.61}$$

But the sums are the same appearing in the proof of the conservativeness (A.56), which yield $\rho_N u_N \varphi_N - \rho_1 u_1 \varphi_1$, thus proving again that expression (A.60) is indeed correct.

Lax-Wendroff consistency. This is exactly as the one shown for the double-splitting, and we do not report it again.

Compact expression. We use again the antisymmetric matrix $\mathcal{A}$

$$\begin{aligned} h_{i+1/2} = \frac{\alpha}{2} \rho_1 u_1 \varphi_1 &+ \alpha \sum_{k=1}^{i} \sum_{l} A_{kl}(\rho_l u_l \varphi_l) + \\ &+ \frac{1-\alpha}{3} \sum_{k=1}^{i} \sum_{l} A_{kl}[u_k(\rho_l \varphi_l) + u_l(\rho_k \varphi_k)] + \\ &+ \frac{1-\alpha}{3} \sum_{k=1}^{i} \sum_{l} A_{kl}[\rho_k(u_l \varphi_l) + \rho_l(u_k \varphi_k)] + \\ &+ \frac{1-\alpha}{3} \sum_{k=1}^{i} \sum_{l} A_{kl}[\varphi_k(\rho_l u_l) + \varphi_l(\rho_k u_k)] \end{aligned} \tag{A.62}$$

and again we consider separately the different sums appearing in this expression.

First "non conservative" sum. By defining

$$f = u \tag{A.63}$$

$$g = \rho\varphi \tag{A.64}$$

we obtain

$$h^{e1}_{i+1/2} = \sum_{k=1}^{i} \sum_{l} A_{kl}[u_k(\rho_l \varphi_l) + u_l(\rho_k \varphi_k)] = \sum_{k=1}^{i} \sum_{l} A_{kl}[f_k g_l + f_l g_k] \tag{A.65}$$

which is identical to the (A.20), thus we can use (A.23) to write

$$h^{e1}_{i+1/2} = \sum_{k=1}^{r}\sum_{l=1}^{k} A_{i-k+l,\,i+l}[u_{i-k+l}(\rho_{i+l}\varphi_{i+l}) + (\rho_{i-k+l}\varphi_{i-k+l})u_{i+l}] \tag{A.66}$$

The same reasoning may be applied to the other two "non-conservative" sums (I will not rewrite them here).

"Conservative" sum. The same reasoning may be applied here. By defining

$$f = u \tag{A.67}$$
$$g = \rho\varphi \tag{A.68}$$

we obtain

$$h^{c}_{i+1/2} = \sum_{k=1}^{i}\sum_{l} A_{kl}(\rho_l u_l \varphi_l) = \sum_{k=1}^{i}\sum_{l} A_{kl}(f_l g_l) \tag{A.69}$$

which is identical to (A.24), so that using (A.32) we obtain

$$h^{c}_{i+1/2} = -\frac{1}{2}\rho_1 u_1 \varphi_1 + \sum_{k=1}^{r}\sum_{l=1}^{k} A_{i-k+l,\,i+l}[\rho_{i+l}u_{i+l}\varphi_{i+l} + \rho_{i-k+l}u_{i-k+l}\varphi_{i-k+l}]$$

Complete flux. Reassembling all together, we obtain

$$h_{i+1/2} = \sum_{k=1}^{i}\sum_{l} A_{i-k+l,\,i+l}\{\alpha[(\rho u\varphi)_{i-k+l} + (\rho u\varphi)_{i+l}] + \tag{A.70}$$
$$+\frac{1-\alpha}{3}[u_{i-k+l}(\rho\varphi)_{i+l} + u_{i+l}(\rho\varphi)_{i-k+l}] + \tag{A.71}$$
$$+\frac{1-\alpha}{3}[\rho_{i-k+l}(u\varphi)_{i+l} + \rho_{i+l}(u\varphi)_{i-k+l}] + \tag{A.72}$$
$$+\frac{1-\alpha}{3}[\varphi_{i-k+l}(\rho u)_{i+l} + \varphi_{i+l}(\rho u)_{i-k+l}]\} \tag{A.73}$$

Alternative expression for the flux. Observing that the quantity in braces may be also expressed as

$$\frac{4\alpha-1}{3}[(\rho u\varphi)_m + (\rho u\varphi)_n] + \frac{1-\alpha}{3}(\rho_m+\rho_n)(u_m+u_n)(\varphi_m+\varphi_n) \tag{A.74}$$

then, if one chooses $\alpha = 1/4$ for zeroing the first term, recovers the fluxes of Pirozzoli (2010)

$$2\frac{(\rho_m+\rho_n)}{2}\frac{(u_m+u_n)}{2}\frac{(\varphi_m+\varphi_n)}{2} \tag{A.75}$$

Thus this is a generalization of the conservative formula given in that paper. However, only $\alpha = 1/4$ brings the conservation of the kinetic energy.

A.4 Energy conservation only for $\alpha_1 = 1/2$, $\alpha_2 = 1/4$

Following again Pirozzoli (2011a), we discard the pressure and viscous contributions, and perform the same manipulations.

Kennedy and Gruber (2008) splitting We start from the equations

$$\frac{\partial \rho}{\partial t} + \alpha_1 \frac{\partial (\rho u_j)}{\partial x_j} + (1-\alpha_1)(u_j \frac{\partial \rho}{\partial x_j} + \rho \frac{\partial u_j}{\partial x_j}) = 0 \tag{A.76}$$

$$\begin{aligned} \frac{\partial (\rho u_i)}{\partial t} + \alpha \frac{\partial (\rho u_i u_j)}{\partial x} + \frac{1-\alpha}{3}\left(u_i \frac{\partial (\rho u_j)}{\partial x} + \rho \frac{\partial (u_i u_j)}{\partial x} + u_j \frac{\partial (\rho u_i)}{\partial x} \right) + \\ + \frac{1-\alpha}{3}\left(\rho u_i \frac{\partial u_j}{\partial x} + \rho u_j \frac{\partial u_i}{\partial x} + u_i u_j \frac{\partial \rho}{\partial x} \right) = 0 \end{aligned} \tag{A.77}$$

The semi-discretized version is

$$\begin{aligned} \frac{\partial \rho_N}{\partial t} + \alpha_1 D_j (\rho u_j)_N + \\ + (1-\alpha_1)((u_j)_N D_j \rho_N + \rho_N D_j (u_j)_N) = 0 \end{aligned} \tag{A.78}$$

$$\begin{aligned} \frac{\partial (\rho u_i)_N}{\partial t} + \alpha_2 D_j (\rho u_i u_j)_N + \\ + \frac{1-\alpha_2}{3}\left((u_i)_N D_j (\rho u_j)_N + \rho_N D_j (u_i u_j)_N + (u_j)_N D_j (\rho u_i)_N \right) + \\ + \frac{1-\alpha_2}{3}\left((\rho u_i)_N D_j (u_j)_N + (\rho u_j)_N D_j (u_i)_N + (u_i u_j)_N D_j \rho_N \right) = 0 \end{aligned} \tag{A.79}$$

We proceed just as before, by multiplying (A.79) by $(u_i)_N$ and subtracting (A.78) multiplied by $(u_i u_i)_N/2$. For conciseness we assume that N does not follow Einstein's convention. Thus we have

$$\frac{\partial k_N}{\partial t} = \left(\frac{1}{3} - \frac{\alpha_1}{2} - \frac{\alpha_2}{3} \right)(u_i u_i)_N D_j (\rho u_j)_N + \tag{A.80}$$

$$+ \left(-\frac{1}{6} + \frac{\alpha_1}{2} - \frac{\alpha_2}{3} \right)(u_i u_i u_j)_N D_j (\rho)_N + \tag{A.81}$$

$$+ \left(-\frac{1}{6} + \frac{\alpha_1}{2} - \frac{\alpha_2}{3} \right)(\rho u_i u_i)_N D_j (u_j)_N + \tag{A.82}$$

$$+ \alpha_2 (u_i)_N D_j (\rho u_i u_j)_N + \tag{A.83}$$

$$+ \frac{1-\alpha_2}{3}(\rho u_i u_j)_N D_j (u_i)_N + \tag{A.84}$$

$$+ \frac{1-\alpha_2}{3}(\rho u_i)_N D_j (u_i u_j)_N + \tag{A.85}$$

$$+ \frac{1-\alpha_2}{3}(u_i u_j)_N D_j (\rho u_i)_N \tag{A.86}$$

hence the conservation in the $\mathcal{P}$ norm follows immediately if we achieve the following equalities

$$\left(\frac{1}{3} - \frac{\alpha_1}{2} - \frac{\alpha_2}{3}\right) = 0 \tag{A.87}$$

$$\left(-\frac{1}{6} + \frac{\alpha_1}{2} - \frac{\alpha_2}{3}\right) = 0 \tag{A.88}$$

$$\frac{1-\alpha_2}{3} = \alpha_2 \tag{A.89}$$

thus for

$$\alpha_1 = \frac{1}{2} \qquad\qquad \alpha_2 = \frac{1}{4} \tag{A.90}$$

such that

$$\sum_N \frac{\partial P_N k_N}{\partial t} = \frac{1}{4}\sum_N (u_i)_N P_N D_j(\rho u_i u_j)_N + \tag{A.91}$$

$$+\frac{1}{4}\sum_N (\rho u_i u_j)_N P_N D_j(u_i)_N + \tag{A.92}$$

$$+\frac{1}{4}\sum_N (\rho u_i)_N P_N D_j(u_i u_j)_N + \tag{A.93}$$

$$+\frac{1}{4}\sum_N (u_i u_j)_N P_N D_j(\rho u_i)_N = \tag{A.94}$$

$$= (u_N k_N - u_1 k_1) \tag{A.95}$$

This is the same result reported by Pirozzoli (2010, 2011a) if we consider a periodic domain.

Bibliography

Jakob Ackeret, F Feldmann, and N Rott. Investigations of compression shocks and boundary layers in gases moving at high speed. Technical Memorandum NACA TM-1113, 1947.

Holger Babinsky and John K Harvey. *Shock wave-boundary-layer interactions*, volume 32. Cambridge University Press, 2011.

Barrett Stone Baldwin and Harvard Lomax. *Thin layer approximation and algebraic model for separated turbulent flows*, volume 257. American Institute of Aeronautics and Astronautics, 1978.

G. Barakos and D. Drikakis. Numerical simulation of transonic buffet flows using various turbulence closures. *International Journal of Heat and Fluid Flow*, 21 (5):620–26, October 2000. ISSN 0142727X. doi: 10.1016/s0142-727x(00)00053-9. URL `http://dx.doi.org/10.1016/s0142-727x(00)00053-9`.

George Keith Batchelor. *An introduction to fluid dynamics*. Cambridge university press, 2000.

Richard M Beam and Robert F Warming. An implicit finite-difference algorithm for hyperbolic systems in conservation-law form. *Journal of computational physics*, 22(1):87–110, 1976.

Richard M Beam and RoF Warming. An implicit factored scheme for the compressible navier-stokes equations. *AIAA journal*, 16(4):393–402, 1978.

GA Blaisdell, ET Spyropoulos, and JH Qin. The effect of the formulation of nonlinear terms on aliasing errors in spectral methods. *Applied Numerical Mathematics*, 21(3):207–219, 1996.

A Bonfiglioli, R Paciorri, and L Campoli. Unsteady shock-fitting for unstructured grids. *International Journal for Numerical Methods in Fluids*, 81(4):245–261, 2016.

Aldo Bonfiglioli and Renato Paciorri. Convergence analysis of shock-capturing and shock-fitting solutions on unstructured grids. *AIAA journal*, 2014.

JP Boris, FF Grinstein, ES Oran, and RL Kolbe. New insights into large eddy simulation. *Fluid dynamics research*, 10(4-6):199–228, 1992.

Jens Brouwer. A study of transonic shock-wave/boundary-layer interactions using conservative, skew-symmetric finite-differences. 2016.

PJK Bruce and H Babinsky. Unsteady shock wave dynamics. *Journal of Fluid Mechanics*, 603:463–473, 2008.

Dean R Chapman, Donald M Kuehn, and Howard K Larson. Investigation of separated flows in supersonic and subsonic streams with emphasis on the effect of transition. 1958.

Tim Colonius and Sanjiva K Lele. Computational aeroacoustics: progress on nonlinear problems of sound generation. *Progress in Aerospace sciences*, 40(6): 345–416, 2004.

TJ Craft, BE Launder, and K Suga. Development and application of a cubic eddy-viscosity model of turbulence. *International Journal of Heat and Fluid Flow*, 17 (2):108–115, 1996.

J. D. Crouch, A. Garbaruk, D. Magidov, and A. Travin. Origin of transonic buffet on aerofoils. *Journal of Fluid Mechanics*, 628(-1):357–69, 2009. doi: 10.1017/s0022112009006673. URL `http://dx.doi.org/10.1017/s0022112009006673`.

J.D. Crouch, A. Garbaruk, and D. Magidov. Predicting the onset of flow unsteadiness based on global instability. *Journal of Computational Physics*, 224 (2):924 – 940, 2007.

J Dandois, P Molton, A Lepage, A Geeraert, V Brunet, JB Dor, and E Coustols. Buffet characterization and control for turbulent wings. *AerospaceLab*, (6):p–1, 2013.

Sébastien Deck. Numerical simulation of transonic buffet over a supercritical airfoil. *AIAA journal*, 43(7):1556, 2005.

Sébastien Deck. Recent improvements in the zonal detached eddy simulation (zdes) formulation. *Theoretical and Computational Fluid Dynamics*, pages 1–28, 2012.

Jean Délery and Jean-Paul Dussauge. Some physical aspects of shock wave/boundary layer interactions. *Shock waves*, 19(6):453–468, 2009.

Jean Délery, John G Marvin, and Eli Reshotko. Shock-wave boundary layer interactions. Technical report, ADVISORY GROUP FOR AEROSPACE RESEARCH AND DEVELOPMENT NEUILLY-SUR-SEINE (FRANCE), 1986.

F Ducros, V Ferrand, Franck Nicoud, C Weber, D Darracq, C Gacherieu, and Thierry Poinsot. Large-eddy simulation of the shock/turbulence interaction. *Journal of Computational Physics*, 152(2):517–549, 1999.

John W. Edwards. Transonic Shock Oscillations and Wing Flutter Calculated with an Interactive Boundary Layer Coupling Method. Technical Memorandum NASA-TM-110484, National Aeronautics and Space Administration, 1996.

R Ewert and W Schröder. On the simulation of trailing edge noise with a hybrid les/ape method. *Journal of Sound and Vibration*, 270(3):509–524, 2004.

William John Feiereisen, William C Reynolds, and Joel H Ferziger. Numerical simulation of a compressible homogeneous, turbulent shear flow. 1981.

A Feo, RE Melnik, and AF Messiter. Shock-wave strength for separation of a laminar boundary layer at transonic speeds. *AIAA Journal*, 9(6):1197–1198, 1971.

Travis C Fisher, Mark H Carpenter, Jan Nordström, Nail K Yamaleev, and Charles Swanson. Discretely conservative finite-difference formulations for nonlinear conservation laws in split form: Theory and boundary conditions. *Journal of Computational Physics*, 234:353–375, 2013.

Mohamed Gad-el Hak and Promode R Bandyopadhyay. Questions in fluid mechanics. *Journal of Fluids Engineering*, 117(3):5, 1995.

Chuanqiang Gao, Weiwei Zhang, and Zhengyin Ye. Numerical study on closed-loop control of transonic buffet suppression by trailing edge flap. *Computers & Fluids*, 132:32–45, 2016.

E. Garnier and S. Deck. Large-eddy Simulation of Transonic Buffet over a Supercritical Airfoil, Direct and Large-Eddy Simulation. *ERCOFTAC series*, 13: 549–54, 2010.

Eric Garnier, Michele Mossi, Pierre Sagaut, Pierre Comte, and Michel Deville. On the use of shock-capturing schemes for large-eddy simulation. *Journal of Computational Physics*, 153(2):273–311, 1999.

Eric Garnier, Nikolaus Adams, and Pierre Sagaut. *Large eddy simulation for compressible flows*. Springer Science & Business Media, 2009.

J. Gibb. The cause and cure of periodic flows at transonic speeds. In *Proceedings 16th Congress of the International Council of the Aeronautical Sciences*, pages 1522–30, 1988.

Fernando F Grinstein, Len G Margolin, and William J Rider. *Implicit large eddy simulation: computing turbulent fluid dynamics*. Cambridge university press, 2007.

A Hartmann, A Feldhusen, and W Schröder. On the interaction of shock waves and sound waves in transonic buffet flow. *Physics of Fluids*, 25(2):026101, 2013.

Charles Hirsch. Numerical computation of internal and external flows. vol. 1-fundamentals of numerical discretization. *New York, Wiley*, 1988.

Charles Hirsch. Numerical computation of internal and external flows. vol. 2-computational methods for inviscid and viscous flows. *Chichester, England and New York, John Wiley & Sons, 1990, 708 p.*, 1990.

Seyed Mohammad Hosseini, Ricardo Vinuesa, Philipp Schlatter, Ardeshir Hanifi, and Dan S Henningson. Direct numerical simulation of the flow around a wing section at moderate reynolds number. *International Journal of Heat and Fluid Flow*, 61:117–128, 2016.

Michael Iovnovich and Daniella E Raven. Reynolds-averaged navier-stokes study of the shock-buffet instability mechanism. *AIAA journal*, 50(4):880–890, 2012.

L. Jacquin, P. Molton, S. Deck, B. Maury, and D. Soulevant. Experimental Study of Shock Oscillation over a Transonic Supercritical Profile. *AIAA Journal*, 47(9): 1985–94, september 2009.

Guang-Shan Jiang and Chi-Wang Shu. Efficient implementation of weighted eno schemes. *Journal of computational physics*, 126(1):202–228, 1996.

Javier Jimenez and Robert D Moser. Large-eddy simulations: where are we and what can we expect? *AIAA journal*, 38(4):605–612, 2000.

Lloyd E. Jones, Richard D. Sandberg, and Neil D. Sandham. DIRECT NUMERICAL SIMULATION OF AN AIRFOIL WITH UNSTEADY WAKE (ECCOMAS 2006), 2006.

Christopher A Kennedy and Andrea Gruber. Reduced aliasing formulations of the convective terms within the navier–stokes equations for a compressible fluid. *Journal of Computational Physics*, 227(3):1676–1700, 2008.

Doyle Knight, Gang Zhou, Nora Okong'o, and Vijay Shukla. Compressible large eddy simulation using unstructured grids. *AIAA paper*, 535:1998, 1998.

Langley Research Center. Turbulence modeling resource. `https://turbmodels.larc.nasa.gov/spalart.html`. Accessed: 2017-08-03.

BE Launder and BI Sharma. Application of the energy-dissipation model of turbulence to the calculation of flow near a spinning disc. *Letters in heat and mass transfer*, 1(2):131–137, 1974.

B. H. K. Lee. Transonic buffet on a supercritical airfoil. *Aeronaut J*, pages 143–52, May 1990.

B. H. K. Lee. Self-sustained shock oscillations on airfoils at transonic speeds. *Progress in Aerospace Sciences*, 37:147–96, 2001. doi: 10.1016/S0376-0421(01)00003-3.

Randall J LeVeque. *Finite volume methods for hyperbolic problems*, volume 31. Cambridge university press, 2002.

Hans Wolfgang Liepmann. The interaction between boundary layer and shock waves in transonic flow. *Journal of the Aeronautical Sciences*, 13:623–637, 1946.

MJ Lighthill. Reflection at a laminar boundary layer of a weak steady disturbance to a supersonic stream, neglecting viscosity and heat conduction. *The Quarterly Journal of Mechanics and Applied Mathematics*, 3(3):303–325, 1950.

MJ Lighthill. On boundary layers and upstream influence. ii. supersonic flows without separation. In *Proceedings of the Royal Society of London A: Mathematical, Physical and Engineering Sciences*, volume 217, pages 478–507. The Royal Society, 1953.

D. G. Mabey. Oscillatory flows from shock-induced separations on biconvex aerofoils of varying thickness in ventilated wind tunnels. In *AGARD Conference Proceedings, No. 296, Boundary Layer Effects on Unsteady Airloads*, pages 11.1–14, 1980.

J. B. McDevitt and A. F. Okuno. Static and dynamic pressure measurements on a NACA 0012 airfoil in the Ames High Reynolds Number Facility. Technical Report NASA-TP-2485, National Aeronautics and Space Administration, 1985.

John B. McDevitt. Supercritical Flow about a Thick Circular-Arc Airfoil. Technical Memorandum NASA/TM-78549, National Aeronautics and Space Administration, 1979.

John B. McDevitt, Lionel L. Levy Jr., and George S. Deiwert. Transonic Flow about a Thick Circular-Arc Airfoil. *AIAA JOURNAL*, 14(5):606–13, 1976.

A. Memmolo, M. Bernardini, and S. Pirozzoli. Scrutiny of buffet mechanisms in transonic flow. *International Journal of Numerical Methods for Heat & Fluid Flow*, in press. doi: 10.1108/HFF-08-2016-0300.

FR Menter. A comparison of some recent eddy-viscosity turbulence models. *Journal of Fluids Engineering*, 118(3):514–519, 1996.

A. R. G. Mundell and D. G. Mabey. Pressure fluctuations caused by transonic shock/boundary-layer interaction. *Aeronaut J*, pages 274–81, 1986.

Y Nagano and C Kim. A two-equation model for heat transport in wall turbulent shear flows. *Journal of heat transfer*, 110(3):583–589, 1988.

Jens Nitzsche. A numerical study on aerodynamic resonance in transonic separated flow. 2009.

Nora Okong'o and Doyle Knight. Compressible large eddy simulation using unstructured grids: channel and boundary layer flows. *AIAA Paper*, (98-3315), 1998.

Paolo Orlandi. *Fluid flow phenomena: a numerical toolkit*, volume 55. Springer Science & Business Media, 2012.

H. H. Pearcey. A method for the prediction of the onset of buffeting and other separation effects from wind tunnel tests on rigid models. Technical report, AGARD Report 223, 1958.

H. H. Pearcey and D. W. Holder. Simple methods for the prediction of wing buffeting resulting from bubble type separation. Technical Report NPL AERO-REP-1024, National Physical Laboratory, 1962.

Allan D Pierce et al. *Acoustics: an introduction to its physical principles and applications*, volume 678. McGraw-Hill New York, 1981.

S Pirozzoli, J Larsson, JW Nichols, M Bernardini, BE Morgan, and SK Lele. Analysis of unsteady effects in shock/boundary layer interactions. *Annu. Res. Briefs*, pages 153–164, 2010a.

Sergio Pirozzoli. Generalized conservative approximations of split convective derivative operators. *Journal of Computational Physics*, 229(19):7180–7190, 2010.

Sergio Pirozzoli. Stabilized non-dissipative approximations of euler equations in generalized curvilinear coordinates. *Journal of Computational Physics*, 230(8): 2997–3014, 2011a.

Sergio Pirozzoli. Numerical methods for high-speed flows. *Annual review of fluid mechanics*, 43:163–194, 2011b.

Sergio Pirozzoli and Tim Colonius. Generalized characteristic relaxation boundary conditions for unsteady compressible flow simulations. *Journal of Computational Physics*, 248:109–126, 2013.

Sergio Pirozzoli, Matteo Bernardini, and Francesco Grasso. Direct numerical simulation of transonic shock/boundary layer interaction under conditions of incipient separation. *Journal of Fluid Mechanics*, 657:361–393, 2010b.

T J Poinsot and SK Lele. Boundary conditions for direct simulations of compressible viscous flows. *Journal of computational physics*, 101(1):104–129, 1992.

Stephen B Pope. Turbulent flows, 2001.

S Raghunathan, RD Mitchell, and MA Gillan. Transonic shock oscillations on naca0012 aerofoil. *Shock Waves*, 8(4):191–202, 1998.

Patrick J Roache. Quantification of uncertainty in computational fluid dynamics. *Annual review of fluid Mechanics*, 29(1):123–160, 1997.

J-Ch Robinet. Bifurcations in shock-wave/laminar-boundary-layer interaction: global instability approach. *Journal of Fluid Mechanics*, 579:85–112, 2007.

Philip L Roe. Approximate riemann solvers, parameter vectors, and difference schemes. *Journal of computational physics*, 43(2):357–372, 1981.

Frederick W Roos. Some features of the unsteady pressure field in transonic airfoil buffeting. *J. AIRCRAFT*, 17(11):781–788, 1980.

Filippo Sabetta. *Gasdinamica*. Università La Sapienza, 2009.

Fulvio Sartor, C Mettot, R Bur, and D Sipp. Unsteadiness in transonic shock-wave/boundary-layer interactions: experimental investigation and global stability analysis. *Journal of Fluid Mechanics*, 781:550–577, 2015.

Philipp Schlatter and Ramis Örlü. Turbulent boundary layers at moderate reynolds numbers: inflow length and tripping effects. *Journal of Fluid Mechanics*, 710: 5–34, 2012.

J Schulze and J Sesterhenn. Optimal distribution of porous media to reduce trailing edge noise. *Computers & Fluids*, 78:41–53, 2013.

Leonid Ivanovich Sedov. *Similarity and dimensional methods in mechanics*. CRC press, 1993.

Chi-Wang Shu. High-order finite difference and finite volume weno schemes and discontinuous galerkin methods for cfd. *International Journal of Computational Fluid Dynamics*, 17(2):107–118, 2003.

Joseph Smagorinsky. General circulation experiments with the primitive equations: I. the basic experiment. *Monthly weather review*, 91(3):99–164, 1963.

Alexander J Smits and Jean-Paul Dussauge. *Turbulent shear layers in supersonic flow*. Springer Science & Business Media, 2006.

P. R. Spalart, W-H. Jou, M. Strelets, and S. R. Allmaras. Comments on the feasibility of LES for wings, and on a hybrid RANS/LES approach. In C. Liu and Z. Liu, editors, *Proc. 1st AFOSR International Conference*, pages 137–147. Greyden Press, 1997.

Philipe R Spalart, Steven R Allmaras, et al. A one equation turbulence model for aerodynamic flows. *RECHERCHE AEROSPATIALE-FRENCH EDITION-*, pages 5–5, 1994.

Philippe R Spalart, Shur Deck, ML Shur, KD Squires, M Kh Strelets, and A Travin. A new version of detached-eddy simulation, resistant to ambiguous grid densities. *Theoretical and computational fluid dynamics*, 20(3):181–195, 2006.

Bo Strand. Summation by parts for finite difference approximations for d/dx. *Journal of Computational Physics*, 110(1):47–67, 1994.

Damien Szubert, Ioannis Asproulias, Fernando Grossi, Régis Duvigneau, Yannick Hoarau, and Marianna Braza. Numerical study of the turbulent transonic interaction and transition location effect involving optimisation around a supercritical aerofoil. *European Journal of Mechanics-B/Fluids*, 55:380–393, 2016.

TETSURO TAMURA and KUNIO KUWAHARA. Numerical analysis on aerodynamic characteristics of an inclined square cylinder. In *20th Fluid Dynamics, Plasma Dynamics and Lasers Conference*, page 1805, 1989.

P Thiede, P Krogmann, and E Stanewsky. Active and passive shock/boundary layer interaction control on supercritical airfoils. Technical report, DEUTSCHE FORSCHUNGS-UND VERSUCHSANSTALT FUER LUFT-UND RAUMFAHRT EV GOETTINGEN (GERMANY FR), 1984.

M. Thiery and E. Coustols. URANS computations of shock induced oscillations over 2D rigid airfoils: influence of test section geometry. *Flow, Turbulence and Combustion*, 74:331–54, 2005.

H. Tijdeman. Investigation of the transonic flow around oscillating airfoils. Technical Report NLR TR 77090 U, National Aerospace Laboratory, 1977.

Emile Touber and Neil D Sandham. Large-eddy simulation of low-frequency unsteadiness in a turbulent shock-induced separation bubble. *Theoretical and Computational Fluid Dynamics*, 23(2):79–107, 2009.

Ricardo Vinuesa, Seyed M Hosseini, Ardeshir Hanifi, Dan S Henningson, and Philipp Schlatter. Pressure-gradient turbulent boundary layers developing around a wing section. *Flow, Turbulence and Combustion*, pages 1–29, 2017.